Subtle traps in sedimentary basins and their importance to hydrocarbon exploration

Nicholas Ian Porteous Ward

Submitted in partial fulfilment of the requirements for the degree of Ph.D.

Cardiff University

July 18

DECLARATION

This work has not been submitted in substance for any other degree or award at this or any other university or place of learning, nor is being submitted concurrently in candidature for any degree or other award.

Signed …… (candidate) Date ……

STATEMENT 1

This thesis is being submitted in partial fulfilment of the requirements for the degree of PhD

Signed ……..…… (candidate) Date ……

STATEMENT 2

This thesis is the result of my own independent work/investigation, except where otherwise stated, and the thesis has not been edited by a third party beyond what is permitted by Cardiff University's Policy on the Use of Third Party Editors by Research Degree Students. Other sources are acknowledged by explicit references. The views expressed are my own.

Signed ……..……..…… (candidate) Date ……

STATEMENT 3

I hereby give consent for my thesis, if accepted, to be available online in the University's Open Access repository and for inter-library loan, and for the title and summary to be made available to outside organisations.

Signed ……..…..….. (candidate) Date ……

STATEMENT 4: PREVIOUSLY APPROVED BAR ON ACCESS

I hereby give consent for my thesis, if accepted, to be available online in the University's Open Access repository and for inter-library loans **after expiry of a bar on access previously approved by the Academic Standards & Quality Committee.**

Signed ……..…… (candidate) Date ……

Abstract

This thesis uses high-quality 3D seismic data from the Broad Fourteens Basin (Southern North Sea), Espírito Santo Basin (SE Brazil), and Taranaki Basin (New Zealand) to characterise the evolution of geological structures related to differential compaction and subsidence; also known as *subtle hydrocarbon traps*. Each chapter tackles deformation over a different geological feature, spanning from salt-withdrawal basins, to submarine channel complexes and associated mass-transport deposits. These chapters subsequently discuss the impact the results have on the hydrocarbon industry. Included in these discussions are the importance of subtle traps on carbon capture and storage, local sealing potential, and reservoir distribution.

The Broad Fourteens Basin dataset was used to investigate concentric faults associated with salt withdrawal from below Triassic units. Throw-depth and throw-distance plots helped to understand the growth histories of the concentric faults. It was shown that these faults formed as a result of the bending of strata due to differential subsidence during salt withdrawal. Slip tendency analyses assessed the likelihood for faults to reactivate and transmit fluids whenever pore fluid pressure is increased. This approach simulated a typical profile during carbon capture and storage. It was shown that concentric faults will reactivate if pore fluid pressures are increased above 30 MPa at the relevant sub-surface depths, leaking fluids (including stored CO_2) past regional seal intervals in the basin.

Data from the Espírito Santo Basin were first used to assess the timing and magnitude of differential compaction over a submarine channel complex. Thickness-relief models helped quantify both the variations in thickness in overburden strata.

Smaller channels associated with downslope knickpoints were located within the channel complex. Differential compaction over channels produced four-way dip closures, as coarse-grained sediments were deposited at the knickpoint base. These provide adequate structural traps after early burial.

The Espírito Santo Basin 3D survey was used in a third chapter to assess how differential compaction affected sediment distribution over a mass-transport deposit. As large remnant and rafted blocks entrained within the MTD were buried, differential compaction produced anticlines over them. This created a rugged seafloor and the topographic highs confined sediment moving downslope, allowing it to pond in discrete depocentres.

Results from the data analysis chapters were compared with compaction-related structures documented in the published literature. A novel classification for subtle structural traps associated with differential compaction was produced, separating each feature into one of four types; Type A: folds over tectonic structures >2 km wide; Type B: folds over sedimentary packages, typically elongate, ~500 m to 5 km wide; Type C: folds over topographic features that are 20 m to 2 km wide; Type D: folds over sub-seismic/outcrop features no larger than 20 m. The results of the classification can be used as a first assessment when recognising a compaction-related fold and to rapidly assess its evolution and effectiveness as a subtle hydrocarbon trap.

Author note and status of publications

The results chapters presented in this thesis have been prepared as scientific papers for publication in international journals. Their present status is as follows:

Chapter 4 has been published as Ward, N.I., Alves, T.M. and Blenkinsop, T.G., 2016. Reservoir leakage along concentric faults in the Southern North Sea: Implications for the deployment of CCS and EOR techniques. *Tectonophysics*, 690, pp.97-116.

Chapter 5 has been published as Ward, N.I., Alves, T.M. and Blenkinsop, T.G., 2018. Differential compaction over Late Miocene submarine channels in SE Brazil: Implications for trap formation. *GSA Bulletin*, 130(1-2), pp.208-221.

Chapter 6 has been published as Ward, N.I., Alves, T.M. and Blenkinsop, T.G., 2018. Submarine sediment routing over a blocky mass-transport deposit in the Espírito Santo Basin, SE Brazil. *Basin Research*, 30(4), pp.816-834.

Although the articles are jointly co-authored with the project supervisors, the work presented in the publications is that of the lead author, Nicholas I. P. Ward. Editorial work was provided by the project supervisors in accordance with a normal thesis chapter.

Acknowledgements

Firstly, and most importantly, I would like to thank my parents. Were it not for their encouragement for me to pursue something I enjoy, I would not be researching something I have come to love. They have supported me throughout my Ph.D. and, along with my family, have always given me a reason to keep smiling.

I would like to thank Tiago Alves for all of his intellectual and moral support. He has gone above and beyond, responding to any query I pose almost immediately (even when on holiday). As my first supervisor, he has provided crucial editorial work and knowledge, especially when starting the doctorate. I am also grateful for the non-academic conversations and drinks we have shared from Cardiff, to Dorset, Toulouse and Cistierna. I was also like to acknowledge Thomas Blenkinsop, my second supervisor, for his editorial work and a strong knowledge base for any structural geology questions.

The work contained in this thesis was conducted as part of the Natural Environment Research Council (NERC) Centre for Doctoral Training (CDT) in Oil & Gas under its Extending the Life of Mature Basins research theme. It is funded by NERC and co-sponsored by Cardiff University. The work has been undertaken in the 3D Seismic Laboratory in the School of Earth and Ocean Sciences, for which Cardiff is thanked for its ongoing support of the lab and facilities. We are also grateful to Tullow Oil and CGG for provision of, and permission to publish examples from, their 3D seismic data volumes, and to Schlumberger for the donation of Petrel seismic interpretation software licences to Cardiff University, and to Midland Valley for Move™. NLOG and TNO are acknowledged for the well data in this work. The reviewers and editors (including J. Crider, I. Davison, T. Wrona, J. Ochoa, D. Schofield, S. Cardona, and R. Bell) for their constructive comments on the published manuscripts. I would also like to thank the staff of Cardiff University throughout both my undergraduate and postgraduate degrees. A special thanks extends to the Cistierna team (Lesley Cherns, Katie Dobbie, and David Buchs) for the fantastic field trips exploring for fossils and butterflies in Northern Spain; I will sorely miss the annual trip. I also thank Gwen Pettigrew for her daily humour and willingness to be disturbed by me most hours of the working day.

In the four years I have been studying for my Ph.D. there have been a number of colleagues in the office, all on journeys of their own, who have made the research more bearable. Whether that is a trip to the squash courts, a quick coffee break, crosswords, or just throwing the ball around, I am very grateful for all the friendships. These are: Chris, Aldina, Qin, Usman, Nathalia, Tao, James, Chantelle, Lilly, Roberto and Song. Outside the office, many people have made the Ph.D. experience so enjoyable, too many people to name. From daily lunchtime discussions on "what constitutes a sandwich", to Bute Park Bobble, to Friday at Five; each activity has been a welcome break from research. I think it vital to add one more activity to that list: T-Ball. Starting as a fun lunch time sport, it developed into a full social activity, reaching out to every new intake. The founding fathers (Bob, George, Michael, Micky and I) have maintained the core of this group and have (hopefully) developed something that will outlive our time at Cardiff University.

Through the NERC CDT, I have had access to bespoke industry training, and I am very grateful to John Underhill, Lorna Morrow, and Anna Clark for all the hard work they have put in to make this project become such a huge success. I have had some of my best times with the cohort and thank you all for being such a great group of people. Most of all, I would like to acknowledge three people who have truly become some of my best friends: Nathaniel, Sean, and Scott.

Finally, but most importantly, I would like to thank my girlfriend Millie. She has been my rock (excuse the pun) throughout the whole doctorate. She has been patient, continued to show me love and support, and has always been there for me when needed. She turns a frown into a smile and knows exactly how to make me laugh. I could not have made it through this Ph.D. without her: so for everything, thank you.

Table of Contents

List of Figures

List of Tables

List of Equations

Table of Nomenclature

Name	Description	Chapters
Anticline α	Inverted anticline in the centre of the Broad Fourteens Basin seismic volume. This is the location of one family of concentric faults in *Chapter 4*, and the structure responsible for anticline α^1.	4 & 7
Anticline β	A smaller anticline northwest of anticline α. It was not discussed in *Chapter 4* as there are no faults crossing it. However, it is the structure responsible for anticline β^1, as discussed in *Chapter 7*.	7
Anticline α^1	Compaction-related anticline over anticline α.	7
Anticline β^1	Compaction-related anticline over anticline β. This structure is smaller than anticline α^1.	7
Anticline γ^1	Compaction-related anticline over a salt diapir located to the west of the first two compaction related folds, Broad Fourteens Basin.	7
Anticline C^1	Compaction-related anticline over the submarine channel complex in the BES-2 survey, Espírito Santo Basin (SE Brazil).	5 & 7
Anticline δ^1	Compaction-related anticline over the Parihaka volcano in the Taranaki Basin, New Zealand. This structure is mentioned in *Chapter 7*.	7
MTD A	Large MTD analysed in *Chapter 6*. It contains very large slide blocks, and differential compaction occurs over each one of these latter.	6 & 7
Parihaka Volcano	Volcano in the Taranaki Basin dataset, part of the Miocene Mohakatino Volcanic Centre, as analysed in *Chapter 7*.	7
H_1	Top boundary of the Zechstein Group (Lower Permian)	4 & 7
H_2	Top boundary of the Upper Germanic Trias Group (Triassic)	4 & 7
H_3	Posidonia Shale (Jurassic)	4 & 7
H_4	Late Kimmerian I unconformity	4 & 7
H_5	Late Kimmerian II unconformity	4 & 7
H_6	Base Tertiary unconformity	4 & 7
C_1	Base of submarine channel complex (SE Brazil)	5 & 7

C_2	Base of isolated channels	5 & 7
C_3	Top of isolated channel fill	5 & 7
D_1	Top of channel complex fill (Unit I)	5 & 7
D_2	Top of overburden with uniform thickness (Unit II)	5 & 7
D_3	Top of overburden deformed by differential compaction (Unit III)	5 & 7
M_1	Base of MTD A	6 & 7
M_2	Top of MTD A	6 & 7
M_3	Top of seafloor-healing strata	6 & 7
M_4	Overburden strata by differential compaction	6 & 7
M_5	Seafloor	6 & 7
TB_1	Base of Giant Foresets Formation	7
TB_2	Continuous seismic reflection folded by differential compaction	7
TB_3	Younger seismic reflection folded by differential compaction	7
TB_4	Sea floor	7

CHAPTER ONE

Introduction and literature review

1. Introduction and literature review

1.1. Rationale and objectives of research

1.1.1. Rationale

The search for subtle fluid traps has interested scientists for decades (Berg, 1982, Baars and Stevenson, 1982, Bramwell et al., 1999, Ziolkowski et al., 1998, Halbouty, 1969, Gabrielsen et al., 1995, Li et al., 1982, Bulling and Breyer, 1989). Enthusiasm for subtle hydrocarbon traps stems from the stark reality that many 'typical' large-scale traps have been exploited in mature basins such as the North Sea, and in onshore regions such as the USA Midwest (Halbouty, 1969, Boldy and Fraser, 1999). Interest for exploration in these areas waned as traditional 2D seismic data became insufficiently accurate to resolve traps over more subtle features (Mostafa et al., 2015). With the advent of widespread 3D seismic data, subtle hydrocarbon traps became more viable exploration prospects. Subtle features could (and can, at present) be imaged in three-dimensions, reducing their overall "exploration risk" (Mostafa et al., 2015, Stirling et al., 2018). In turn, this new level of interest not only rejuvenated exploration in mature basins, but also became vital to frontier exploration work: many similar subtle traps have already been proven to contain large volumes of oil and gas (Stirling et al., 2018). The economic value of subtle traps in mature basins relies on the relative price of oil and exploration costs (including drilling). With improving technology and a

fluctuating oil price, if timed well, subtle traps can be economically beneficial and prolong the life span of mature hydrocarbon-rich basins (Malvić and Rusan, 2009, Boldy and Fraser, 1999).

The term 'subtle trap' was first suggested by Levorsen (1966) as a means to describe obscure traps that were not related to typical structural closures. Following the definitions of Levorsen (1966), Martin (1966), Halbouty (1969), and Gabrielsen et al. (1995), subtle traps have been classified as: a) true stratigraphic traps, caused by a lateral change in facies or reservoir properties; b) palaeogeomorphic traps, *i.e*. the shape of the surface of land or seabed; c) mixed traps, which are a combination of the trap in a) and b), and/or structural trap types. However, most formal definitions of 'subtle traps' in the literature do not account for structural closure. Recently, literature studies have adopted a descriptive definition of subtle traps; those traps that are hard to identify on seismic data or are much smaller than the 'typical' structural trap in many hydrocarbon prospects (Camp, 2008, Aizebeokhai and Olayinka, 2011).

Differential compaction and subsidence can be responsible for forming subtle closures. Commonly, these subtle closures form over discrete stratigraphic or sedimentary features, *e.g*. a location with a discrete lithological variation (Perrier and Quiblier, 1974, Trask, 1931, Corcoran, 2006, Aplin et al., 1995). Passive continental margins often contain discrete geological features (*e.g*. salt diapirs, volcanoes, channel systems, carbonate platforms) buried by thick,

undisturbed sedimentary packages. Most mature basins are also located on passive continental margins such as the North Sea, peri-Atlantic margins, West Siberia, and North Africa. Therefore, the drive to understanding subtle structural traps on passive margins compliments the ability to enhance the life of mature basins on continental margins across the world.

1.1.2. Research objectives

This thesis rigorously assesses the mechanisms forming subtle closures on passive continental margins. Differential compaction and differential subsidence provide the necessary driving forces behind the formation of the subtle traps analysed here. Hence, this work excludes subtle stratigraphic traps associated with local onlapping strata, pinch-outs and lateral facies variations that do not show clear structural controls on their formation (Halbouty, 1969). Faults, associated with local bending, subsidence and catastrophic fluid release, were also analysed as they can either greatly hinder, or enhance, petroleum prospects below subtle traps. In this thesis, high-quality 3D seismic data enabled the assessment of these structures in three different settings: a salt withdrawal basin (Broad Fourteens Basin, North Sea), an isolated submarine channel complex (Espírito Santo Basin, SE Brazil), and a mass-transport complex (Espírito Santo Basin, SE Brazil). A fourth dataset was analysed towards the end of the thesis, focusing on subtle traps formed over a large, buried volcano (Taranaki Basin,

New Zealand). These analyses were used to answer the following research hypotheses:

- **Concentric faults promote seal bypass of fluids, consequently hindering the trapping properties of subtle hydrocarbon traps**. If true, fluid flow features associated with these faults will be identified on 3D seismic and well data. If false, concentric faults will not be associated with fluid flow features, and will not reduce the integrity of subtle hydrocarbon traps – *see Chapter 4*.
- **During early burial, differential compaction deforms the sea floor, controlling sediment distribution in a basin on multiple scales**. If true, sediment transport systems, such as submarine channels and canyons, will be confined by the deformed structures. If false, the structures may be eroded and have no association with submarine sediment transport systems – *see Chapter's 5 and 6*.
- **The evolutions of subtle hydrocarbon traps is markedly distinct when considering different locations and geological features**. If true, there will not be a way to broadly classify these features and would need assessment on a case-by-case scenario. If false, then a classification scheme can be developed to categorise subtle hydrocarbon traps – *see Chapter 7*.

The following section comprises a literature review of the relevant topics studied in this thesis, detailing differential compaction (the processes behind it and where it occurs) and fault mechanics (specifically related to the results in *Chapter 4*).

1.2. Differential compaction

Differential compaction is a process that occurs in many a sedimentary basin around the globe (Alves, 2010, Carminati and Santantonio, 2005, Saller, 1996, Carver, 1968, Rusciadelli and Di Simone, 2007, Xu et al., 2015, Cosgrove and Hillier, 1999, Maillard et al., 2003, Mueller and Wanless, 1957, Laubach et al., 1999, Davies et al., 2009, Gómez and Vergés, 2005, Anderson and Franseen, 1991, Corcoran, 2008). This process generally occurs in basins that are not influenced by orogenic stresses during their sediment burial and subsequent compaction phases (Perrier and Quiblier, 1974, Rusciadelli and Di Simone, 2007, Bjørlykke and Høeg, 1997). To fully understand differential compaction, one must understand the mechanics and physics behind compaction. The vast portion of literature addressing the processes of compaction revolves around trying to understand the subsidence history of basins and, therefore, estimate the their burial histories, how compaction affects the seafloor morphology, and the influence compaction has on the subsequent deposition of sediments (Weller, 1959). It was suggested during a literature review by Aplin et al. (1995) that

compaction can exert a strong influence on fluid movement through sedimentary basins, the development of (local) overpressure and subsequent seal failure, evolution of porosity with burial depth, and the development of hydrocarbon maturation models. Being such a fundamental topic spanning geomechanics, structural geology, geophysics and sedimentary geology, this section provides a detailed description of the physics and processes involved in sediment compaction, and the causes of differential compaction in sedimentary basins.

1.2.1. Compaction terminology

The first formal documentation of compaction was by Athy (1930), who described compaction as being the reduction in volume of strata as a pressure is applied; in other words, a reduction in porosity with subsequent increase in density. Many scientists since have used the simple description of compaction as a reduction in pore volume in sediments under a lithostatic load (Perrier and Quiblier, 1974, Rusciadelli and Di Simone, 2007, Corcoran, 2008). Some other authors give more detailed explanations, including in the original definition differences between mechanical and chemical compaction, the reduction of strata thickness, and changes in effective stress at multiple scales of observation (Bjørlykke, 2014, Osborne and Swarbrick, 1997, Verwer et al., 2009, Aplin et al., 1995, Lahann and Swarbrick, 2011). One common thread to all the published definitions is that all sediments with a certain value for porosity are subject to

compaction once they are buried under a significant thickness of younger sediment (Perrier and Quiblier, 1974).

The most commonly accepted term used to express compaction is the porosity-depth function (Athy, 1930). This equation is an empirical formula and reflects an exponential or power-law function (Aplin et al., 1995). The porosity (φ) at a certain depth (z) relates to an initial porosity (φ_0) so that:

$$\phi = \phi_0 e^{-bz}$$

Equation 1.1

where b is the calibration constant (in m^{-1}) for the compacting unit. When plotted onto a graph representing porosity against depth, the trend line is logarithmic; a rapid decrease in porosity is recorded during the initial stages of burial, with the rate of porosity loss decreasing with depth (Fig. 1.1). Porosity continually decreases until a minimum porosity is attained in a volume of rock or sediment. This decrease in porosity is, in turn, controlled by the difference between pore fluid pressure (P_f) and vertical stress (σ_v), *i.e.* when the effective vertical stress reaches 0 and the pore fluids are able to support the weight of the overburden within the sediment pores (Lahann and Swarbrick, 2011, Smith, 1971, Osborne and Swarbrick, 1997). The vertical stress in a sedimentary basin can be expressed as:

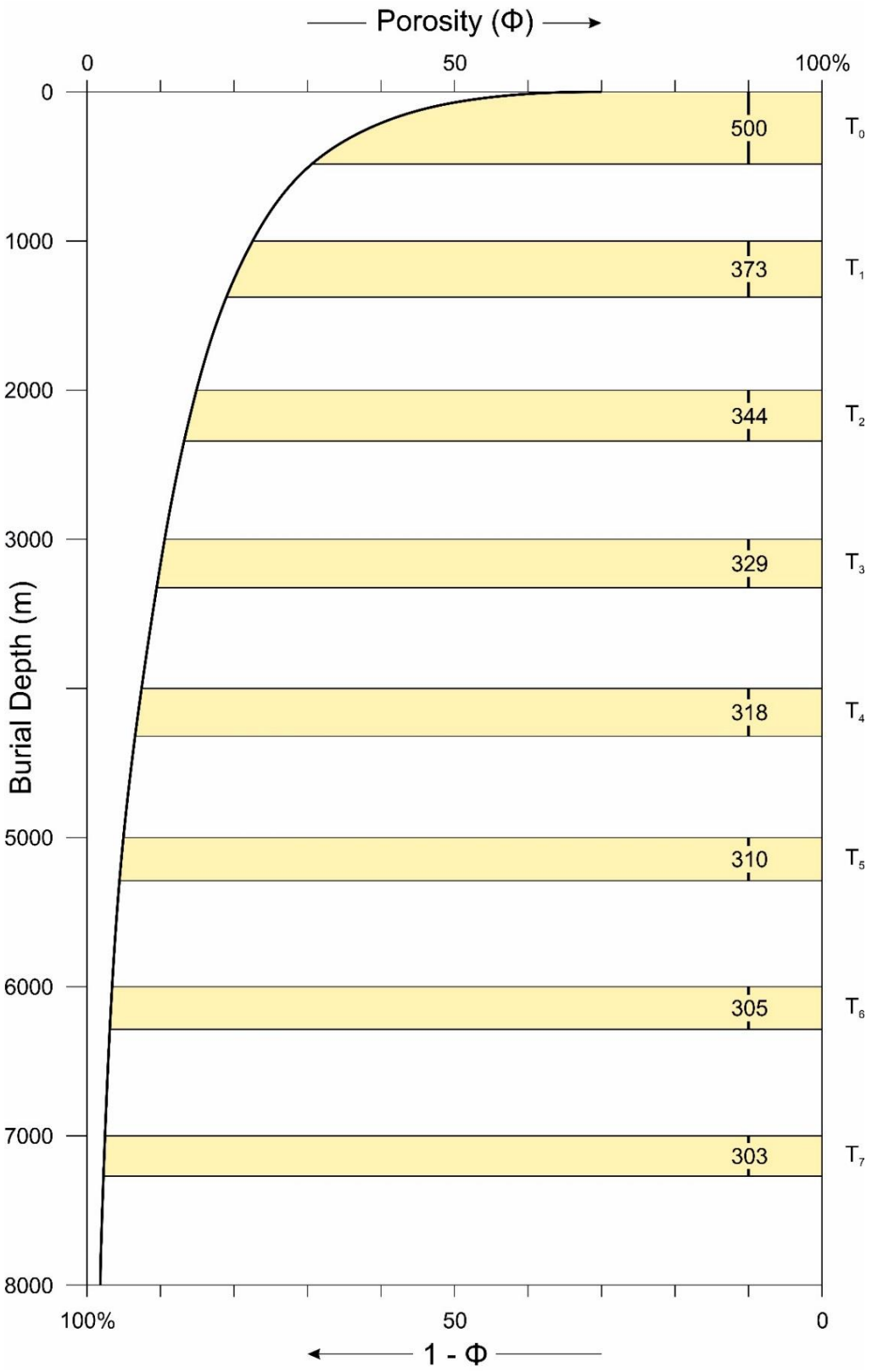

Fig. 1.1 Graph comparing changes in porosity with increasing burial depth. The thickness of a single unit (T_0) is used to represent the decrease in the rate of compaction at greater burial depths. Notice how the porosity never reaches 0% even when considering sub-surface depths of 8000 m. *Modified from Perrier and Quiblier (1974).*

$$\sigma_v = \rho g h$$

Equation 1.2

where ρ is the average bulk density, g is the standard acceleration due to gravity (9.8 m/s^2), and h is the vertical height of the overburden. The effective vertical stress (σ_v') is therefore given as:

$$\sigma_v' = \sigma - P_f$$

Equation 1.3

This equation is important because if the pore-fluid pressure decreases, the effective stress will increase and subsequent compaction will occur (Osborne and Swarbrick, 1997, Bjørlykke, 2014).

1.2.1.1. Mechanics of compaction

Compaction is either mechanical or chemical, depending on the processes causing it. To understand differential compaction, one must know whether a rock is primarily compacted by mechanical processes that occur during early burial to ~2-3 km depth, or by chemical compaction at depths >600 m (Bjørlykke, 2014, Powers, 1967, Bjørlykke and Høeg, 1997, Pouya et al., 1998, Davies, 2005, Lahann

and Swarbrick, 2011). Compaction via mechanical processes can, therefore, be deemed the dominant process at shallow burial depths, whereas chemical compaction tends to dominate at deeper burial depths (Pouya et al. 1998; Bjørlykke 2014).

When mechanical compaction is considered in the literature, it is often described as the rearrangement and breaking up of grains, expulsion of interstitial water from pore spaces, and the movement of softer minerals between more resistant minerals (Trask, 1931, Weller, 1959, Athy, 1930, Bjørlykke and Høeg, 1997, Davies, 2005, Snarskiy, 1961, Magara, 1976). As previously noted, compaction is directly linked to a reduction in porosity. One of the most important consequences of the destruction of pores is fluid expulsion. Pore water entrained between grains will slowly be forced out and into the surrounding rocks as the strata is buried (Snarskiy, 1961, Weller, 1959, Athy, 1930, Powers, 1967, Corcoran, 2008). Darcy's Law suggests that the water is expelled upwards into the overlying rocks, as long as there is no permeability barrier (Smith, 1971, Magara, 1976). In theory, the volume of water expelled will increase with depth until a point where no porosity or permeability remain (Magara, 1976). Powers (1967) suggests that by ~ 3000 ft (~ 915 m) below the surface most of the water in a mudstone should be expelled, with the remaining water forming a basal surface that cannot be squeezed out by the confining pressures associated with burial. In the event of there being a permeability barrier, overpressure can form (Osborne and Swarbrick, 1997, Smith, 1971, Lahann and Swarbrick, 2011).

Overpressure is used to describe pore fluid pressures that are higher than estimated for a normal hydrostatic fluid gradient at a given depth (Fig. 1.2). The hydrostatic gradient is the rate of change in fluid pressure with depth, i.e. the pressure exerted by a continuous column of fluid (Osborne and Swarbrick, 1997, Gaarenstroom et al., 1993). If the pore water is not expelled quickly enough, porosity can be preserved at depth as long as cementation does not take place within the pores. However, as there is no such thing as a 'perfect seal', fluids will slowly move through the rock units and overpressure will diminish through geological time (Osborne and Swarbrick, 1997).

As pressures and temperatures increase during progressive burial, chemical compaction starts to occur (Bjørlykke and Høeg, 1997, Davies, 2005, Powers, 1967, Corcoran, 2008, Pouya et al., 1998, Lahann and Swarbrick, 2011, Bjørlykke, 1999). Such a process is controlled by dissolution, precipitation, and later transformation of minerals (Pouya et al., 1998). The first two controls are intrinsically linked; thermogenic fluids dissolve minerals in the rocks, subsequently precipitating them within pores as cement (Dewers and Ortoleva, 1990, Osborne and Swarbrick, 1997, Bjørlykke and Høeg, 1997, Bjørlykke, 2014). This same phenomenon of *pressure solution* is a common cause of porosity reduction and chemical compaction in sandstones and limestones (Osborne and Swarbrick, 1997, Dewers and Ortoleva, 1990). The dissolution of mineral phases can cause minerals to pack closer together, but this depends on their type and

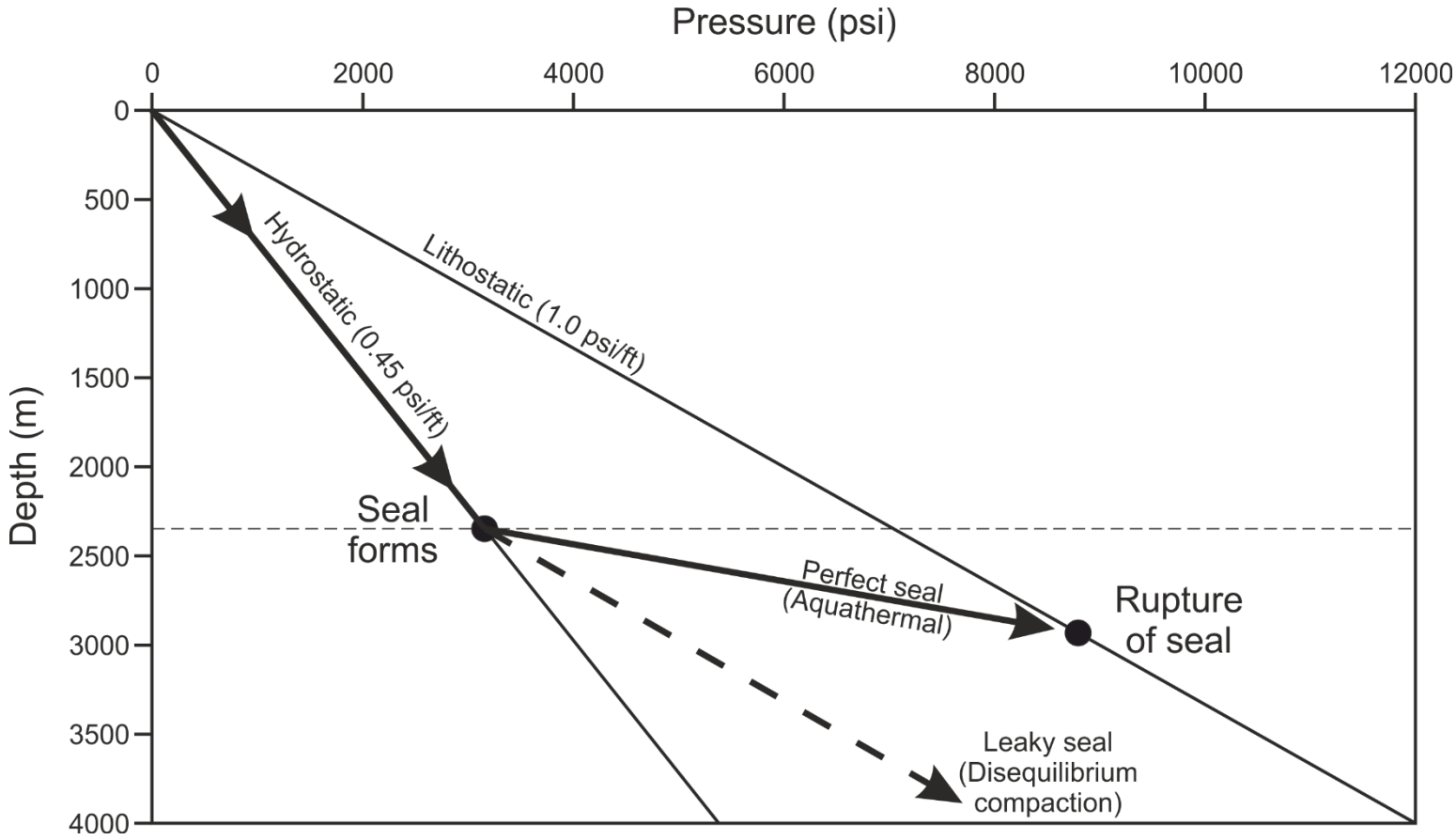

Fig. 1.2 Lithostatic and hydrostatic fluid gradients plotted to represent the boundary conditions of rocks under compaction. If the pore pressure falls along the hydrostatic line; it has maintained the pressure expected for a fluid at that given depth; presuming it is connected to the surface. A deviation from that line implies overpressure and, as a result, the pore fluids will take on the load of the overburden. *Modified from Osborne and Swarbrick (1997)*.

texture (Bjørlykke and Høeg, 1997). It is also important to note that the precipitation of cement leads to an increase in density (Bjørlykke, 2014).

The chemical conversion of minerals from one state to another is known as *diagenesis*. Chemical reactions driven by thermodynamics and kinetics alter mineral assemblages towards a more stable state with lower Gibbs Free Energy. Increasing the temperature can speed up the reaction rate, moving the mineral towards equilibrium (Bjørlykke, 2014). The depths and temperatures at which minerals will change are thus dependent on its chemical composition and texture (Bjørlykke and Høeg, 1997). For example, Powers (1967) noticed that montmorillonite changes to illite between ~1850 m and ~3050 m as it desorbs the remaining water within the mud. The water then undergoes a volume increase, creating an abnormally high pore-fluid pressure in the rock. This conversion does not happen in muds that are originally illite or kaolinite. In addition, Osborne and Swarbrick (1997) found that smectite to illite transformation also drive off water to increase the pore-fluid pressures, although this same increase is not enough to create overpressure in deeply buried rocks. The transformation of gypsum to anhydrite has also been discussed as a way of increasing subsurface fluid pressure. This was counteracted by Lahann and Swarbrick (2011) who believe that the smectite-illite conversion is capable of producing overpressure. They argued that when there is no mechanism for fluid transport, the vertical load is transferred to the expanding fluids.

Finally, Davies (2005) investigated the common change from silica Opal A to Opal B in silica-rich sediment. This process is capable of reducing volume in sediment and is primarily controlled by temperature. This conversion only requires burial depths of 500-700 m and can reduce the porosity of the rocks from ~70% to 30 %. In similar geological conditions to those described in Davies (2005), Bjørlykke (2014) identified carbonates that can undergo chemical compaction after only ~600 m burial, indicating that chemical compaction is not restricted to large burial depths typically beyond the extent of mechanical compaction (*i.e.* 2-3 km) (Bjørlykke 2014).

1.2.1.2. Lithological controls on differential compaction

Of all the controls on differential compaction, variations in lithology and mineralogical texture are regarded as the most influential (Trask, 1931). Differences in mineral size and texture is how siliciclastic sediments (i.e. muds, silts and sands) are defined. Mudstone, very fine grained, compacts more than sandstone, coarse grained (Athy, 1930, Mueller and Wanless, 1957, Perrier and Quiblier, 1974, Osborne and Swarbrick, 1997, Aplin et al., 1995, Bjørlykke and Høeg, 1997). During the initial stages of compaction water is driven out of the pores. It is therefore logical to assume that the rocks with the largest volume of pore space and fluids filling that space will compact the most under hydrostatic conditions. The relationship of water content to grain size is shown in Figure 1.3.

This graph shows that the initial water content of fine grains is much larger than that of coarse grains. Sandstones are estimated to have an initial porosity (prior to burial) between 35-50% (Nur et al., 1998, Osborne and Swarbrick, 1997). This is reduced to approximately 15-25% after mechanical compaction and chemical dissolution (Osborne and Swarbrick, 1997). Mudstones have an initial porosity between 65-80% (Osborne and Swarbrick, 1997, Smith, 1971), a value that can be reduced to 5-10% porosity due to the grain rearrangement, enhanced ductility at depth, and expulsion of fluids (Snarskiy, 1961, Osborne and Swarbrick, 1997, Perrier and Quiblier, 1974). Such a stark contrast in the porosity-depth profiles of sandstone and mudstone means the thickness changes due to compaction depend almost entirely on lithological variations within a sedimentary column (Fig. 1.4).

Relatively few studies have been completed on the compaction trends of other sedimentary rocks. Limestones and chalks can behave similarly to sandstones during gravitational loading (Anderson and Franseen 1991). However, the rock can be composed of minerals such as aragonite and high-Mg calcite, which are not as mechanically or chemically stable as quartz and feldspar. The carbonate minerals may dissolve and then precipitate as cement, reducing the pore space even at shallow depths (Bjørlykke and Høeg, 1997). Evaporites are the only (chemical) rocks that do not compact as they lack initial pore space. However, they can undergo a reduction in volume during burial, e.g. gypsum transforming to anhydrite at ~100 m depth (Perrier and Quiblier, 1974). Coal may

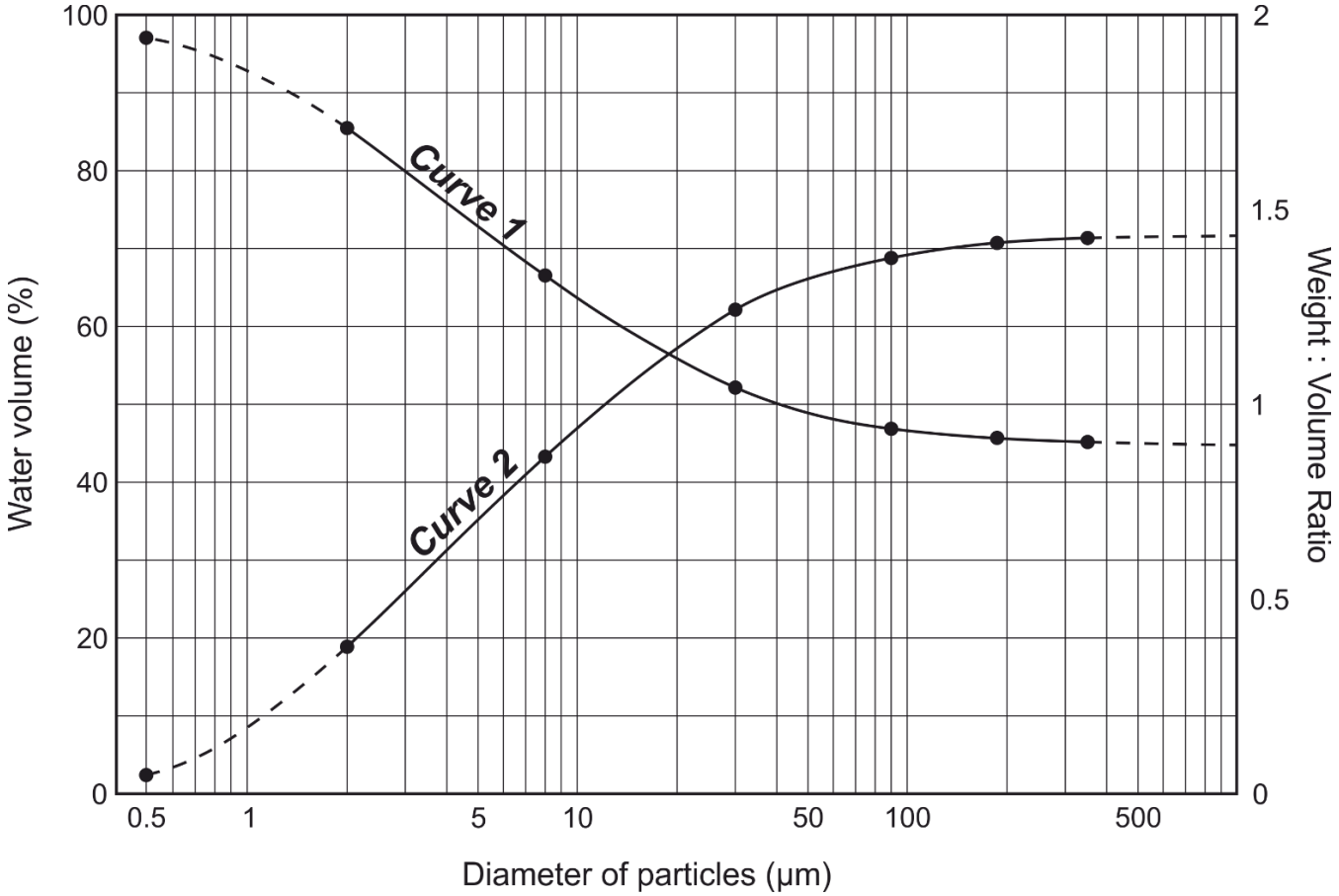

Fig. 1.3 Relationship between water content and particle sizes. Curve 1 represents the initial water volume in the pore space for particles of different sizes. Smaller particle sizes contain a higher percentage of water. Curve 2 correlates the weight:volume ratio of water in a rock to the particle size. This curve shows a reverse correlation when compared with curve 1; smaller particles have a lower weight:volume ratio when compared to larger particles. *Modified from Trask (1931).*

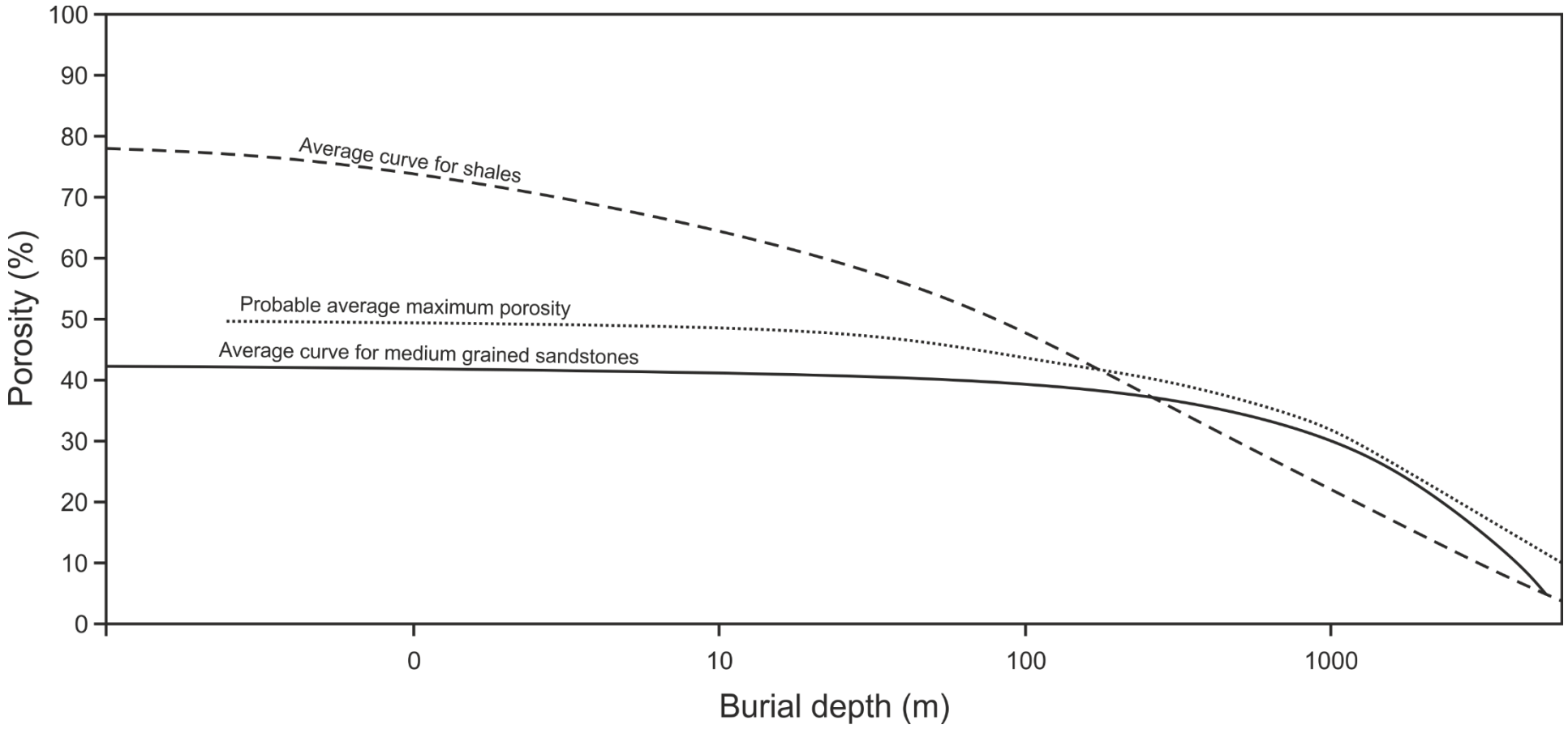

Fig. 1.4 Graph showing the porosity for sands and shales plotted against depth. Shales have a high initial porosity (<80 %), whereas sandstones have a much lower initial porosity (>40 %). The porosity profiles switch after a few hundred metres of burial, as shales compact more intensely during early mechanical burial when compared with sandstones. *Modified from Perrier and Quiblier (1974).*

compact significantly, but as they represent such a small amount of the basin stratigraphy, their reduction in thickness is often minimal (Perrier and Quiblier, 1974).

1.2.2. Differential compaction: from basin to outcrop scale

Differential compaction driven by changes in lithology can (and should) occur at any scale, if there is a noticeable difference in grain size and texture. At outcrop scale, lithified rocks or boulders are more competent that sediments surrounding them, and will compact less. On the seismic scale, sedimentary fairways can contain large quantities of sand compared to the hemipelagic fallout common to deep ocean basins. On a basin scale large, prograding deltas or submarine fans will contain more coarse-grained sediment than surrounding deposits. This section looks at examples of differential compaction from the literature at each of these three scales.

1.2.2.1. Differential compaction at basin scale

There are few examples of differential compaction on the scale of a sedimentary basin. Not least of all, most basins in the world have experienced some sort of tectonic event that was capable of overwriting the impact of differential compaction at a local scale (Gómez and Vergés, 2005). Nevertheless,

differential compaction is able to enhance deformation caused by tectonic compression. Gómez and Vergés (2005) studied how tectonics and differential compaction acted together to form structural highs along the Helland Hansen Arch and Vema Dome, on the Mid-Norwegian extensional margin. The structural highs that separate two adjacent basins are characterised by a relatively thin sedimentary cover, which did not compact as much as the thick sedimentary package deposited within the basin (Fig. 1.5a). In this example, tectonic folding was previously used as an explanation for the observed strata folding. Gómez and Vergés (2005) discovered that the deformation over the domes had periods where differential compaction was the only cause for the folding. They concluded that post-break-up deformation in sedimentary basins can be largely overestimated if the effects of differential compaction are ignored.

Considering compaction over structural highs, Maillard et al. (2003) investigated how a basement step affected differential compaction in the Ligurian-Provençal Basin, NW Mediterranean (Fig. 1.5b). The basement step is effectively a faulted block; a sudden increase in depth of the basement due to the downthrown hanging-wall of a normal fault (*see Figure 1.5b* for an example of a basement step caused by faulting). Pre-Messinian sediments were accumulated adjacently to the basement step, over the footwall, and were subsequently buried by the Messinian evaporites. As vertical load increased, the pre-Messinian

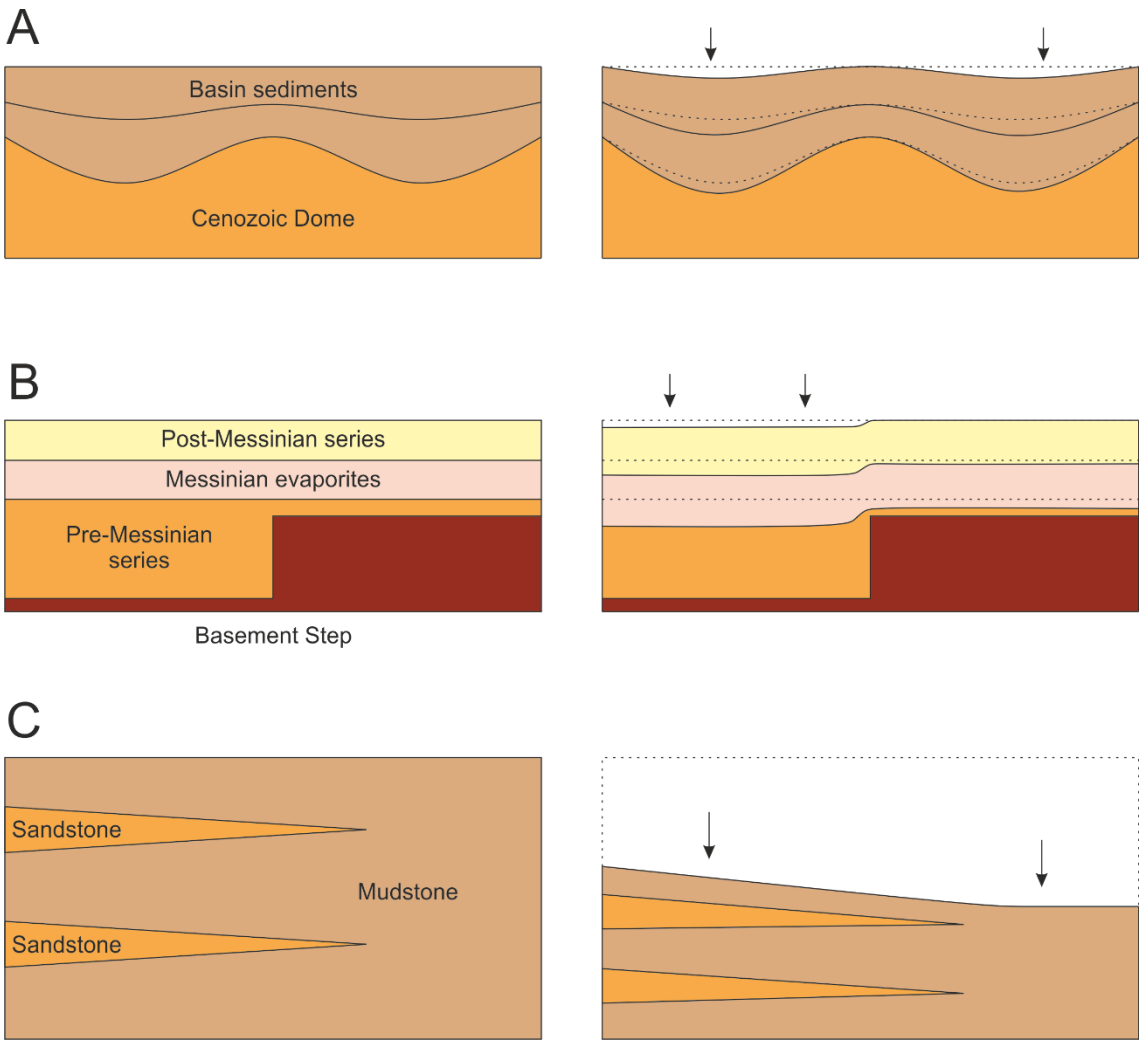

Fig. 1.5 Diagrams showing where differential compaction may occur within a sedimentary basin. a) Differential compaction over a structural high. Sediments in the lows compact more than sediments on the structural high, creating topographic relief on the sea floor. *Modified from Gómez and Vergés (2005)*. b) A basement step causes differential compaction as the adjacent strata compacts more than the basement rocks on this same morphologic step. *Modified from Maillard et al. (2003).* c) Sandstone wedges resist compaction when compared to a mudstone, therefore dipping the seafloor towards the mudstone. *Modified from Carver (1968).*

sediment started to compact. Basement rocks resisted compaction and a fold developed in the Messinian and post-Messinian series (Fig. 1.5b).

Faults will form during differential compaction whenever there is a large enough difference in compaction rates between adjacent volumes of sediment (Nunn, 1985, Maillard et al., 2003, Carver, 1968, Xu et al., 2015). In the Gulf of Mexico, Carver (1968) identified faults on the updip side of major facies and thickness changes; sandstone wedges interbedded within a thick mudstone unit. A model was, therefore, created by the latter authors to replicate the thickness changes occurring during compaction between the sandstone and mudstone. The results showed that during differential compaction, simple shear failure accommodated the difference in thickness reduction between the sandstones and mudstones (Fig. 1.5c). The faults generated by this process were perpendicular to the direction of facies changes, correlating to faults in the Gulf of Mexico. Xu et al. (2015) also analysed faults developed along a sandstone-mudstone boundary in the northern Bozhong Subbasin, Bohai Bay Basin, China. They explained the existence of three groups of faults to be related to: i) forced compaction of porous clay sediments, ii) areas buried by rapid sedimentation accumulation (e.g. turbidite channels), and iii) the updip side of facies or thickness changes.

1.2.2.2. Differential compaction at trap scale

Folds produced by differential compaction can form very effective structural traps for hydrocarbons (Cosgrove and Hillier, 1999, Corcoran, 2006, Gay et al., 2006b, Xu et al., 2015, Alves, 2010), as well known oil and gas fields in the North Sea are producing from compaction-related traps (Cosgrove and Hillier, 1999, Corcoran, 2006), to provide an example. Tertiary traps are formed over sedimentary fairways and turbidite channels, where sands were deposited along the thalweg, and mudstones accumulated on its margins (Fig. 1.6a). This leads to mounding over the sedimentary body after it is buried (Corcoran, 2006, Cosgrove and Hillier, 1999). Of the many Palaeogene fields in the North Sea relating to submarine channels and fans, some of the most well-known are: Alba field, Gannet Field, Maculloch Field, Brenda Field, Callanish Field and Chestnut Field (Armstrong et al., 1987, Corcoran, 2006). Each of these fields have reservoir rocks deposited along the base of the sediment fairway, are trapped by differential compaction, and are sealed both laterally and vertically by mudstone (*see Figure 1.6b* for an example of this type of closure).

If overpressure moves the pore fluid pressure beyond the fracture pressure (pressure needed to fracture the rocks), faults will form and catastrophic fluid escape may occur (Osborne and Swarbrick, 1997, Cosgrove and Hillier, 1999, Gay et al., 2006b). This can lead to migration of hydrocarbons from

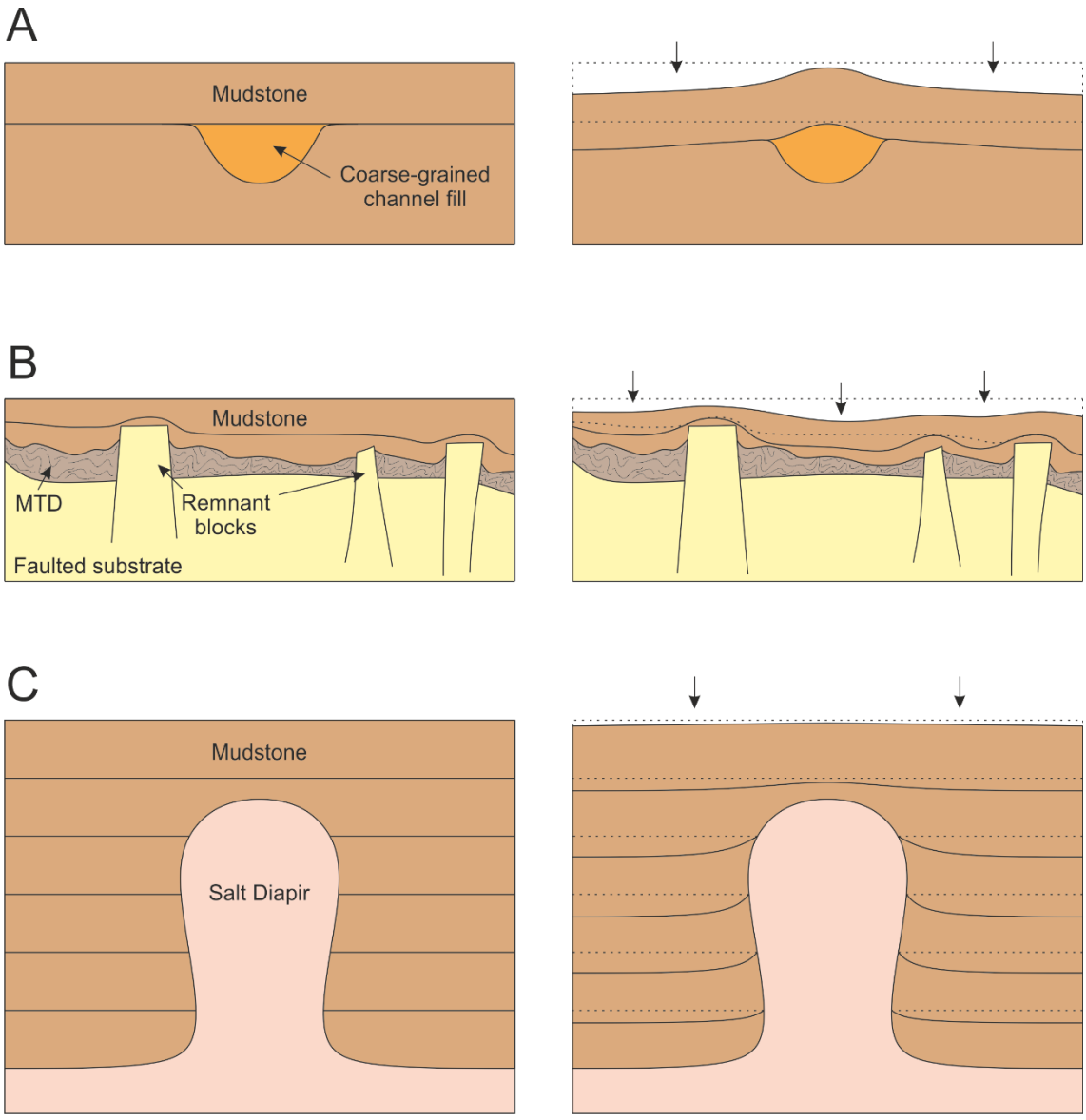

Fig. 1.6 Diagrams showing where differential compaction may create effective hydrocarbon traps. a) Coarse-grained channel fill, often comprising turbidite sands, do not compact as much as overbank and overlying fine-grained strata. This creates an anticline over the channel axis. *Modified from Ward et al. (2018)*. b) Differential compaction over a mass transport deposit (MTD) can lead to anticlines over large, lithified blocks, and depressions between them, as the debrites compact more. *Modified from Alves (2010)*. c) Salt does not compact. Therefore, the adjacent sediments will deform around a salt diapir during differential compaction, creating drag folds. *Modified from Stewart (2006)*.

reservoir intervals towards the surface. Xu et al. (2015) and Gay et al. (2006b) found this latter process within the Bozhong Sub-basin, China, and the Lower Congo Basin, offshore West Africa.

Burial of mass transport deposits (MTDs) can also lead to differential compaction (Alves, 2010, Alves and Cartwright, 2010). The rheological changes between the intact blocks and the surrounding debrites means that the overburden will be folded, creating anticlines above competent (lithified) slide blocks, and depocentres over the compacting debrites (Fig. 1.6b).

Salt diapirs are complex structures in the subsurface, often deforming the surrounding stratigraphy. Stewart (2006) and Perez-Garcia et al. (2013) highlighted drag fold geometries in strata adjacent to diapirs. Stewart (2006) used examples from the North Sea, Caspian Sea, Gulf of Mexico, and the South Atlantic Ocean, whereas Perez-Garcia et al. (2013) used an example from the Sørvestsnaget Basin, SW Barents Sea. The cause of differential compaction in these two examples is that salt is incompressible and will not exhibit thickness loss during compaction (Perrier and Quiblier, 1974, Stewart, 2006). However, the strata surrounding a salt diapir will compact (Fig. 1.6c). With a 5-km-tall diapir the adjacent strata may compact as much as 300 m (Stewart, 2006). The sediments over the crest of the diapir may also fold as a result of differential compaction, once again due to the relative incompressibility of the salt when compared with the surrounding strata (Fig. 1.6c). A crestal horst may develop atop the diapir,

possibly causing faults to form, dipping towards the crest (Stewart, 2006, Perez-Garcia et al., 2013).

1.2.2.3. Differential compaction at outcrop scale

Evidence for differential compaction at outcrop covers a wide range of scales. The outcrops can show sub-metre changes in compaction around small blocks (Bryant and Miall, 2010, Corcoran, 2008), or can show tilting of units over a couple of hundred metres (Carminati and Santantonio, 2005, Verwer et al., 2009, Corcoran, 2008, Laubach et al., 1999, Saller, 1996, Rusciadelli and Di Simone, 2007).

The most widely documented type of outcrop displaying evidence of differential compaction are carbonate platforms. Carminati and Santantonio (2005) measured bedding dips of basin strata onlapping a carbonate platform in the Central Apennines, Italy. The fine-grained basin sediments were deposited horizontally, onlapping unconformably against an inclined carbonate reef (Fig. 1.7a). Compaction was greater in the fine-grained basin sediments compared to the carbonate platform, increasing the dip of the strata towards the centre of the basin. This, in essence, is very similar to the outcrop observed by Rusciadelli and Di Simone (2007). A cemented Cretaceous carbonate platform (once again located in the central Apennines, Italy) resisted compaction and a wedge-shaped unit of

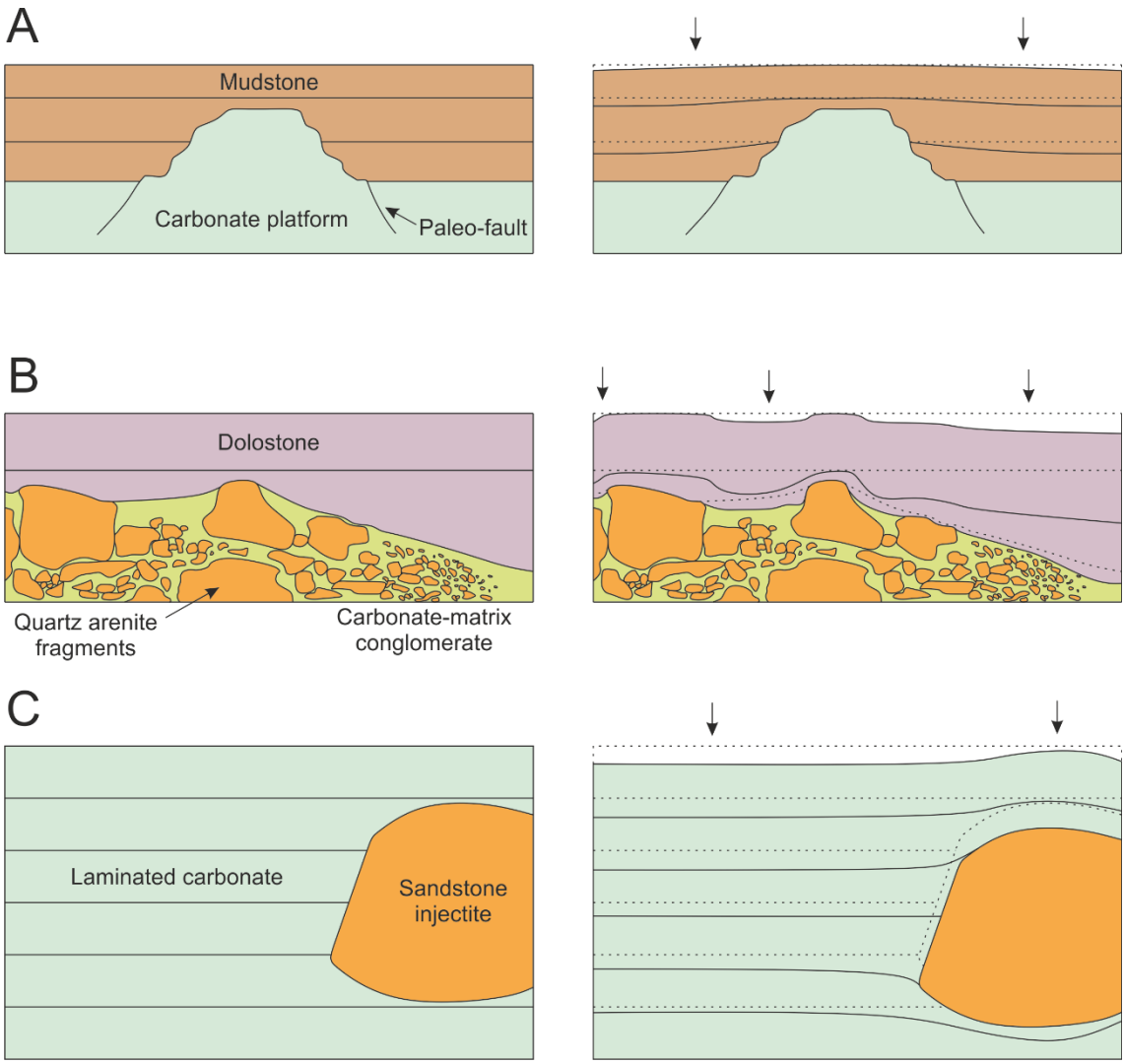

Fig. 1.7 Diagrams showing differential compaction at outcrop. a) An isolated carbonate platform shaped by ancient faults acts as a structural high. Differential compaction occurs over and around this carbonate platform as the onlapping basin strata is compacted more than the strata on the platform. *Modified from Carminati and Sanantonio (2005)*. b) Dolostones folded over the top of very hard quartz arenite fragments within a carbonate-matrix conglomerate. The matrix undergoes differential compaction with respect to the fragments and blocks, producing folds over the fragments. *Modified from Corcoran (2008)*. c) Differential compaction associated with a sandstone injectite during early burial. The sandstone was forced downwards into the laminated carbonates, which were folded over the top of the injectite. *Modified from Bryant and Miall (2010).*

highly compactible slope sediments onlapped the platform to record considerable compaction during burial. Not only did differential compaction increase the dip of the strata, it also created basinward thickening and divergence of sediment packages. In contrast to data from Italy, Verwer et al. (2009) used geopetal structures as evidence to rule out rotation of the basin strata was due differential compaction. They did agree that differential compaction led to an exaggeration of slope angle, rotating it by ~4%.

On a local scale, differential compaction can occur over isolated, competent rocks within a less competent matrix. For example, Corcoran (2008) studied a carbonate matrix conglomerate, made up of quartz arenite fragments. The boulders were up to 5 m in width and were overlain by dolostones. These units acted in a very similar way during compaction to the MTD in s*ection 1.2.2.2.* The dolostone draped over the boulders as the carbonate matrix compacted significantly, tilting the strata above the areas in which the conglomerate was absent (Fig. 1.7b). Significant thinning was also observed over the crest of the quartz arenite fragments, indicating that differential compaction occurred early in the burial process (Alves, 2010, Corcoran, 2008, Bryant and Miall, 2010). Similar structures are found above sandstone injectites (Bryant and Miall, 2010) (Fig. 1.7c). In the Navajo Canyon of the Colorado Plateau, USA, deformation above injected sandstones occurred in the shallow subsurface where the overlying carbonate muds were recently consolidated, but not fully compacted.

1.3. Fault mechanics and kinematics

It is essential to understand fault mechanics and kinematics when investigating processes of fluid flow and compartmentalisation in a reservoir interval. During differential compaction, these faults can be generated by force folding over the less compacted strata (Carver, 1968, Xu et al., 2015, Maillard et al., 2003). Fault mechanics regards the interaction of faults with a given stress field, how they can grow and propagate, and their displacement/length histories (Scholz, 2007). Fault kinematics show the strain history of a fault and its motion through time (Stewart, 2006).

1.3.1. Normal, reverse, and strike-slip fault mechanics

Anderson (1905) and (1951), described the relationships between distinct fault planes and the corresponding stresses acting perpendicular to each other, with one stress always being near vertical (σ_v) and the other two horizontal ($\sigma_H > \sigma_h$). The orientation of each principal stress denotes the type of fault produced. Using the typical 'Andersonian model' (*i.e.* Fig. 1.8), in faults recording normal displacements the maximum principal stress (σ_1) is vertical, whereas the minimum principal stress (σ_3) is horizontal (Fig. 1.8). Therefore, the intermediate principal stress (σ_2) can be inferred as being parallel to the fault plane. In thrust faults σ_1 is horizontal and σ_3 is vertical. The intermediate stress (σ_2) is again

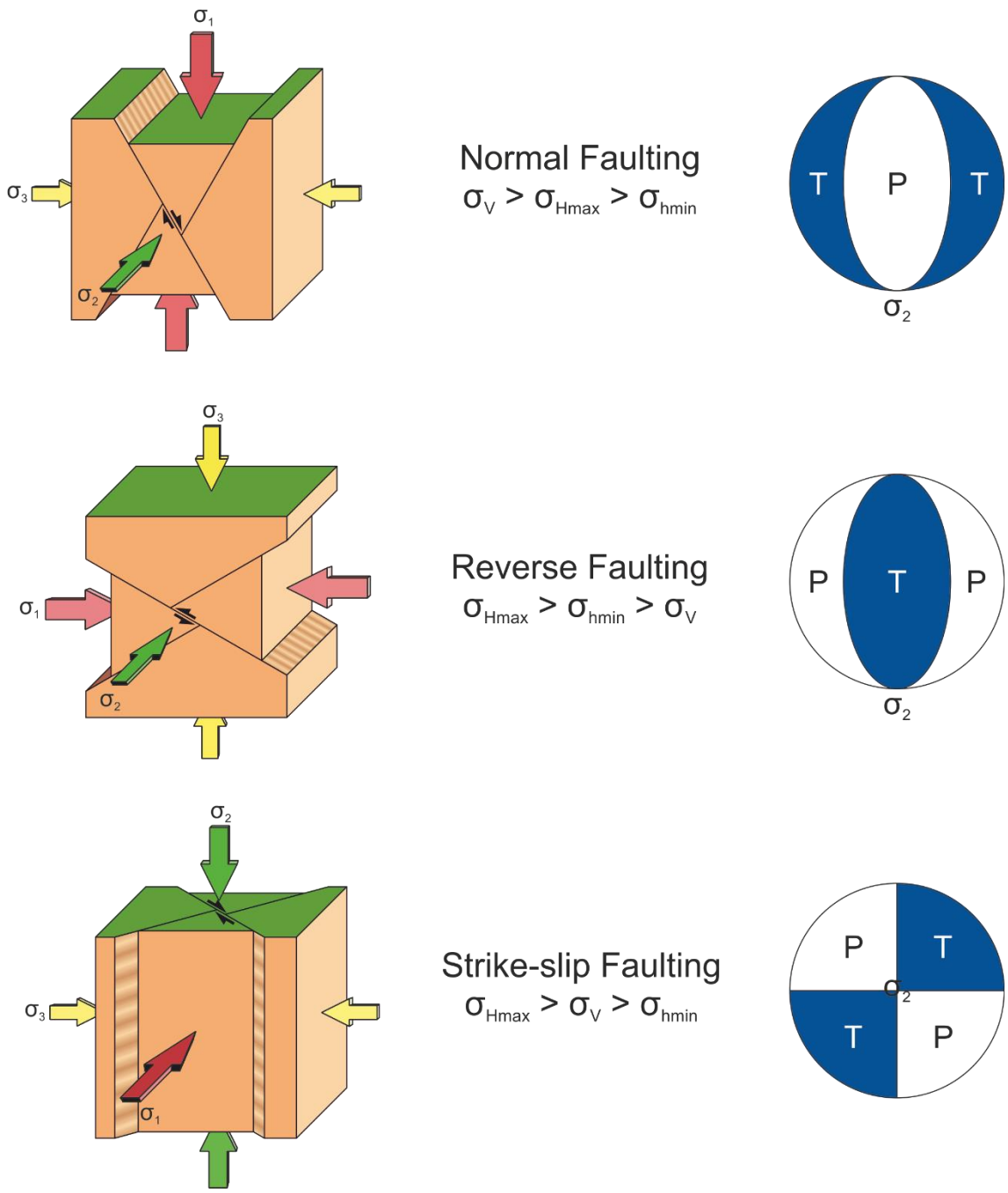

Fig. 1.8 Beach-ball diagrams demonstrating Anderson's classification scheme for the orientations of principal stresses in conjugate sets of faults. In the beach ball diagram, "P" – component of the rock under compression, "T" – component of rock under tension.

horizontal, parallel to the strike of the fault plane. In strike-slip faults both σ_1 and σ_3 are roughly horizontal, indicating that σ_2 is the vertical stress axis (Anderson, 1905). Often, such end members do not occur in the crust. Four other examples are outlined by Bott (1959); radial extension, radial compression, normal/strike-slip faulting and reverse/strike-slip faulting. In the case of radial extension, $\sigma_v >> \sigma_H = \sigma_h$, where $\sigma_1 = \sigma_v$, and σ_2, σ_3 are σ_H, σ_h respectively. Therefore, normal faults can occur in any direction in radial extension. With radial compression, $\sigma_H = \sigma_h >> \sigma_v$, where σ_1, σ_2 are σ_H σ_h respectively and $\sigma_3 = \sigma_v$. The other two styles of tectonic faulting are described in detail in *section 1.3.2* and are intermediate cases. Both examples comprise a mix of strike-slip and either normal or reverse faulting. Such intermediates are known as oblique slip and the most commonly occur in reactivated faults. Normal-oblique slip occurs when $\sigma_v = \sigma_H > \sigma_h$. Reverse-oblique slip occurs when $\sigma_H > \sigma_v = \sigma_h$ (Bott, 1959).

In a homogeneous crust with typical values of internal friction, faults develop at ~ 30° to σ_1. Obeying Andersonian stress states, end-member normal faults should dip at ~ 60°, thrust faults at ~ 30° and strike-slip faults at ~ 90° (Sibson, 1985, Holohan et al., 2013, Ranalli, 2000, Scholz, 2002).

1.3.2. Oblique-slip fault mechanics

Oblique-slip faulting refers to movement along a fault that is not parallel or perpendicular to σ_h. It will thus have a component of dip-slip and strike-slip (Crider, 2001, Bott, 1959, Holohan et al., 2013) (Fig. 1.9). The majority of oblique-slip faults is generated by the reactivation of original faults; primary slip conforms to a classical 'Andersonian' faulting regime, with secondary slip being reoriented along the same fault. As failure depends on the stress regime, displacement can occur in every direction (Bott, 1959). Primary oblique faults are less common, though examples may include fractures above basement faults and concentric faults (Bott, 1959). New faults likely form at a similar orientation to strike of the basement fault, as it locally reduces the stress needed for failure. Consequently, if the orientation of the main stress component is oblique to the strike of the fault, an oblique-slip fault will form (Bott, 1959). In some circular subsiding basins (e.g. salt withdrawal basins), concentric faults will accommodate such type of displacement. Along a single fault, there may be segments that have opposing senses of movement, meaning there must be a transition zone between them with predominant oblique-slip (Holohan et al., 2013).

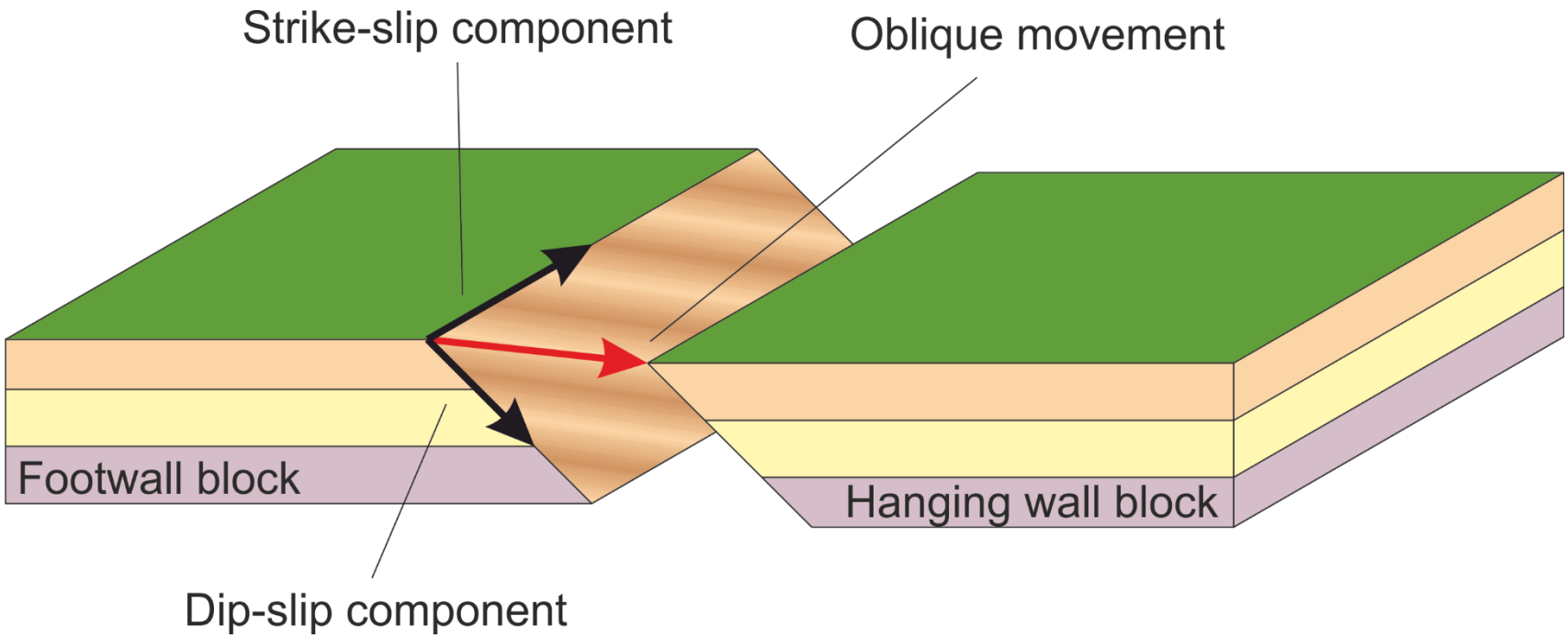

Fig. 1.9 Block diagram showing the strike-slip and dip-slip components that are established during oblique faulting.

1.3.3. Fault growth and stress relationships

1.3.3.1. Growth faults

Faults can grow both laterally and vertically, often developing by the coalescence of separate fault segments (Baudon and Cartwright, 2008, Childs et al., 2003, Childs et al., 1996, Jackson and Rotevatn, 2013, Walsh et al., 2002, Gupta et al., 1998). Vertical propagation of faults is often controlled by reactivation; two distinct modes of growth have been used to explain this.

Mansfield and Cartwright (1996), Childs et al. (1996) and Baudon and Cartwright (2008) compared in their work the processes of "upward propagation" and "dip linkage". Upward propagation considers an original fault that grows vertically by propagating through the overlying rocks. Laterally, small sections of the fault may remain inactive, when other sections continue to be displaced. Upward propagation is known to occur in reactivated faults, but it is unclear whether the same mechanics apply for non-reactivated faults (Walsh et al., 2002). "Dip linkage" involves the nucleation of younger faults in overlying cover and subsequently interacting with older faults. The dip and strike of the younger and older faults have to be similar (Mansfield and Cartwright, 1996). Stewart and Coward (1995) noticed soft linkage between sub- and supra-salt faults that could help define many more faults as growing via "dip linkage"; a term used to describe a similar phenomenon documented by Jackson and Rotevatn (2013).

Lateral propagation of faults increases the length of the fault trace during deformation. Previous theories propose the length of faults increase proportionately to vertical displacement (Cowie and Scholz, 1992, Gillespie et al., 1992, Cartwright et al., 1995, Dawers and Anders, 1995). However, since the late 1990's, studies suggest faults establish a maximum length early in a faults evolution (Childs et al., 1996, Childs et al., 2003, Walsh et al., 2002, Gupta and Scholz, 2000). Early lateral propagation of fault tips link separate small faults, forming 'hard links'. When this occurs, segments join to create a single, large fault, with growth subsequently constrained to the tips of the outermost segments. This abruptly decreases the speed of lateral growth (Childs et al., 1996, Childs et al., 2003). Walsh et al. (2002) suggested that as most of these interactions occur quickly on a geological timescale, lateral propagation should slow through time, while vertical displacement maintains a steady rate. However, Ze and Alves (2017) explain that care needs to be taken when interpreting segment linkage and lateral growth of faults on seismic data, as growth models are often dependant on the scale of interpreted data, and the scale a fault is analysed.

Throw-distance (*T-x*) plots show how fault displacement and lateral growth are related (*section 3.6.1*). Initial plots comparing displacement and lateral growth were linear, such that lateral propagation occurred at the same rate as displacement (Cowie and Scholz, 1992, Gillespie et al., 1992). Cartwright et al. (1995) documented step-like increments along the *T-x* plots, interpreted as sudden lateral growth with interrupted stages of fault linkage. More recently

Walsh et al. (2002) discovered a non-linear trend: lateral propagation occurs rapidly, with vertical displacement successively being the main process of deformation. Therefore, a progressive increase in T:x reflects the maturity of a system, a concept also presented in Kim and Sanderson (2011). The two ideas of linear and non-linear T-x plots are not mutually exclusive. Individual segments of faults showing tip line propagation obey the 'isolated fault model' and have a linear trend, whereas when some closely spaced segments link, they obey the 'coherent fault model' and display a non-linear trend (Jackson and Rotevatn, 2013, Walsh et al., 2003) (Fig. 1.10).

1.3.3.2. Reactivation

Anderson's (1951) ideal model for fault orientations demonstrates how faults form at ~ 30° to σ_1. Therefore, normal faults dip at ~ 60°, and reverse faults dip at ~ 30°. This is only true when stress trajectories remain vertical and horizontal. For reactivation to take place on either of these types of faults, the angle for reactivation (θ_r) is approximately 60°. Such an angle requires either a friction coefficient (μ) < 0.55, or the minimum principal stress (σ_3') < 0 (Sibson, 1985). However, natural faults are rarely identical to the models. For example, listric faults have a continual change in dip, with shallower fault dip observed at depth. Reactivation then occurs preferentially at the lowest θ_r, which is the deepest part of the fault (Sibson, 1995), gradually propagating deformation onto

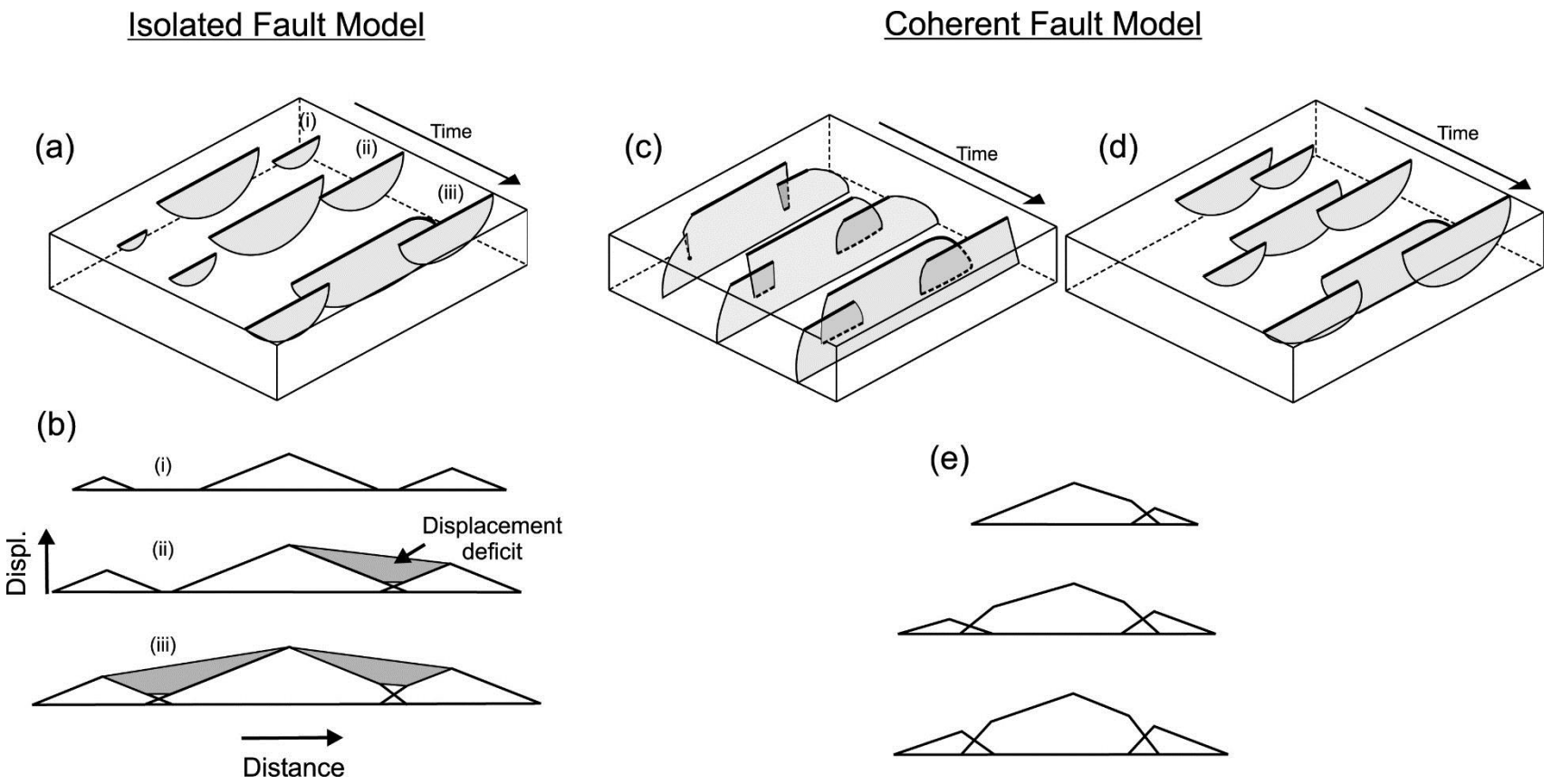

Fig. 1.10 Schematic representations of "isolated fault" and "coherent fault" models. a) Block diagram of the growth stages (i-iii) of a segmented fault array obeying the isolated fault model. b) Displacement-distance plots of the fault traces in a). c) and d) Block diagrams to show the growth stages of (c) hard-linked, and (d) soft-linked faults. e) Displacement-distance plots for the fault traces in c) and d). *Taken from Walsh et al. (2003).*

the surface. Strike-slip faults are also controlled by similar factors. When a fault strikes at a similar orientation to the maximum principal stress (σ_1'), reactivation is common. Nalpas et al. (1995) calculated that when the angle between the direction of σ_1' and the orientation of a normal fault (α) is < 45°, reactivation is much more likely to occur.

Another principal controlling factor for reactivation is frictional resistance. Obeying Coulomb Criterion, failure occurs on a rock when shear stress (τ) exceeds the frictional resistance (Lisle and Srivastava, 2004) (Equation 3.1). Frictional resistance can be reduced by the presence of a weaker material (e.g. montmorillonite-rich gouge) or a smoother fault plane, e.g. a larger fault having experienced significant previous slip (Sibson, 1995, Baudon and Cartwright, 2008, Ranalli, 2000). Weakening of rocks can be achieved by increasing the pore water pressure. This reduces the effective stress on a rock, making it more susceptible to failure. Even in unfavourable orientations of stress on a fault, localised high fluid pressure can allow selective reactivation (Moeck et al., 2009, Sibson, 1995, Ranalli, 2000).

Nalpas et al. (1995) used sandbox experiments to demonstrate the style of reactivated faults in a basin. One of the key variables in their experiments was the change in sedimentary cover thickness, as observed at different locations in the Broad Fourteens Basin. Results showed that thick Mesozoic sediment cover hindered the reactivation of normal faults during oblique-compression and, as a

result, strike-slip faults dominated within the graben. When the sedimentary cover was thin, compression reactivated normal faults and low angle thrust-faults developed in the graben margin. The experiment was summarised by De Lugt et al. (2003), who described reactivation favouring oblique-slip over the formation of new low-angle reverse faults. It should be noted that reactivated faults do not necessarily deform over the whole length of the fault; instead, preferential movement occurs in individual fault segments (Baudon and Cartwright, 2008).

1.3.4. Concentric faulting

Concentric faults have been described in numerous geological features including on collapsed calderas, impact craters, salt withdrawal basins, salt dissolution hollows, gas pockmarks and sand volcanoes (Stewart, 1999). Published work seems to focus on faults above dissolved salt diapirs (a known area for gas accumulation) or caldera collapse (Waite and Smith, 2002, Miura, 2005, Davison et al., 2000b, Maione and Pickford, 2001, Bertoni and Cartwright, 2005, Price and Cosgrove, 1990). This research will be using examples of concentric faults to compare and contrast their mechanics and kinematics in salt withdrawal basins developed within different geological settings.

1.3.4.1. Stress and style of faulting

As would be expected in a curved fault, slip orientations change in relation to the strike. Zhang et al. (2013) noticed how the northern flank of the fault responsible for the Lushan earthquake, China can display sinistral slip, whereas the southern flank displays dextral slip. Similar results were found by Miura (2005), who studied the collapse of Kumano caldera, and Holohan et al. (2013) who analysed subsiding calderas in Olympus Mons (Mars), Miyakejima (Japan) and Dolomieu (La Reunion). The change in orientation of the fault allows pop-up structures to form, complying with similar mechanics to a transpressional regime. Different strains accommodating stress either side of the fault have a larger transpressional component on its concave side (Dufréchou et al., 2011).

Quantification of slip along a concentric fault is difficult. If the kinematics of a simple block model are assumed, then the motion along the plane should equal the slip vector. Zhang et al. (2013) presented a calculation to relate the slip vector with slip and rake on a fault plane as:

$$u = s \cdot \cos(\alpha - \beta),$$

Equation 1.4

$$v = s \cdot \sin(\alpha - \beta)/cos\delta,$$

Equation 1.5

$$slip = \sqrt{u^2 + v^2},$$

Equation 1.6

$$\mathrm{r}ake = \arctan(v, u),$$

Equation 1.7

where α is strike and δ is dip angle of the fault plane, s is size and β is azimuth of slip vector. This assumes the fault is straight, therefore its strike and rake will be constant. In contrast to this latter the geometry, the strike of a concentric fault continually varies and, consequently, its rake will also change. Another consequence of dealing with concentric fault geometries is that if stress is unloaded on one part of the fault (i.e. an earthquake occurs), stress may be transferred to another part of the fault that faces a different orientation (Zhang et al., 2013).

Two models summarised by Miura (2005) and Holohan et al. (2013) have been used to describe the relative motions of concentric faults during subsidence, both involving a certain amount of oblique-slip along these structures (Fig. 1.11). The first (named "piecemeal" by Miura (2005) and the "camera iris effect" by (Holohan et al., 2013)) forms around a symmetrical feature. As the basin subsides, shortening of the rock occurs both radially and concentrically. Vertical displacement is greater than horizontal and movement is predominantly towards

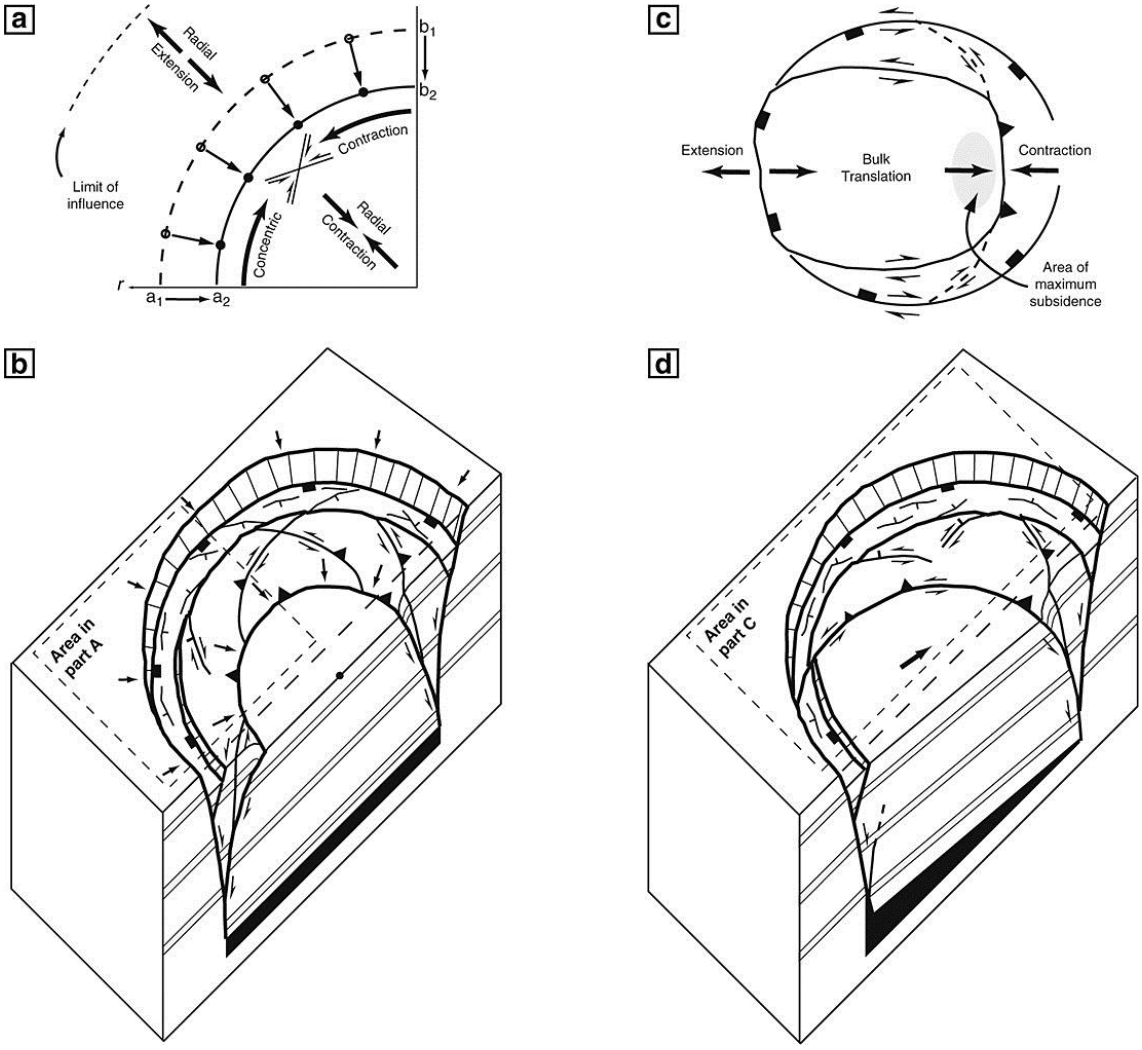

Fig. 1.11 Schematic diagrams of oblique-slip along concentric faults. a) and b) Piecemeal/camera iris effect style of displacement. Circumferential shortening occurs as material points move radially inwards. This forms round a symmetrical feature. c) and d) Sliding trapdoor effect style of displacement developed during off-centre subsidence. *Taken from Holohan et al. (2013).*

the central feature. However, inward radial movement generates concentric compression along the horizontal plane. Significant strike-slip displacement occurs both to accommodate shortening and compression (Fig. 1.11a-b).

The second model, named "sliding trapdoor effect" by both Miura (2005) and Holohan et al. (2013), occurs around an asymmetrical feature and is more common. Here, maximum subsidence is preferential to one side of the basin, causing contraction. The opposite side of the basin experiences extension and normal concentric faults. At the apex of these concentric faults, displacement is purely dip-slip. Increasing strike-slip components therefore occur away from the point of maximum contraction to accommodate the horizontal translation of the subsiding overburden (Fig. 1.11c-d).

1.4. Thesis layout

This thesis is divided into eight chapters. The current chapter (*Chapter 1*) provides an overview of the thesis. The research rationale and aims are followed by an extensive literature review, which highlights the key concepts covered throughout this thesis: namely differential compaction and fault mechanics. The literature review continues with a geological setting chapter (*Chapter 2*), which outlines the evolution of the three areas covered in this thesis and the petroleum systems in each study area. *Chapter 3* presents a detailed description of the

interpreted 3D datasets and how were they acquired. The methods (both statistical and interpretation) are then described.

Chapters 4, *5*, and *6* are results chapters, all published in international journals at the time of submission of this work. *Chapter 4* investigates the evolution of concentric faults in a salt withdrawal basin in the Broad Fourteens Basin, southern North Sea. *Chapter 5* uses a new method to evaluate the timing and magnitude of differential compaction over a submarine channel complex in the Espírito Santo Basin, SE Brazil. *Chapter 6* also uses data from the Espírito Santo Basin to analyse how differential compaction over a blocky mass-transport deposit affects (and affected in the past) sedimentary transport systems on a continental slope. The results are compiled in *Chapter 7* to discuss their wider importance. A novel classification scheme is proposed in *Chapter 7* for subtle structural traps related to differential compaction. Final conclusions for each chapter are presented in *Chapter 8*.

CHAPTER TWO

Geological settings of the Broad Fourteens, Espírito Santo and Taranaki basins

2. Geological Settings

2.1. Introduction

This chapter aims to review the geological settings for each of the datasets used in the thesis. Each section will review the tectonic evolution of the basin, and the petroleum systems within them. It starts with the Broad Fourteens Basin, North Sea (*Chapter 4*), followed by the Espírito Santo Basin, offshore Brazil (*Chapter's 5 and 6*), finishing with the Taranaki Basin, New Zealand (*Chapter 7*).

2.2. Broad Fourteens Basin, North Sea

The Broad Fourteens Basin is located in the Dutch sector of the southern North Sea, encompassing blocks K, L, P, and Q offshore The Netherlands (Fig. 2.1). The basin trends northwest-southeast and is approximately 120 km long by 45 km wide (Verweij and Simmelink, 2002). It is bound by the Texel-Ijsselmeer High to the northeast, the Central Netherlands Basin to the southeast, the West Netherlands Basin to the southwest, and the Cleaver Bank High to the north (Fig. 2.2).

2.2.1. Tectonic evolution of the Broad Fourteens Basin

The Broad Fourteens Basin, part of the larger South Permian Basin, records a complex history of rifting, halokinesis and inversion (Verweij and Simmelink, 2002, Van Wijhe, 1987, Ziegler, 1990, Nalpas et al., 1995, Duin et al., 2006). It was formed during the Mesozoic in response to E-W extension associated with opening of the Atlantic Ocean (Verweij and Simmelink, 2002). The evolution of the basin can be divided into three intervals with distinct deformation styles and histories: a) Carboniferous-Permian; b) Triassic-Jurassic; c) Late Cretaceous-Cenozoic.

2.2.1.1. Carboniferous – Permian pre-rift evolution

Towards the end of the Carboniferous, the Variscan Foreland basin developed in the Southern North Sea. Thick lacustrine and deltaic intervals with interbedded coal seams were deposited as part of the Limburg Group (Fig. 2.3). Included in this unit are the Westphalian Coal Measures, a major source of gas in the Southern North Sea (Gerling et al., 1999, Van Wijhe, 1987). Oblique-slip normal faulting predominated after the Variscan Orogeny, with the largest faults cutting through the Variscan fold belt to propagate along older NW-SE trending basement faults. The present-day structural grain of the Southern North Sea

follows horst and graben structures formed by these faults (Ziegler, 1990, Duin et al., 2006, Van Wijhe, 1987, Oudmayer and De Jager, 1993) (Fig. 2.1).

Sedimentation in the Permian was interrupted by thermal upwelling from dolerite intrusions through oblique-slip dextral normal faults. This hiatus is expressed in the form of a Saalian unconformity separating Lower from Upper Rotliegend strata (Van Wees et al., 2000) (Fig. 2.3). Subsidence resumed in the Late Permian, and the South Permian Basin became separated from the North Permian Basin by the Mid North Sea High (Duin et al., 2006). Upper Rotliegend terrestrial sandstones of the Slochteren Formation were deposited above the Saalian unconformity and became the major reservoir for the Permian gas plays offshore The Netherlands (Verweij and Simmelink, 2002).

The Zechstein Sea subsequently flooded the study area in the Latest Permian. Carbonate-evaporite cycles in Zechstein evaporites reflect fluctuations in sea level, but thick deposits of Zechstein evaporites in the North of the Broad Fourteens Basin became an effective seal rock for Permian gas plays (Coward, 1995) (Fig. 2.3).

2.2.1.2. Triassic – Jurassic syn-rift evolution

Rifting intensified during the Triassic, allowing for differential subsidence in the Southern North Sea (Alves and Elliott, 2014, Duin et al., 2006). In the

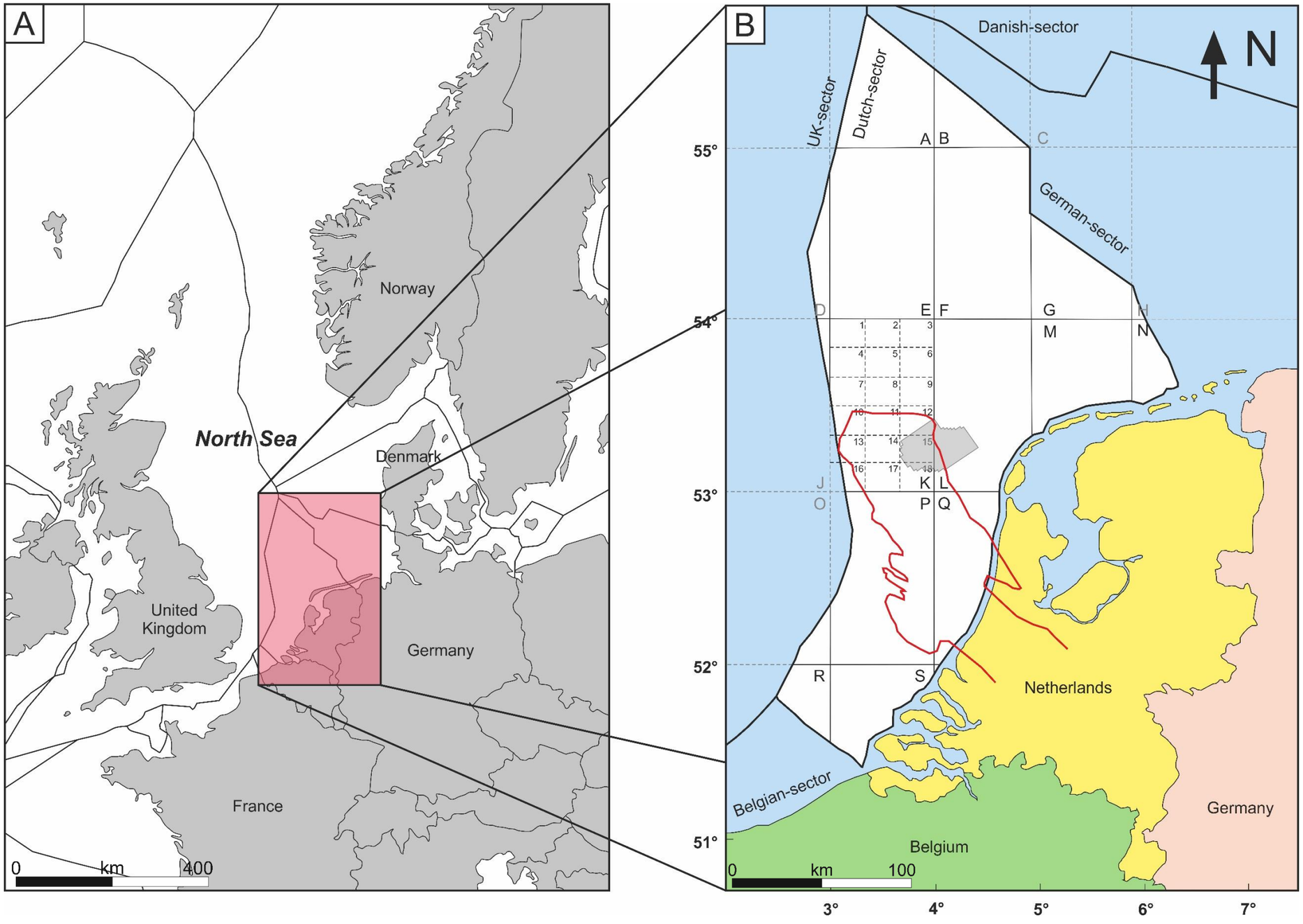

Fig. 2.1 a) Map of Western Europe, showing political and continental shelf boundaries. b) Enlarged location map of the Dutch sector of the Southern North Sea highlighting its position relative to Western Europe. The Broad Fourteens Basin is shown by the red line, and the 3D seismic survey used in *Chapter 4* is shown by the grey box.

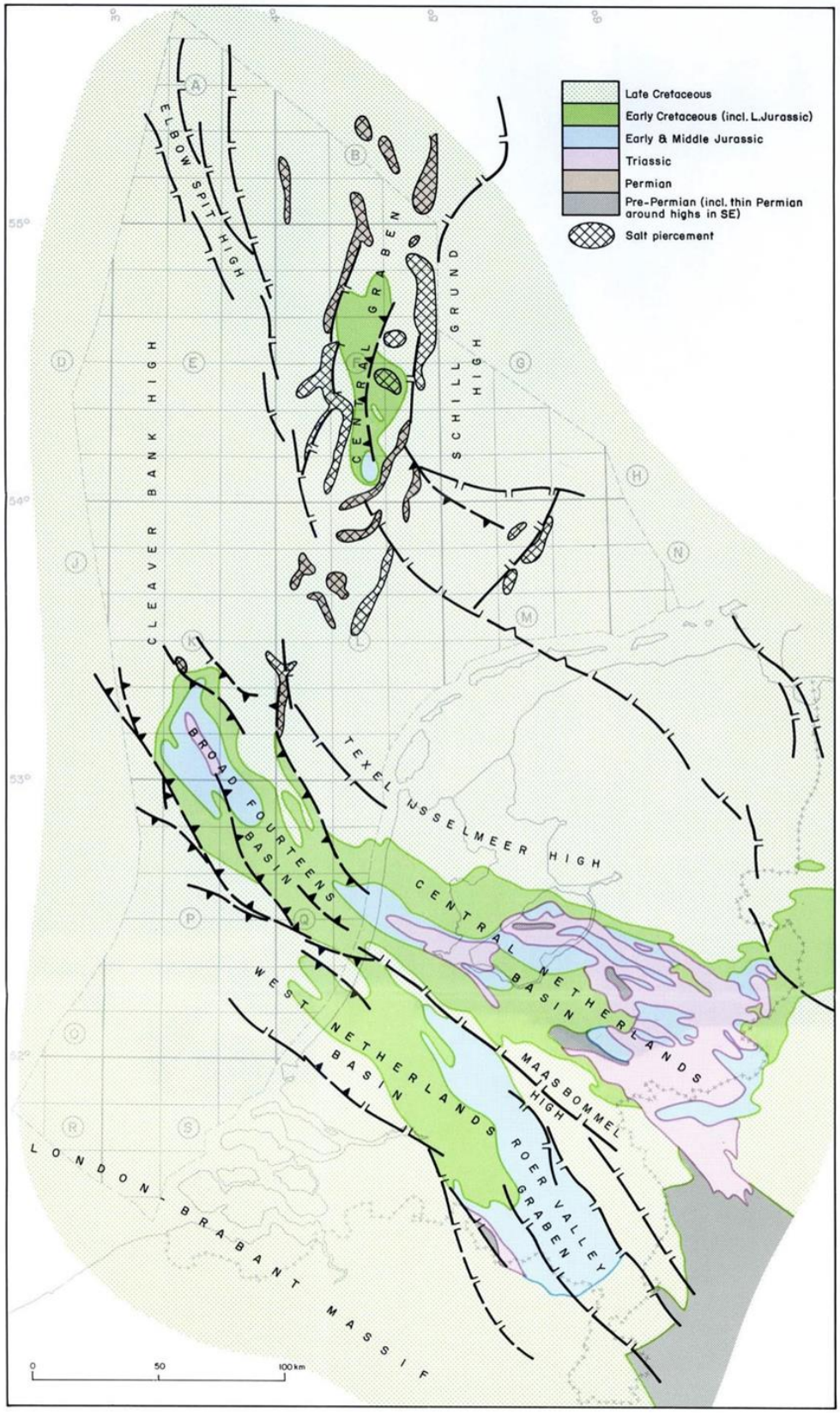

Fig. 2.2 Major structures of the Dutch North Sea surrounding the Broad Fourteens Basin. *From Van Wijhe (1987).*

rapidly subsiding Broad Fourteens Basin, aeolian sands and lacustrine claystones from the Lower and Upper Germanic Trias Group were deposited (Fig. 2.3). The Lower Buntsandstein is a prolific gas reservoir, particularly where Zechstein salt has been withdrawn and welds have formed between Triassic sequences and the Rotliegend Group (Van Hulten, 2010b).

Towards the end of the Triassic, salt tectonics and reactive diapirism became concentrated along extensional boundary faults (Stewart and Coward, 1995, Ziegler, 1992). Rift-raft tectonics led to the further deepening of the Broad Fourteens Basin and open marine conditions (Alves and Elliott, 2014, Penge et al., 1993). As a result, the deep-water Altena Shales were deposited in the Broad Fourteens Basin, with the more bituminous Posidonia Shale Formation comprising the source interval for Jurassic oil plays in the basin, accompanying the significant isolation of the Southern North Sea, in the form of confined sub-basins, that occurred at this time (Nalpas et al., 1995, Duin et al., 2006).

Deposition of the Altena Shales stopped during the Mid-Kimmerian upwarping event (Middle Jurassic). In areas of greatest uplift, up to 1500 m of Jurassic rocks are thought to have been eroded (Heim et al., 2013). Despite this localised uplift event, sharp pulses of NE-SW rifting continued to rotate the Broad Fourteens Basin to its present-day orientation. Increased erosion of Triassic, Zechstein and Rotliegend rocks on active structural highs generated thick successions in the Delfland Subgroup and Vlieland Sandstone - both

comprising reservoirs for oil sourced from the Posidonia Shale (Van Wijhe, 1987, Verweij and Simmelink, 2002, Duin et al., 2006).

2.2.1.3. Late Cretaceous – Cenozoic basin inversion

A major episode of sea-level rise, accompanied by post-rift subsidence, led to the accumulation of thick layers of chalk both in individual basins and on adjacent marginal highs (Van Wijhe, 1987, Verweij and Simmelink, 2002). In the Turonian, N-S Alpine compression interrupted subsidence and Subhercynean inversion reactivated Variscan faults with a reverse-dextral motion (De Lugt et al., 2003, Nalpas et al., 1995). In such a setting, the localisation of a salt (Zechstein) décollement layer to the North of the Broad Fourteens Basin accounts for the lack of connectivity between sub-salt and supra-salt faults (Van Wijhe, 1987). Maximum erosion (~3000m) took place in the centre of the inverted basin, close to the axis of inversion (Nalpas et al., 1995, De Lugt et al., 2003).

Three additional inversion events took place in the Broad Fourteens Basin, separated by periods of subsidence. The Laramide inversion in the Cenozoic reactivated Subhercynean faults, creating a prominent Cretaceous-Tertiary unconformity (Oudmayer and De Jager, 1993, De Lugt et al., 2003). Major basin inversion events are recorded in the Cenozoic, the largest of which coincided with the Pyrenean Orogeny (Oligocene) and created an unconformity at the base

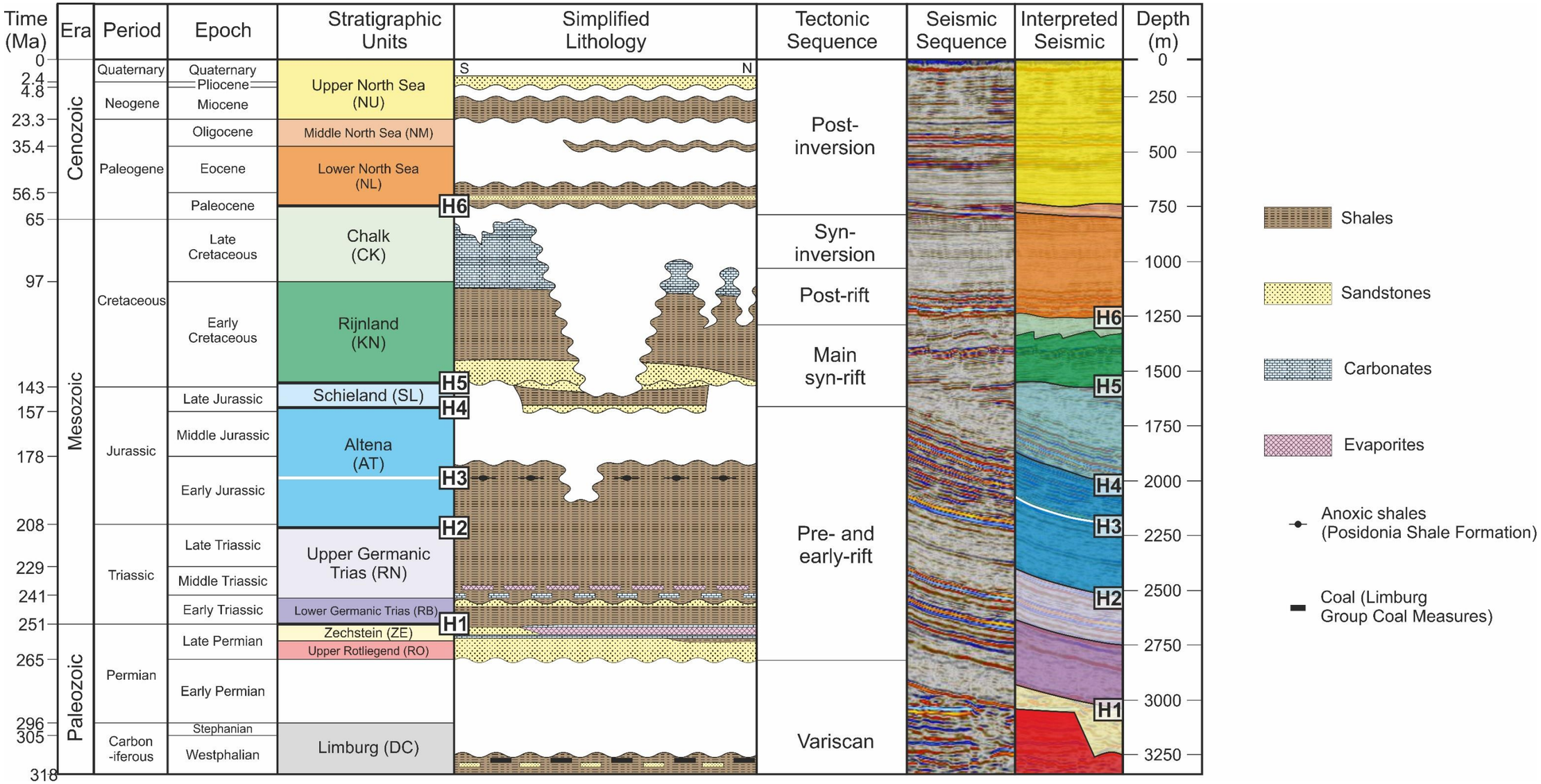

Fig. 2.3 Stratigraphic units, main lithologies and tectonic sequences in the Broad Fourteens Basin. Seismic data and interpretations are included in this figure as well as key horizons. Lithologies, ages, and depths are based on the borehole data interpreted in *Chapter 4*. *Modified from Alves and Elliott (2014), and Verweij and Simmelink (2002).*

of the Miocene (Oudmayer and De Jager, 1993, Verweij and Simmelink, 2002). It separated the Lower North Sea Group from the Middle North Sea Group (Wong et al., 2001) . The boundary between the Middle and Upper North Sea Groups is based on a break of sedimentation resulting from regional uplift and global low in sea level, associated with the Alpine Orogeny (Savian unconformity, Middle Miocene) (Oudmayer and De Jager, 1993, Wong et al., 2001). Associated with these tectonic phases is the present-day up-dip migration of hydrocarbons (Van Balen et al., 2000, Verweij and Simmelink, 2002, Isaksen, 2004). Broad folds formed in response to the inversion events, causing reservoirs to be tilted beyond spill-point, allowing secondary migration of fluids into shallower reservoirs (Van Balen et al., 2000). Since compression initiated in the Late Cretaceous, contemporaneous faulting and diapirism created fluid flow pathways (Isaksen, 2004).

2.2.2. Petroleum systems of the southern North Sea

Oil and gas prospects can be found in almost all horizons, from the Carboniferous to the Cenozoic, in the Broad Fourteens Basin (Van Hulten, 2010a). Stratigraphic sequences including source, reservoir and seal rocks create economic and large hydrocarbon fields. Subsidence and uplift histories, along with fluctuations in eustatic sea-level have produced this stratigraphy and enabled the maturation and charging of the oil and gas (Verweij and Simmelink,

2002, Verweij et al., 2003, Glennie and Provan, 1990, Van Hulten, 2010a, Van Wijhe, 1987).

2.2.2.1. Permian gas plays

During the Westphalian stage, the Variscan Orogeny created a foreland basin in the southern North Sea. The equatorial terrestrial setting recorded at this time allowed the basinwide deposition of thick lacustrine sediments prograding into deltaic and fluvial fine-grained siliciclastics with intercalations of coal (Verweij and Simmelink, 2002, Van Wees et al., 2000, Quirk, 1993, Glennie and Provan, 1990). The majority of coal seams belong to either the Ruurlo or Maurits Formations of the Limburg Group (Fig. 2.3). It is a kerogen type III coal, with a total organic content (TOC) of at least 70%, and comprising the main source rock in the Permain gas plays of the southern North Sea. Coal content reaches 4% in the Ruurlo Formation, and 6% in the Maurits Formation (Verweij and Simmelink, 2002, Van Hulten, 2010a). The Limburg group has been measured to be >1000 m thick (Quirk, 1993), with individual coal seams having a cumulative thickness >10 m. Because the Limburg Group so widely reaching and thick, the basin could have been charged with gas several times as different coal seams reached the gas window (Van Hulten, 2010a). Verweij and Simmelink (2002) suggested that the central part of the Broad Fourteens Basin entered the gas window during the

Jurassic (main syn-rift sequence), with peak gas expulsion in the Cretaceous (pre-inversion). The northern part of the basin likely remained out of the gas window.

The Upper Rotliegend Group lies unconformably over the Variscan basement; sandstones of this group are the main reservoir for Permian gas. The sandstones consist largely of the Slochteren and Silverpit Formations (Fig. 2.3). Thick aeolian and fluvial coarse-grained clastics of the Slochteren Formation were deposited in the late Permain throughout the southern North Sea. Finer-grained desert lake deposits of the Silverpit Formation increase in thickness towards the north of the basin (Verweij and Simmelink, 2002, Glennie and Provan, 1990). Thickness variation often depends on the palaeotopography of previous structures, with thinner deposits being recorded on structural highs and thicker strata occurring in late Permian basins.

Facies changes in the Upper Rotliegend Group occur at a large scale in the basin, and are very gradual compared to the high concentration of faulting. Therefore, gas is often structurally trapped by dip closures rather than stratigraphically across the Broad Fourteens Basin (Van Hulten, 2010a). Secondary permeability has been lowered due to diagenetic illite growth. Expulsion of K-rich brines from underlying Westphalian coal and overlying Zechstein salts led to the illitization of kaolin group minerals during the Kimmerian, when the Rotliegends subsided to a depth of about 4000 m (Glennie, 1997, Glennie and Provan, 1990, Lanson et al., 1996, Purvis, 1992).

Deposition during the Late Permian (Zechstein Group) conformably overlies Upper Rotliegend rocks. The southern parts of the Broad Fourteens Basin is rich in thick bordering facies of siliciclastics and carbonates, whereas the northern parts are characterised by diapiric salt (Nalpas et al., 1995, Verweij and Simmelink, 2002). Peri-marine carbonates make prospective reservoirs for Permian gas, in particular the Ze2 and Ze3 horizons, with original thicknesses nearing 1000 m (Van Hulten, 2010a, Glennie and Provan, 1990). However, the distinguishing feature of the Zechstein Group was the deposition of thick evaporite layers. Five evaporite sequences are recognised in the Dutch offshore, each a contribution to the sealing capabilities of the Zechstein Group (Van Hulten, 2010a). It was estimated by Quirk (1993) that halite in the Broad Fourteens Basin is between 100-1500 m thick. However, estimations of true and original thickness are hard because of the effects of halokinesis. Halite flowed diapirically during the Jurassic, allowing salt to be completely withdrawn around diapirs to create salt welds between Triassic and Rotliegend sandstones (Glennie and Provan, 1990, Davison et al., 2000b).

Another important reservoir in The Netherlands belongs to the Lower Germanic Trias Group (Stewart and Coward, 1995) (Fig. 2.3). The Bunter Sandstone (referred to as Buntsandstein in Dutch and German literature) was deposited during the Triassic in a desert environment comparable to the Permian Rotliegends. Aeolian and fluvial sandstones are the dominant facies in the Buntsandstein and are constant over a large area (Van Hulten, 2010a, Verweij and

Simmelink, 2002). The Bacton Group (containing Bunter Sandstone) displays a coarsening upwards sequence, relating to a fall in eustatic sea level (Coward, 1995). It has a varying thickness within the Broad Fourteens Basin, but attains a maximum thickness between 1000-1500m (Van Wijhe, 1987). Gas migrates upwards in areas where salt welds developed between Permian Rotliegend rocks and the Bunter Sandstone, and through basin-margin faults (Verweij and Simmelink, 2002). This gas can accumulate between units of the Lower Germanic Trias Group and diapirs which were activated during the Triassic (Van Hulten, 2010a).

2.2.2.2. Jurassic oil plays

By the end of the Triassic, the Rhaetian transgression raised the eustatic sea level. Thick open marine Jurassic clays were restricted to basin centres and the Altena Group was subsequently deposited (Verweij and Simmelink, 2002, Van Wijhe, 1987) (Fig. 2.3). The original lateral extent of the Altena Group is uncertain due to Cretaceous tectonic inversion and its almost complete removal across structural highs (Duin et al., 2006, Van Hulten, 2010a). The onset of the Toarcian Oceanic Anoxic Event (T-OAE) coincided with the deposition of a thin layer of bituminous clays in the Posidonia Shale Formation. This 15-30 m thick sequence is the main source rock of the Jurassic oil plays in the Broad Fourteens Basin and contains kerogen type II oil, with TOC values around 5 % (Van Hulten,

2010a, Verweij and Simmelink, 2002, De Jager et al., 1996). Maturation was reached in the centre of the basin during the Lower Cretaceous (latter part of syn-rift sequence). The northern edge reached the oil window later in the Cretaceous (during post-rift sequence) (Verweij and Simmelink, 2002). Inversion in the latest Cretaceous and Palaeocene reduced the temperature of oil and allowed access of meteoric waters: aerobic bacteria consequently biodegraded the oil (De Jager et al., 1996).

Overlying the Posidonia Shales is the Delfland Subgroup, which acts as both reservoir and a secondary source rock. Fluctuations in sea level during the Jurassic generated fluctuations of lacustrine and fluvial deposits, resulting in the deposition of sandstone and interbedded bituminous shales and dispersed lignitic material (Verweij et al., 2003).

The main reservoir unit in the Broad Fourteens Jurassic oil plays is the Vlieland Sandstone Formation. Transition from coastal to shallow marine deposits occurred during the Lower Cretaceous, characterised by slow sedimentation (Verweij and Simmelink, 2002, Verweij et al., 2003). This can be resolved seismically as a rapid change of facies, a character indicating a potential stratigraphic trap (Van Hulten, 2010a). The Vlieland Formation can only be found in depocentres, as it has been eroded from structural highs – similarly to the Altena Group of the Lower Jurassic (Duin et al., 2006). Charging of the Vlieland reservoir occurred by the Palaeocene. Migration of Posidonia oils linked to basin

inversion filled the Vlieland Sandstones, with the Werkendam and Delfland sandstones act as secondary reservoirs, thus containing much lower volumes of hydrocarbons (Verweij et al., 2003). The Vlieland Shale Formation is the top seal member for the Jurassic oil plays (Bruijn, 1996). However, shales, like the Cretaceous Vlieland Shale Formation, make an ineffective seal and most of the oil accumulations are structurally trapped by faulted anticlines formed in the Cretaceous-Palaeocene inversion (De Jager et al., 1996).

2.3. Espírito Santo Basin, Brazil

The Espírito Santo Basin is one of a number of Mesozoic rift basins located on the continental slope of southeast Brazil (Fig. 2.4). It is bounded by the Abrolhos Plateau in the north, a volcanic complex built by Late Cretaceous to Eocene volcanic rocks and sediments from a narrow continental shelf (Bruhn and Walker, 1997, Chang et al., 1992, Fiduk et al., 2004). In the south, the Vitória-Trindade High separates the basin from the Campos and Santos basins (Alves et al., 2009) (Fig. 2.4). The Espírito Santo Basin, which is largely detached from the Campos Basin by a political border (Fiduk et al., 2004), covers an area of 125,000 km^2, of which 107,000 km^2 are offshore. Running through the centre of the basin, the Rio Doce Canyon System scours the sea floor (Fig. 2.5).

2.3.1. Tectonic evolution of Espírito Santo Basin

The tectonic evolution of the Espírito Santo Basin is typical of passive margins - spanning continental rifting, crustal extension and rupture, and subsequent seafloor spreading - and shares a very similar geological history to other basins from Southeast Brazil, namely the Campos and Santos basins (Bruhn and Walker, 1997). The Espírito Santo Basin developed from the Late Jurassic to Cretaceous, coevally with the opening of the South Atlantic and the breakup of Gondwanaland (Chang et al., 1992, Davison, 1999, Fiduk et al., 2004). Three phases are generally recognised in the Basin: the syn-rift phase, post-rift (transitional) phase, and the drift phase. These are summarised in Figure 2.5 and by the stratigraphic column in Figure 2.6 (Ojeda, 1982).

Structural deformation in the Espírito Santo Basin was largely controlled by thin-skinned gravitational gliding over Aptian evaporites (Demercian et al., 1993, Fiduk et al., 2004). This process occurred through the Cenozoic, peaking during the Eocene-Early Oligocene, and was chiefly caused by differential loading of the Aptian salt as a result of sediment progradation onto the continental slope (Alves et al., 2009, Alves, 2012). Structural styles change from thin-skinned extension in proximal areas of the continental margin, to diapirism in the mid-slope region, and compression in the distal parts of the continental slope (Mohriak et al., 1995, Demercian et al., 1993, Fiduk et al., 2004) (Fig. 2.5). Halokinesis and salt deformation in the mid-slope regions is expressed by NNW-

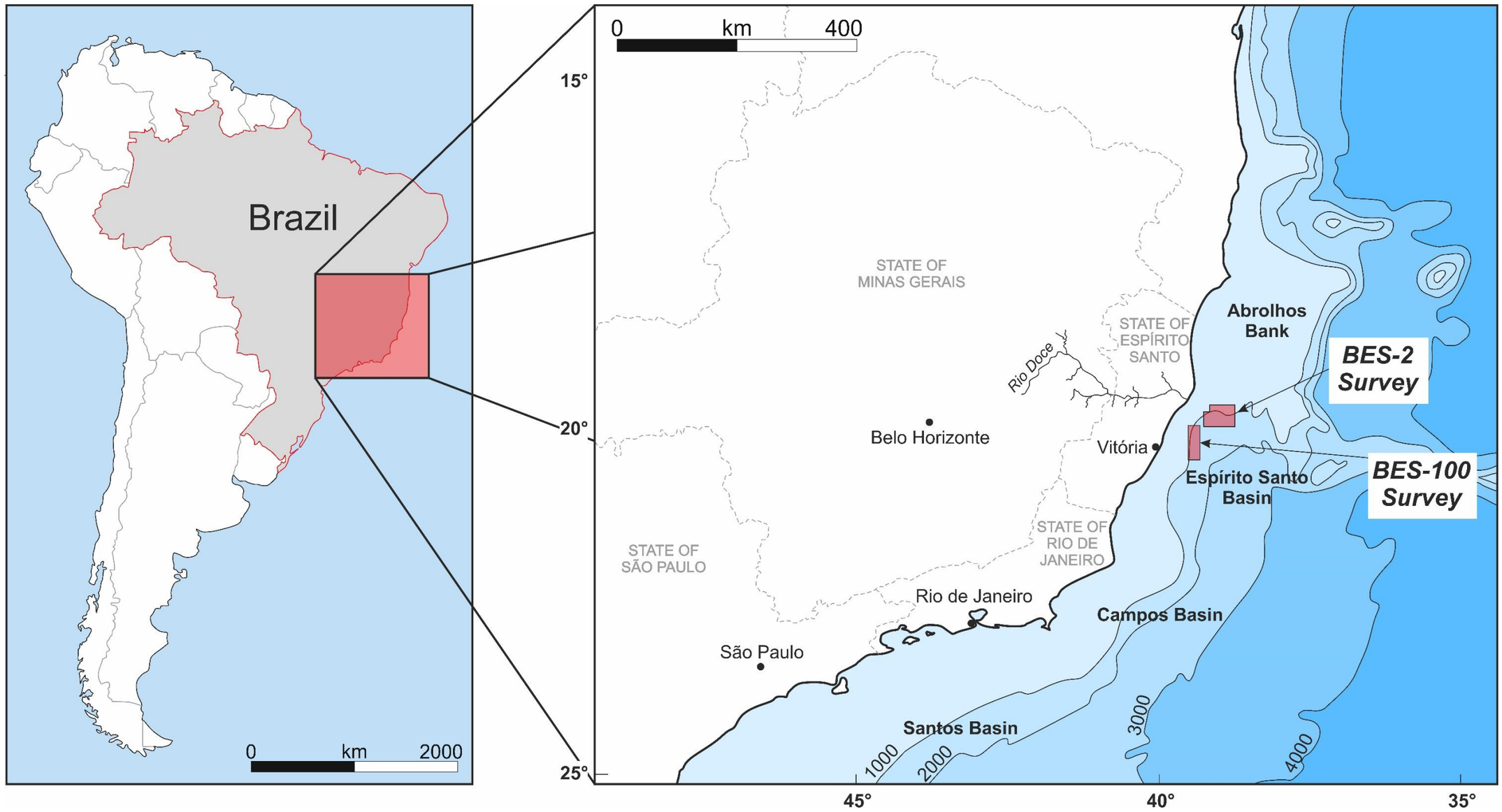

Fig. 2.4 Regional map of the SE Brazilian margin; showing the Santos, Campos and Espírito Santo Basins. The interpreted three-dimensional (3D) seismic surveys used in *Chapters 5* and *6* (BES-2 and BES-100, respectively) are highlighted by red boxes.

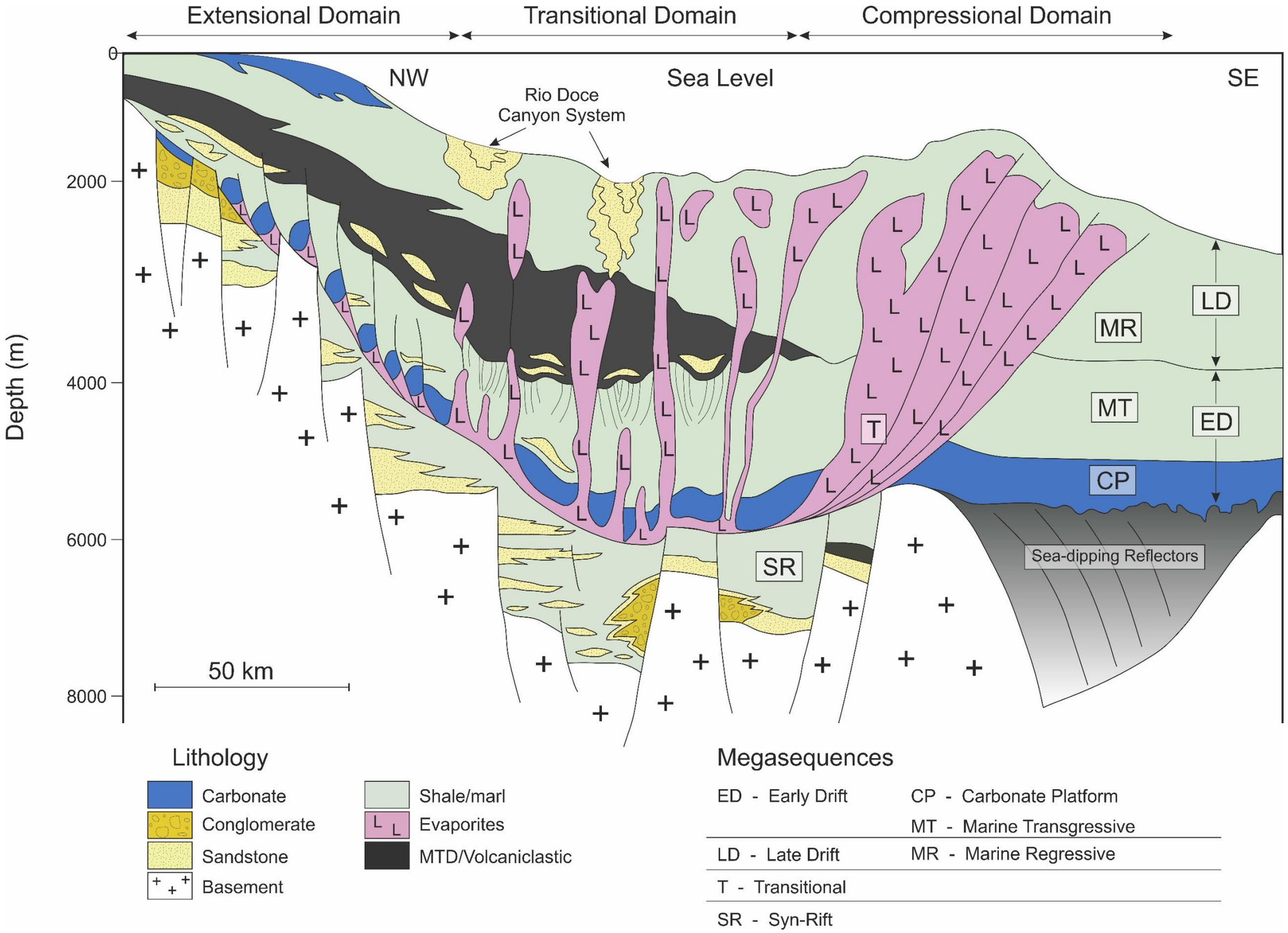

Fig. 2.5 Schematic diagram showing main megasequences in the Espírito Santo Basin. The diagram also shows key structural domains within the basin. The study areas lie within the transitional domain, and focus on the late drift sequences. *Modified after Fiduk et al. (2004) and Gamboa et al. (2010).*

SSE salt-cored anticlines, which control sediment distribution in this area (Gamboa et al., 2010). During extension, gravitational collapse of these salt-cored anticlines led to the formation of extensional faults (Baudon and Cartwright, 2008, Alves, 2010, Alves et al., 2009). Crestal and axial fault sets are associated with peaks in halokinesis, but have also experienced younger reactivation (Baudon and Cartwright, 2008).

2.3.1.1. Berriasian – Aptian syn-rift phase

The oldest strata deposited in the Espírito Santo Basin consists of syn-rift sediments (Ojeda, 1982) (Fig. 2.6). Although the exact date of rifting and deposition of sediments is uncertain, this phase is believed to have started in the Berriasian and continued to the early Aptian (Davison, 1999, Chang et al., 1992). This sediment was deposited over Neocomian volcanic rocks, mostly comprising tholeiitic basalts (Mohriak et al., 2008, Davison, 1999). The syn-rift megasequence is commonly divided into two or three sequences (Chang et al., 1992, Fiduk et al., 2004). The sequences reflect the influence of faults; syn-rift I strata is very moderately affected by faults and is widespread through Southeast Brazil, whereas syn-rift II (and III) strata are intensely faulted and deposited in local, active rift basins (Fig. 2.5).

As suggested, the syn-rift phase coincides with the opening of the South Atlantic Ocean and formation of the East Brazil Rift System (Demercian et al., 1993, França et al., 2007) (Fig. 2.7a). Intense rifting between Africa and South

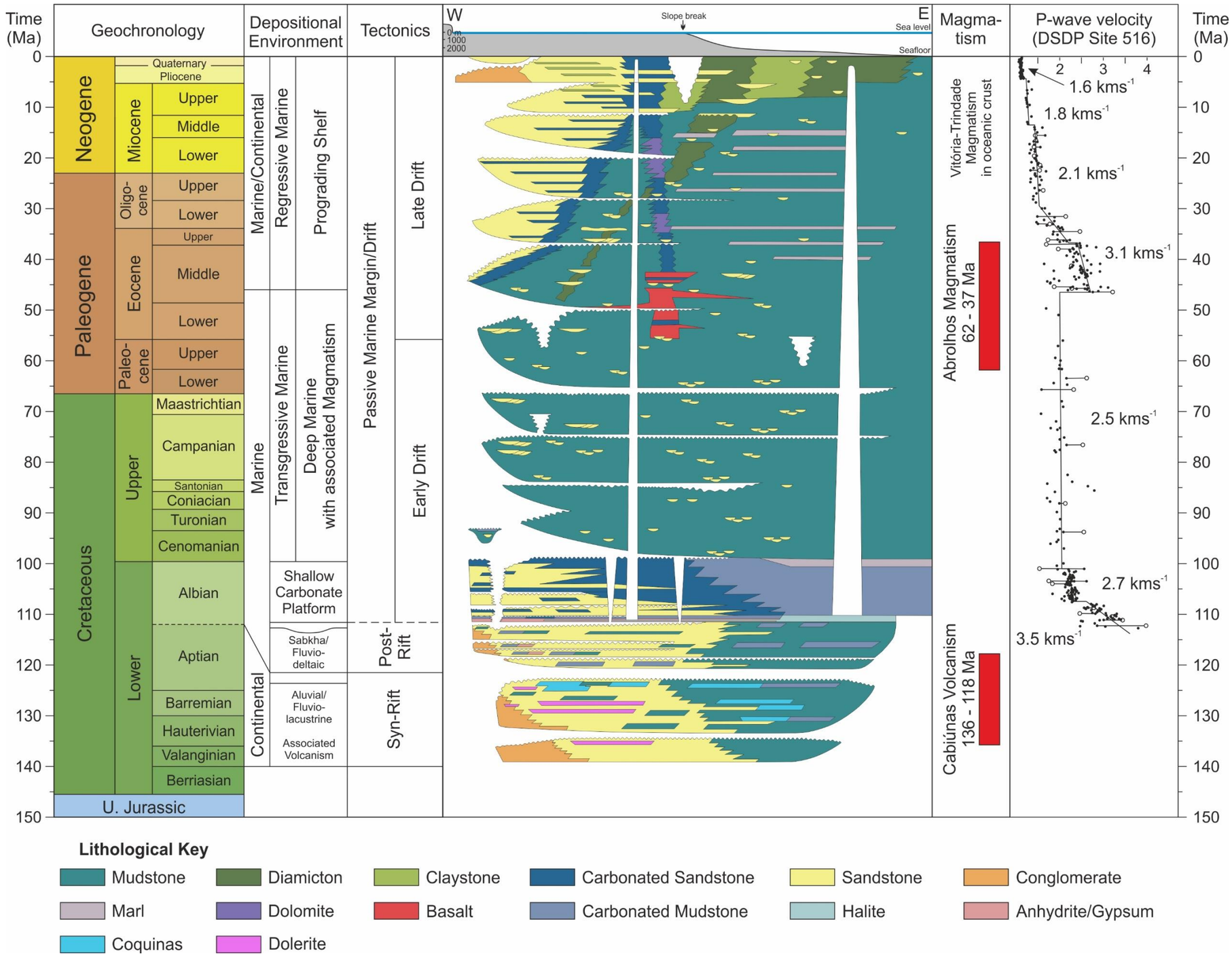

Fig. 2.6 Stratigraphic column showing the ages and depositional environments of strata within the Espírito Santo Basin, together with the principal phases of, tectonic and magmatic activity. *Modified from França et al. (2007)*. The P-wave velocity data for Aptian-Holocene strata is derived from the Rio Grande Rise and correlated with the Espírito Santo Basin. It is based on DSDP Site 516 (*Barker et al., 1983)*.

America created long rift valleys, including the large central graben, as well as asymmetric rift valleys between the grabens and continental cratons (Ojeda, 1982). Some of the valleys reached lengths of 1500 km (Chang et al., 1992). The basic structural-stratigraphic framework in the basins started to form as half grabens striking parallel to the future continental margin (Ojeda, 1982). Sedimentation in elongate lacustrine grabens and half-grabens involved clastic, non-marine, fluvial, deltaic and deep-water basinal strata (Ojeda, 1982). Deposition in these structural lows was dominated by continental sandstones, silts and shales, along with fault-associated syn-tectonic conglomerates (Ojeda, 1982, Gamboa et al., 2010, Baudon and Cartwright, 2008, Chang et al., 1992). This coarse clastic material alternated with basaltic volcaniclastic rocks (Chang et al., 1992). At this time, fluvial and deltaic depositional systems proximal to the continental margins were affected by untilted step-fault blocks, synthetic to the continental slope. In contrast, prodelta and basinal shales in the distal parts were deformed by tilted step-fault blocks antithetic to the continental slope (Ojeda, 1982).

2.3.1.2. Aptian post-rift (transitional) phase

Stable tectonic conditions prevailed in the Aptian, when the post-rift (or transitional) phase occurred (Baudon and Cartwright, 2008, Mohriak et al., 2008, Demercian et al., 1993, Ojeda, 1982, Bruhn and Walker, 1997). Rocks in this phase

are separated from syn-rift strata by an angular unconformity of regional expression (Chang et al., 1992, Davison, 1999, Mohriak et al., 1995). The palaeographic make-up of the south Atlantic strongly controlled sediment deposition during the post-rift stage (Fig. 2.7b). Prior to the early Aptian, the Rio Grande-Walvis ridge created a barrier to the south (Davison, 1999). This barrier was subsequently breached, flooding the central graben, and resulting in the formation of the Paripueira Gulf (Ojeda, 1982, Mohriak et al., 2008) (Fig. 2.7b). Structural highs separated the Paripueira Gulf from the marginal basins, yet sufficiently saline marine waters entered these basins from the gulf, depositing a thick halite layer: the Paripueira evaporitic sequence (Mohriak et al., 2008). A widespread regression followed the evaporite deposition, forming thick sections of fluvial-deltaic and lagoonal sediments (Ojeda, 1982). Intense erosion of the marginal basins resulted in an unconformable surface over the Paripueira evaporitic sequence (Ojeda, 1982).

In the late Aptian, cycles of evaporitic-carbonate-clastic rocks (the Ibura evaporitic sequence) were deposited unconformably over the Paripueira evaporitic sequence (Ojeda, 1982, Mohriak et al., 2008, Gamboa et al., 2010, Davison, 2007). Marine transgression covered most areas occupied by the Paripueira Gulf, shifting the marginal evaporitic basins towards the South American continent in the west, and creating deep-marine conditions in the basin axis (Ojeda, 1982). Towards the end of the late Aptian, geological barriers

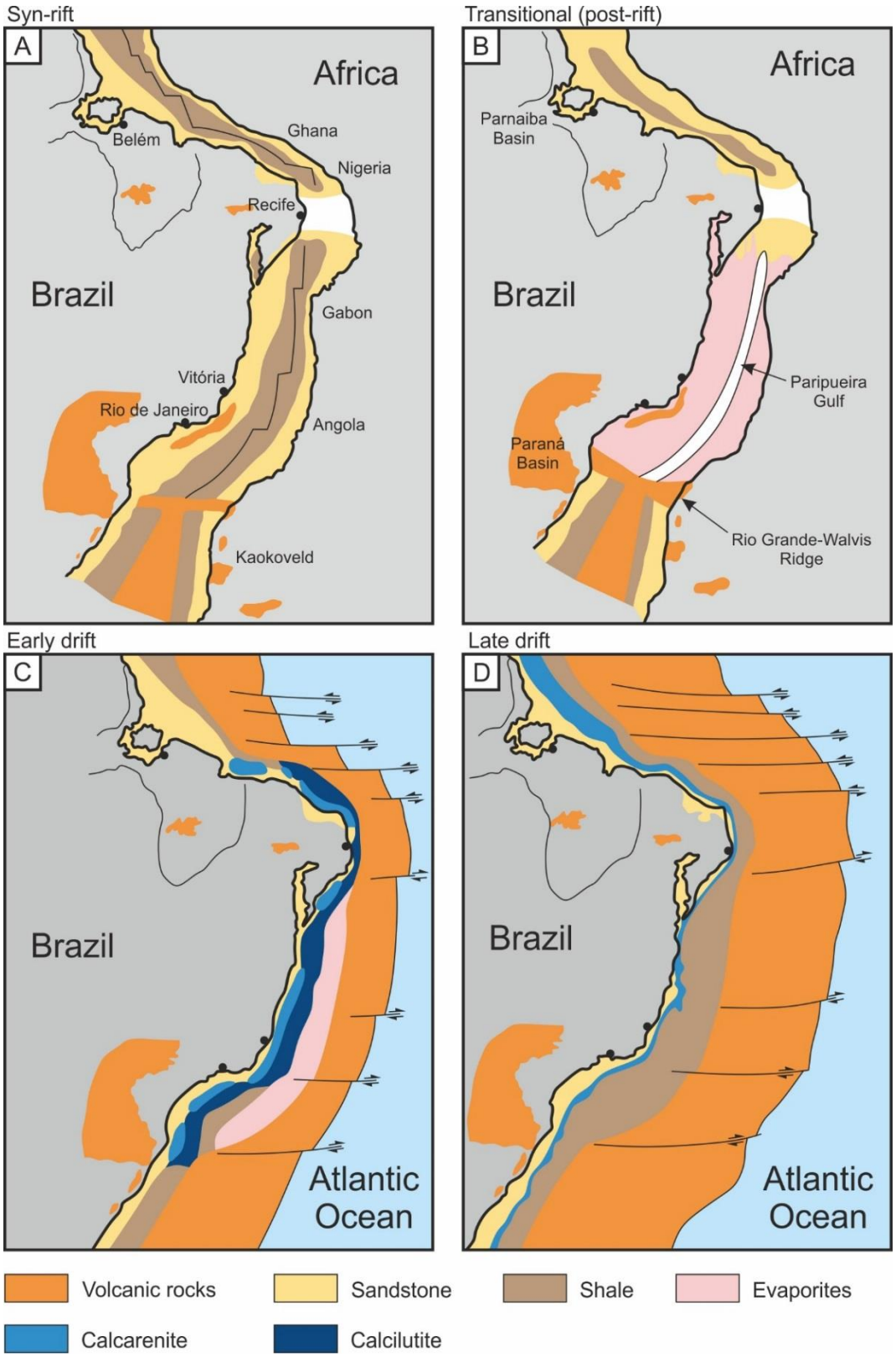

Fig. 2.7 Palaeogeographic maps of the South American-Africa Atlantic margin, focussed on SE Brazil. The four main palaeogeographic stages are shown as: a) syn-rift (pre-Aptian); b) post-rift (Aptian); c) early drift (Albian); d) late drift (Cenozoic open marine). *Modified from Ojeda (1982).*

prevented marine-water from central gulf to mix with marginal basins. This, together with a sabkha climate, allowed thick accumulations of Ibura evaporites to build up (Mohriak et al., 2008). The end of the transitional cycle is marked by the onset of extrusive igneous activity, related to the oceanic spreading ridge (Mohriak et al., 2008, Ojeda, 1982, Davison, 1999).

2.3.1.3. Albian – Recent drift phase

The drift phase comprises two main depositional megasequences, the early drift and the late drift (Fiduk et al., 2004) (Figs. 2.5 and 2.6). Starting in the Albian, oceanic conditions developed in parallel to the formation of oceanic crust (Ojeda, 1982). This was a sign that the continents had started 'drifting' apart, and the South Atlantic Ocean was then connected to the Equatorial margin of Brazil and Central Atlantic (Ojeda, 1982) (Fig. 2.7c). The early drift stage therefore represents two marine-transgressive sequences, with a shallow-water carbonate platform developing from the late Albian to Cenomanian (Chang et al., 1992). This platform is overlain by shales of Turonian to Paleocene age, indicating deepening of the basin (Gamboa et al., 2010, Gamboa et al., 2011, Ojeda, 1982, Demercian et al., 1993).

A mid-Eocene sequence boundary occurs across the entire southeast Brazilian margin and separates the early from the late drift stages (Gamboa et al., 2011). Above this boundary, Eocene to Holocene siliciclastic units were deposited

during a regressive period associated with sediment progradation on the continental slope (Demercian et al., 1993, Chang et al., 1992). At the time, clastic sediment filling the basin were derived from the erosion of coastal mountain ranges and from relatively local volcanic activity on the Abrolhos Plateau, which generated a mid-Eocene unconformity in the basin (Chang et al., 1992, Gamboa et al., 2010). Tuffs, volcanic breccias and hyaloclastites represent the bulk of the volcanoclastic input, whereas fine to coarse massive sandstones, conglomerates and siltstones were eroded from nearby mountains (Gamboa et al., 2010) (Fig. 2.7d).

Sediment transport occurred on Brazil's eastern margin in both drift phases, but was particularly concentrated in Late Oligocene to Holocene channel systems (Viana et al., 2003, Fiduk et al., 2004, Alves, 2010). At least eight episodes of submarine-canyon incision and mass-wasting occurred in the Espírito Santo Basin since the Late Cretaceous (Fiduk et al., 2004). Between the Early/Mid Eocene and the Holocene, mass-transport deposits (MTDs) were also deposited in response to the uplift of coastal mountain ranges, local slope oversteepening and halokinesis (Mohriak et al., 2008, Alves and Cartwright, 2010). Cenozoic successions, comprise sediment aggraded during transgressive and highstand system tracts, and prograding strata associated with lowstand (i.e. regressive) systems tracts and associated submarine-canyon incision (Fiduk et al., 2004, Alves, 2010). Hence, in the Espírito Santo Basin mud-rich depositional tracts (shelf-margin deltas and hemipelagic wedges) deposited in highstand and

transgressive sea-level conditions alternate with gravitational and sandy depositional tracts (canyons, deltas and meandering channels) accumulated during sea-level lowstands (Alves, 2010). Some of the largest sediment flows are thought to have been deposited during a Late Miocene regressive episode (Alves and Cartwright, 2010, Alves et al., 2009, Mohriak et al., 2008).

The modern continental slope comprises turbidites, calcarenites and calcareous mudstones, and overlies Early Cenozoic carbonates and shales belonging to the Early Urucutuca and Regência Formations (Alves and Cartwright, 2010, Mohriak et al., 2008).

2.3.2. Petroleum systems from offshore SE Brazil

Exploration offshore Brazil has been continually growing since the first offshore oil and gas discovery in the Campos Basin, back in 1974 (Bruhn et al., 2017). Since that time, exploration has moved from shallow offshore to ultra-deep prospects, allowing many new oil and gas plays to be exploited (Carminatti et al., 2008). In general, mature source rocks are located along the whole of the Brazilian margin, and have been generating hydrocarbons since the Late Cretaceous (Davison, 1999). With improving technology, exploration efforts are now being directed to 'pre-salt' reservoirs, stratigraphically below the drift-phase evaporites (Carminatti et al., 2008, Bruhn et al., 2017). Especially in the Espírito Santo Basin, thick evaporite sequences can prevent hydrocarbon migration from

pre-salt source rocks; only salt welds and growth faults may permit fluid flow past the salt (Davison, 1999). However, new discoveries are being made below the Aptian salt of Espírito Santo, and this region is now a global frontier basin (Carminatti et al., 2008, Bruhn et al., 2017). Below is an overview of the main hydrocarbon plays currently being explored offshore Brazil (Fig. 2.8).

2.3.2.1. Syn-rift plays

The syn-rift petroleum plays have prolific source rocks. Neocomian (Early Cretaceous) source rocks are believed to be the most important for both the Espírito Santo and Campos oils (Davison, 1999). Fiduk et al. (2004) separated the source rocks into syn-rift I and syn-rift II types. The first (syn-rift I) were deposited from the late Berriasian to middle Barremian. They comprise thin layers of black to dark-grey lacustrine freshwater shales with TOC values ranging from 1-6%. They predominantly comprise Type I kerogen (Davison, 1999, Fiduk et al., 2004, Mello and Maxwell, 1990). Deposition of this source rock occurred in narrow, deep, highly asymmetrical rift basins, confined to the basin axes, recording a high sediment input (Gibbs et al., 2003, Fiduk et al., 2004).

Syn-rift II source rocks were deposited from the middle to late Barremian in broad, shallow, saline lacustrine basins with a low sediment input (Gibbs et al., 2003, Mello and Maxwell, 1990, Fiduk et al., 2004). Syn-rift II source rocks

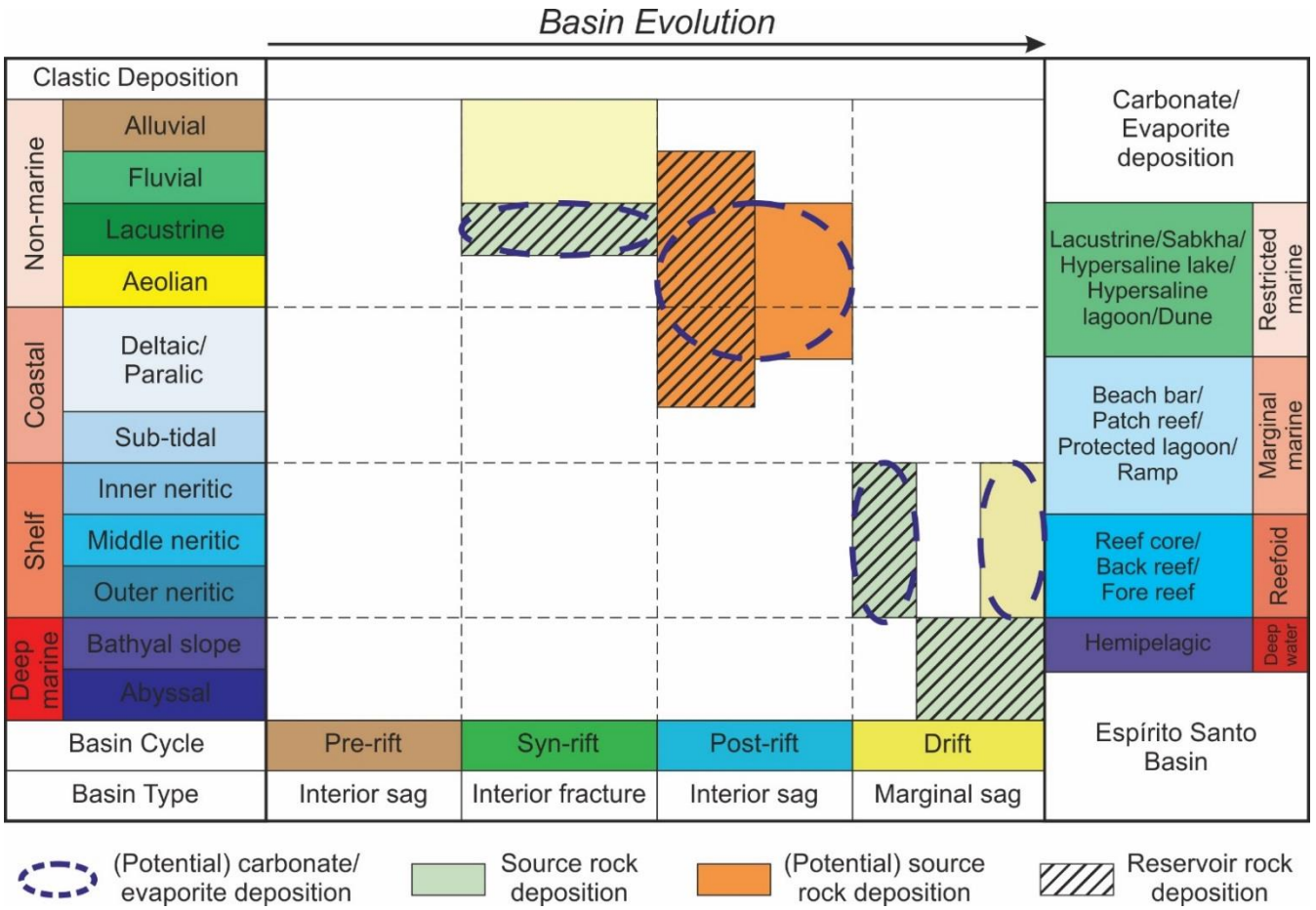

Fig. 2.8 Overview of the main petroleum systems in the Espírito Santo Basin, SE Brazil. The depositional environment is shown on the y-axis, with the different stages on the x-axis. *Modified from Beglinger et al. (2012).*

occur across the Espírito Santo Basin as thick-bedded, laminated calcareous black shales, and are considered the dominant source rock in the study area (Fiduk et al., 2004). TOC values for this unit are less than 9%, and comprises either type I or type II kerogen (Fiduk et al., 2004, Davison, 1999, Mello and Maxwell, 1990).

Several reservoir intervals are associated with these syn-rift source rocks. However, for post-salt reservoirs to be charged, hydrocarbon migration must have occurred through faults cross-cutting the thick Aptian evaporites (Ojeda, 1982, Meisling et al., 2001). Alternatively, syn-rift reservoirs from Berriasian to Aptian age can hold large volumes of hydrocarbons (Davison, 1999). Coarse fan sandstones on the margins of the basin, and turbidite sandstones deeper in the basin, are sufficiently large enough for commercial production of hydrocarbons (Davison, 1999, Ojeda, 1982). These reservoirs are particularly effective where syn-rift tilt-blocks containing source and reservoirs intervals have not been too deeply buried, and remained in close proximity to each other (Davison, 1999).

2.3.2.2. Transitional plays

Transitional phase petroleum plays are less extensive than their syn-rift counterparts, but can still generate large quantities of oil (Ojeda, 1982). Source rocks associated with the Aptian evaporite successions occur in the Ibura evaporites (Ojeda, 1982, Fiduk et al., 2004, Beglinger et al., 2012). These are thin, black, organic-rich shales and contain type II kerogen with a wide range in TOC

values; from 1.5% to 14% (Davison, 1999). These source rocks were deposited in hyper-saline marine lagoons that were oxygen starved (Mello and Maxwell, 1990, Estrella et al., 1984, Davison, 1999, Fiduk et al., 2004). For this reason, there is a strong herbaceous and woody input of organic matter (Type I kerogen) in transitional source rocks (Davison, 1999).

Most oil and gas produced in the transitional phase relies on basal conglomerate reservoirs underlying the evaporitic sequence (Ojeda, 1982, Estrella et al., 1984, Beglinger et al., 2012). These have a close stratigraphic relationship to the transitional source rocks, so the oil does not need to travel a long distance. Instead, they migrate down into the conglomerates (*e.g.* the Alagoa sands) and towards paleostructural traps (Ojeda, 1982, Estrella et al., 1984). Most of the traps in this play are fault-bounded structures, drape folds and depositional pinch-outs that were formed during the final stages of fault activity of the post-rift phase (Beglinger et al., 2012).

2.3.2.3. Drift plays

A variety of fields in the Espírito Santo Basin have been developed from the drift-phase sequence, owing to its multiple hydrocarbon plays (Beglinger et al., 2012, Davison, 1999, Fiduk et al., 2004). The oldest drift-phase source rocks are Albian in age and comprise deep-marine shales and carbonates from an open-marine supersequence (Beglinger et al., 2012, Davison, 1999). An example in the

Espírito Santo Basin is the Urucutuca Formation (Beglinger et al., 2012). These are commonly type II oils with TOC values ranging from 1% to 4% (Davison, 1999). Another important source interval from this sequence are the Cenomanian to Campanian organic rich black shales (Fig. 2.8). Although they are not believed to be as well developed on the Brazilian margin compared to the African margin, they can still be expected to occur in the extreme north and south of the Espírito Santo Basin (Davison, 1999, Fiduk et al., 2004). Similar to the Albian shales, TOC values for the Cenomanian-Campanian anoxic shales range from 1% to 4% (Davison, 1999). Kerogen is chiefly of type II and generates higher API oil and gas than older source rocks (Mello and Maxwell, 1990). Emplacement of the Abrolhos Plateau led to a pulse of heat during the early to middle Eocene, which could have helped mature otherwise immature source rocks, or could have caused the rocks to become overmature (Gibbs et al., 2003, Meisling et al., 2001).

The final source rocks to be deposited in the drift-phase comprise Maastrichtian to Holocene open-marine shelf shales. These may have developed near the Amazon delta, where plant debris was washed into the basin from the Amazon rainforest (Davison, 1999). These source rocks tend to be relatively poor, with low TOC values (<2%), and are mainly type III.

The drift-phase is also characterised by a wide range of reservoir rocks. Albian carbonates, the oldest of those reservoir intervals, were accumulated during a period of marine transgression. They mostly comprise ooilitic marine

shoals and platform carbonates (such as the Regência carbonates), and were formed over salt-induced highs in shallow-marine conditions (Fiduk et al., 2004, Beglinger et al., 2012). These Albian carbonates can retain porosity values of up to 20% at their current burial depths (Davison, 1999). Overlying the carbonates are fan-deltas and shallow-marine clastics, suggesting that a prograding clastic wedge eventually drowned the Albian carbonate platform (Davison, 1999, Beglinger et al., 2012). From the Campanian to Maastrichtian, transgressive marine sands were deposited in submarine channels, canyons, and fan complexes in deep waters, often ponding in salt withdrawal basins or faulted grabens (Fiduk et al., 2004, Davison, 1999). These marine sands are often very clean, well sorted, and highly connected, making them extremely effective reservoirs (Davison, 1999).

The Cenozoic regressive episode permitted the deposition of marine sands in continental-slope and deep basin environments (Fiduk et al., 2004). Submarine channels and canyons cut through the continental shelf and slope, shedding sediment basinwards via turbidity currents (Fiduk et al., 2004, Davison, 1999, Ojeda, 1982). Distal turbidites and fan deposits, therefore, occur downslope of feeder channels (Fiduk et al., 2004, Carminatti et al., 2008). Both the transgressive and regressive sands are important reservoirs in the Espírito Santo Basin, as most reserves have been discovered at these stratigraphic levels (Ojeda, 1982, Beglinger et al., 2012).

2.4. Taranaki Basin, New Zealand

The Taranaki Basin is located on the west coast of New Zealand's North Island, extending offshore into the Tasman Sea, and onshore onto the Taranaki Peninsula (Fig. 2.9). It covers an offshore area of approximately 100,000 km^2, is up to 60 km wide, and extends 350 km in a north-south direction (Ilg et al., 2012, King and Thrasher, 1996, Giba et al., 2010). The basin formed during a period of Cretaceous rifting, coeval with the opening of the Tasman Sea, and has continued to develop through the Holocene (Holt and Stern, 1994). It is broadly divided into two regions: a) the Western Stable Platform, and b) the Eastern Mobile Belt (Fig. 2.9). The Western Stable Platform is relatively tectonically inactive, but the Eastern Mobile Belt is structurally very complex, incorporating the Northern and Central Grabens, the Tarata Thrust Zone, and the Southern Inversion Zone (Hansen and Kamp, 2004, King and Thrasher, 1996). Furthermore, a Miocene andesitic volcanic trend (the Mohakatino Volcanic Centre) runs north to south along the Northern Graben, and was most recently active 6 – 8 Ma (Hansen and Kamp, 2004, Thrasher et al., 2002).

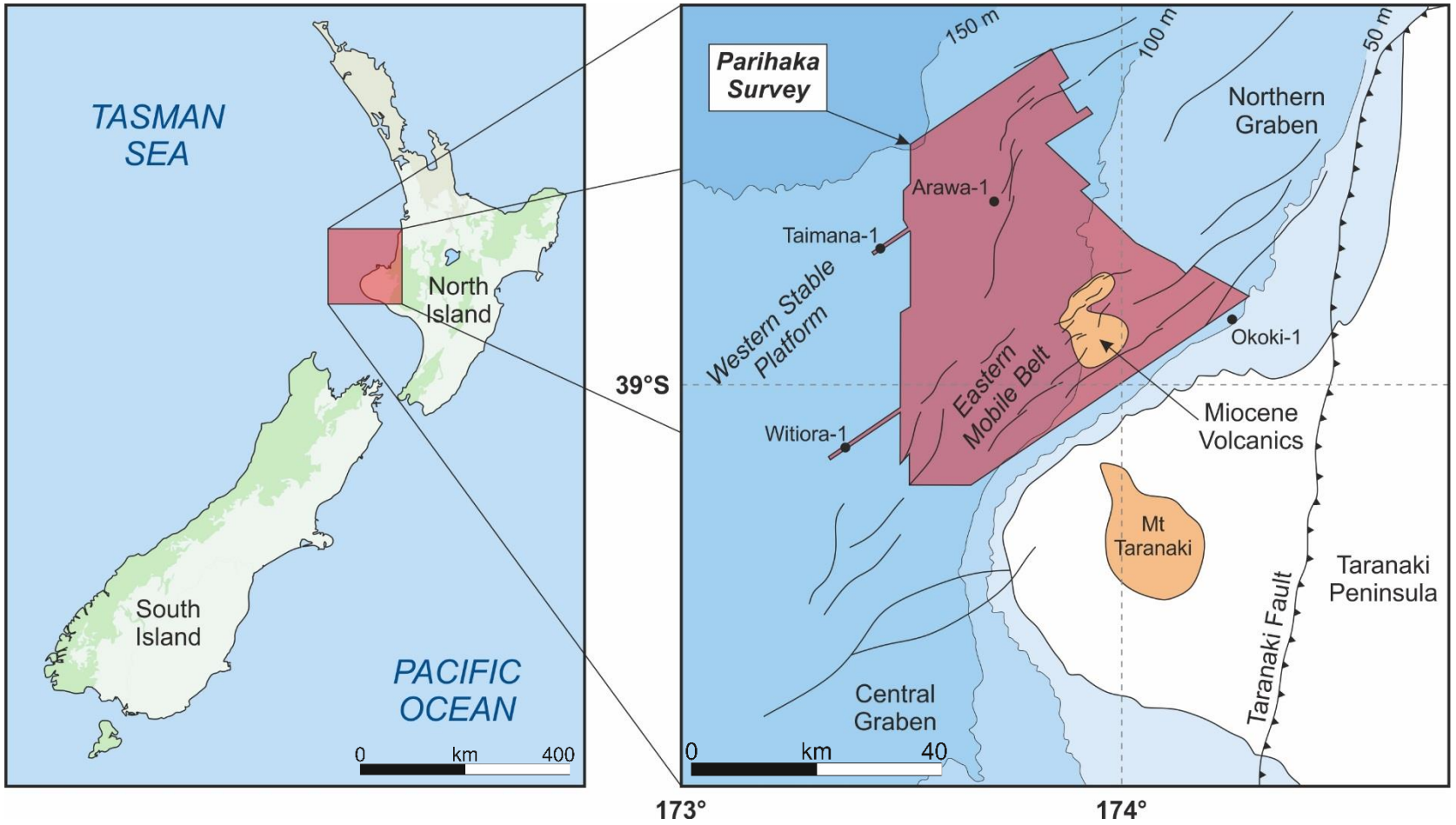

Fig. 2.9 A regional map of the Taranaki Basin, New Zealand. The location of major fault systems and Miocene volcanics are shown. The Parihaka seismic survey, used in *Chapter 7*, is highlighted in red.

2.4.1. Tectonic evolution of the Taranaki Basin

The eastern boundary of the Taranaki Basin is the Taranaki Boundary Fault; a giant suture zone that runs from the west coast of the North Island into the Alpine Fault in the South Island (Stagpoole and Nicol, 2008) (Fig. 2.9). The Taranaki Boundary Fault contains the earliest exposed rocks in the area, part of a Permian ophiolite emplaced from late Palaeozoic to Late Jurassic - suturing of an accretionary wedge onto the New Zealand margin of Gondwanaland (Carter and Norris, 1976, Knox, 1982, Holt and Stern, 1994). Towards the end of the Mesozoic, the fault underwent normal movement as the Tasman Sea opened and the Taranaki Basin was formed (Holt and Stern, 1994).

Following Cretaceous extension, tectonic activity remained relatively low. The basin became a shallow-water passive margin in the Early Oligocene, deepening towards the northwest (King and Thrasher, 1996). This phase was superseded by rapid subsidence in the Late Oligocene to Early Miocene (Holt and Stern, 1994). Compressive deformation from the west overlapped this subsidence causing reverse movement on the Taranaki Boundary Fault (Stagpoole and Nicol, 2008). The Cape Egmont Fault Zone comprises evidence for west verging thrusting from the Late Miocene to Early Pliocene. The timing of motion along this fault zone is consistent with the migration of the active thrust front (Holt and Stern, 1994, Knox, 1982). The Northern Graben is situated

between the Cape Egmont Fault Zone in the west and the Turi Fault Zone in the East (Fig. 2.9).

In parallel to the latter tectonic events, subduction of the Pacific plate along the Hikurangi Trough caused back-arc extension to dominate in the Taranaki Basin (Giba et al., 2010, Holt and Stern, 1994). The Mohakatino Volcanic Centre developed during this period, and remained active from ~12 Ma to 4.8 Ma.

The sedimentary succession in the Taranaki Basin contains an almost complete Miocene to Holocene record of volcanics and faulting (Giba et al., 2010). In some areas, strata are up to 8 km thick for this time period (Giba et al., 2010, King and Thrasher, 1996). The lowermost unit of interest in the area is the Mangaa Formation, which was deposited during the Late Miocene as submarine basin fan systems (Hansen and Kamp, 2004). Lying above this section is the widespread Giant Foresets Formation. By the Late Pliocene, a continental margin wedge had infilled graben structures, and had begun prograding onto the Western Stable Platform (Hansen and Kamp, 2004, Holt and Stern, 1994). Continental scale clinoforms stacked on top of each other to produce a ~2000 m thick unit, the Giant Foresets Formation, with regular occurrences of incised channels (Hansen and Kamp, 2002, King and Thrasher, 1996).

2.4.2. Petroleum systems of the Taranaki Basin

Hydrocarbon exploration in New Zealand has been almost entirely constrained to the Taranaki Basin. Reserve estimates point out to at least 180 million BOE left in the basin (Ilg et al., 2012, Webster et al., 2011). However, 70% of the already discovered reserves have comprised natural gas, not oil (Webster et al., 2011). Intense exploration in the basin has supplied significant subsurface information, especially in the south of the basin which contains the most productive oil and gas fields (Stagpoole and Nicol, 2008, Ilg et al., 2012) (Fig. 2.10). Most of the main plays lie in Upper Cretaceous to Lower Tertiary coal measures, which contain source rocks, reservoir rocks and seals (Pilaar and Wakefield, 1984).

Source rocks in the Taranaki Basin are pretty much exclusively Late Cretaceous to Early Eocene coal measures (Webster et al., 2011). They are responsible for major discoveries in the west of the Basin, including the Maui, Maari, and Tui fields (Pilaar and Wakefield, 1984, Ilg et al., 2012, Webster et al., 2011). Thick coal measures deposited in graben structures also provide oil for most onshore fields (Fig. 2.10).

Due to the presence of such a thick sedimentary succession, and the proximity of the basin to the continental margin, there are multiple reservoir intervals in the Taranaki Basin. The stratigraphically lowest are Cretaceous to Paleocene well-sorted sands, deposited in delta systems. These are the major

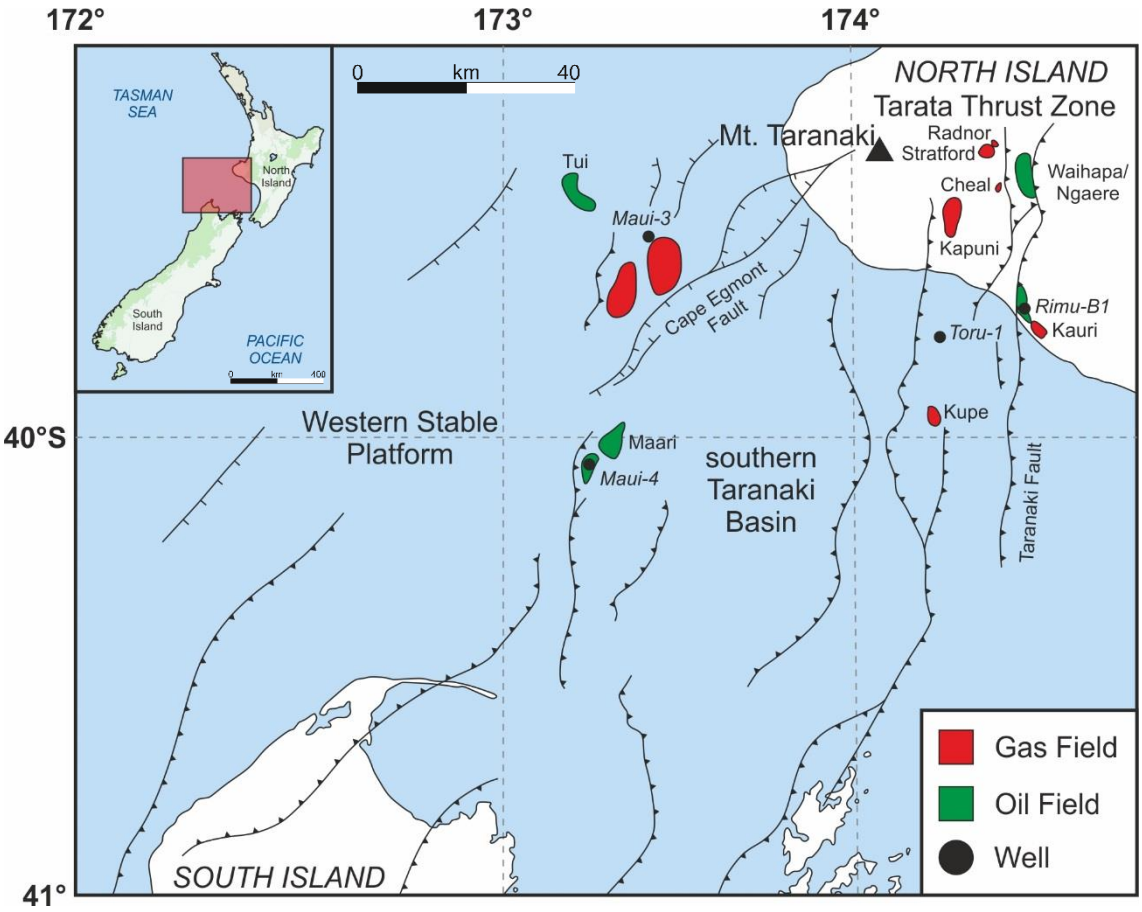

Fig. 2.10 A map of the southern Taranaki Basin showing major faults in the region and principal oil and gas fields. *Modified from Ilg et al. (2012).*

reservoir intervals for the Maui, Pohakura, Tui and McKee fields (Webster et al., 2011, Pilaar and Wakefield, 1984) (Fig. 2.10). Among the sandstones are fluvial and paralic sediments that house gas/oil condensate. The Eocene reservoirs above comprise sediments deposited in the lower alluvial plains, coastal plains and in marginal marine areas (Ilg et al., 2012). During the Oligocene, foredeep fans became reservoir intervals for condensate gas and oil found in the Tariki and Ahuroa fields. Fractured limestones from this age comprise the reservoir unit in the Waihapa oil field (Webster et al., 2011).

Deep-water sediment transport systems were responsible for the the deposition of Miocene reservoir rocks; thick turbidites in the Maari oil field, and thin channel-levee and slope deposits in onshore oil fields (Webster et al., 2011). Volcaniclastic sediments derived from the Mohakatino Volcanic Centre comprise the main reservoir interval in the Kora oil field (Webster et al., 2011).

Structural traps in the basin consist of inversion anticlines, fault-dependent closures and overthrusts (Webster et al., 2011). The plays are generally sealed by Eocene – Oligocene and Lower Miocene siltstones and marls representing flooding maxima (Ilg et al., 2012). Migration of oil and gas from the Cretaceous coal measures began in the Middle Miocene (~15 Ma), and has continued until the present day (Ilg et al., 2012, Armstrong et al., 1996). Hydrocarbons relied on late stage normal faults to migrate to the shallowest reservoirs, passing vertically through 3 to 4 km of sediment en route (Ilg et al.,

2012). The source rocks reached maturity at different times in the basin; in the Taranaki Graben, the source rocks are fully mature and expelling mainly gas. In the Western Stable Platform, there is a decrease in maturity to the west and northwest, where source rocks are mostly immature (Pilaar and Wakefield, 1984).

CHAPTER THREE

Data and methods

3. Data and methods

3.1. Introduction

This PhD employs three-dimensional (3D) seismic volumes to interpret deep-water geological features in the subsurface. The interpreted seismic surveys have been shot for exploration purposes, and are being used in Cardiff University's 3D Seismic Lab to aid with research. All the data is high-quality, enabling detailed interpretations of subsurface features at resolutions previously unattainable.

This chapter aims to give a broad overview of how the seismic data is acquired, processed, and interpreted. It will also provide detailed information on the datasets used. Specific methods related to each chapter are provided in the corresponding chapter.

3.2. Seismic data

Three-dimensional (3D) seismic data is arguably one of the most significant advances in hydrocarbon exploration, especially considering the exploration of deep-water depositional systems (Posamentier and Kolla, 2003, Bull et al., 2009). Further ashore, exploration has led to widely accessible high-quality 3D seismic data in sedimentary basins across the globe (Posamentier and

Kolla, 2003). The data provides an excellent tool for visualising and mapping subsurface geological features and understanding geological processes (Cartwright, 2007). Unlike two-dimensional (2D) seismic data, which only gives a cross-section of the subsurface, 3D seismic data provides a complete image of geological structures, which inherently have a more intricate geometry than when they are imaged in two dimensions (Biondi, 2006).

3.2.1. Seismic acquisition

As suggested by the name, seismic acquisition involves the detection of vibrations in the ground, or seismic waves (Fig. 3.1). More accurately, it is the detection of sound waves moving through and bouncing off different layers of rock (Fig. 3.1). These sound waves are created artificially; an energy source emits an acoustic pulse, which is acquired (or received) after a certain amount of time by hydrophones (or receptors) that are geometrically arranged according to the purpose of the survey. For offshore seismic surveys (which include all the datasets used in this thesis), the energy source is often an array of air guns tuned to give a downwards concentrated pulse of acoustic energy (Bacon et al., 2007). An explosion, or expansion and collapse of an air bubble produced by the gun, creates compressional waves (P-waves) that penetrate the sea floor and reflect off

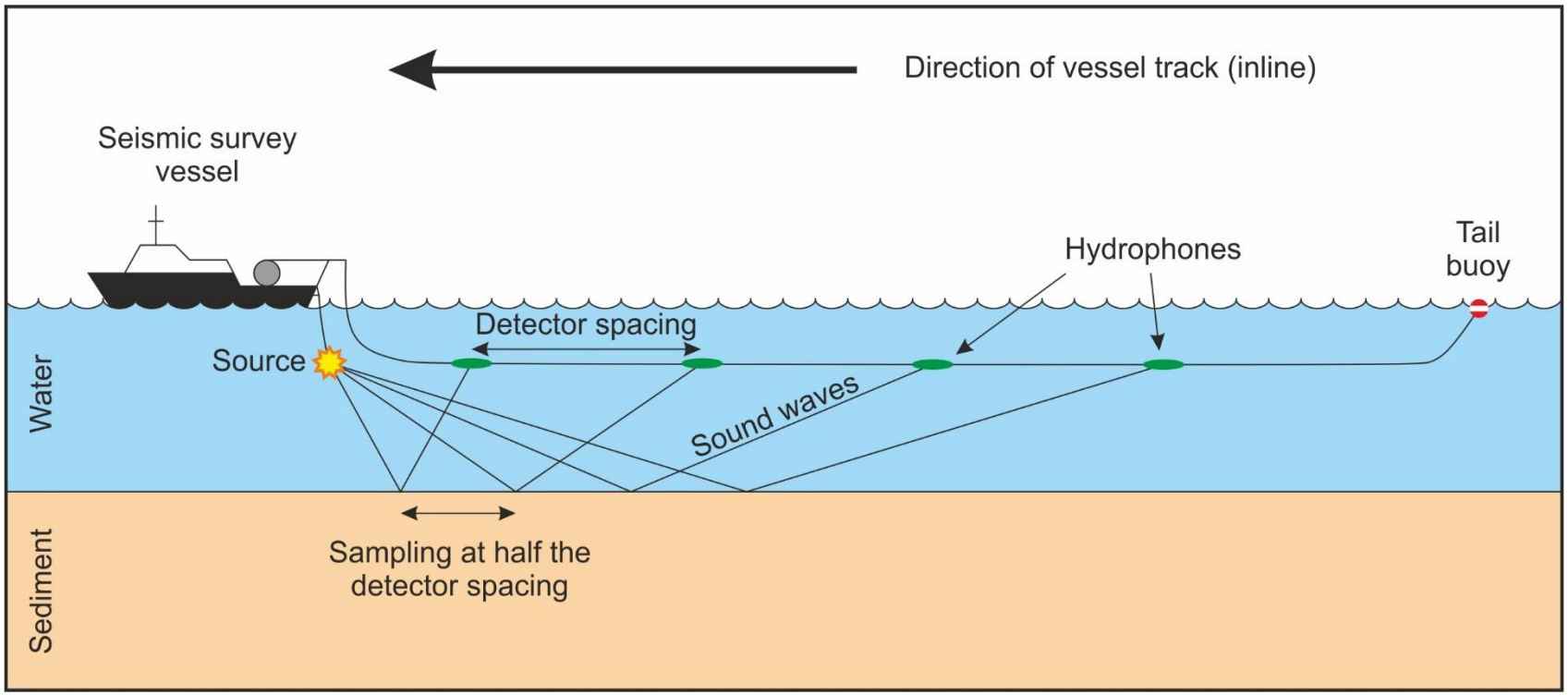

Fig. 3.1 Cartoon illustrating the method behind the acquisition of 3D seismic data. The seismic survey vessel tows an acoustic source near the surface, which emits a loud soundwave. These waves travel through the water and into the sediment layer, reflecting back to the receiver (hydrophones). *Modified from Bacon et al. (2007).*

subsurface geological interfaces (Bacon et al., 2007, Kearey et al., 2013, Gluyas and Swarbrick, 2013). Data is received by streamers of hydrophones normally towed by a length of cable (usually up to 8 km long, but longer if deeper wave penetration is needed) behind the survey vessel (Fig. 3.1). The vessel tracks backwards and forwards, creating a three-dimensional grid, with the direction of the boat movement known as an 'inline', and the perpendicular section being a 'crossline' (Brown, 2004). Trace spacing between the separate inlines or crosslines normally vary from 12.5 to 50 m (Yilmaz, 2001).

In general, seismic data is a graphical representation of the time it takes for the seismic signal to travel from the source, to a geological interface, and back to the receiver (Kearey et al., 2013, Bacon et al., 2007). The depth (or z-axis) is measured in two-way time, *i.e.* the time it takes for a seismic wave to be produced, reflected, and received at the hydrophones or receivers. The main parameter to control on a seismic survey is, therefore, the movement of acoustic waves through the subsurface geology. Normally, marine seismic surveys only record P-wave velocities, as S-waves (shear-waves) do not propagate through the water column (Veeken, 2006, Kearey et al., 2013). But S-wave data can be acquired at a greater expense either on land (negating the effect of the seawater on the shear-waves) or using a source and/or receiver on the seafloor (Kearey et al., 2013, Veeken, 2006).

The speed at which a sound wave will travel through the subsurface depends on the acoustic properties of the rock (Gluyas and Swarbrick, 2013). This is expressed as the velocity and frequency of an acoustic wave. The interval velocity (v) is the time taken for a wave to move through a certain thickness of rock (Kearey et al., 2013). P-wave velocity through a rock layer is dependent on its physical properties, including the composition, cementation, density, porosity and pore fluids. Upon reaching a sufficient velocity contrast, such as sedimentary bedding plane, unconformity, or change in pore-fill characteristics, the seismic wave is partially reflected off that boundary, and partially transmitted through it (Veeken, 2006, Gluyas and Swarbrick, 2013, Kearey et al., 2013). The magnitude of seismic waves reflected back onto the surface depends on the velocity (v) and density (ϱ) contrasts between two rock units. Hence, the dispersal of transmitted and reflected waves is known as the acoustic impedance (Z), and is expressed as:

$$Z = \rho \cdot v$$

Equation 3.1

The larger the energy reflected from a boundary, or interface, the greater will be the contrast in acoustic impedance (Kearey et al., 2013). The relative amplitudes of transmitted and reflected energy also depend on the angle of incidence, or the angle at which the P-wave interacts with the geological boundary (Gluyas and Swarbrick, 2013) (Fig. 3.2). To quantify this, a reflection

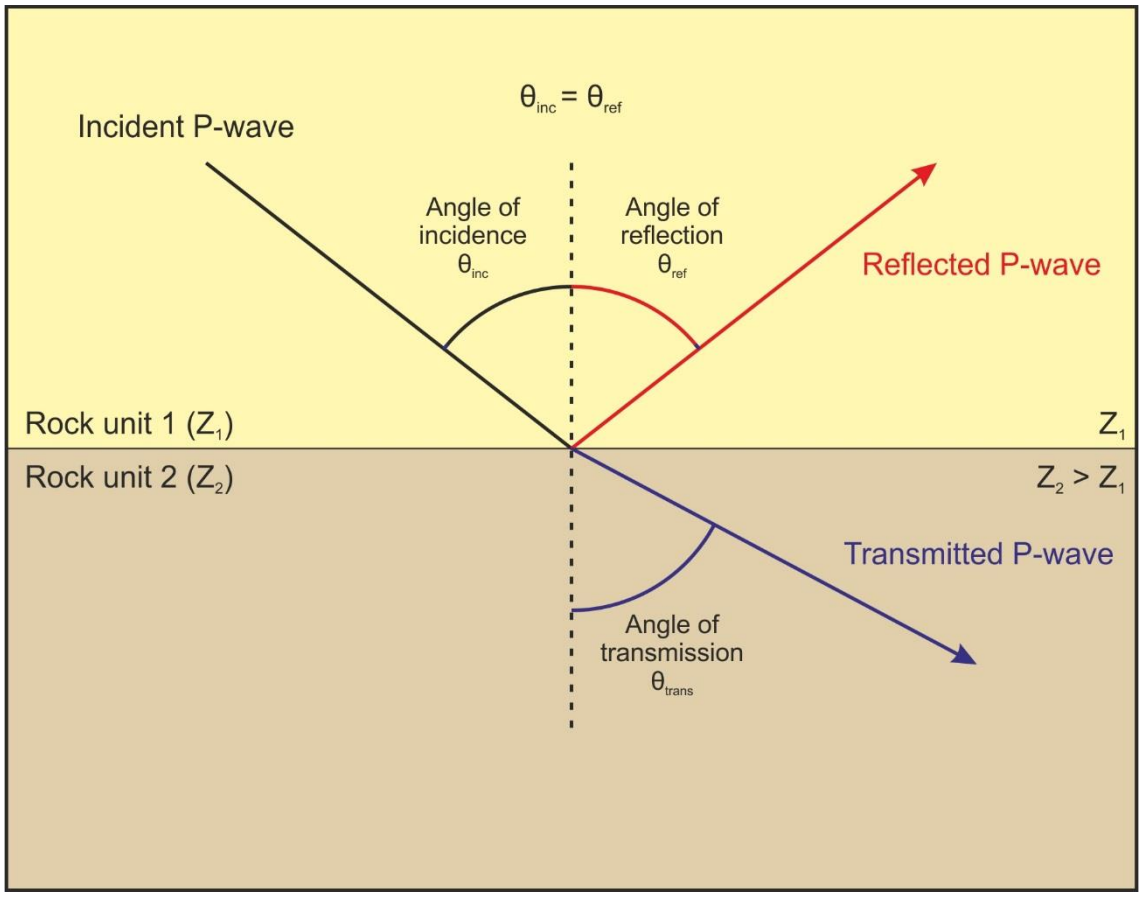

Fig. 3.2 Conversion and reflection of P-wave energy as it contacts an acoustic impedance surface. Some energy is reflected towards the surface, whereas some energy is transmitted (or refracted) into the rock layer below. The angle of reflected waves is equal to the angle of incidence. The angle of refraction varies according to rock type. *Modified from Veeken (2006) and Kearey et al. (2013).*

coefficient (R) is calculated as being the measure of the effect acoustic impedance has on wave propagation when reflected, such that:

$$R = \frac{Z_2 - Z_1}{Z_2 + Z_1}$$

Equation 3.2

The inverse of this equation is the transmission coefficient (T), which is the measure of the effect acoustic impedance has on wave propagation when transmitted (Kearey et al., 2013, Veeken, 2006):

$$T = \frac{2Z_2}{Z_2 + Z_1}$$

Equation 3.3

Seismic data are displayed as sinusoidal transverse waves, or wavelets (Gluyas and Swarbrick, 2013) (Fig. 3.3). Wavelets comprise an absolute representation of signal amplitude, which is in turn perpendicular to the propagation of the wave. An increase in acoustic impedance results in a positive amplitude, or a peak, whereas a decrease in acoustic impedance results in a negative amplitude, or a trough (Sheriff and Geldart, 1995). Therefore, the amplitudes of peaks and troughs are proportional to reflection strength (Gluyas and Swarbrick, 2013).

Typically, waves are displayed in discrete colours, such as the 'SEG (Society of Exploration Geophysicists) normal polarity classification' (Fig. 3.3).

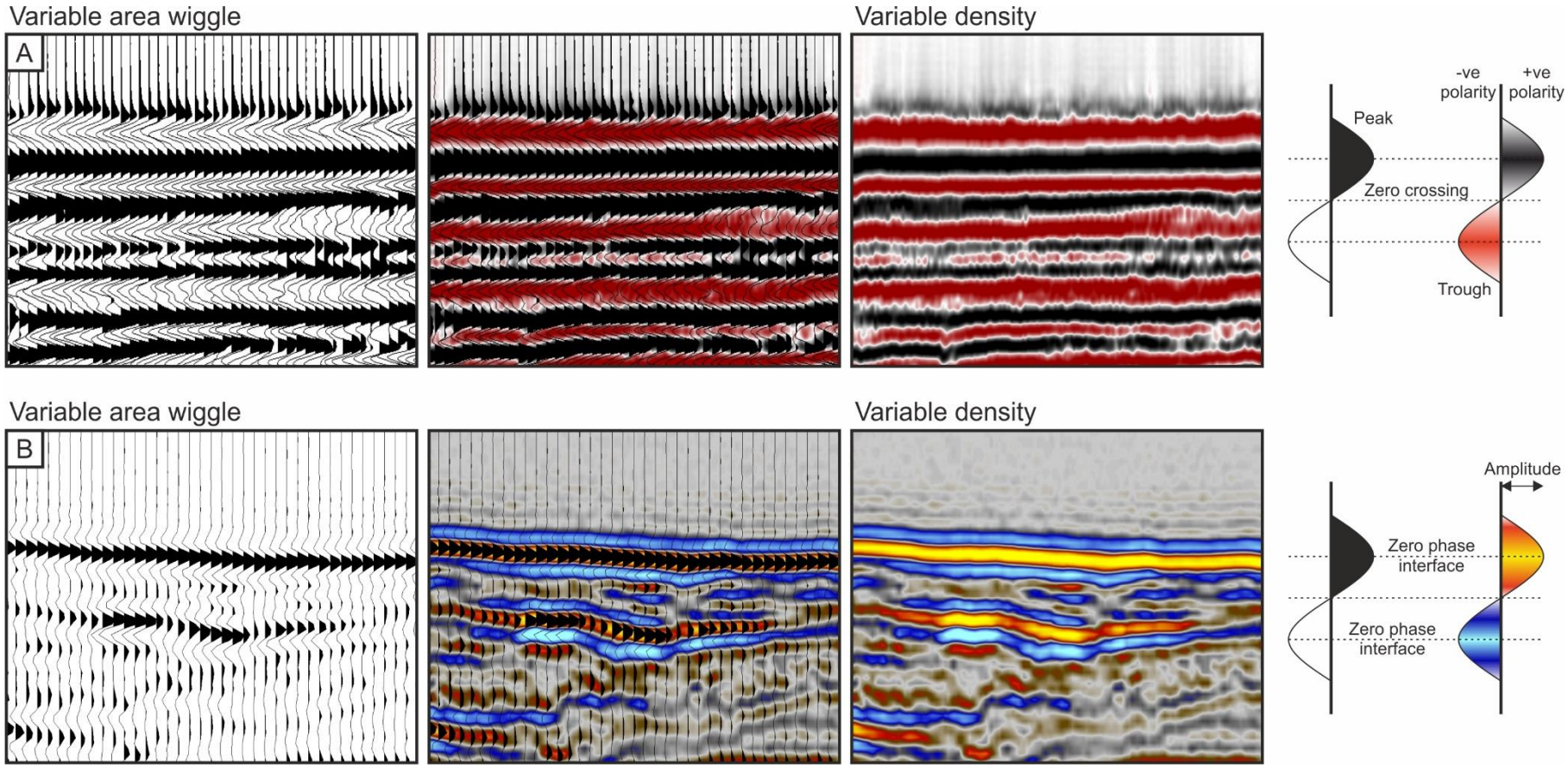

Fig. 3.3 Seismic display of how variable-area wiggles are converted into variable density using differing colour schemes. a) Black to red colour scheme adopted in the BES-2 and Parihaka datasets (*Chapters 5* and *7*), where black is positive polarity, and red is negative. *N.b.* the polarity is swapped in the BES-2 survey (*Chapter 5*). b) Yellow to cyan colour scheme adopted for the Broad Fourteens Basin and BES-100 datasets (*Chapters 4* and *6*), where yellow is positive and cyan is negative.

The classification recommends that the waves are displayed as peaks and troughs with a gradational colour scheme between them, *e.g.* black (positive values), through white (zero amplitudes), to red (negative amplitudes) (Hart, 1999). This way of representing the seismic waves guides the interpreter to dim spots, as well as bright spots, which may have been ignored were a simple black and white colour scheme to be used. In *Chapter 5*, such a colour scheme was adopted, whereas in *Chapters 4* and *6*, the European convention was the preferred one, effectively grading from yellow (very positive), through red (positive), through white (zero), through blue (negative), to cyan (very negative) (Fig. 3.3).

3.2.2. Seismic resolution

One of the key parameters concerning the quality of seismic data is seismic resolution. It controls the ability to visualise individual, closely spaced points, whether they are two reflectors at depth, or geological features along a surface. Vertical resolution describes the former: the recognition of different reflections at depth, whereas horizontal resolution controls the size of features that can be observed along a horizontal surface (Kearey et al., 2013, Brown, 2004, Veeken, 2006, Yilmaz, 2001).

3.2.2.1. Vertical resolution

The vertical resolution of a seismic volume is determined by the seismic source signal and how it is filtered through the Earth (Bacon et al., 2007). This is measured in terms of the seismic wavelength (λ) as a quotient of velocity (ν) and frequency (f), such that (Brown, 2004):

$$\lambda = \frac{\nu}{f}$$

Equation 3.4

As seismic waves travel deeper into the subsurface, higher frequency waves will be absorbed (Kearey et al., 2013). In addition, increased compaction and diagenesis in deeply buried rocks will increase the velocity of a seismic wave, which, in turn, will lead to an increase in wavelength (Veeken, 2006, Brown, 2004). Vertical resolution therefore decreases as a function of depth.

The maximum resolution of a single wavelet from a reflected pulse is equal to approximately one-quarter to one-eighth of the dominant wave length of the original seismic pulse (Sheriff and Geldart, 1995). As a consequence, the smallest seismically resolvable features are an order of magnitude larger than what a geologist might observe at outcrop (Kearey et al., 2013).

Attenuation of vertical resolution can be improved during processing with the deconvolution tool (Kearey et al., 2013). This involves shortening the pulse length using inverse filtering, commonly with an anti-aliasing filter (Veeken, 2006, Kearey et al., 2013). Shallow seismic surveys often give much higher resolutions (centimetre scale) as higher frequencies are used, but the acoustic signal only penetrates the near surface strata, making shallow seismic surveys less useful for hydrocarbon exploration (Veeken, 2006).

3.2.2.2. Horizontal resolution

Horizontal resolution is controlled by two factors: 1) the spacing of detectors behind a ship, and 2) the physical process of reflection. The combination of both factors makes the quantification of horizontal resolution more complex than vertical resolution (Kearey et al., 2013). As shown in Figure 3.1, the horizontal sampling of a flat reflector is half the length of the detector spacing. Because of this, the length of the reflector sampled by any detector spread is equal to half the actual spread length (Kearey et al., 2013).

The latter factor (process of reflection) controls the absolute limit of horizontal resolution. Seismic signal is better described as an infinite number of point scatters that are reflecting off an interface, and thus the actual reflected pulse that is detected results from an interference of an infinite number of backscattered rays (Kearey et al., 2013). The area surrounding the reflected

energy, which contributes to the signal at that reflection point, is known as the *Fresnel Zone* (Bacon et al., 2007) (Fig. 3.4a). It is the radius of this zone that represents the absolute limit on horizontal resolution and is dependent on the wavelength of the acoustic signal and the depth of the reflector (Kearey et al., 2013, Veeken, 2006). Any reflector that is separated by a distance smaller than the radius of the Fresnel zone is not seismically resolvable. The size of the Fresnel zone (w) increases as a function of reflection depth (z):

$$w = \sqrt{2z\lambda}$$

Equation 3.5

where λ is the dominant wavelength of the source (Kearey et al., 2013). Similar to the vertical resolution, horizontal resolution decreases with depth due to the increase in radius of the Fresnel zone (Fig. 3.5a). With this in mind, it should be noted that the geophone spacing should be no more than one-quarter the width of the Fresnel zone.

During data processes, the collection of seismic reflections falling in the same area consists of a common midpoint (CMP) gather. This is also known as stacked, or non-migrated, data (Veeken, 2006, Yilmaz, 2001). To improve the horizontal resolution, the stacked data is then migrated by repositioning out of place reflections (due to the dip of reflectors), focussing the energy spread out

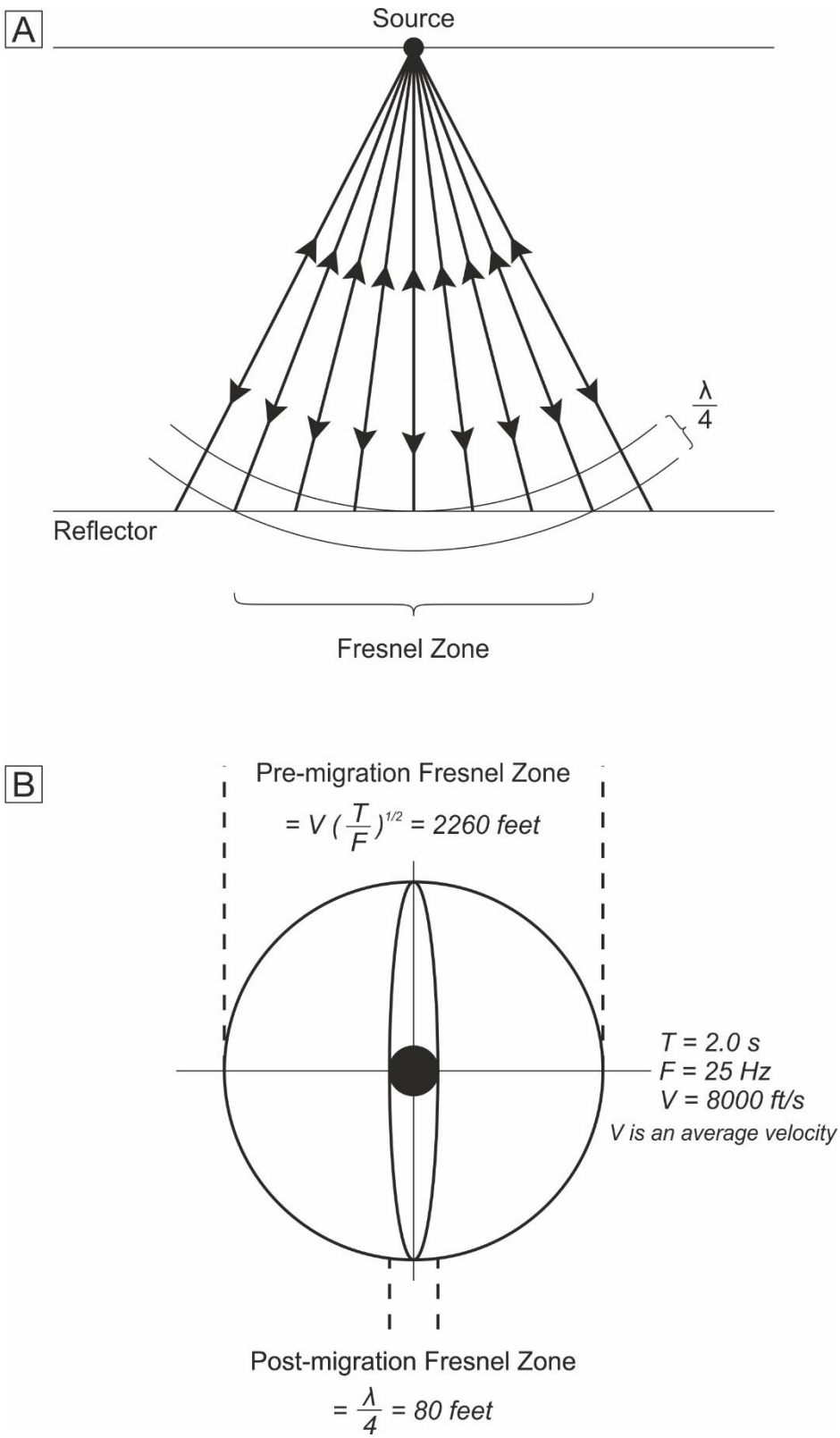

Fig. 3.4 a) Energy returning from the surface of a reflector. The portion of energy returning equal to half the wavelength of the initial reflected arrival is the Fresnel zone. *Taken from Kearey et al. (2013)*. b) The effect migration has on the Fresnel zone. The larger circle represents the Fresnel zone prior to migration, which is then reduced (ideally) to quarter of the wavelength post-migration. Values are provided to give an example. *Taken from Brown (2004).*

over the Fresnel zone, and collapsing the diffraction patterns from the points and edges (Brown, 2004, Bacon et al., 2007). In 3D seismic data, the circle of a Fresnel zone will ideally be reduced to an ellipse with the radius of one-quarter of the wavelength (Fig. 3.4b).

3.3. 3D seismic datasets in this study

3.3.1. Broad Fourteens Basin seismic survey

Seismic data was provided by Tullow Oil plc and were interpreted on Schlumberger's Petrel 2013 software. Well logs uploaded from the NLOG (Netherlands Oil and Gas Portal) website were tied to the seismic data in order to constrain the principal stratigraphic horizons. Coherence slices were used initially to locate discrete fault families and identify specific pockmarks where gas may be leaking. Faults and horizons were interpreted on seismic volumes using Petrel 2013's 'Autotracking' function (*see section 3.4.1*). Each interpretation was subsequently mapped to ensure the automatic function was valid and there were no anomalies in the data. Smoothing surfaces were created to remove any unnecessary gaps and peaks in the interpreted horizons.

The 3D seismic volume interpreted in *Chapter 4* covers ~842 km^2 of the Broad Fourteens Basin (BFB), offshore Netherlands (Fig. 2.1). The seismic volume

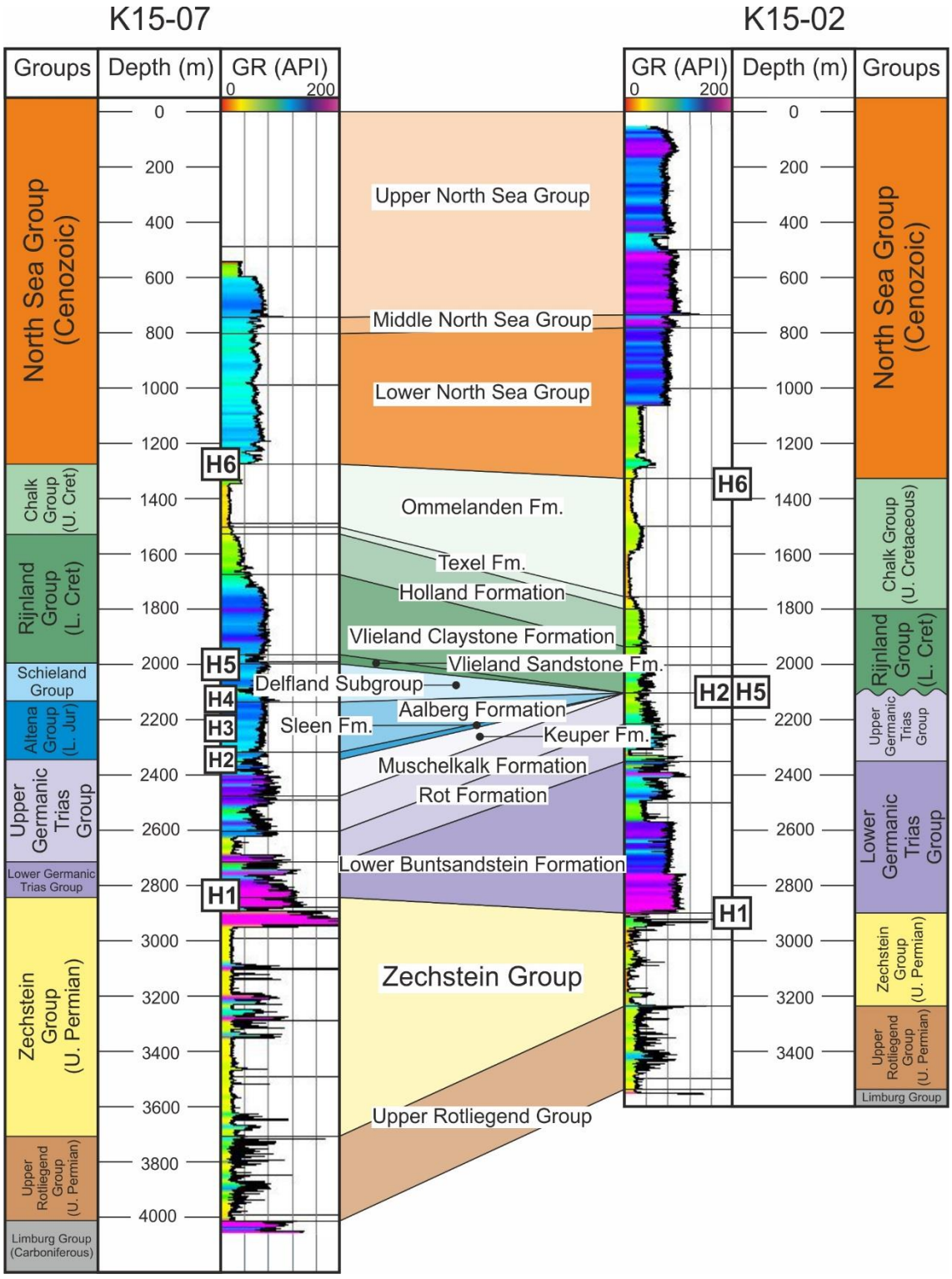

Fig. 3.5 Correlation panel between wells K15-02 and K15-07. The figure highlights the thickness variations observed across the study area. K15-07 is drilled through an inverted anticline, whereas well K15-02 is located close to a salt diapir. Gamma Ray (GR) logs are measured in American Petroleum Institute (API) units.

has an inline spacing of 25 m, and was processed to a 25 m x 25 m bin. Vertical resolution reaches ~10 m based on seismic-borehole ties (Figs. 3.5 and 4.2).

3.3.2. Espírito Santo Basin BES-2 survey

The BES-2 three-dimensional seismic survey used in *Chapter 5* covers an area of 1600 km^2 on the southern slope of the Abrolhos Plateau (Fig. 2.4). Water depths across the study area range from 1000 – 1800 m. The data was acquired using six, 5700 m long arrays of streamers and a dual airgun array. The seismic signal was sampled every 2 ms prior to the application of an anti-aliasing filter and re-sampling at 4 ms. The data are zero-phased migrated with a bin spacing of 12.5 x 12.5 m. The processing sequence of the data included resampling, spherical divergence corrections and zero-phase conversions undertaken prior to stacking, 3D pre-stack time migration using the Stolt algorithm, and one-pass 3D migration.

3.3.3. Espírito Santo Basin BES-100 survey

The three-dimensional (3D) seismic volume used in *Chapter 6* (BES-100) covers an area of 2450 km^2 on the mid-continental slope of Espírito Santo, offshore Brazil (Fig. 2.4). The interpreted zero-phased migrated volume was acquired using a dual airgun array and six 5700 m-long streamers, and later

processed within a 12.5 m x 12.5 m bin grid. Data was sampled every 2 ms following inline and cross-line spacings of 12.5 m. Data processing included data resampling at 4 ms, amplitude recovery, anti-aliasing filtering, time-variant filtering, and predictive deconvolution, prior to stacking and 3D pre-stack time migration using the full Kirchhoff algorithm. All time-depth conversions used an estimated seismic velocity of 1800 m/s TWTT. Main seismic-stratigraphic units were identified using published well data from the Deep-Sea Drilling Project (DSDP) Sites 356 (Kumar et al., 1977) and 515/516 (Barker et al., 1983, Barker, 1983), and the work of Chang et al. (1992), Viana et al. (2003), Fiduk et al. (2004), Alves et al. (2009), Meisling et al. (2001), Gamboa and Alves (2015b).

3.3.4. Parihaka survey – Taranaki Basin

Chapter 7 concerns the interpretation of the Parihaka 3D seismic survey from the Taranaki Basin (Fig. 2.9). The survey covers an area of approximately 1520 km^2, at a maximum water depth of ~132 m. Eight (8) 4500 m array of streamers was used, each with 360 geophones, and a bin spacing of 12.5 x 12.5 m. Data processing included zero-phase conversions, data resampling to a 4 ms vertical sampling window, High-Resolution Radon Transform (XRLIN) linear noise attenuations, TAU-P domain predictive deconvolutions, and NMO corrections to the 60-fold coverage of the seismic trace. A 1 km grid had the full Kirchhoff time migration algorithm applied to it.

3.4. Seismic interpretation

The basis of all analyses in this thesis is seismic interpretation. Interpretation was undertaken in the 3D Seismic Lab, Cardiff University, on Schlumberger's Petrel © 2013, 2014, and 2015.

3.4.1. Horizon and fault mapping

Horizon mapping is fundamental to seismic interpretation. Without well data tied to the seismic reflections on screen, it is still possible to complete facies analyses by identifying and mapping horizons with a high acoustic impedance. In *Chapter 4*, exploration wells were tied to the data to help identify key stratigraphic units (Fig. 3.5). Initially, horizons in all the chapters were manually picked along the brightest (either very high or very low amplitude) seismic reflections, as these indicated unconformities and other key boundaries of depositional sequences (Hart, 1999). By manually picking horizons along inlines and crosslines, a grid is produced (Fig. 3.6). Depending on the complexity of the structures, the interpretations were spaced every 20 lines to 2 lines. The manually mapped grid was subsequently used as a seed point for Petrel's autotracking function. Once selected, the autotracker identifies seismic reflections with similar amplitudes and phase and fills in the gaps left by the grid (Hart, 1999). Any

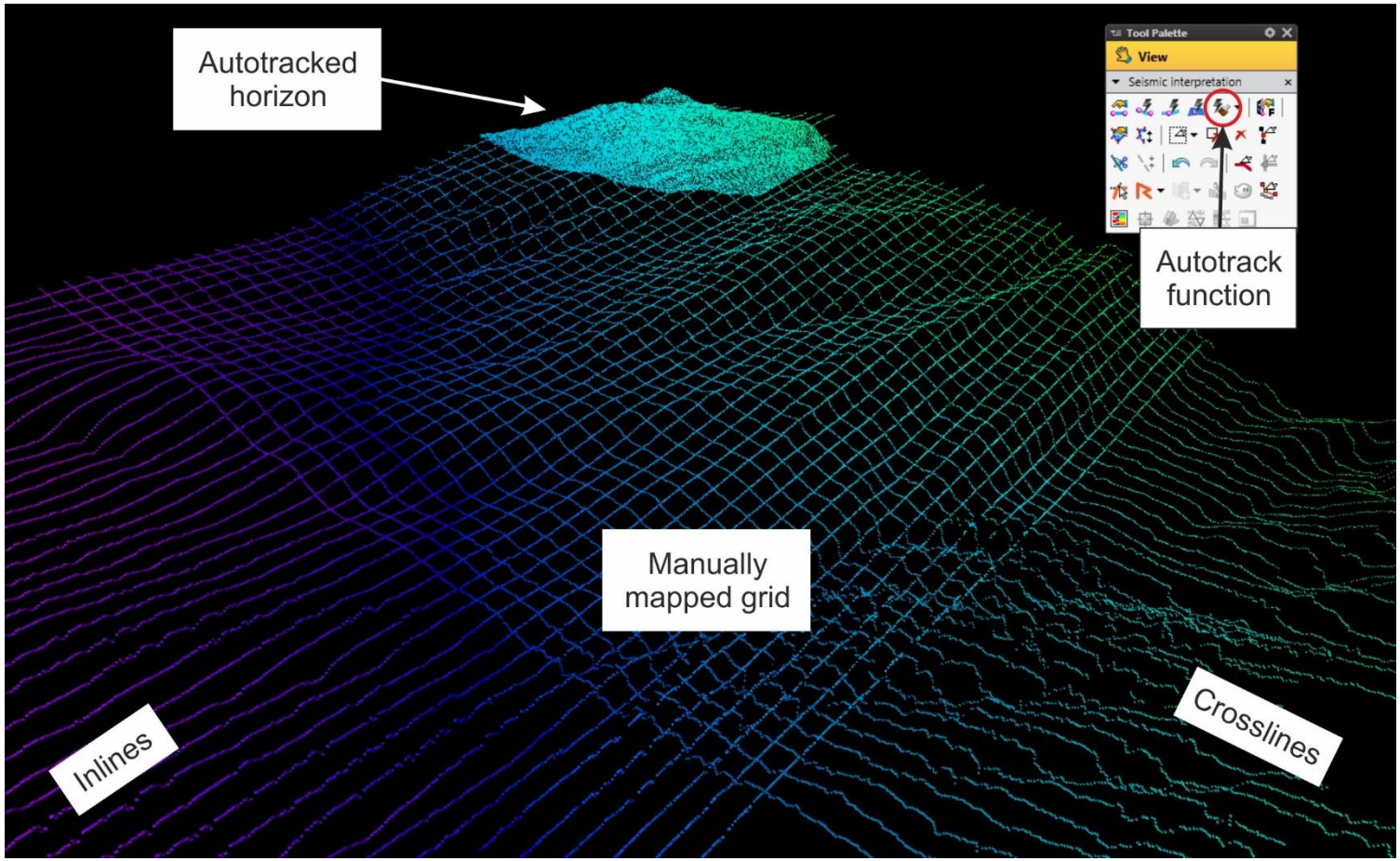

Fig. 3.6 3D window showing how a seismic horizon is interpreted and mapped. A grid is first mapped manually, followed by the application of the autotracking function in Petrel © 2015.

anomalous picks created by the program were manually removed to provide a smooth and accurate structural map. Figure 3.7 highlights the key structural maps interpreted in *Chapter 4*, and how they relate to the seismic lines. Examples of the structural maps are shown in Figure 3.8b.

In *Chapter 4*, the fault interpretation tool was chosen to produce slip tendency analyses (*see section 3.5*). To achieve the best results, faults require detailed interpretation using arbitrary lines (oblique to inlines and crosslines) perpendicular to the fault surface. Each fault was interpreted every line when possible, due to the complexity and curvature of the faults.

3.4.2. Seismic attribute analyses

Horizon or volume attributes are used to help visualise the geological features once interpretation has been completed. This is largely due to the subtlety of some features, which may be overlooked by an interpreted due to slight phase shifts or amplitude changes along a horizon. A wide array of seismic attributes are available to use on Petrel; this thesis focussed on using variance, isochron, and amplitude maps.

Variance (or coherence) (Fig. 3.8c): Variance maps are created from a seismic volume, meaning the model produced has not yet been interpreted, and is therefore presented without any interpretation bias. This method uses

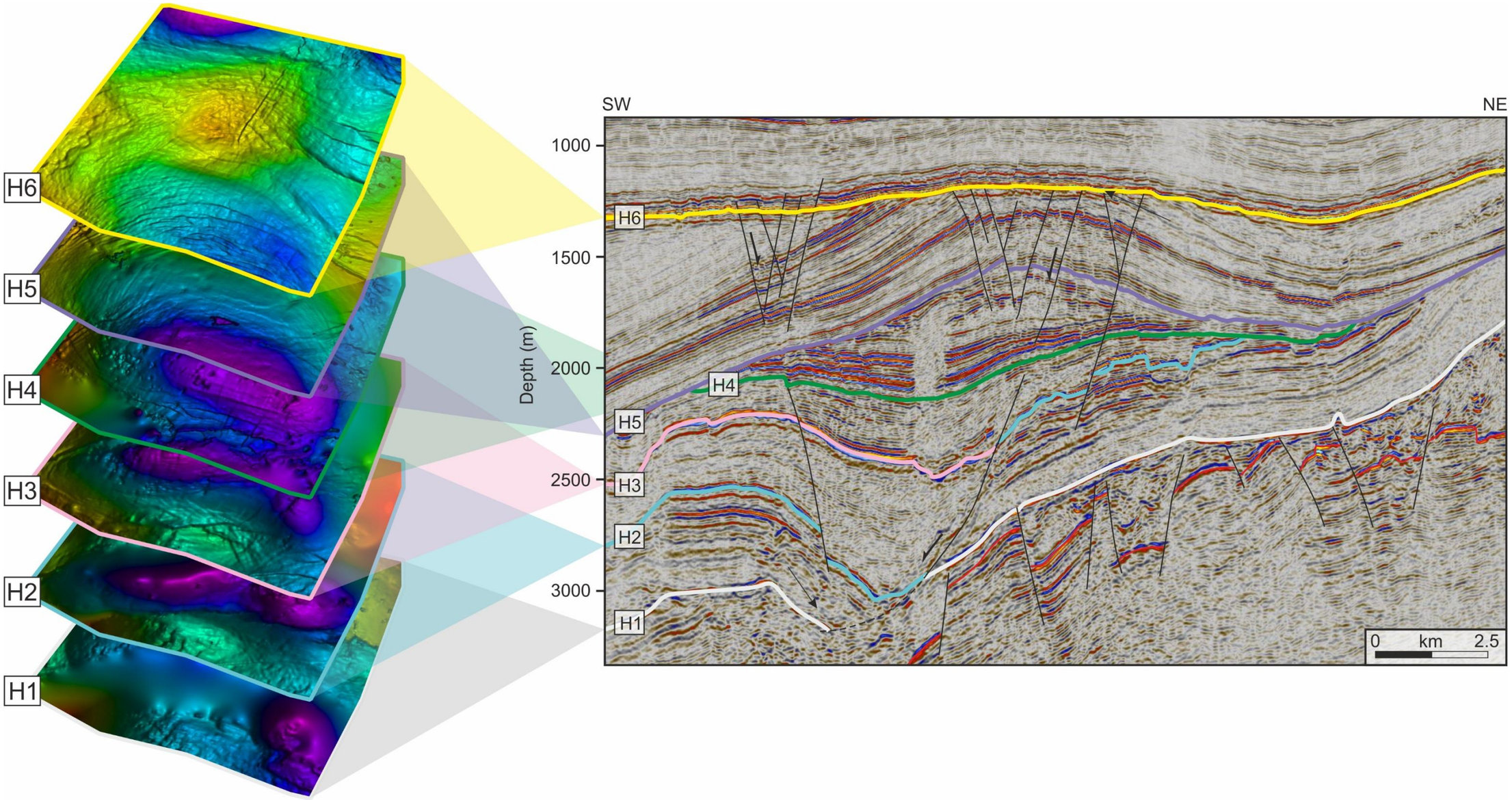

Fig. 3.7 Diagram showing how seismic data relates to the structural maps produced after interpretation. Key horizons in *Chapter 4* are shown in this figure.

algorithms to compare the similarity of adjacent waveforms, converting the seismic-amplitude volume of continuity into a volume of discontinuity (Brown, 2004). Therefore, it captures geological discontinuities along a horizon, such as a fault, channel, or MTD.

Isochron (Fig. 3.8d): Also known as thickness maps, they record the time difference between two selected horizons. The resulting map is then overlain on one of the selected horizons to provide information on the thickness and lateral extent of stratigraphic units. They are key to this thesis as they can reveal very subtle changes in thickness that would not be easily documented by using simple measurements.

Amplitude (Figs. 3.8e and 3.8f): Reflection amplitude is a widely used attribute that measures the largest displacement of a wavelet from the base to its crest, and is shown as a positive (maximum) or negative (minimum) amplitude. When extracted over one horizon, it is often known as an horizon slice (Brown, 2004). Alternatively, two reference horizons may be inputted, and an amplitude extraction can be created, identifying the absolute value summation of the acoustic impedance of a whole unit.

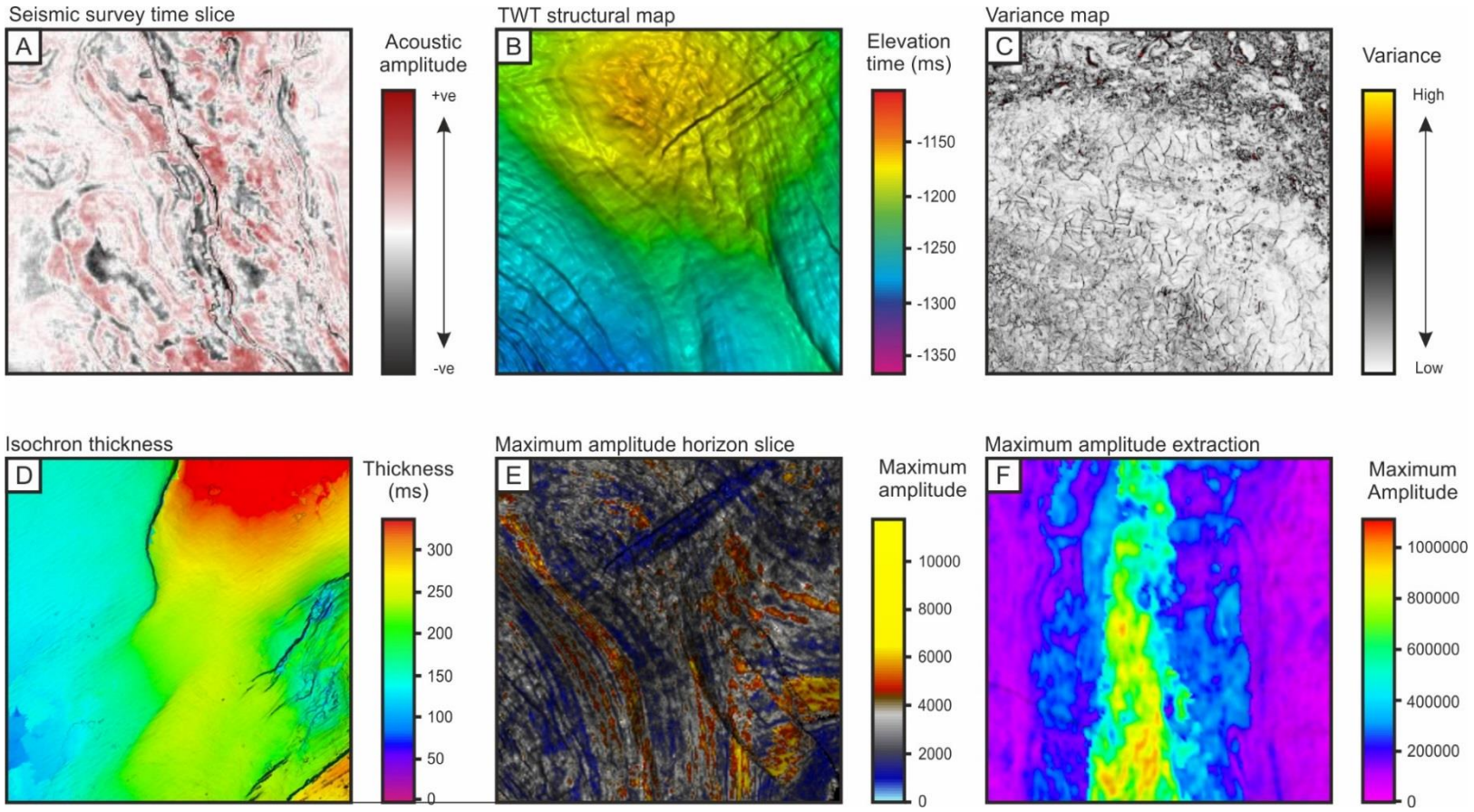

Fig. 3.8 Examples of different seismic attributes and structural maps used in this thesis: a) time slice through original seismic survey; b) interpreted TWT structural map; c) variance map (1/coherence); d) isochron thickness map between two interpreted horizons; e) maximum amplitude horizon slice along an interpreted horizon; f) maximum amplitude extraction between two interpreted horizons.

3.5. Slip tendency analysis

Slip tendency analyses were first presented by Morris et al. (1996). It enabled the rapid assessment of stress states and its effects on the potential for fault activity. Whether slip along a surface occurs is largely dependent on the frictional characteristics of rocks and the ratio of shear stress (τ) to normal stress (σ_n) acting on the fault. Sliding will happen when the resolved shear stress ≥ frictional resistance, which is proportional to the normal stress acting on a fault surface. In other words, on a cohesionless surface, sliding happens when:

$$\tau = \mu \cdot \sigma_{\text{n eff}} \geq F$$

Equation 3.6

and,

$$\mu = \tau / \sigma_{\text{n eff}}$$

Equation 3.7

where μ is the coefficient of static friction, F is the frictional resistance to sliding, and σ_{neff} is the effective normal stress (normal stress – pore pressure) (Byerlee, 1978, Jaeger et al., 2009). Slip tendency (T_s) is defined as the ratio of shear stress to normal stress, and is dependent on the orientation of the fault surface with respect to the given stress field (Morris et al., 1996, McFarland et al., 2012), such that:

$$T_s = \tau/\sigma_{\text{n eff}}$$

Equation 3.8

Comparing equation 3.8 and 3.9 clearly shows that the coefficient of static friction (μ) is the value of T_s that causes slip. The value that is reached at failure is commonly called fault "strength"; the lower the T_s, the lower the cohesion, and the weaker the fault.

For known values of principal stresses (σ_1, σ_2, σ_3), the shear stress, normal stress and shear direction can be found (Lisle, 2004). Jaeger (1969) related the shear and normal stresses for known principal stresses to the orientation of a failure plane:

$$\sigma_n = \sigma_1 l^2 + \sigma_2 m^2 + \sigma_3 n^2$$

Equation 3.9

and

$$\tau = [(\sigma_1 - \sigma_2)^2 l^2 m^2 + (\sigma_2 - \sigma_3)^2 m^2 n^2 + (\sigma_3 - \sigma_1)^2 l^2 n^2]^{1/2}$$

Equation 3.10

where *l*, *m*, and *n* are the direction cosines of the plane's normal with respect to the principal stress axes, σ_1, σ_2, and σ_3, respectively.

The amount of slip can be influenced by the magnitude of σ_2 relative to σ_1 and σ_3. This value, Φ, reflects the existence of an incomplete stress tensor, and

governs the shape of a 3D Mohr arbelo (Lisle, 2004, Alves, 2014). It includes the directions of principal stress axes and the ratio of stress differences:

$$\Phi = (\sigma_2 - \sigma_3)/(\sigma_1 - \sigma_3)$$

Equation 3.11

Dilation of faults is controlled by the resolved normal stress, which is a function of the lithostatic and tectonic stresses, and fluid pressure. Using Equation 3.11, the magnitude of normal stress can be calculated for all surfaces within a known stress field, which can then be normalized by comparison with the differential stress. This gives the dilation tendency (T_d) of a surface (Moeck, 2009):

$$T_d = (\sigma_1 - \sigma_n)/(\sigma_1 - \sigma_3)$$

Equation 3.12

3.6. Statistical analyses

3.6.1. Throw-depth (T-z) and throw-distance (T-x) plots

Throw-depth (*T-z*) and throw-distance (*T-x*) plots are interpretation techniques that document the growth histories (both vertical and lateral) of a fault. Both techniques involve the analysis of fault throw along a specific horizon. Throw is measured by the distance between the top of a horizon on the hanging-

wall, and the respective horizon on the footwall (Fig. 3.9). The depth is then taken at the top of the horizon on the hanging-wall. *T-z* plots are a collection of throw measurements taken at every resolvable horizon intersecting the fault on a single seismic line. *T-x* plots are throw measurements on a single horizon taken at regular intervals along the fault strike. Therefore, they document the throw gradients from both tips (where throw is 0 m) and the throw maximum.

Throw-depth plots help distinguish between different mechanical processes involved in vertical fault propagation histories. They can be analysed to determine whether a fault is a blind fault or a growth fault, and if the fault has been reactivated or not (Baudon and Cartwright, 2008, Jackson and Rotevatn, 2013). A reactivation surface is considered to have a stepped vertical throw profile. If there is a throw minima and a negative gradient between an erosional/unconformable surface, fault growth is considered to be a result of "dip linkage" (Mansfield and Cartwright, 1996). If, however, the throw has a stepped profile, but maintains a positive gradient, the fault is believed to have grown via "upward propagation" (Baudon and Cartwright, 2008).

Throw-distance plots are used to develop models for lateral fault growth. They show the geometric evolution of faults and the mechanical interaction between undeformed rock and the fault at its lateral tips (Jackson and Rotevatn, 2013, Cartwright et al., 1995). Idealistic faults have a central throw maximum, but this is often not the case. When there are multiple peaks of throw maximum, the

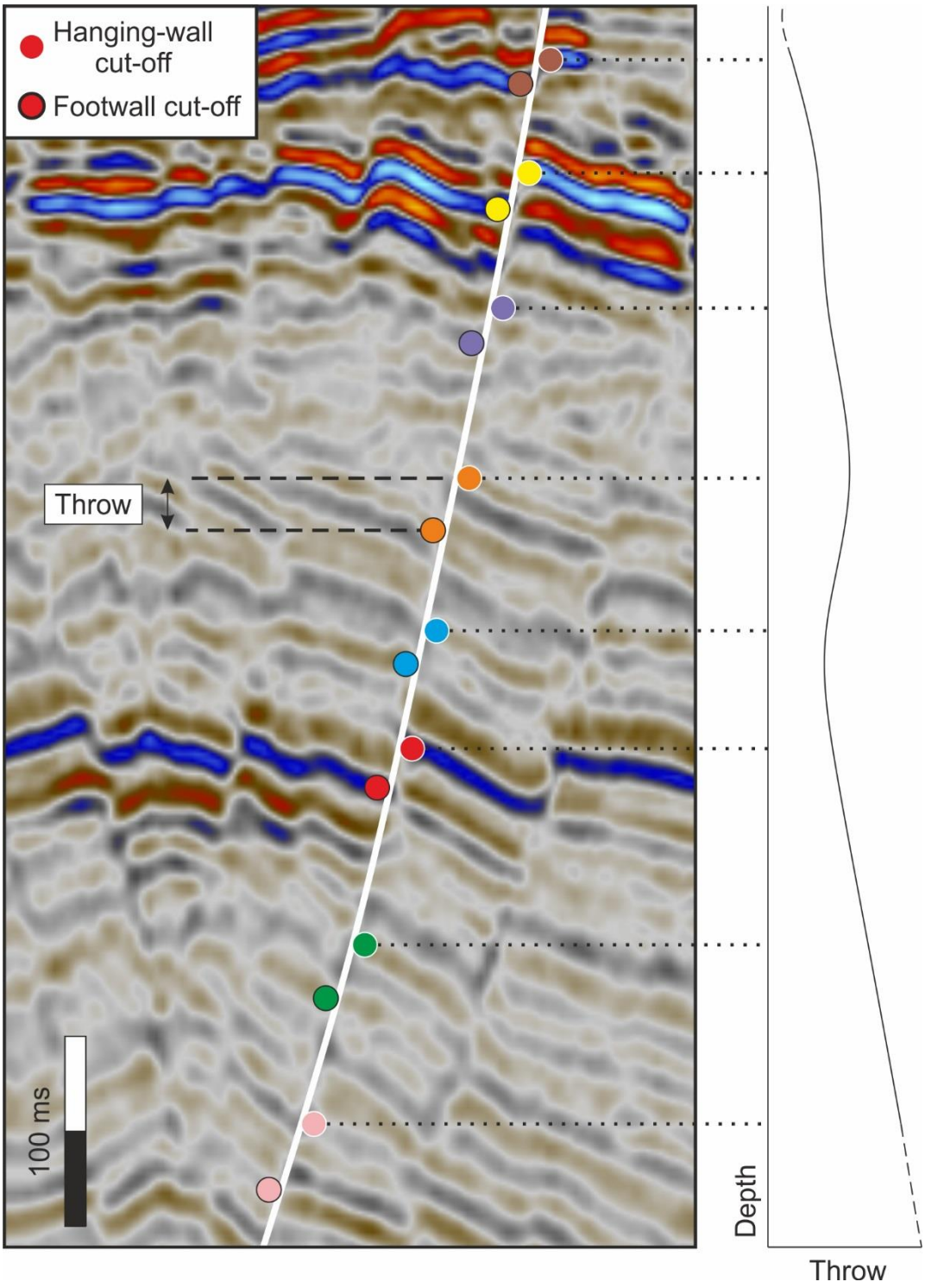

Fig. 3.9 Seismic horizon with an interpreted fault stick showing the basic concept behind the throw-depth method. Throw is calculated as the difference in depth between the same horizon on the hanging wall and footwall cut-offs either side of the fault. A schematic throw-depth plot is illustrated for the given fault.

fault can be interpreted as having grown by segment linkage (hard linkage of numerous separate fault segments) (Cartwright et al., 1995).

3.6.2. Thickness-relief method

A thickness-relief technique based on Perrier and Quiblier (1974) and applied in Alves and Cartwright (2010) and Alves (2012), was used in this thesis to quantify the degree and relative timing of differential compaction over a submarine channel complex. The method uses vertical simple shear to flatten a horizon, such that the area and the vertical thickness of a horizon is preserved (Gonzalez-Mieres and Suppe, 2006).

Thickness-relief measurements follow the principle that, in a closed cross-sectional system, the area that has been displaced below a given horizon is equal to the area of relief above (Gonzalez-Mieres and Suppe, 2006). This structural analysis is not as easily applied to differential compaction above a channel, as the cross sectional displacement below a given horizon does not necessarily equal the relief above it. However, the method can be used to distinguish the relative timing of differential compaction by identifying thickness changes along individual horizons (Figs. 3.10 and 3.11). This change in thickness (T) can therefore be calculated by finding the difference in depth between a fixed horizon (H_f) and all the deformed horizons above ($H_{1,2,3\ etc...}$) and below ($H_{-1,-2,-3\ etc...}$), for example (Fig. 3.10):

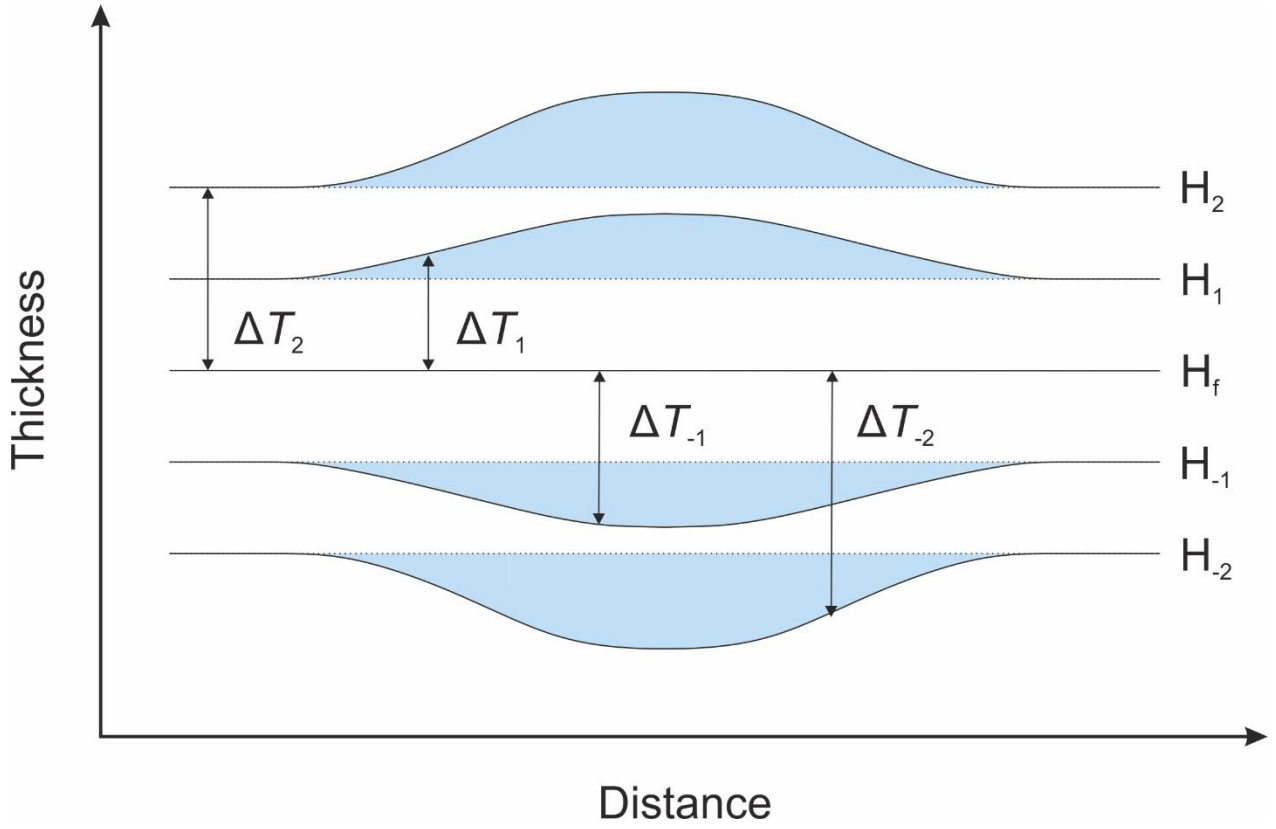

Fig. 3.10 Example of the thickness-relief method derived from *Gonzales-Mieres and Suppe (2006)*. This cross-section measures the thickness differences above and below a flattened horizon. The quality of this thickness-relief method depends on finding an appropriate horizon to flatten when assessing thickness changes and the initiation of structural features. ΔT is the change in thickness.

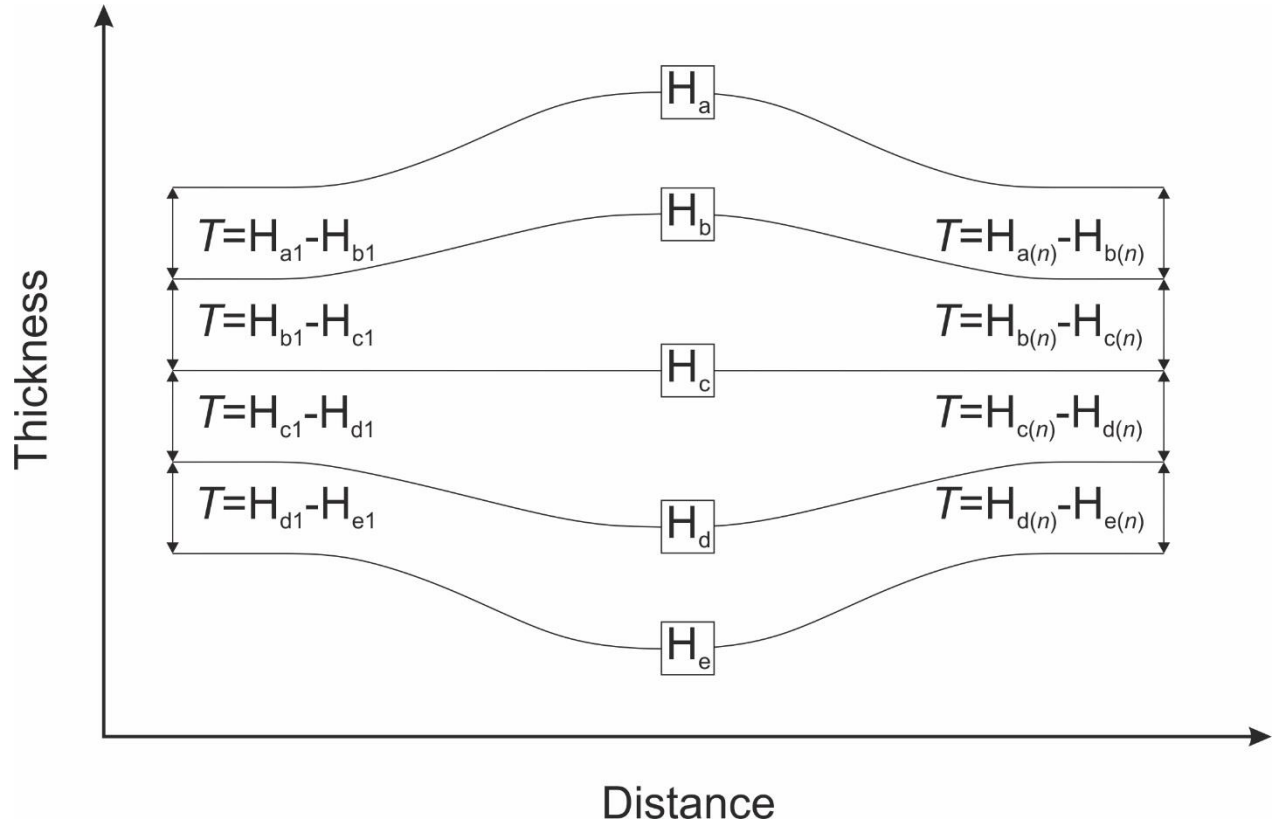

Fig. 3.11 Throw-Envelope Profile (TEP) method adapted from *Alves (2012)*. This method illustrates the change of thickness between two adjacent reflections. It has been used in Chapter 5 to compare the change of thickness between two seismic reflections at a specific point with the mean thickness along the whole reflection. H_x—measured horizon, assigned a letter from a-e. Subscript numbers refer to the point along the horizon where a measurement has been taken. T—thickness between two successive horizons.

$$T_1 = H_1 - H_f$$

Equation 3.13

When assigning different reflections for H_f, it is possible to find the relative age of compaction by whether or not there is topographic expression of the anticlinal structure. Pitfalls in this method can occur with inaccurate picking. Disrupted and transparent reflections (common among MTC's) can lead to anomalous thickness variations when compared with a flat, continuous reflection. It is also important to select an appropriate reflection to flatten on.

Thickness variations will occur when there is either topographic expression of a structure, represented by increased accommodation space and thicker reflections on the flanks, or when lithologies compact in different amounts. The general formula for identifying thickness changes (T) is subtracting the depth of a point along a horizon (H_{a1}) by the same point along the horizon below (H_{b1}), such that (Fig. 3.11):

$$T = H_{a1} - H_{b1}$$

Equation 3.14

In order to reduce the error of poorly picked seismic horizons, thickness measurements were compared with the mean thickness along the same horizon, such that:

$$D = T - \bar{x}_t$$

Equation 3.15

where D is the difference value in TWT, T is the measured thickness and $\bar{x}_t$ is the mean thickness along the horizon. The mean thickness was calculated using up to 791 measurements of each horizon on a cross section of the channel complex. The measurements were taken 1400 m either side of the channel complex axis. By subtracting the mean thickness from the measured thickness on a single horizon, a direct comparison is made between units of different sizes (*see Chapter 5*).

CHAPTER FOUR

Reservoir leakage along concentric faults in the Southern North Sea: Implications for the deployment of CCS and EOR techniques

An abridged version of this chapter has been published as:

Ward, N.I., Alves, T.M. and Blenkinsop, T.G., 2016. Reservoir leakage along concentric faults in the Southern North Sea: Implications for the deployment of CCS and EOR techniques. *Tectonophysics*, *690*, pp.97-116.

Co-author contributions to the paper:

Tiago Alves – checked for grammatical errors, ensured the scientific content was accurate and appropriately presented.

Thomas Blenkinsop – checked for any errors in the theme of structural geology, provided feedback on paper.

4. Concentric faults and fluid flow

4.1. Abstract

High-quality 3D seismic and borehole data in the Broad Fourteens Basin, Southern North Sea, is used to investigate newly recognised concentric faults formed in salt-withdrawal basins flanking reactivated salt structures. Throw-depth and throw-distance plots were used to understand the growth histories of individual faults. As a result, three families of concentric faults are identified: a) intra-seal faults within a salt-withdrawal basin, b) faults connecting the seal and the reservoir on the crest of an inverted anticline (anticline α), c) raft-bounding faults propagating into reservoir units. They have moved obliquely and show normal separation, even though they formed during a period of regional compression. Faults in the salt-withdrawal basin and on anticline α are highly segmented, increasing the chances of compartmentalisation or localised fluid flow through fault linkages. Slip tendency analysis was carried out on the distinct fault families to compare the likelihood of slip along a fault at different pore fluid pressures and within different lithologies. Our results show that sections of the faults are optimally oriented with regards to maximum horizontal stresses (σ_{Hmax}), increasing the slip tendency. The identified faults cut through a variety of lithologies, allowing different values of pore fluid pressures to build up before faults reactivate. Within the Vlieland Sandstones, pore fluid pressures of 30 MPa are not sufficient to reactivate pre-existing faults, whereas in the deeper

Posidonia Shales faults might reactivate at pore fluid pressures of 25 MPa. Fluid flow features preferentially occur near fault segments close to failure. Heterogeneity in slip tendency along concentric faults, and high degrees of fault segmentation, present serious hazards when injecting CO_2 into the subsurface. This study stresses the importance of high-quality 3D seismic data and the need to evaluate individual fault systems when investigating potential reservoirs for carbon capture and storage and enhanced oil recovery.

4.2. Introduction

Concentric faults are curved structural features formed in response to the evacuation of subsurface sediment and ensuing basin subsidence (Maione and Pickford, 2001, Stewart, 1999, Stewart, 2006, Underhill, 2009, Bertoni and Cartwright, 2005, Price and Cosgrove, 1990, Ge and Jackson, 1998, Alsop, 1996). Concentric faults have been documented above collapsed salt diapirs (Bertoni and Cartwright, 2005, Stewart, 2006, Cartwright et al., 2001), but few studies have discussed them in salt-withdrawal basins (Maione and Pickford, 2001, Underhill, 2004). In this chapter, high quality 3D seismic data has unveiled some of these concentric faults within, and proximal to, a salt-withdrawal basin generated in the Broad Fourteens Basin, Southern North Sea (Fig. 4.1). They have a net normal separation, have reactivated obliquely and formed during a period of

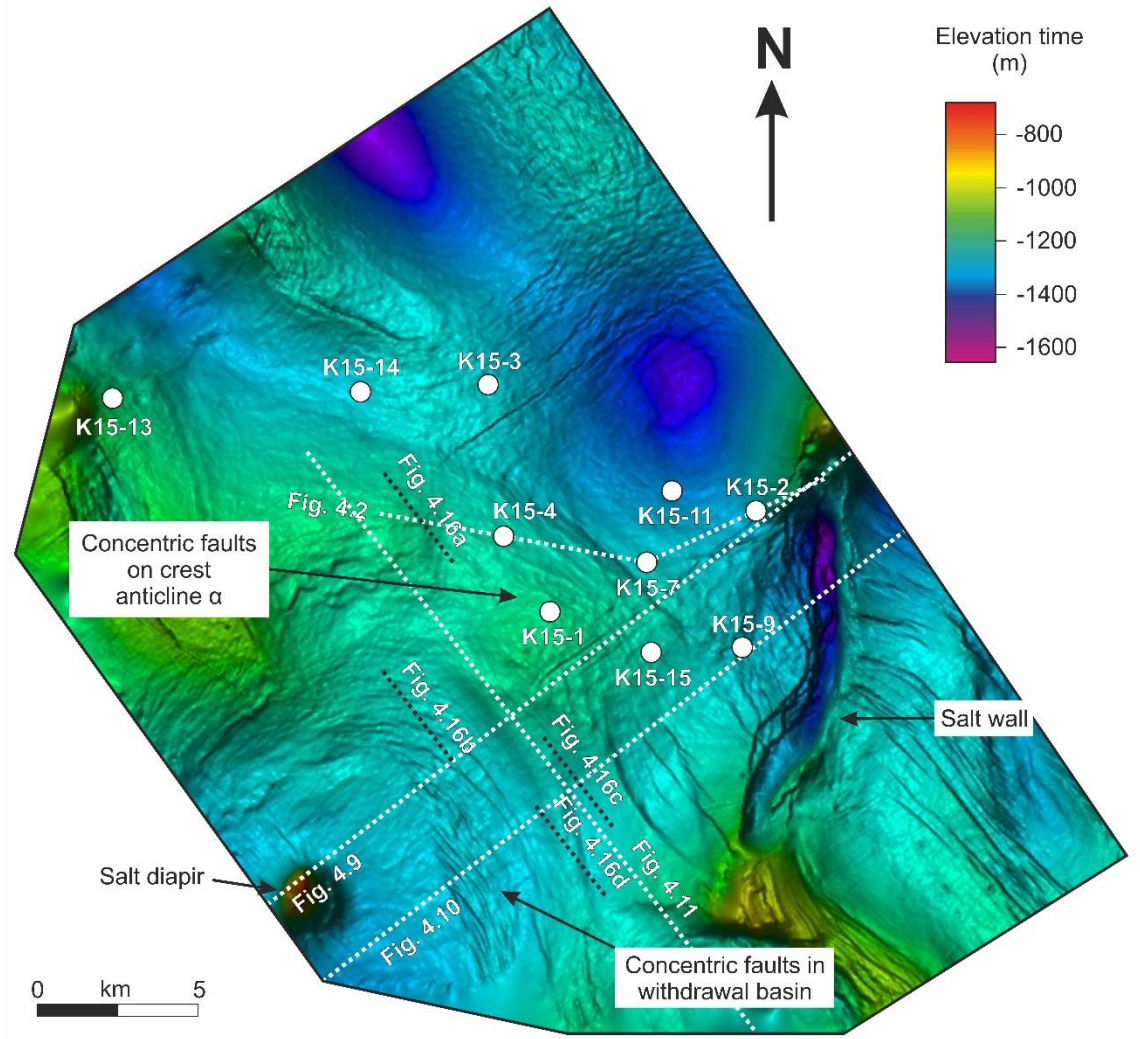

Fig. 4.1 Interpreted Horizon H_6 (Base Tertiary) displaying key features and seismic lines studied in this chapter, as well as the wells interpreted in the study area.

compression, demonstrating a compound history (Nalpas et al., 1995, Maione and Pickford, 2001, Oudmayer and De Jager, 1993). Their occurrence may present an important caveat for the implementation of carbon capture and storage (CCS) and enhanced oil recovery (EOR) techniques in strata flanking salt structures in the North Sea, and in equivalent salt-rich basins (Cawley et al., 2015).

In the Southern North Sea, the dominant control on concentric fault distribution is the movement of Zechstein salt, which is present throughout most of the offshore region of the Netherlands (Alves and Elliott, 2014, Verweij and Simmelink, 2002). The majority of hydrocarbon discoveries in the Dutch sector of the North Sea are within conventional anticlinal traps and fault-dip closures (Herber and De Jager, 2010, Van Hulten, 2010b). However, the gradual decline in production and increasing costs of maintaining current infrastructure has led to a greater emphasis on understanding oil and gas plays in more complex structures, with the ultimate aim of deploying CCS and EOR techniques in otherwise mature fields (Lokhorst and Wildenborg, 2005, Van Hulten, 2010a), and in Jurassic source intervals (Weijermars, 2013). The implementation of these techniques, however, may be impeded by faults and other structural complexities, which can act both as conduits and barriers to fluid flow (Bentham et al., 2013, Cartwright et al., 2007). For example, active faults that cross-cut seal units may allow fluid to escape to the surface. In parallel, tectonically 'locked' faults may be reactivated if fluid pressure reduces the effective stress so that faults become critically stressed (Wiprut and Zoback, 2000, Wiprut and Zoback,

2002). Conversely, faults that are barriers to fluid flow could potentially compartmentalise reservoir units, resulting in an increase in costs as more wells are needed to retrieve hydrocarbons (Hardman and Booth, 1991).

In this chapter the evolution of concentric faults is investigated, as well as the effects these faults have on seal integrity in a hydrocarbon producing region where CCS and EOR techniques are being implemented. Feasibility studies into CCS are being deployed in the Broad Fourteens Basin as of 2015, including in Block K15 where the study area is located (Bentham et al., 2013, Neele et al., 2012) (Fig. 2.1). Fault growth and propagation histories are assessed using throw-depth (*t*-*z*) and throw-distance (*t*-*x*) plots. Displacement data provide information on nucleation, segmentation, linkage and reactivation along a fault (Omosanya and Alves, 2014, Baudon and Cartwright, 2008). The likelihood for faults to slip and act as fluid-flow pathways is quantitatively analysed in this chapter by calculating slip tendency for interpreted fault families (Morris et al., 1996). The modelling of increasing pore fluid pressures along concentric faults demonstrates the effects fluid injection (CCS) might have on the seal integrity. In summary, the following research questions are addressed in this chapter:

a) What is the propagation history of the concentric faults and how did they form?

b) How does the timing of hydrocarbon maturation and migration relate to concentric faults?

c) What are the implications of finding concentric faults for the implementation of CCS and EOR techniques?

4.3. Chapter specific data and methods

The three-dimensional seismic volume used in this chapter was acquired in the Broad Fourteens Basin, Southern North Sea. For a full description on the acquisition and processing parameters of the survey, please sea *section 3.1.1.1.* Thirteen well logs (in addition to the two described in *section 3.1.1.1.*) were tied to the seismic data to correlate the horizons and constrain the stratigraphy across the study area (Figs. 3.5, 4.1, and 4.2). Correlation panels between different wells show thickness variations and the absence of strata on the footwall of the larger faults (Fig. 3.5).

Schlumberger's Petrel® was used to interpret six key seismic horizons (Figs. 4.3 – 4.8). Seismic horizons were mapped across the study area so that root-mean-square (RMS) amplitude and variance maps could be computed to provide clear images of faults and gas pipes (Brown, 2004, Alves and Elliott, 2014). Mapped horizons highlight the changes in fault architecture and fluid pipe morphology through the Mesozoic stratigraphic sequences (Figs. 4.3 – 4.8). Once identified, fault surfaces were mapped manually every five composite lines (~125 m), perpendicular to strike. These data were exported to Midland Valley Move™

so that slip tendency and fluid flow analyses could be undertaken (see *section 3.2.* for a full description of these analyses).

Present-day differential stresses found in the Broad Fourteens Basin were estimated for use in the slip tendency model. Principal stress orientations were based on measurements proximal to the Broad Fourteens Basin using the World Stress Map (Heidbach et al., 2008). Stress magnitudes were calculated using the style of deformation in the basin and the proposed depth of injection for CCS. At present the Broad Fourteens is experiencing oblique-dextral compression derived from tectonic activity in the Alps, which accommodate convergence between the African and Eurasian Plates (Heidbach et al., 2008, Verweij and Simmelink, 2002, Frikken, 1999). As a result of this setting, $\sigma_{Hmax} = \sigma_1$, $\sigma_V = \sigma_2$, and $\sigma_{hmin} = \sigma_3$ (Heidbach et al., 2008). Using an average clastic rock density of 2.3 g cm^{-3} and a hydrostatic pressure gradient increase of ~10 MPa km^{-1}, the vertical principal stress increases at a rate of 23 MPa km^{-1} (Zoback, 2010).

An average depth of 1,500 m was estimated for the interpreted fault families based on well data, with the resulting vertical principal stress approaching 35 MPa. According to Andersonian Fault theory (Anderson, 1951), compressive fault regimes (strike-slip or reverse faults) have similar values of σ_3 and σ_v; i.e. the ratio of σ_3/σ_v is close to 1. Grollimund et al. (2001) postulate a σ_3/σ_v

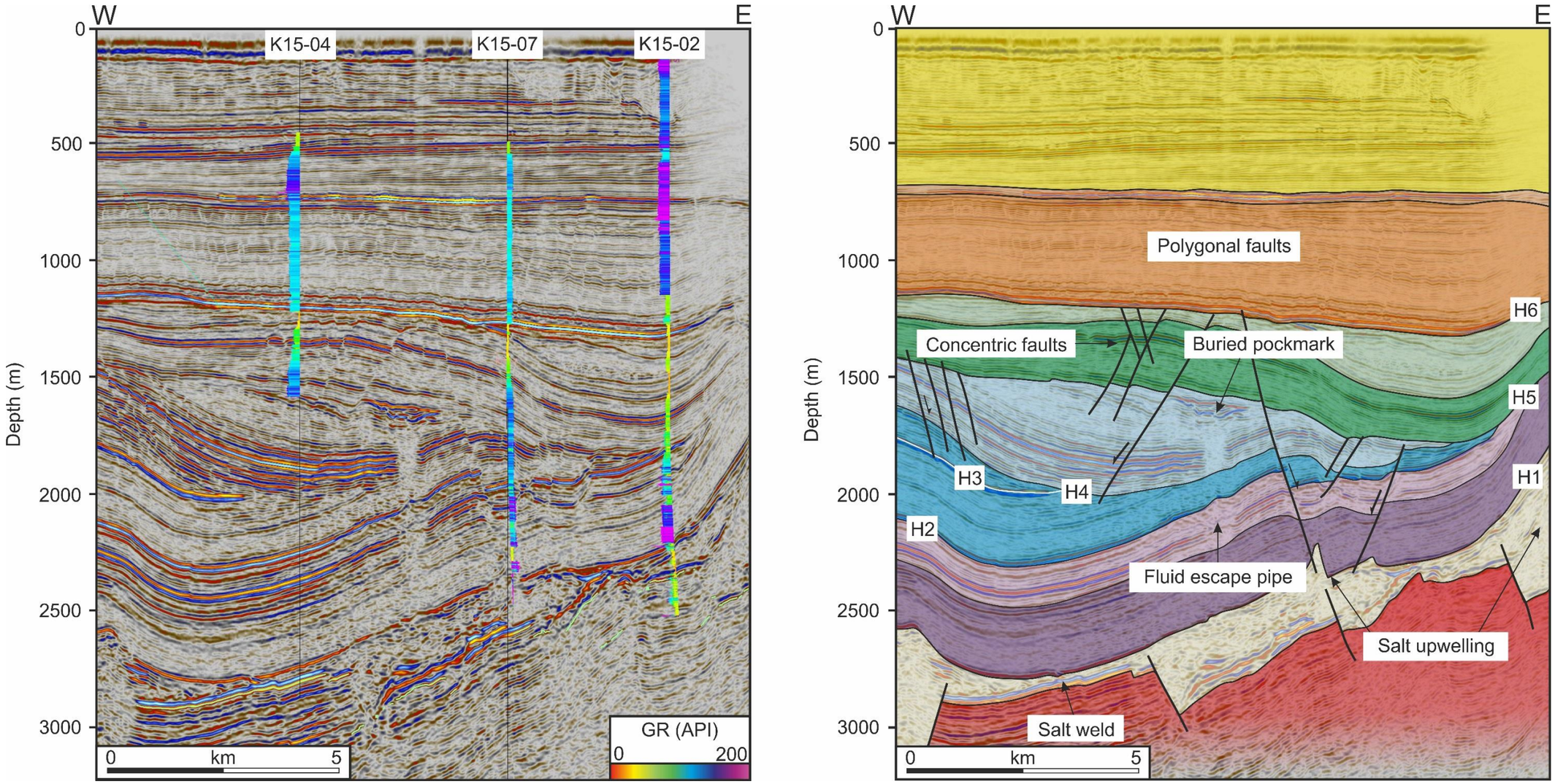

Fig. 4.2 Wells K15-04, K15-07 and K15-02 are tied to the seismic data to help with identify different lithologies and seismic-stratigraphic units. Both interpreted and un-interpreted seismic sections are shown. The section used is highlighted in Figure 4.1. Colours in Figure 3.5 correspond to those used in this figure for distinct stratigraphic units. The wireline data shown comprise gamma-ray logs (GR) measured in American Petroleum Institute (API) units.

ratio between 0.9 and 1 for the southern Norwegian North Sea, commenting on similar stress conditions throughout NW Europe. As faults are currently undergoing oblique-reverse movements in the study area, the ratio of 0.9 was used in the stress analyses. Therefore: $\sigma_{hmin} = 0.9\ \sigma_v \sim 31.5$ MPa. Sensitivity tests show that slight variations of σ_{hmin} (± 0.1) does not dramatically change the results of the study. The stress difference ratio (Φ) can be used to calculate the maximum horizontal stress (Morris et al., 1996, Alves and Elliott, 2014):

$$\Phi = (\sigma_2 - \sigma_3) / (\sigma_1 - \sigma_3)$$

Equation 4.1

An average stress difference ratio value of 0.25 was calculated for present day conditions, making $\sigma_{Hmax} = 45.5$ MPa (Newnes, 2014, Hillis and Nelson, 2005, van Gent et al., 2009). The stress difference ratio value varies with a range of ± 0.13, although an average value for the wide data range seemed appropriate, even though σ_{Hmax} would change by a maximum of ± 15 MPa (Hillis and Nelson, 2005, van Gent et al., 2009, Newnes, 2014).

The effective normal stress used for slip tendency analyses takes into account pore fluid pressure (P_f). As the fluid pressure increases, the effective stress decreases, making a fault more likely to slip (Handin et al., 1963). At the depth in which concentric faults are located, pore fluids appear to hydrostatic,

i.e., they have no overpressure (Verweij and Simmelink, 2002). Injecting CO_2 into reservoirs at this depth will therefore increase the pore fluid pressure.

Throw-depth (*t-z*) and throw-distance (*t-x*) analyses were performed to understand fault propagation histories (Baudon and Cartwright, 2008, Omosanya and Alves, 2014, Mansfield and Cartwright, 1996, Jackson and Rotevatn, 2013). Throw values were measured along the same composite lines used to map the faults. Using *t-z* plots, the age and depth of fault reactivation can be estimated, as well as the horizon reactivation took place on. The mode of vertical propagation of fault could be distinguished using *t-z* plots (Baudon and Cartwright, 2008). *T-x* plots show the history of lateral propagation and give evidence of any fault segment linkage (Cartwright et al., 1995).

4.4. Seismic stratigraphy

The main seismic units interpreted in this study are bounded by regional unconformities. Each unit consists of a series of mapped horizons (Figs. 4.1, and 4.3 – 4.8). In this section, nineteen (19) wells were tied to the interpreted seismic volume. Exploration wells K15-02, K15-04, and K15-07 were used to describe the lithologies crossed by the wells and illustrate stratal thickness variations across the interpreted seismic volume (Fig. 3.5).

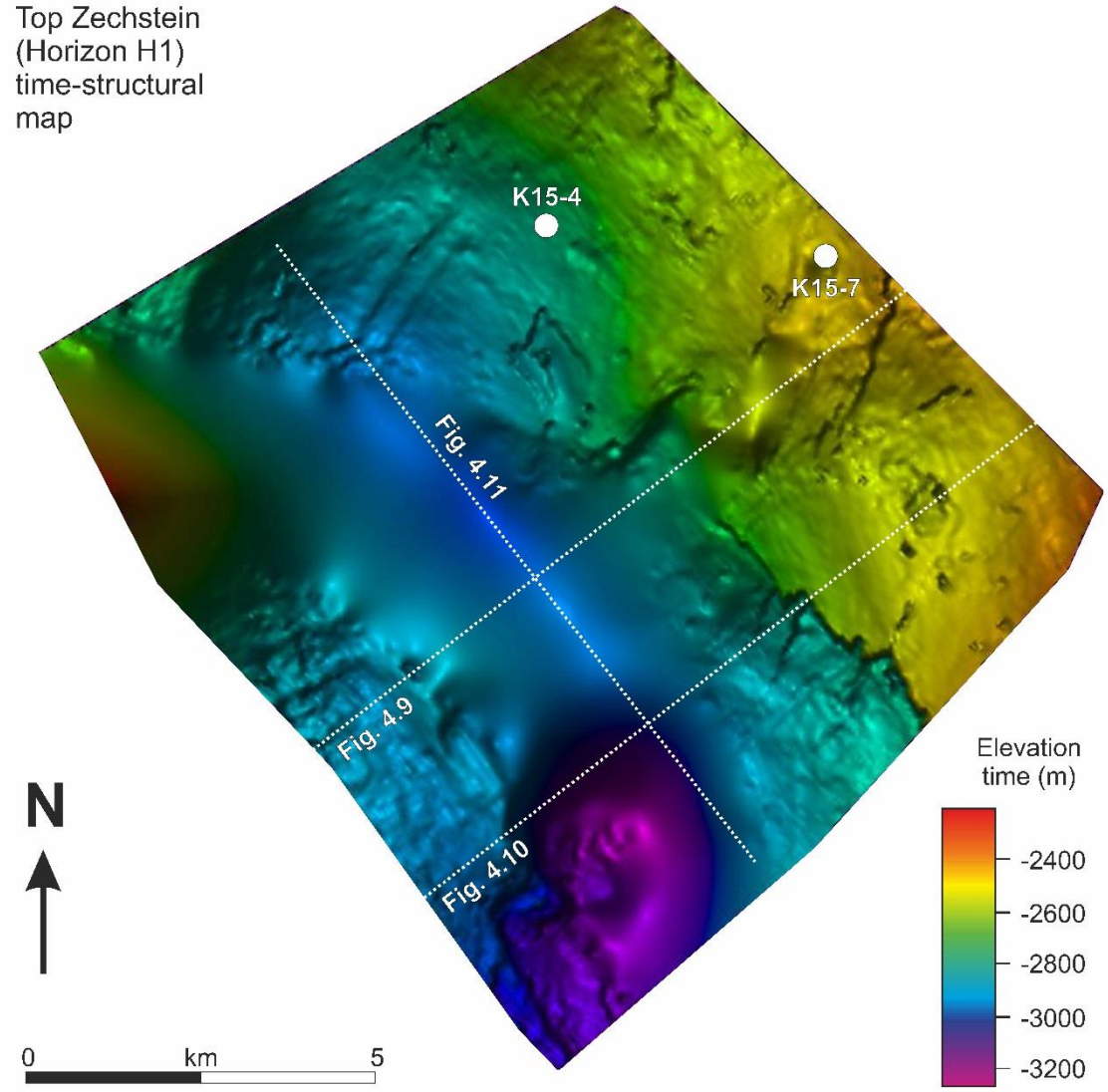

Fig. 4.3 Structural map of the top Zechstein horizon (H_1). Wells tied to seismic data in Figure 3.5 are shown. Seismic profiles in Figures 4.9 – 4.11 are also highlighted.

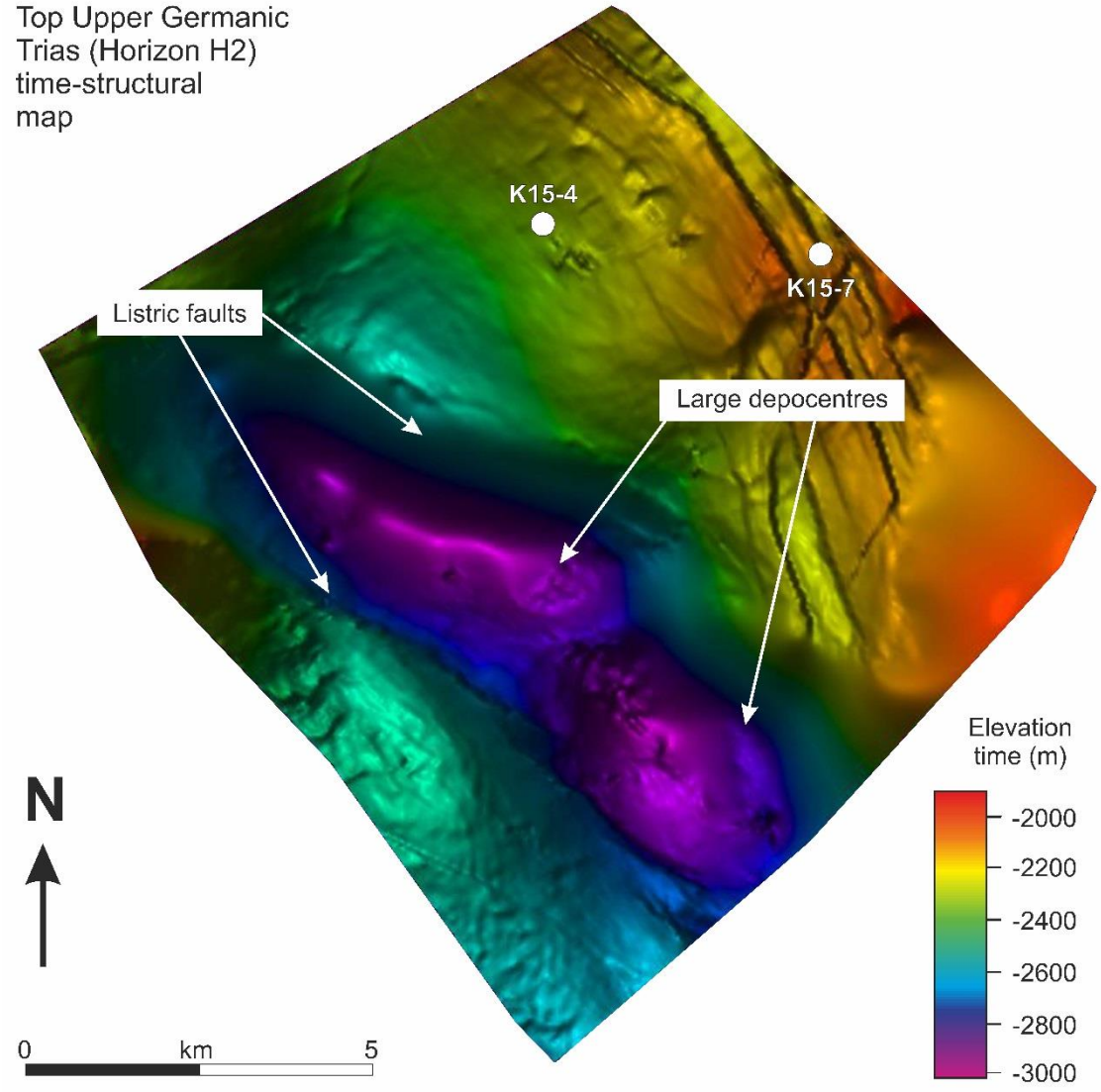

Fig. 4.4 Structural map of the top Upper Germanic Trias horizon (H_2). Listric faults are shown to bound a developing minibasin. This minibasin is displayed as two large depocentres in purple.

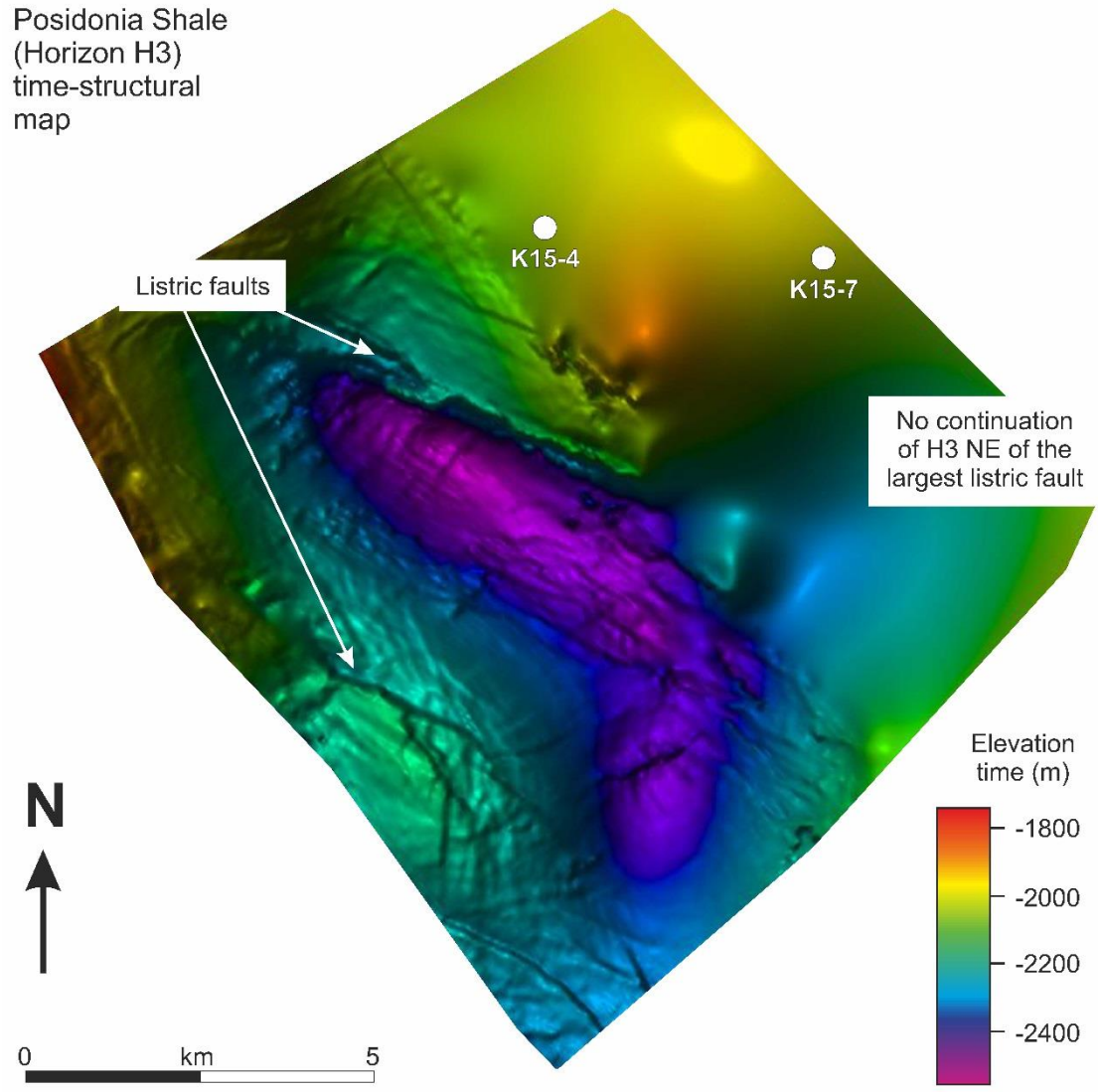

Fig. 4.5 Structural map of the top Posidonia Shale horizon (H_3). Listric faults are still observed at this stratigraphic level. Horizon H_5 does not continue past the listric fault in the NE portion of the study area, as it was eroded due to footwall uplift.

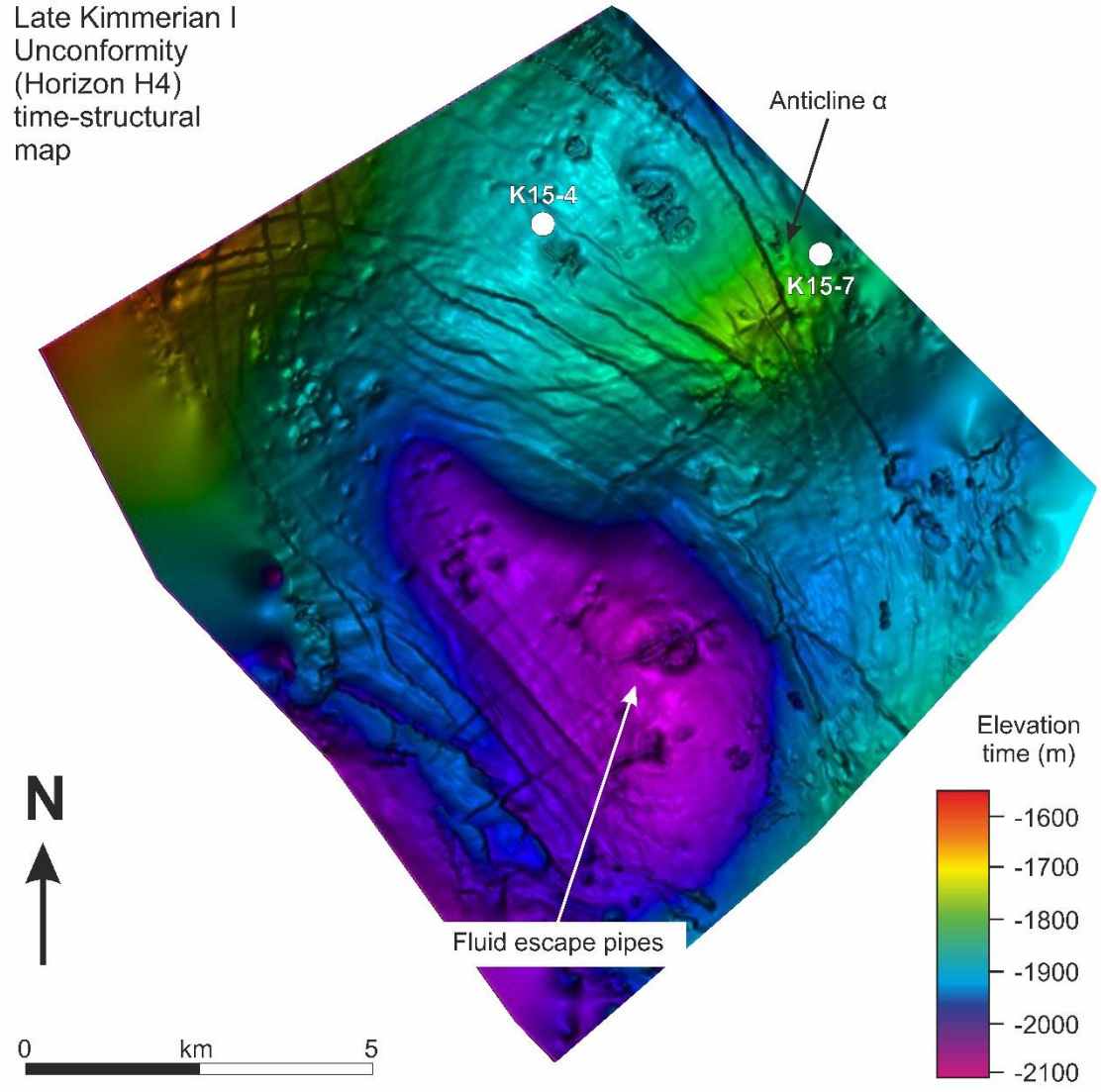

Fig. 4.6 Structural map of the Late Kimmerian I Unconformity (Horizon H_4). The crest of anticline α is now obvious at this level, and pockmarks cover Horizon H_4.

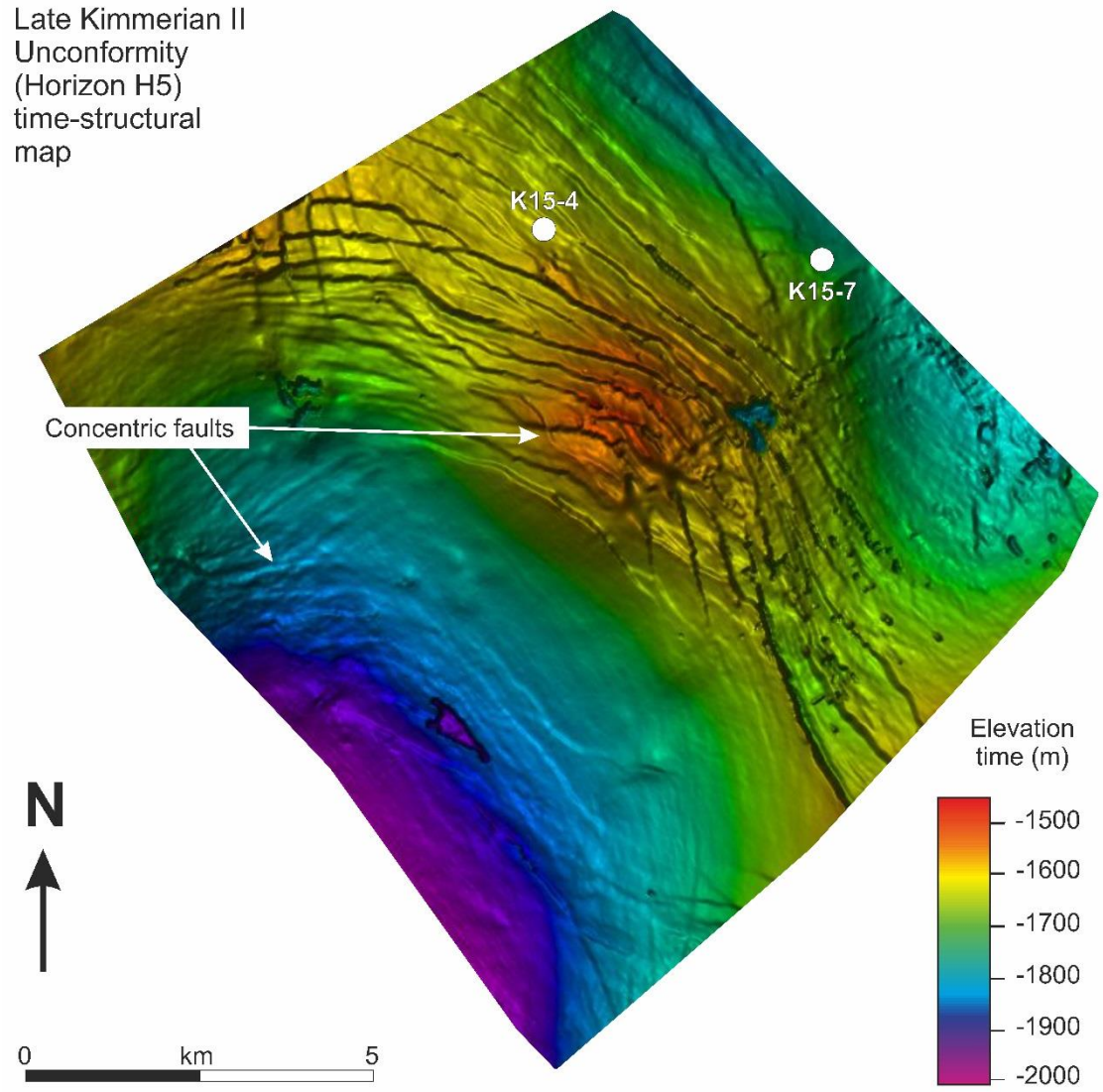

Fig. 4.7 Structural map of the Late Kimmerian II Unconformity (Horizon H_5). Crossing this horizon are concentric faults located in the salt withdrawal basin and on the crest of anticline α.

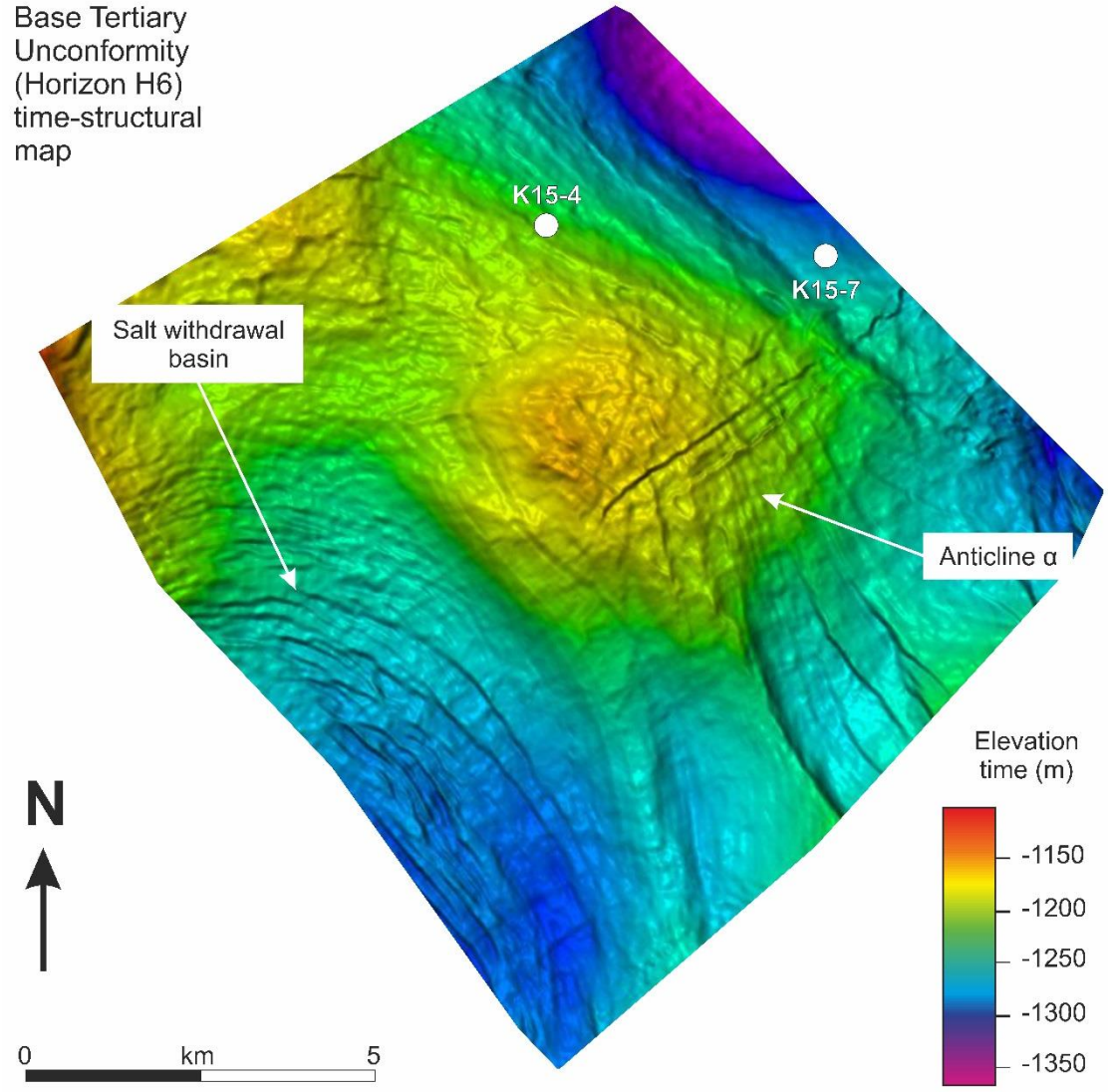

Fig. 4.8 Structural map of the Base Tertiary Unconformity (Horizon H_6). The concentric faults within the salt withdrawal basin are prominent, whereas only the largest faults near anticline α show any offset.

Well K15-02 was drilled close to a salt wall, on the footwall of a listric, south-dipping fault (Figs. 4.1 and 4.2). Well K15-07 was drilled on the northern flank of anticline α. This well crossed a relatively thin Upper Jurassic interval and an intrusion of salt at a depth of 2205 m. Well K15-04 reached its maximum depth at the base of the Rijnland Group, but a deviation well K15-04-S2 continued through to the Permian Rotliegendes Group. It was drilled SW of a large listric fault, recording the thickest succession of Schieland Group (~640 m) (Figs. 4.1 and 4.2). No wells were drilled in either the crest anticline α or the SW salt-withdrawal basin, so seismic horizons in this zone were tied to the wells closer to this region.

4.4.1. Rotliegend Group Sandstones (Autunian to Tatarian)

The Rotliegend Group sandstones are the deepest resolvable unit on 3D seismic data (Fig. 4.9). A bright reflection along the upper boundary separates the Upper Rotliegend from the Zechstein Group. Similar gamma-ray curves in wells K15-07 and K15-02 reflect an abundance of sand in both locations. Maxima in gamma-ray values on these logs indicate localised accumulations of gas (Fig. 3.5). The drilled Rotliegend sandstones consist largely of terrestrial course grained deposits (e.g. Slochteren Formation) and finer grained desert lake deposits (e.g. Silverpit Formation) (Verweij and Simmelink, 2002).

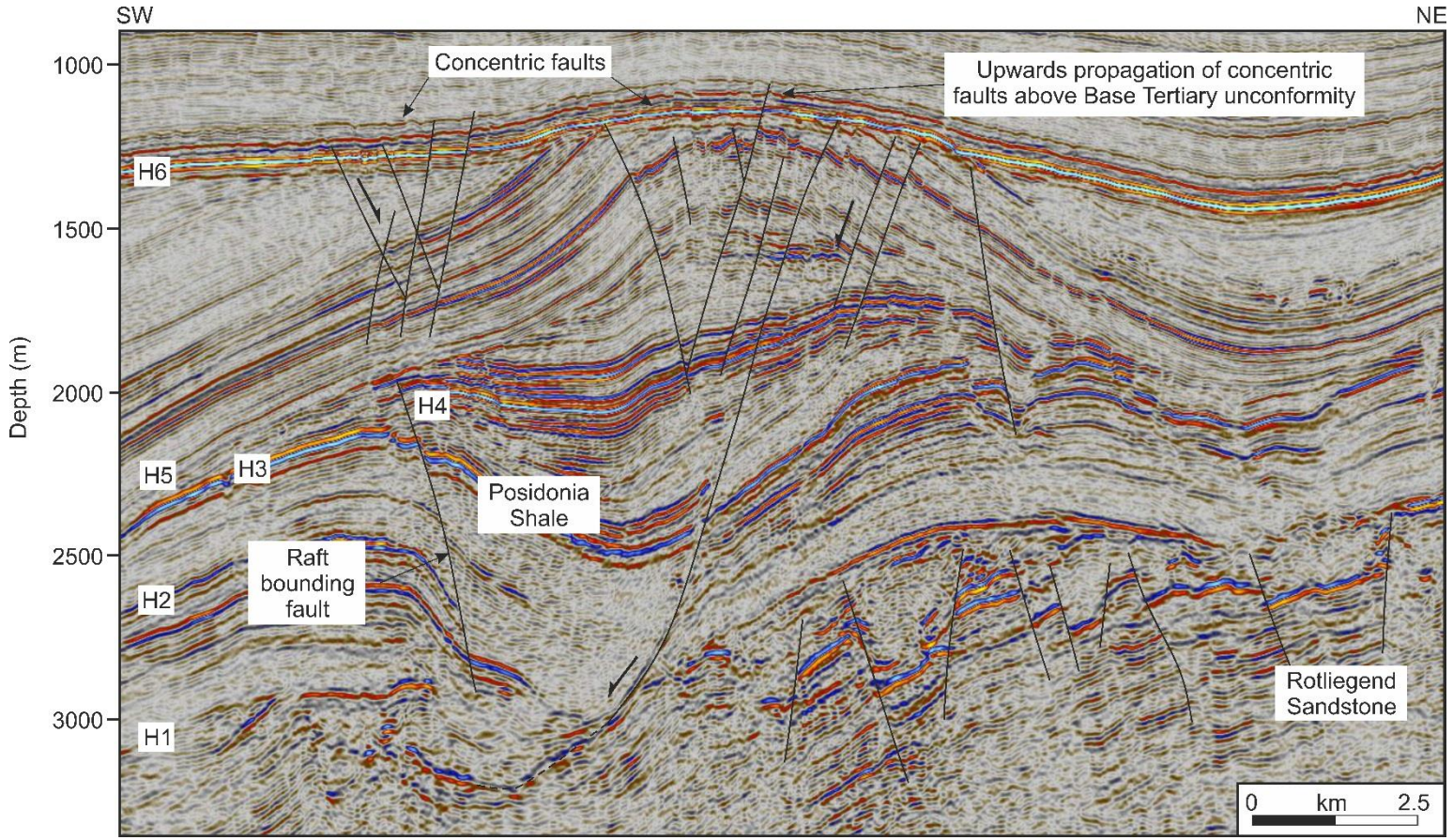

Fig. 4.9 Seismic profile highlighting the styles of faulting in the study area, Broad Fourteens Basin. In this profile, the concentric faults cutting through anticline α propagate above the Base Tertiary Unconformity (Horizon H_6). The Rotliegend Sandstones are deformed by multiple faults showing large offsets. Raft-bounding listric faults delimit the Posidonia Shale – the unit only occurs in the SW and within the minibasin.

Parallel reflections are truncated by large E-W trending Variscan faults (Fig. 4.9). These faults can reach displacement values of ~300 m. The base of the unit is hard to identify because the overlying salt dims the internal reflections of Rotliegend strata. There is little variation in thickness across the basin, irrespective of large fault displacements (Figs. 4.9 – 4.11).

4.4.2. Zechstein Group (Late Permian)

A high-amplitude seismic reflection separates the Zechstein from the Rotliegend Groups (Figs. 4.2 and 4.3). The upper boundary of the Zechstein Group is a continuous mid-high amplitude reflection (Horizon H_1) that is disrupted where salt has penetrated through younger Triassic rocks, forming salt diapirs (Figs. 3.5 and 4.2). Low amplitude, chaotic internal reflections onlap the faulted internal reflections typical of the Rotliegend Group (Fig. 4.2). Where salt has completely evacuated, the bottom reflection connects to the top reflection H_1 (Fig. 4.10).

Low gamma-ray values are typical of thick salt layers (Passey et al., 1990). Figure 3.5 shows the presence of thick layers of salt separated by cyclical carbonate intervals (Coward, 1995). This figure also shows marked thickness variations across a small distance. At the top of the Zechstein Salt there is a unit of rocks with high gamma-ray values that can be traced between wells (Fig. 3.5).

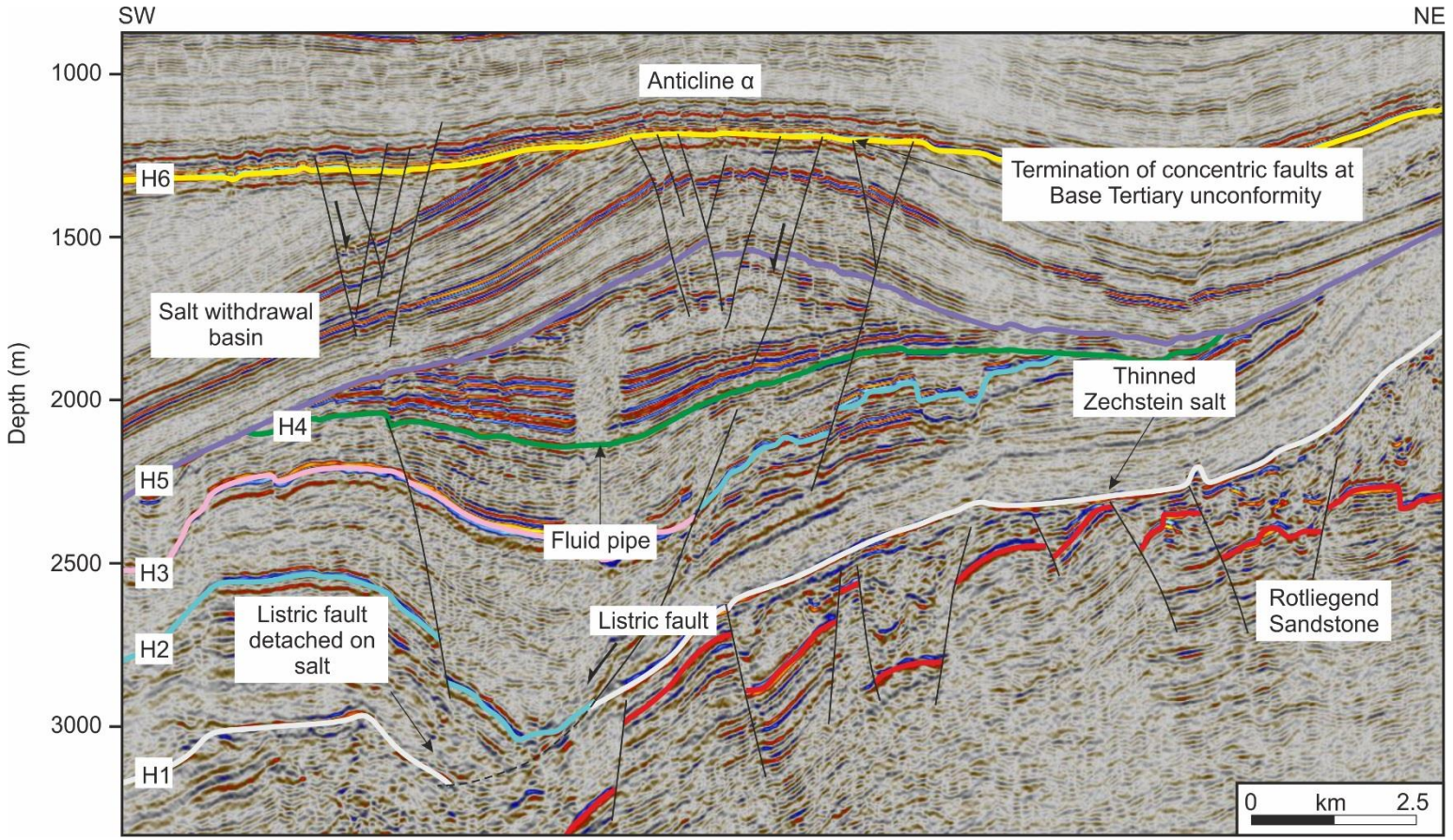

Fig. 4.10 Seismic profile showing some of the fluid escape features observed in the study area. Concentric faults in anticline α are truncated by Horizon H_6 – the Base Tertiary Unconformity. Thinned areas of the Zechstein Salt correspond to a salt weld between the Rotliegend Sandstone and the Lower Germanic Trias Group. Interpreted horizons are shown in colour.

4.4.3. Upper and Lower Germanic Trias Groups (Latest Permian to Norian)

The Trias Group comprises Triassic siliciclastic rocks (Verweij and Simmelink, 2002). The bright reflection at the base (Horizon H_1) indicates a change from high-velocity Zechstein evaporites to relatively low-velocity aeolian sandstones and lacustrine claystones of the Lower Germanic Trias Group (~500m thick) (Figs. 3.5 and 4.2). The Lower Buntsandstein Formation has a similar gamma-ray character in wells K15-07 and K15-02. However, well K15-07 is situated on the northern flank of anticline α and has a condensed section showing a similar decreasing gamma-ray trend above the Zechstein Salt (Fig. 3.5).

High gamma-ray values at the base of the Lower Germanic Trias Group indicate a higher content in organic matter, which continues at least 50 m into the Zechstein Group (Figs. 3.5 and 4.2). The transition between Zechstein Evaporites and Lower Buntsandstein Formation is the Zechstein Upper Claystone Formation (Van Adrichem Boogaert and Kouwe, 1994-1997). The overlying Upper Germanic Trias Group comprises ~500 m of marine carbonates and evaporites. The constant thicknesses observed in both the Rot (~100 m) and Muschelkalk Formations (~150 m) and the similar gamma-ray profiles, suggest tectonic quiescence. In well K15-02, the upper boundary of the Muschelkalk Formation marks the top of Triassic strata (Fig. 3.5).

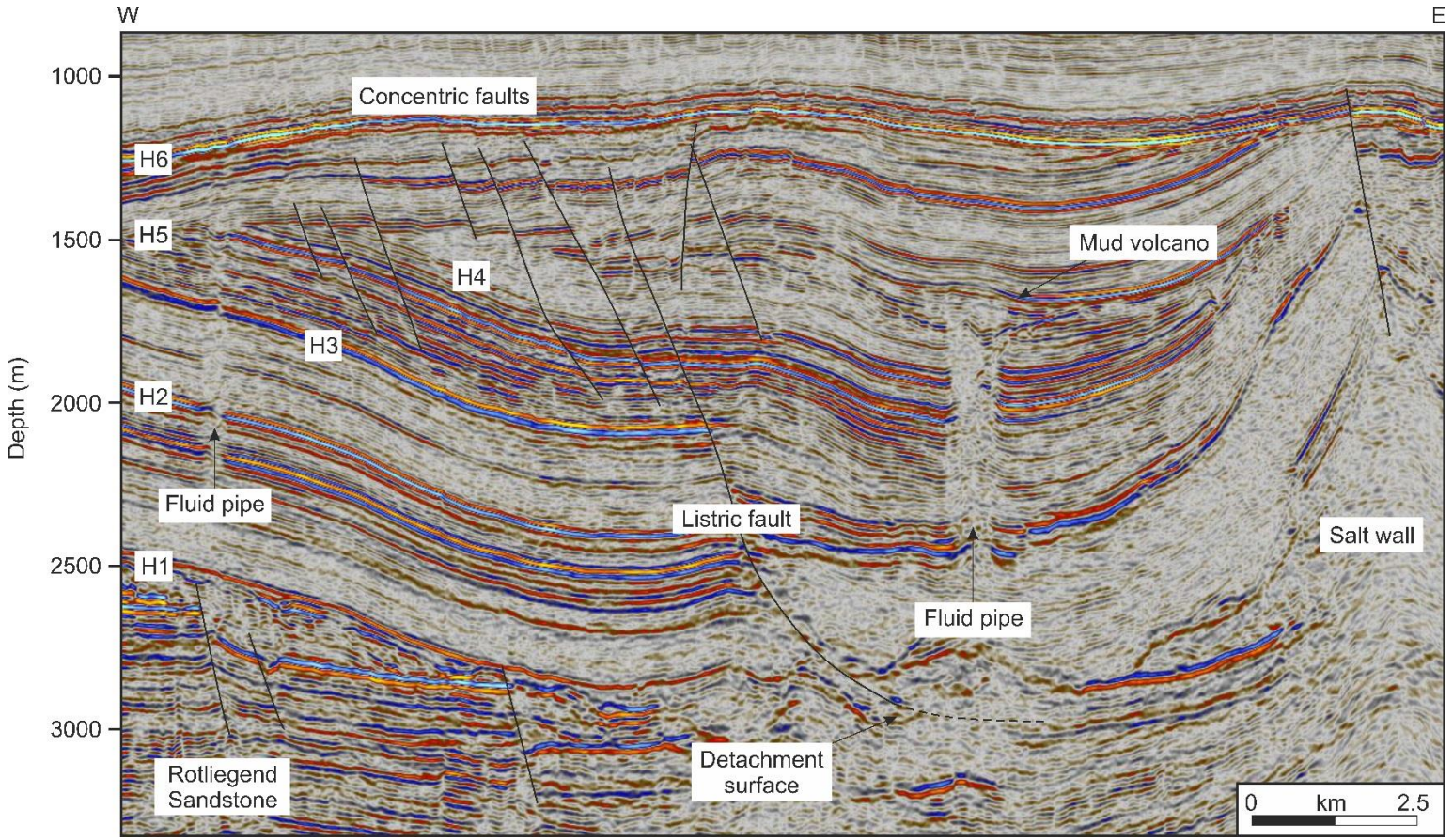

Fig. 4.11 Seismic profile oriented parallel to the large listric faults. These faults are detached on the Zechstein Salt, which generated a salt wall in the eastern part of the cross-section. A mud volcano at the upper terminus of a fluid pipe is likely sourced from strata older than the Triassic.

4.4.4. Altena Group (Rhaetian to Oxfordian)

Towards the axis of the inverted anticline that dominates the study area, ~800 m of Altena Group strata is preserved conformably over the Keuper Formation of the Upper Germanic Trias Group (Figs. 3.5 and 4.2). Deep-water argillaceous shales were deposited in the Broad Fourteens Basin and are topped by Horizon H_4 (Figs. 3.5, 4.2 and 4.6). The brightest reflection on the interpreted seismic data is the Posidonia Shale - Horizon H_3 (Fig. 4.5). This horizon was not crossed by the interpreted wells. Significant individualisation of sub-basins and erosion associated with Mid-Kimmerian upwarping and Late Kimmerian I rifting caused the removal of Jurassic strata in the NE of the study area (Verweij and Simmelink, 2002). In addition, the first signs of raft tectonics occur in the Early Jurassic (Alves and Elliott, 2014), and a large listric fault offsets the strata in this unit, with thickness variations either side of the fault (Fig. 4.2). The top horizon (Horizon H_4) of Unit I drapes over the raft and has little offset across the fault (Fig. 4.6).

4.4.5. Schieland Group (Kimmeridgian to Valanginian)

The Schieland Group is a lensoidal package of rock bounded by Horizons H_4 and H_5 (Figs. 3.5 and 4.2). In the study area, these intervals are part of the Delfland Subgroup and contain carbonaceous claystones and thick-bedded sandstones belonging to the Breeveertien Formation (Van Adrichem Boogaert

and Kouwe, 1993). They occur only within anticline α (K15-07) and are thickest at the inversion axis (~710 m) (Figs. 4.9 and 4.10). Both the upper and lower boundaries of the unit are unconformities. The lower boundary (Horizon H_4) reflects the Late Kimmerian I rifting event and the upper boundary (Horizon H_5) represents the Late Kimmerian II rifting event. Most faults located on anticline α displace these intervals, but rarely continue into the Altena Group. The unit is localised and does not occur to the SW in the salt-withdrawal basin, or NE towards the salt wall (Fig. 4.9). Importantly, all gas escape features in the study area are capped by Horizon H_5 (Figs. 4.7 and 4.10). Morphologies and mechanisms for pipe termination are discussed in *section 4.7*.

4.4.6. Rijnland and Chalk Groups (Vlanginian to Danian)

The lower and upper boundaries of the Rijnland and Chalk Groups are regional unconformities. The base is the Late Kimmerian II unconformity (Horizon H_5) and the top is the Base Tertiary unconformity (Horizon H_6) (Figs. 2.2, 4.7, and 4.8). Deposition of coastal-shallow marine Vlieland Sandstone developed only in the basin axis. Calcareous claystones of the Vlieland Claystone Formation and marls of the Holland Formation (Rijnland Group) have a relatively constant thickness throughout the study area (~300 m and ~110 m, respectively) (Figs. 4.9 – 4.11). Deposition on the basin margins was sandier than in the basin centre as demonstrated by higher gamma-ray values in well K15-07

when compared to well K15-02 (Fig. 3.5). Unlike the strata below, the Ommelanden Formation (Chalk Group) is thicker away from anticline α (~650 m) (Fig. 4.9). This is due to uplift being concentrated above the listric fault in the centre of the basin. Therefore, erosion during the Laramide and Pyrenean inversions removed more rock from the axis than the margin (Nalpas et al., 1995).

In the SW salt-withdrawal basin, concentric faults are nearly all concentrated in these units; few offset younger tertiary strata above horizon H_6. On anticline α, concentric faults pass through into the Schieland Group, but rarely continue into Tertiary strata (Figs. 4.8 and 4.9). No fluid pipes can be identified.

4.5. Analysis of fault families

Three fault families were identified and analysed in this chapter (Fig. 4.12). Listric faults constrained to Altena Group and Triassic units are associated with the gravitational gliding of individual rafts - isolated, fragmented blocks that are displaced over a décollement layer (Alves and Elliott, 2014, Alves, 2012, Penge et al., 1993). Shallower concentric faults occur within the salt-withdrawal basin and above anticline α. Comparisons are made between the three sets of faults.

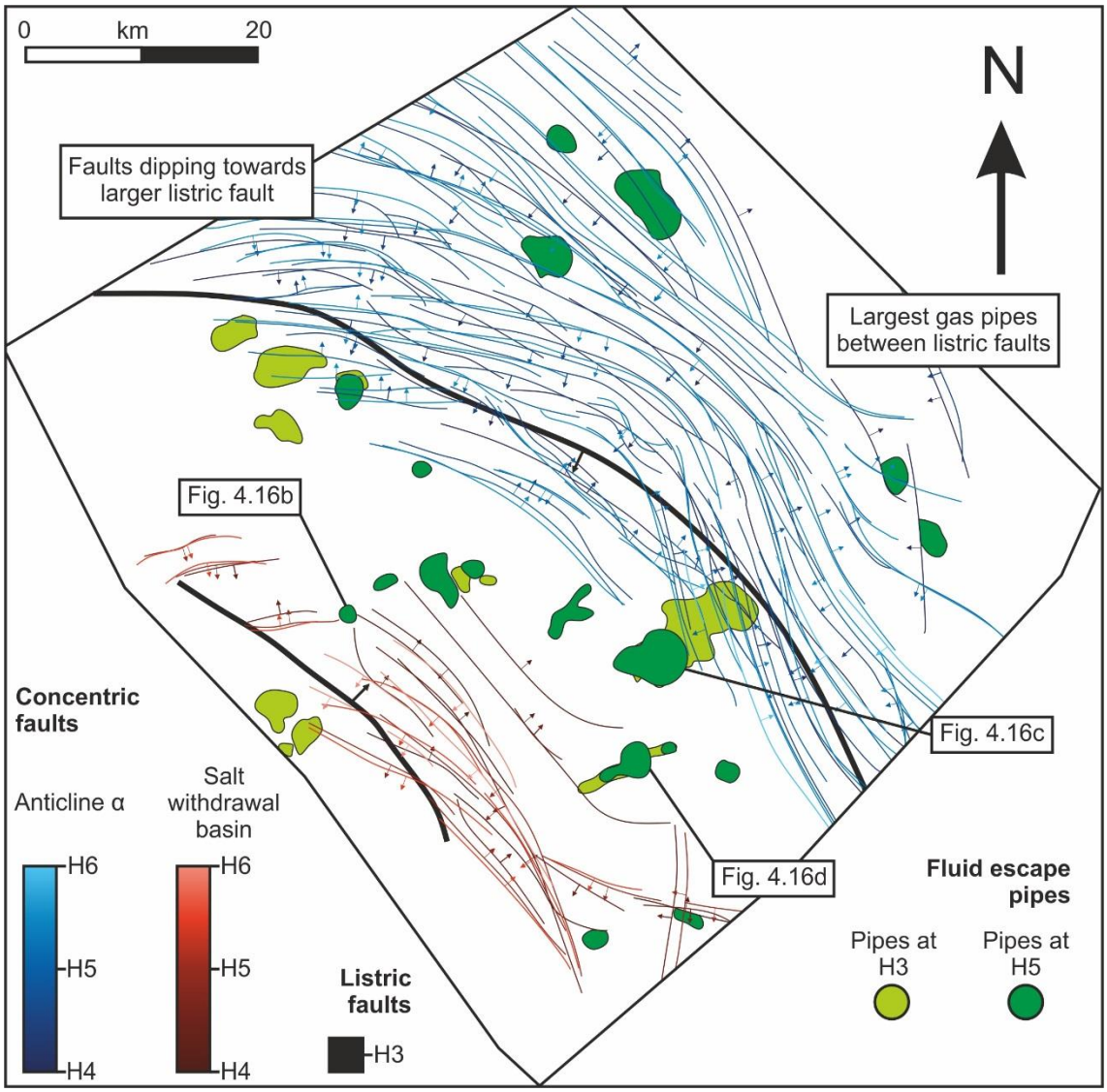

Fig. 4.12 Fault overlay diagram for all concentric faults interpreted in the study area of the Broad Fourteens Basin. Faults were drawn from multiple seismic reflections observed between the Ommelanden Formation (Chalk Group) and the Delfland Subgroup (Schieland Group). Concentric faults in the salt withdrawal basin are shown in red, concentric faults crossing anticline α are shown in blue, and listric faults are shown in black. Darker coloured faults indicate greater depth. Arrows show the dip direction of the faults. The morphology of gas pipes at their upper terminus (Horizon H_5), through Horizon H_3, are drawn to show their spatial relationship to faults. Fluid escape pipes from Figures 4.16b-d are labelled.

Fault overlay diagrams display the geometry and spatial relationship between different faults (Fig. 4.12). Slices through different horizons have been stacked for each family and the largest gas pipes identified on the seismic data have been illustrated. One observation that can be drawn from this figure is the spatial relationship the shallow faults have with the deeper listric faults. There are two clusters of faults separated by 10-20 km of undeformed rock (Fig. 4.12). In the NE, crestal faults on anticline α tend to dip towards the deeper listric fault, whereas in the SW, most salt- withdrawal basin faults dip away from the side of the listric fault further away from the salt diapir. Faults on anticline α located furthest east curve away from the previously mentioned salt diapir (Fig. 4.12).

4.5.1. Faults in salt-withdrawal basin

Concentric faults in the salt-withdrawal basin are restricted to Cretaceous Rijnland/Chalk Groups and the earliest Tertiary Lower North Sea Group units. At the lower tips of these faults, throw values are negligible within the Rijnland Group, never cross-cutting horizon H_5 (Figs. 4.9, 4.10, and 4.13d-f). As a comparison, SW-dipping faults terminate above the Base Tertiary unconformity (Horizon H_6). Throw-depth (T-z) plots reveal a distinct decrease in throw above H_6, attributed to reactivation and upward propagation of the fault (Baudon and Cartwright, 2008) (Fig. 4.13d-e). Maximum throw (~20 m) is recorded towards

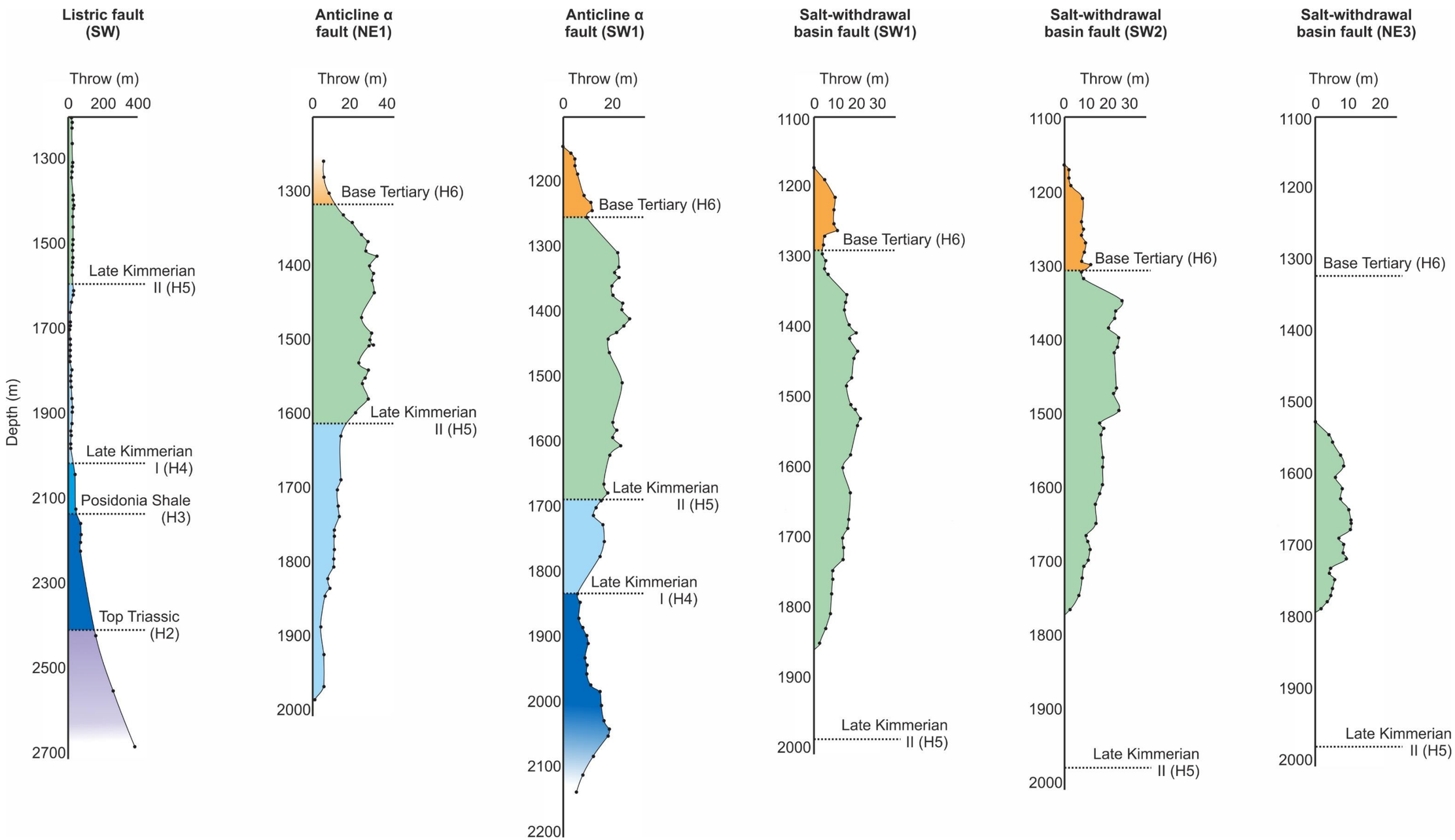

Fig. 4.13 Throw-depth (t-z) profiles for six representative faults. Local unconformities associated with points of reactivation and linkage in faults are highlighted with a dashed line. Multiple throw maxima in a single plot provide evidence for reactivation along a fault. The colours used represent the units identified in Figure 3.5. Figure 4.13a - listric fault; Figures 4.13b-c - anticline α fault; Figures 4.13d-f - salt withdrawal basin fault.

the top of the Cretaceous Chalk Group, interpreted to be the locus of fault nucleation. Strata deformed by the first stage of faulting have been eroded by the inversion events, so the throw recorded above H_6 must have been caused by renewed, post-inversion stresses. Both interpreted horizons and t-x plots show evidence of fault segment linkage as multiple peaks in throw maxima are observed (Fig. 4.14d-f) (Cartwright et al., 1995). Faults dipping SW are more numerous, but smaller conjugate NE dipping faults cut across the SW fault set. The concave side of the faults are focussed towards the salt diapir ~4000 m to the southwest (Fig. 4.2).

4.5.2. Crestal faults on anticline α

Crestal faults on anticline α are not truncated at H_5 and displace Jurassic Schieland Group, Cretaceous Rijnland Group and the Texel Formation of the Cretaceous Chalk Group, even though at the present day they occur at the same depth as the faults crossing the salt withdrawal basin (Fig. 4.13b-c). Faults on anticline α rarely propagate into Tertiary strata. Faults that do propagate above the Base Cretaceous Unconformity (H_6) have throw values of <10 m (Fig. 4.13b-c). Figure 4.13 shows that maximum throws (~35 m) are reached between the Chalk Group and the Rijnland Group.

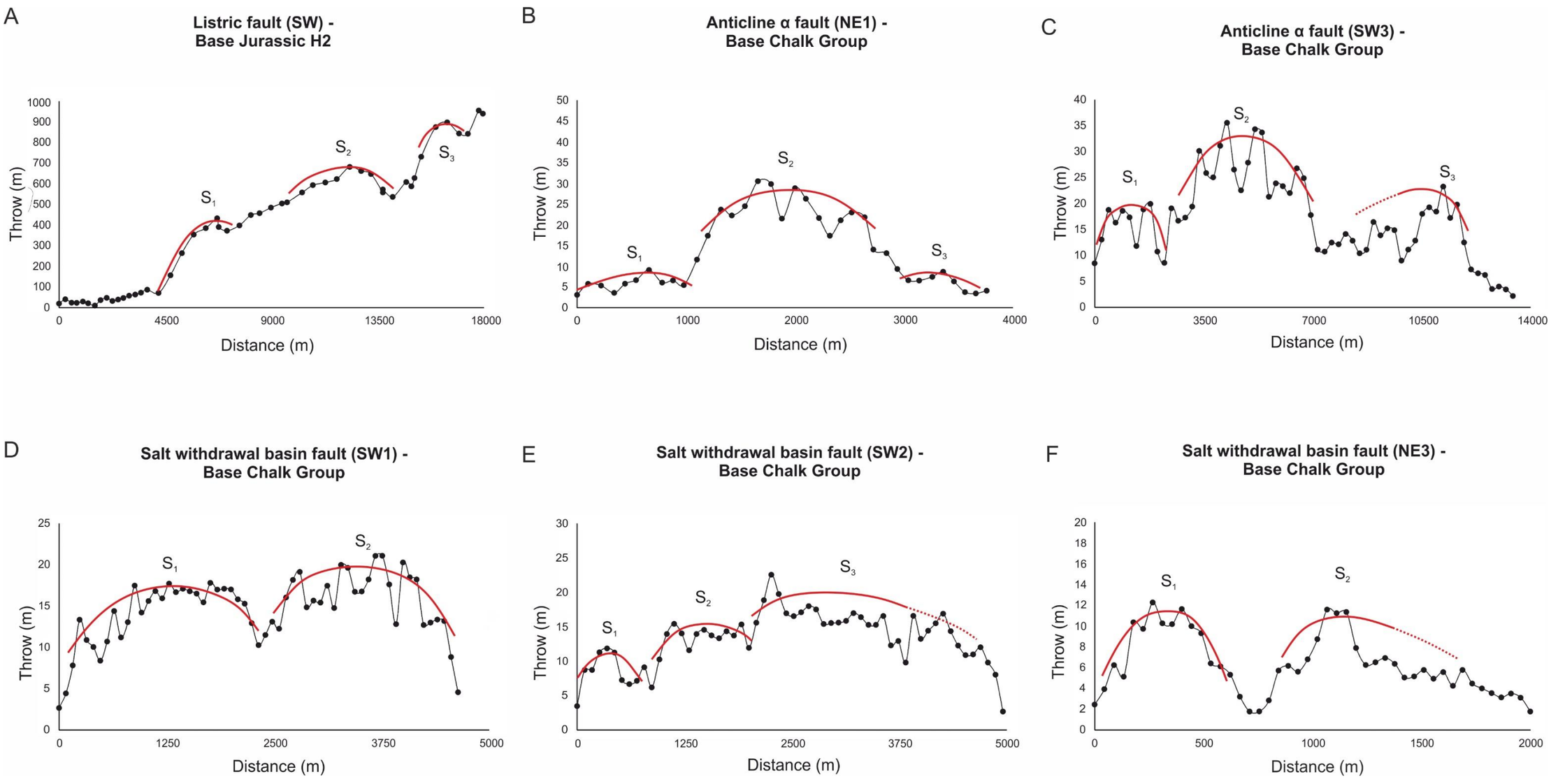

Fig. 4.14 Throw-distance (t-x) profiles for the faults analysed in Figure 4.13. Multiple peaks in throw values indicate different fault segments; highlighted by the red lines and corresponding labels S1, S2 and S3. Concentric faults crossing anticline α and in the salt withdrawal basin show the most obvious segment linkage, but listric faults have stepped profiles as the throw suddenly increases with the addition of a new segment towards the salt wall in the east. Figure 4.14a - listric fault; Figure 4.14b-c - anticline α fault; Figure 4.14d-f - salt-withdrawal basin fault.

Along H_5 (Jurassic-Cretaceous boundary) there is a throw minimum, leading to another increase in throw down dip (Fig. 4.13c). This character reflects reactivation via dip linkage, where two separate faults have propagated towards each other (Omosanya and Alves, 2014, Baudon and Cartwright, 2008). Multiple throw peaks on t-x plots show fault segment linkage is a common process (Fig. 4.14c). With a dense mesh of faults occurring above anticline α, the fault traces are difficult to image, leading to inaccuracies in how the faults interact at this point. However, using variance slices and mapped horizons, it is clear that maximum curvature occurs at the top of the anticline and where many fault segments connect (Fig. 4.12).

4.5.3. Listric faults

Listric faults are less common in the study area and bound individual Triassic-Jurassic rafts (Alves and Elliott, 2014). These faults sole-out in the Zechstein Salt, which acts as a décollement layer. Along strike, single listric faults are linked to multiple fault segments on anticline α (Fig. 4.15). Where the lower tips of the faults on anticline α join to the upper tip of the listric fault (H_4), throw decreases from ~100 m to ~30 m (Fig. 4.13a). This sudden jump in throw values suggest the listric fault was reactivated, with the multiple fault segments on anticline α connecting to the listric fault, providing evidence that reactivation caused vertical propagation via dip linkage. Two sudden gradient changes occur

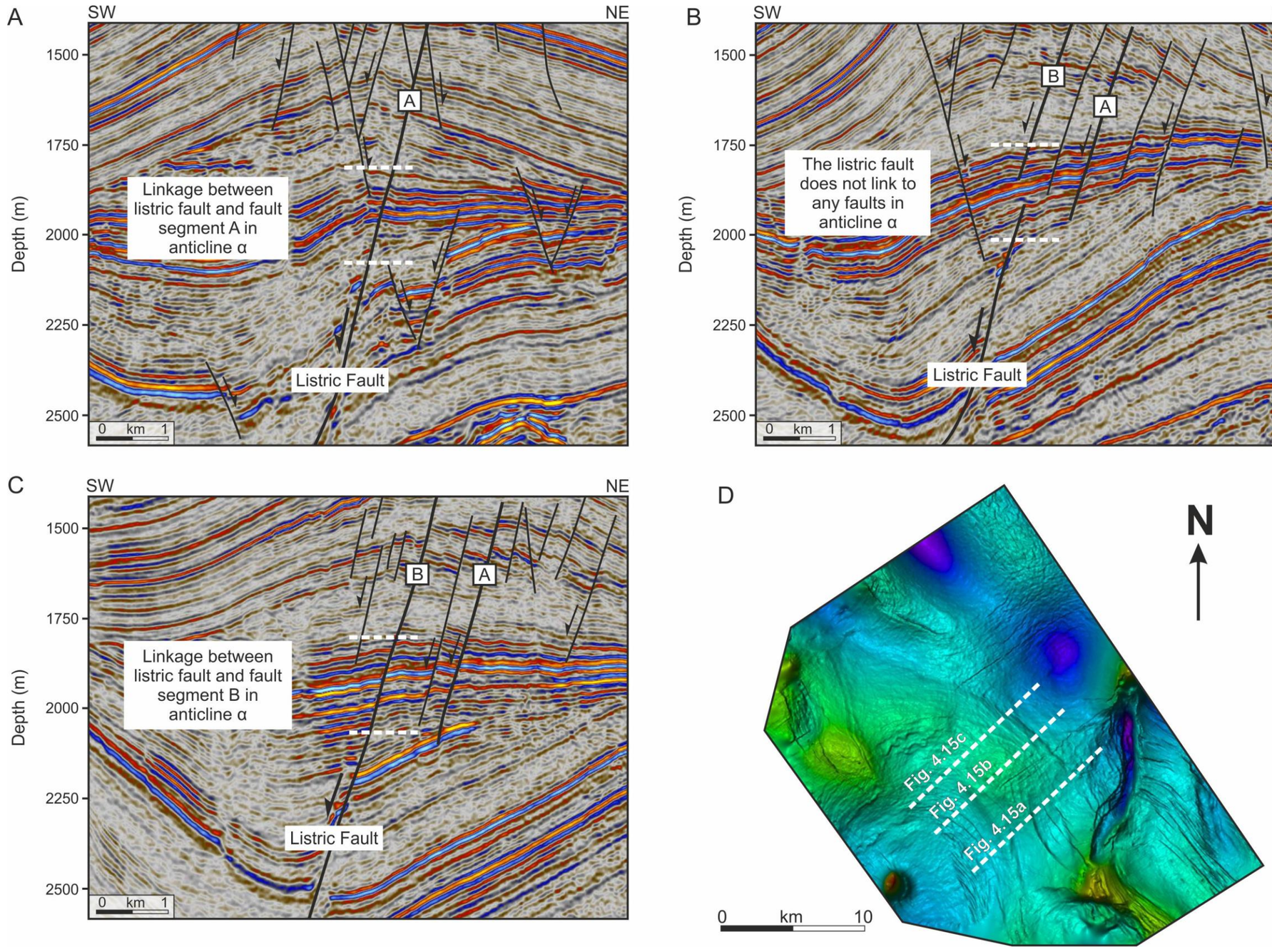

Fig. 4.15 Seismic lines depicting the way raft-bounding listric faults propagate upwards to link with discrete fault segments in anticline α. White lines represent the area where the links between the listric fault and other structures are observed across anticline α. Fault segment A is linked to the listric fault to the SE of anticline α (Fig. 4.15a). The segments are then isolated in the centre of anticline α (Fig. 4.15b). Fault segment B is then linked to the listric fault located to the NW side of anticline α (Fig. 4.15c), whilst the tip-line of segment A does not link to the listric fault here. Figure 4. 15d shows the locations of Figures 4. 15a, b, and c.

on t-x plots of listric faults where throw increases by ~300 m. Three fault segments are highlighted in Figure 4.14a, each separated by a trough in the along strike throw profiles. Maximum displacement along this fault is observed at its SE tip, where the fault intersects a salt wall (Figs. 4.2 and 4.14a). The fault does not continue on the east side of the salt wall, suggesting the movement of salt has influenced the variations in along strike displacement. Thickness variations between the footwall and the hanging-wall of the listric faults show they are syn-sedimentary (Childs et al., 2003).

4.6. Evidence for fluid expulsion

Highly localised vertical to sub-vertical pathways of focused fluid flow (fluid escape pipes) are seen on seismic data as columns of disrupted reflection continuity (Gay et al., 2007, Cartwright and Santamarina, 2015, Hustoft et al., 2007). The locations of pipes are often controlled by underlying structures such as fault zones, salt diapirs, erosional surfaces or anticlinal crests (Gay et al., 2007). Fluid escape pipes are generally clustered (Cartwright and Santamarina, 2015, Gay et al., 2007, Hustoft et al., 2010). Within the studied polygon, 14 clusters of 109 individual pipes (clustered and non-clustered) were measured (Fig. 4.12). The upper terminus of individual pipes range in width from ~200 m to ~1200 m, whereas their height depends on the depth of the root zone and ranges from ~300 m to ~1100 m. Most of the gas pipes are rooted in the Lower Germanic Trias

Group, crossing the Posidonia Shale (Fig. 4.16). All the gas pipes terminate at the Jurassic-Cretaceous boundary (Horizon H_5-Late Kimmerian II rifting event) (Figs. 4.7, 4.8, 4.10, 4.11 and 4.16).

Different morphologies of the upper terminus of fluid escape pipes are observed in Figures 4.6, 4.12 and 4.16. All are circular to slightly elliptical in planform, but are characterised by variations in the shape in cross-section and size. Strata above and within fluid escape pipe a) have been upwarped to form a mound (Fig. 4.16a). Reflections above H_5 are also mostly continuous across the pipe, maintaining their thickness and not onlapping the structure (Fig. 4.3). In Figure 4.16b, fluid escape pipe b) is small compared to other examples and is strongly elliptical in planform. There is no topographic expression above H_5, although reflections thin out towards the upper terminus of pipe b), indicating numerous stages of growth and pulses of fluid flow (Cartwright and Santamarina, 2015). Fluid escape pipe c) has the same shape as mud volcanoes described in Kopf (2002) (Fig. 4.16c). Reflections onlap the flanks both within and

---

Fig. 4.16 (Next page) Seismic character of fluid-escape pipes in the study area. Each diagram (fluid pipe a-d) shows a seismic slice with fluid pipes and relevant features. All the fluid pipes terminate at H_5 and are sourced in strata that are deeper than the Jurassic units. a) Upwarped reflections above the fluid pipe forming a mound. There is no thinning in these horizons, indicating sediment was deposited before fluid escape occurred. b) A small fluid pipe with downwarped reflections at its upper terminus. The observed thinning of seismic reflections below H_5 suggests multiple stages of growth. c) A mud volcano is observed at the upper terminus of the fluid pipe, which expelled sediment onto the palaeoseafloor. d) Cluster of fluid pipes that are rooted in the Zechstein Salt (H_1).

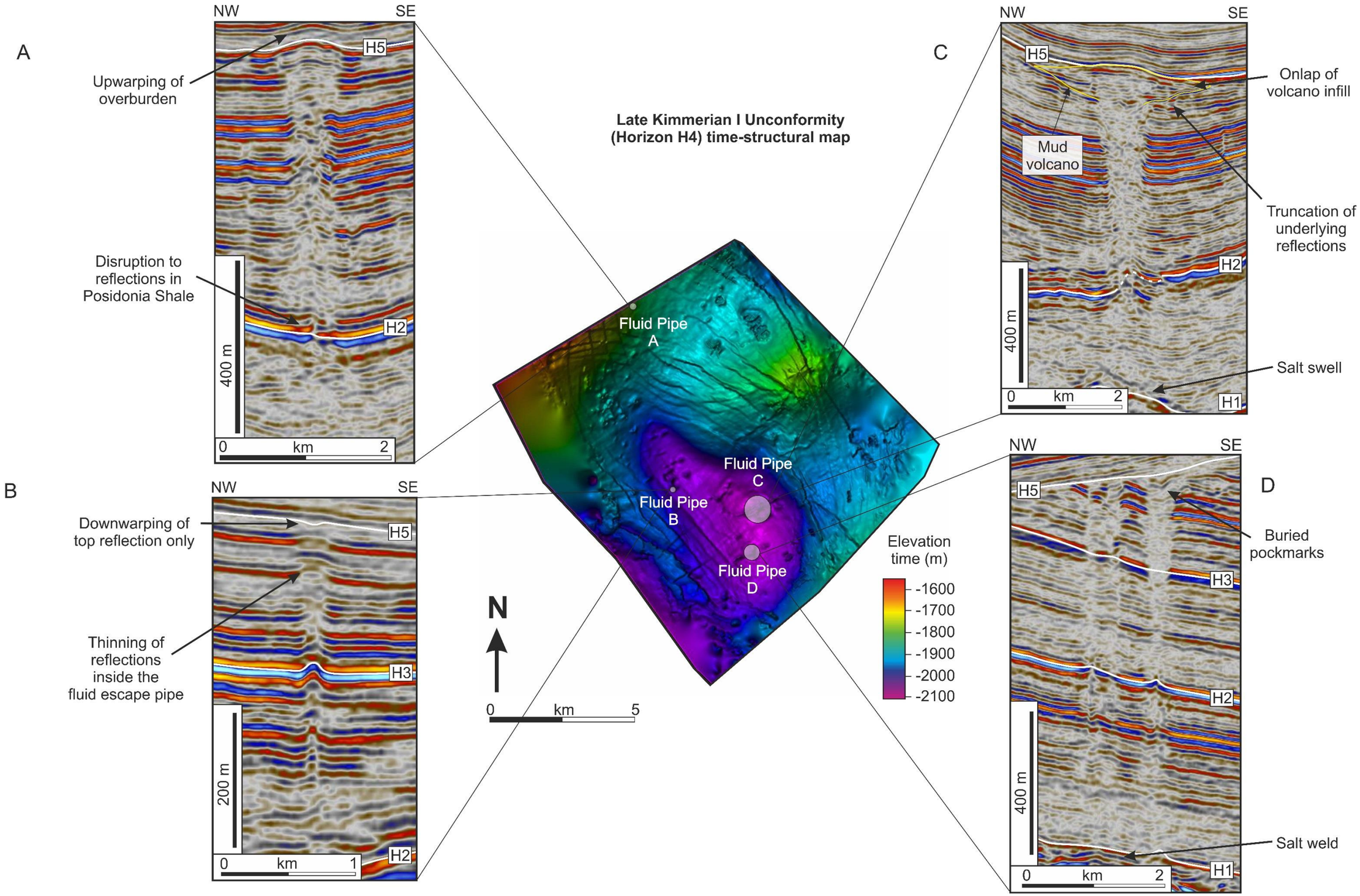
A
NW
SE
H5
Upwarping of overburden
Disruption to reflections in Posidonia Shale
H2
400 m
0 km 2
B
NW
SE
Downwarping of top reflection only
H5
Thinning of reflections inside the fluid escape pipe
H3
200 m
H2
0 km 1
Late Kimmerian I Unconformity
(Horizon H4) time-structural map
Fluid Pipe A
Fluid Pipe B
Fluid Pipe C
Fluid Pipe D
N
0 km 5
Elevation time (m)
-1600
-1700
-1800
-1900
-2000
-2100
C
NW
SE
H5
Onlap of volcano infill
Mud volcano
Truncation of underlying reflections
H2
400 m
0 km 2
Salt swell
H1
D
NW
SE
H5
Buried pockmarks
H3
H2
400 m
Salt weld
0 km 2
H1

outside the structure. It tapers to a root zone within the Lower Germanic Trias Group, ~100 m above a small salt swell. Above H_5, topographic relief has caused sediments to onlap onto the SE flank and thin over the crest of the structure. Fluid escape pipe d) is a cluster of smaller individual pipes (Figs. 4.12 and 4.16d). They each show examples of buried pockmarks (Andresen and Huuse, 2011, Cartwright and Santamarina, 2015). The pipes root to the Zechstein Salt, disrupting reflections in H_1. The geometry of the upper terminus is consistent with those described by Andresen and Huuse (2011) as depressions, interpreted as pockmarks, having erosional bases and onlapping fill.

4.7. Slip tendency analyses for concentric faults

4.7.1. Slip tendency results and effects of changing pore fluid pressure

Due to the curvature of the concentric faults, some sections of the fault surfaces may be optimally oriented for reactivation in the modern stress field. Slip tendency analyses demonstrate how the likelihood for a fault to fail can change along the strike of a curved concentric fault (Figs. 4.17 – 4.20). The results calculated on Move™ are provided as a value normalised to the maximum slip: $\overline{T_s} = T_s/T_{max}$, so that 1 indicates the highest expected level of slip and 0 is no slip (Healy et al., 2015). This allows direct comparisons between different sets of

results (McFarland et al., 2012, Healy et al., 2015). Fault models in Figures 4.17 – 4.20 show slip tendencies on the fault surfaces and include the orientations of principal stresses. Maximum normalised slip tendency values occur on sections of the fault that strike 30° to the orientation of σ_1. When P_f = 0 MPa, segments of faults in the north striking 30° to σ_1 have $\overline{T_s}$ values approaching 0.2, whereas in the south, the faults segments are striking < 30° to σ_1 and have $\overline{T_s} \geq 0$ (Fig. 4.17a). Relatively high slip tendencies are also observed in shallower faults with lower dips, as fault reactivation in a compressional setting favours low-angle thrusts (Wiprut and Zoback, 2002). Smaller faults in the SW salt-withdrawal basin have higher $\overline{T_s}$ values than faults on anticline α and listric faults as they are an ideal orientation for fault reactivation. They are generally smaller and less curved, and hence the slip tendency is more homogeneous along strike (Figs. 4.17 – 4.20). Along these sets of faults, a zone of high $\overline{T_s}$ values occur on faults that strike ~295°, 30° to the orientation of σ_1 and optimal for strike-slip reactivation (De Lugt et al., 2003, Nalpas et al., 1995).

We plotted Mohr circles to help visualise and quantify how increasing pore fluid pressure reduces the effective normal stress (σ_n'), therefore increasing the $\overline{T_s}$ moving the fault towards failure (Fig. 4.21a). Two Coulomb failure envelopes have been plotted on this diagram to show the conditions required to reactivate a fault (fault failure) or create new faults in an intact rock (intact rock failure). An average fault depth of 1500m was considered and boundary conditions for the angle of internal friction (ϕ) and cohesion (C) of 30° and 10

MPa were used respectively (Barton, 1973). The same angle of internal friction was assumed for fault reactivation, but cohesion was set to 0 MPa (Morris et al., 1996).

The assumption of a cohesionless surface for the fault plane does not represent a true fault surface. All faults will have some amount of roughness within the joints that increases the amount of friction (Barton, 1973). However, approximating a cohesionless fault will give the lowest boundary for failure along a fault plane. These failure envelopes allow us to predict optimum fault orientations for reactivation by measuring the angle between σ_1 and the point of intersection between the envelope and the Mohr circle (2θ). The fault strike where reactivation is likely to occur is consequently $90 – (\theta/2)$. The Mohr circle in Figure 4.21a at 25 MPa intersects the fault failure envelope between 103.5° and 136.5° from σ_1. This indicates that faults striking at ~ 21.75° – 38.25° to σ_1 are most likely to fail, matching the results found on the fault models. As pore fluid pressure is increased to 30 MPa, optimum angles for reactivation are extended to ~ 3.5° - 56.5° to σ_1. This is emphasised by the fault models in Figures 4.19 and 4.20, where at 30 MPa, anything above the fault failure envelope has a $\overline{T_s} \approx 1$.

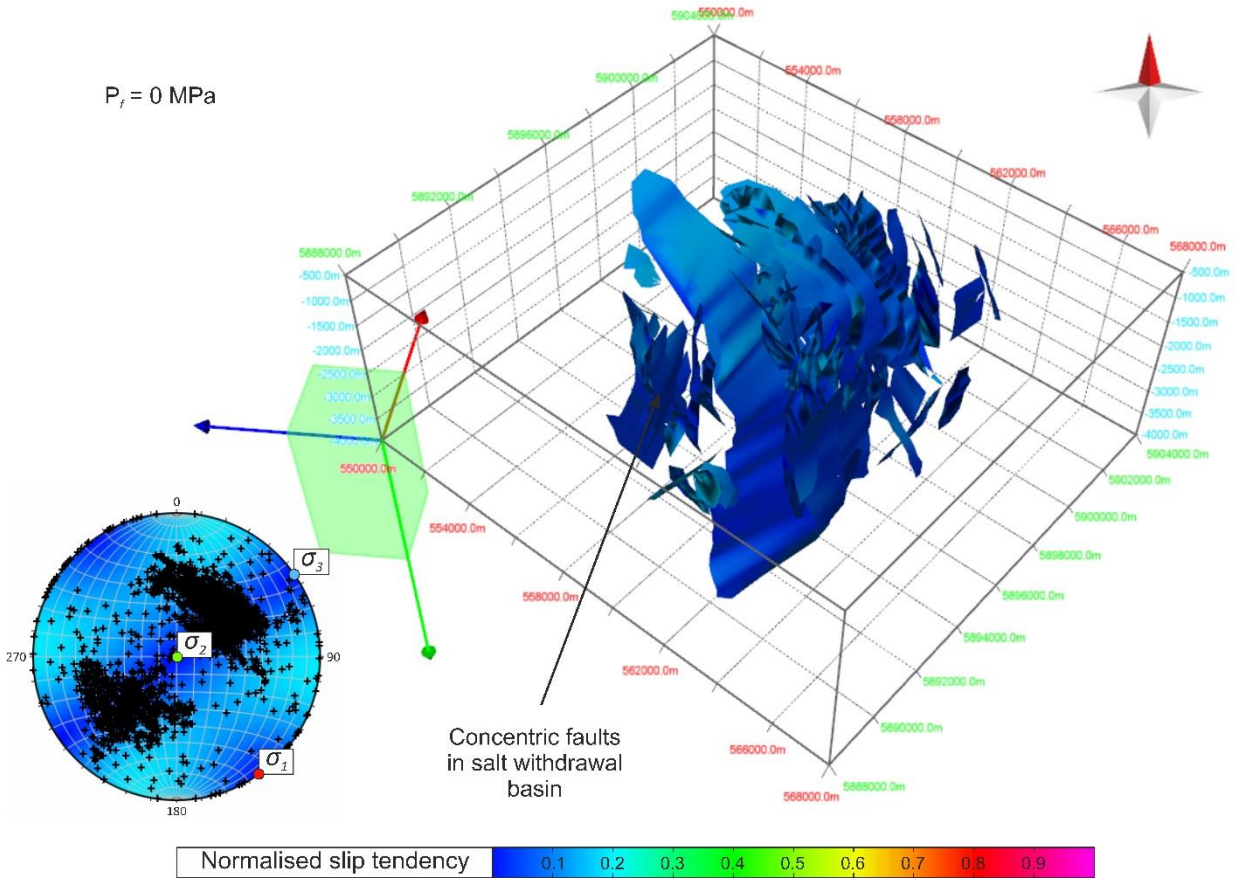

Fig. 4.17 Normalised results for slip tendency overlain on fault models. Red/pink represents a higher chance of slip, blue/turquoise represent lower chances of a fault to slip. This model assumes pore-fluid pressure (Pf) at 0 MPa, *i.e.* without fluid injection or local fluid overpressure.

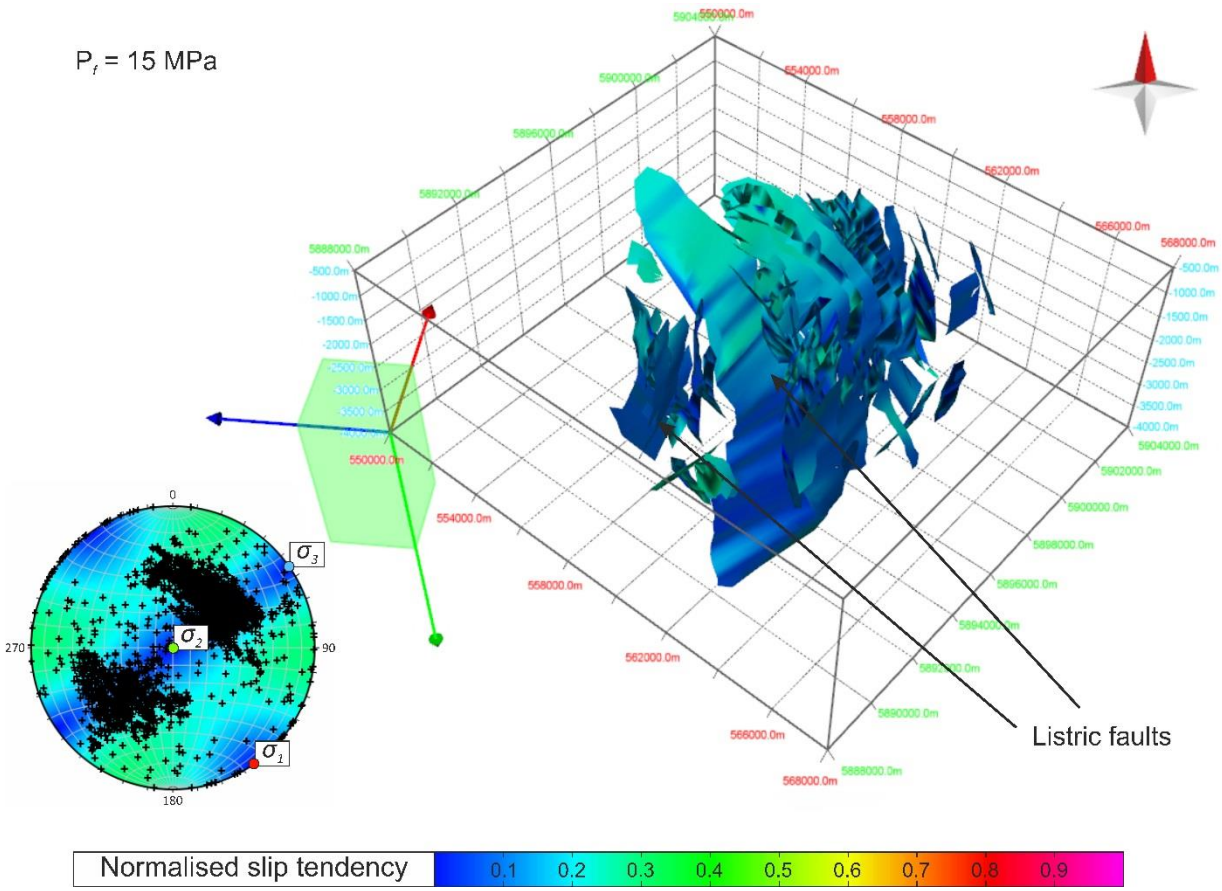

Fig. 4.18 Normalised results for slip tendency overlain on fault models. This model assumes pore-fluid pressure (Pf) at 15 MPa. It is shown together with a stereonet revealing the poles to the interpreted fault planes.

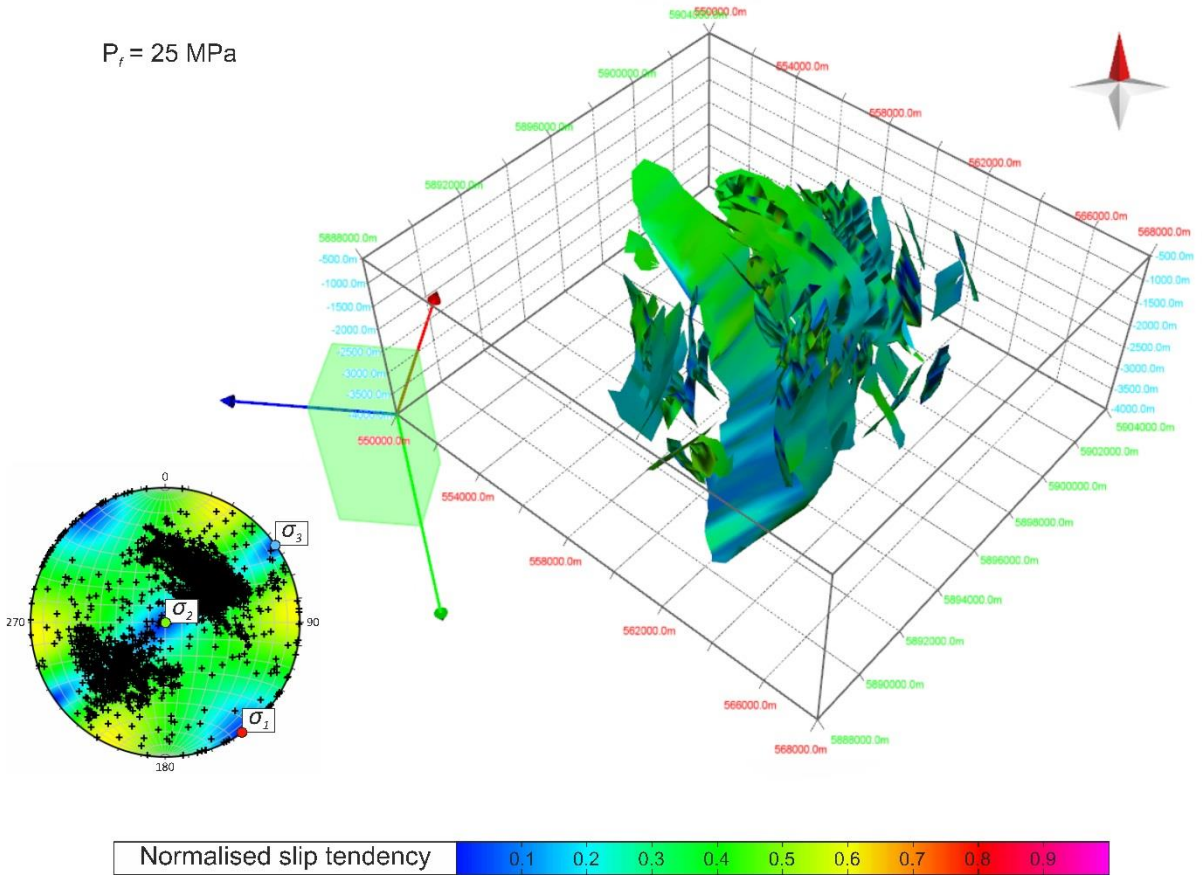

Fig. 4.19 Normalised results for slip tendency overlain on fault models. This model considers pore-fluid pressure (Pf) at 25 MPa, *i.e.* nearing the pressures used in fluid injection during Carbon Capture and Storage (CCS). It is shown together with a stereonet representing the poles to the interpreted fault planes.

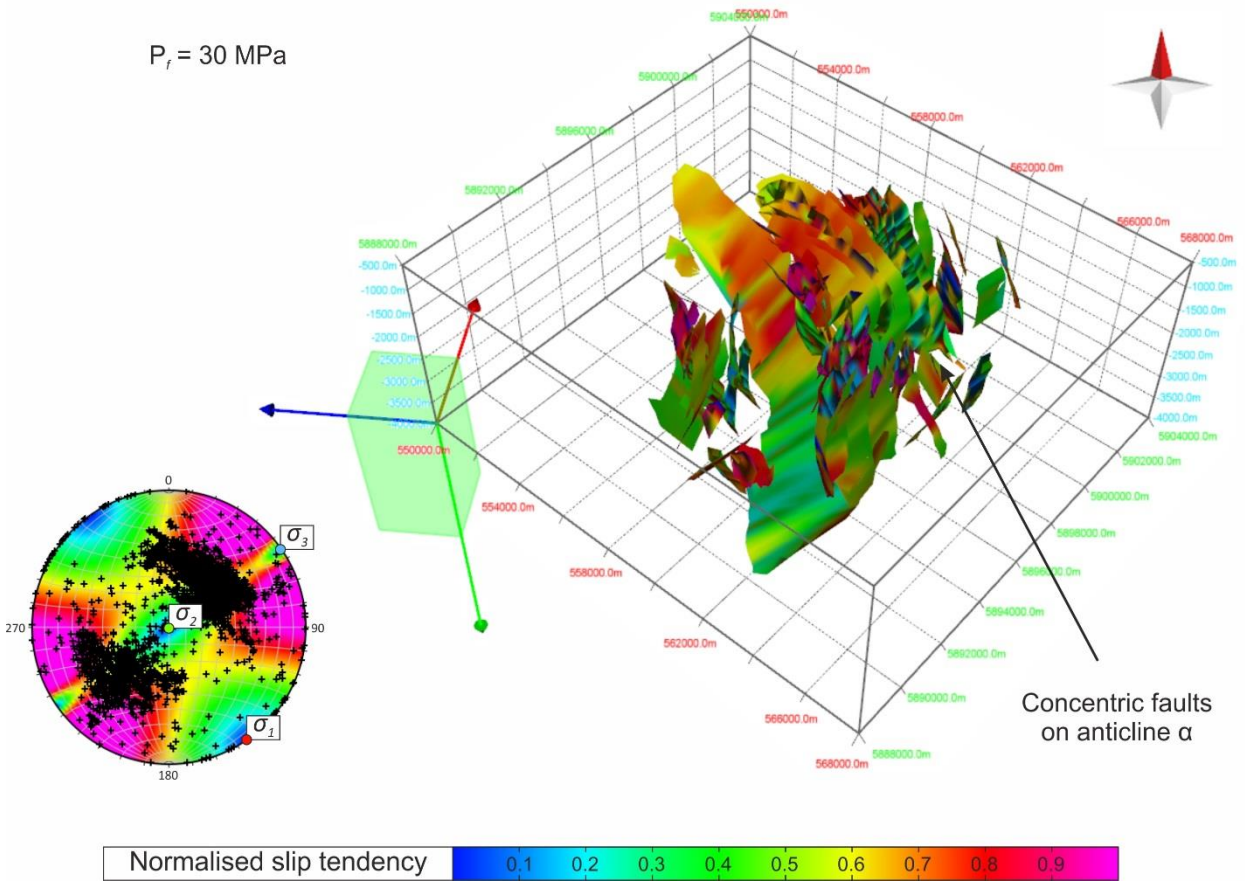

Fig. 4.20 Normalised results for slip tendency overlain on fault models. This model assumes pore-fluid pressure (Pf) at 30 MPa. Vertical red patches indicate areas of high slip tendency where the fault is most likely to reactivate during CCS.

4.7.2. Slip tendency analysis using different lithologies

To help understand the behaviour of different sets of concentric faults, representative Mohr circles have been created for key lithologies. Measurements of ϕ and C for each lithology were taken from Farmer and Jumikis (1968). Figure 4.21b shows Mohr circles for the faults within the salt-withdrawal basin. The average depth of these faults is ~1600 m, and the most common lithology they displace is chalk. As in *section 4.7.1*, two failure envelopes were added to the diagrams; ϕ = 39° for both, and C = 3.5 MPa for the failure within the intact rock and 0 MPa for fault reactivation. Results show that faults are only likely to reactivate when pore fluid pressures reach 30 MPa and the fault strikes ~ 11.5° - 40° relative to σ_1. New faults are not expected to form under these conditions. Concentric faults on the inverted anticline have an average depth of ~ 2000 m and cut into the Vlieland Sandstone, a small but important reservoir rock. A cohesion value of 8 MPa and a ϕ value of 35° was calculated for a sandstone (Farmer and Jumikis, 1968). Between pore fluid pressures of 0 MPa and 30 MPa, $\overline{T}_s$ never exceeds 0.5 (Fig. 4.21c). Even when pore fluid pressures reach 30 MPa, the Mohr's circles do not pass the fault failure envelope, indicating that faults are unlikely to reactivate under these conditions (C = 0 MPa).

The height of the listric faults is > 1 km, so the Posidonia Shale was chosen as a representative horizon, as it is a prolific source rock in the Southern North Sea (Duin et al., 2006). The average depth of the Posidonia Shale is 2400 m and

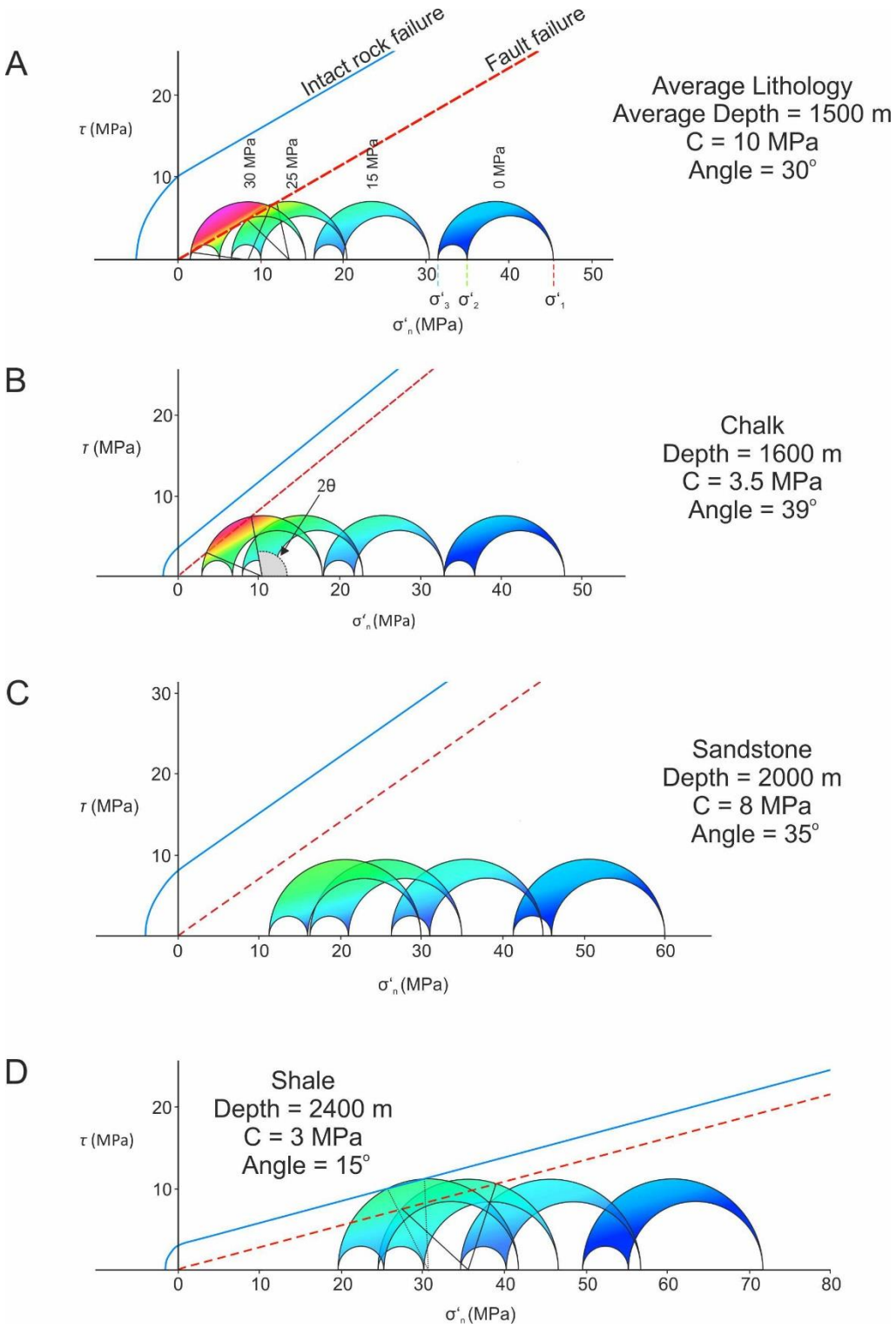

Fig. 4.21 Mohr's Circle diagrams of different lithologies documented in the study area of the Broad Fourteens Basin, and the effects of increasing pore-fluid pressure. a) Diagram demonstrating how increasing the pore fluid pressure makes a fault more likely to reactivate. An average depth and lithology was assumed for the parameters shown. b-d) Diagrams showing the likelihood of faults to reactivate in the Chalk Group, Vlieland Sandstone and Posidonia Shale. Values of cohesion (C) and angle of internal friction (ϕ) were estimated by Farmer and Jumikis (1968).

predicted C and ϕ are 3 MPa and 15° respectively (Farmer and Jumikis, 1968). Such a low angle of internal friction means that an increase in P_f greatly increases the chances of fault reactivation. At 25 MPa, faults oriented between 21° and 54° to σ_1 are likely to reactivate (Fig. 4.21d). When P_f = 30 MPa, not only are faults striking 15.5° - 59.5° to σ_1 likely to fail, but new faults striking 31.5° - 43.5° to σ_1 start to form.

4.8. Discussion

4.8.1. Propagation history of concentric faults

The throw profiles in Figures 4.13 and 4.14 help determine the timing of fault initiation. In the study area, it is not possible to infer the exact age of fault initiation, but chronological boundaries can be estimated for the interpreted fault families. Figure 4.22a-d shows a schematic evolution of the study area, highlighting the ages for concentric fault formation.

Faults generated in salt-withdrawal basins occur only above Horizon H_5. The unconformity H_6 truncates faults, so their formation must have occurred prior to the erosion of Chalk Group units at the end of the Cretaceous. The faults appear to be blind as there is no growth of strata across them. Normal offset and steep dips of the faults imply that they must have formed during an extensional

phase, the most recent being prior to the Laramide inversion (Verweij and Simmelink, 2002).

Faults on anticline α have maximum throw values in the Rijnland Group of Early Cretaceous age, displacing older strata than faults in the salt-withdrawal basin. The faults on anticline α have steep dip and normal offset, similar to the faults in the salt-withdrawal basin, indicating extensional forces were acting upon them. However, results indicate faults formed during the Late Cretaceous which was dominated by reverse movement along low-angle thrust faults. Figure 4.12 hints at a spatial relationship between faults on anticline α and in the salt-withdrawal basin, formed in the Cretaceous, and listric faults, forming through the Triassic and Jurassic. Possible mechanisms for the formation of concentric faults on anticline α and in the salt-withdrawal basin are:

- Using the Zechstein salt as a detachment layer, raft bounding faults were reactivated during discrete tectonic pulses. Bending and differential subsidence of strata draping these faults could have allowed extensional failure over the edge of the footwall block (Oudmayer and De Jager, 1993, De Lugt et al., 2003) (Fig. 4.22).
- Halokinesis in the Southern North Sea occurred from the Late Triassic onwards. During the three inversion events, salt was squeezed up through older reactivated faults, being withdrawn

from within the basin (Coward and Stewart, 1995). Thus, extensional faulting developed as secondary rim synclines formed, bending the strata towards the subsiding minibasin adjacent to the salt diapir (Fig. 4.22) (Nalpas et al., 1995, Maione and Pickford, 2001, Coward and Stewart, 1995). Maione and Pickford (2001) described the geometry of the extensional faults reflecting that of the salt diapir which explains how the whole length of the concentric fault experiences normal offset.

Although the relative timing of initiation between these faults is unknown, it is postulated that both mechanisms were involved in forming the different faults. All faults were reactivated during the Early Tertiary (Fig. 4.22). Faults in the salt-withdrawal basin and on anticline α cross the Base Tertiary Unconformity (H_6) and have a typical reactivated *t*-*z* profile with a stepped gradient, suggesting upward propagation during reactivation (Baudon and Cartwright, 2008). Reactivation of anticline α faults and listric faults connecting the two families appears to be caused by dip linkage (Figs. 4.13a and 4.15), with throw maxima separated by a throw minimum (Baudon and Cartwright, 2008). Extensional faults (dipping at ~60^{o}) would be hard to reactivate with reverse-slip. In many settings it is easier to form new, low-angle thrusts behind the normal fault than reactivate it. Without the presence of low-angle thrust faults (and stress

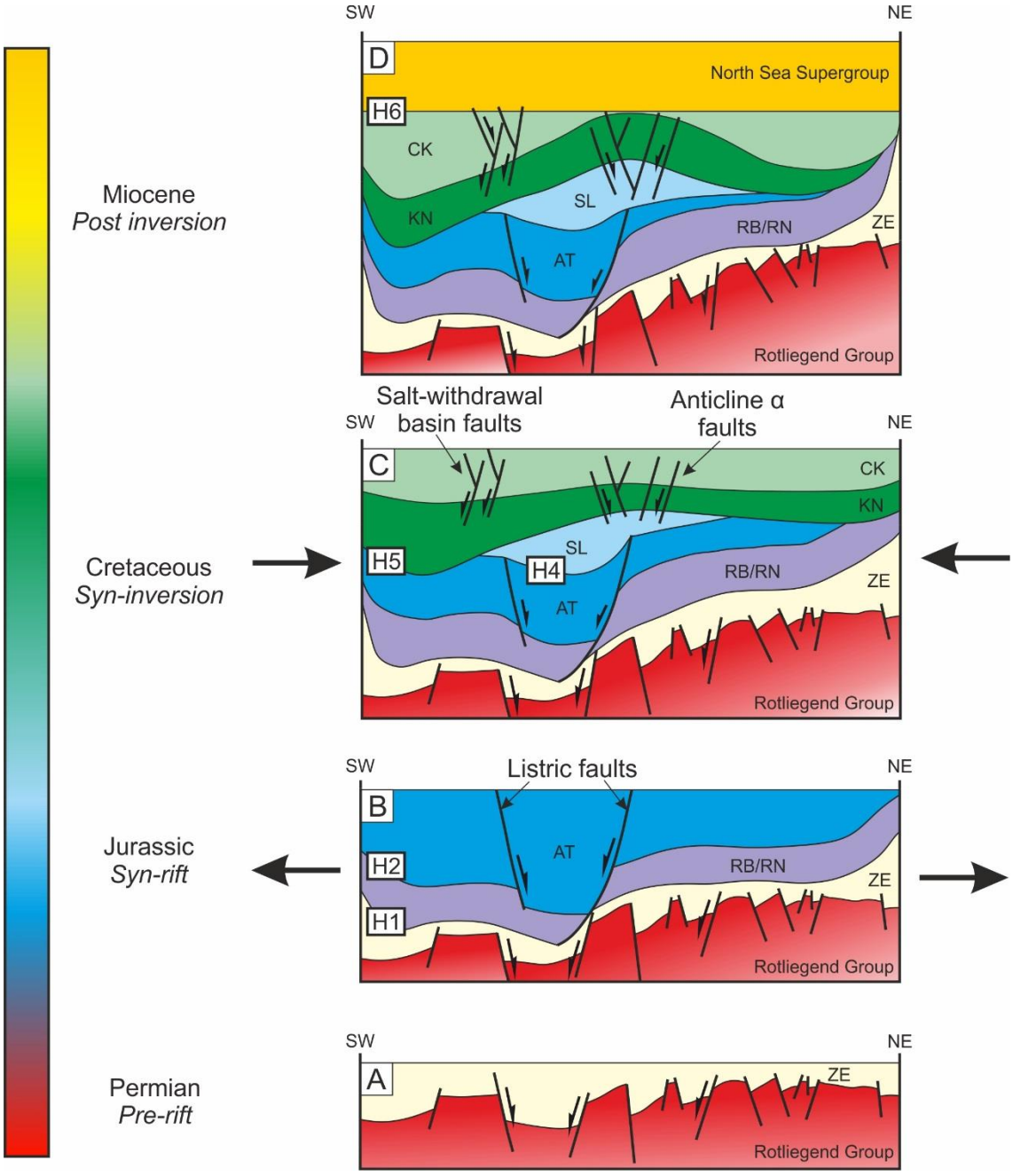

Fig. 4.22 Schematic diagram of the geological evolution of the study area, Broad Fourteens Basin (based on Figure Fig. **4.9**). The figure highlights the age and growth of different fault families. The diagram shows that listric faults were active during Jurassic syn-rift in association with rift-raft tectonics. Shallower concentric faults are formed in the Late Cretaceous in response to the evacuation of salt (salt withdrawal) and differential subsidence on the footwall of a listric fault (faults crossing anticline α). ZE, Zechstein Group; RB, Lower Germanic Trias Group; RN, Upper Germanic Trias Group; AT, Altena Group; SL, Schieland Group; KN, Rijnland Group; CK, Chalk Group.

orientations <30° to the fault strike) these faults are considered to have reactivated obliquely (De Lugt et al., 2003, Hooper et al., 1995). Transpressional or transtensional forces may have acted on parts of the concentric faults, but no structures are observed to provide evidence for this.

Lateral propagation of fault segments may have increased the curvature of the faults. Though it is hypothesised that the concentric faults formed due to differential subsidence or salt-withdrawal, fault segment-tips may have propagated along a curved path and intersected the next fault. This curvature is due to the influence of the nearby fault on the stress field of the propagating fault (Ferrill et al., 1999). This would explain why, in the NW of Figure 4.12, smaller segments curve into larger faults.

4.8.2. Timing of pockmark and fluid pipe formation and their relationship to concentric faults

It is important to understand fluid expulsion processes because they can be primary or secondary pathways for hydrocarbon migration through a sedimentary basin, potentially by-passing a seal unit (Cartwright and Santamarina, 2015, Cartwright et al., 2007). Carbon sequestration and CCS efforts could be hindered by fluid escaping through the overburden, with evidence for such events occurring in the Sleipner pilot project (Arts et al., 2004, Cathles et al., 2010).

The morphology of the upper termination of fluid escape pipes aids in determining its timing of formation (Cartwright and Santamarina, 2015, Løseth et al., 2009, Andresen and Huuse, 2011, Hustoft et al., 2010, Van Rensbergen et al., 2007). Examples of past movement is described and interpreted in this section from the seismic data. Multiple phases of fluid flow are hard to analyse, as each new migration event obscures previous seismic evidence of fluid flow (Cartwright and Santamarina, 2015). Mud volcanoes and pockmarks are both topographic features that formed at the surface. In a pockmark, basin fill onlaps underlying rocks, whereas sediments onlap the flanks of a topographically elevated mud volcano (Kopf, 2002, Andresen and Huuse, 2011). Thinning of reflections over high relief structures (mud volcanoes/mounds) is another indication of palaeo-fluid flow. Upwarping of the overburden indicates that sediment had been deposited and buried before the fluid escape pipe formed (Frey-Martinez et al., 2007). Fluid pipes may terminate at boundaries that prevent them from propagating vertically, instead diffusing horizontally into a more permeable reservoir (e.g. Schieland Group) (Cartwright and Santamarina, 2015, Hustoft et al., 2007).

Overpressured conditions are often a prerequisite for generating fluid escape pipes. In general, Rotliegend reservoirs in the Broad Fourteens Basin are currently hydrostatic (Verweij and Simmelink, 2002). Overpressured conditions last occurred in the Late Jurassic when sedimentation rates were exceptionally high (Verweij and Simmelink, 2002, Osborne and Swarbrick, 1997). Fluid escape

features described in *section 4.6* terminate at the Jurassic-Cretaceous boundary, coinciding with Late Jurassic overpressure (Osborne and Swarbrick, 1997). Most of the pipes in the study area are rooted below the Lower Germanic Trias Group, either from the Main Buntsandstein Formation or the Rotliegend Sandstone. Very few pipes root at the Posidonia Shale indicating that hydrocarbons in the fluid pipes were largely fed by gas sourced from Carboniferous coal.

According to Verweij et al. (2003) peak Carboniferous gas expulsion and migration occurred in the Early Cretaceous pre-inversion time. Breaching of the Zechstein seal during inversion allowed vertical escape of gas towards Vlieland Sandstones. The morphologies of pipes and generation of Carboniferous gas point towards concentrated fluid flow syn-rift/pre-inversion, prior to formation of concentric faults. Reactivated faults on anticline α may have leaked gas out of the reservoir that was charged by flow along deeper listric faults during inversion.

Slip tendency data indicate that the greatest amount of slip will occur in vertical channels (Figs. 4.17 - 4.20). Discrete, vertical patches of high slip tendency coincide with the formation of fluid escape pipes above the listric faults. Figure 4.12 shows the escape pipes mainly clustered between the two listric faults. This diagram only shows the faults at a single horizon, although the arrows indicate the faults dipping below base of the fluid escape pipes. Large vertical pipes can also be seen rising from base of the listric faults in Figures 4.10 and 4.11. Pipe-like

fluid flow is more conductive than flow along a planar surface (Blenkinsop, 2004). The combination of vertical fluid pipes associated with concentric faults and vertical patches of high slip tendency indicates that the whole length of the fault does not need to reactivate for it to be able to transmit fluid through a seal rock. Due to the high degree of segmentation, optimally oriented patches of the fault may fail and transmit fluids, whilst other parts of the fault remain inactive.

4.8.3. Implications for CCS and EOR

Both CCS and EOR require injection of high pressured fluids into the subsurface. This study explores the possibilities of CO_2 storage in post salt reservoirs and recovering unconventional oil from Posidonia Shale. Current efforts into the capture and storage of CO_2 offshore Netherlands include the P18-4 gas field ROAD (Rotterdam Capture and Storage Demonstration) Project, which is planning to store ~5 Mt CO_2 in the Main Buntsandstein Subgroup over 5 years (Arts et al., 2012). Injection pressures are expected to be maintained at 35 MPa for the duration of the project.

At an average fault depth of 1500 m, pore fluid pressures of 25 MPa are sufficient to induce slip on optimally oriented fault surfaces; at 30 MPa, most fault orientations will likely fail. The Vlieland Sandstone (a possible reservoir for CO_2 storage) is competent and faults are unlikely to reactivate even at P_f = 30 MPa, whereas in shales at 2400 m depth, new faults can form at P_f = 30 MPa (Fig. 4.21).

These estimates are only representative of the main lithologies considered. With a resolution of ~10 m, small scale lithological changes are highly likely and will influence the C and ϕ.

Fault segmentation is common in this part of the Southern North Sea. The degree of segmentation in this area increases the variability of fault orientation along strike (Fig. 4.12). Leveille et al. (1997) discussed the relationship between orientation, timing and magnitude of deformation relative to faults and their sealing ability. Thus, segmented concentric faults will have different sealing abilities along the horizontal fault trace (Kattenhorn and Pollard, 2001). When injecting CO_2 into the reservoir that is compartmentalised by fault segments, the pore fluid pressure would increase in a single compartment, but would not in other compartments (Kattenhorn and Pollard, 2001, Leveille et al., 1997). Therefore the slip tendency would depend on where the gas was being injected. The model presented in this chapter does not take into account the compartmentalisation of the reservoir, which could have major implications on the slip tendency and thus the location of CO_2 injection.

Alternatively, the locus of fault segment linkage may increase the permeability of the rocks. Where the fault segments interact, active fracturing provides a pathway for fluids (Curewitz and Karson, 1997). The highest concentration of fault-segment linkage is in the low permeability Rijnland and Chalk Groups (Figs. 4.7 and 4.12), which are the expected seal units for the

Delfland Subgroup and Vlieland Sandstone reservoirs (Bouw and Essink, 2003). Though these faults occurred after the fluid pipe generation, future vertical migration of fluid through the interaction zones is possible if there is any of reactivation along the fault whilst injecting CO_2. Concern for failure of seal cutting faults during pore fluid pressure increases may explain why no wells have been drilled into, or south of, anticline α.

4.9. Chapter specific summary

The main conclusions of the study are:

- Concentric faults with a normal offset developed contemporaneously with regional compression. Local stresses did not represent the overall stress regime in the Southern North Sea during their evolution. One set of faults adjacent to the salt diapir formed in response to local extensional stresses. Salt was withdrawn around the diapir and a rim syncline started to subside, creating new extensional faults as the strata bent into the minibasin. Concentric faults on an inversion anticline (anticline α) are closely related to deeper raft bounding faults, with differential subsidence creating extension about the raft boundary.

- Growth histories of concentric faults can be complex, with vertical linkage from multiple phases of reactivation during inversion and horizontal segment linkage via lateral propagation. Fault segment linkage can increase the curvature of faults as each segment curves towards the propagating larger fault.

- Slip tendency analyses shows patches of high slip along parts of the fault that are optimally oriented with respect to the present day stress field, increasing the chances of fluid leakage. The heterogeneity of fault slip along strike increases with the length and curvature of a fault, making evaluation of each individual fault necessary. Sub-vertical patches of high slip tendency along a single fault occur near vertical fluid pipes. Variations in lithology and depth of faults have a strong influence on the slip tendency and the failure profiles. Even at depth, faults cross-cutting the Posidonia Shales are much more likely to reactivate than those within shallower sandstones as pore fluid pressure increases.

- Fluid escape features found on 3D seismic data provide evidence for vertical migration of fluids from Carboniferous Gas reservoirs. Overpressured conditions in these reservoirs occurred most recently during the Late Jurassic allowing fluid to flow to the

surface and form pockmarks and mud volcanoes, indicating that most fluid pipes are palaeo-features.

- In anticline α, where the Vlieland Sandstone reservoir is still preserved, concentric faults cut through the strata and create a pathway for fluids to leak. Faults are unlikely to reactivate at pore fluid pressures < 30 MPa in the sandstones, however, they may reactivate within the chalk seal above. Although faults may provide pathways to fluid flow, they can also compartmentalise a reservoir. If this is the case, then an increase in pore fluid pressure on one fault might not have the same effect the other side of the fault.

- Storage of CO_2 in Block K15 is possible at pore fluid pressures similar to those being implemented in the Southern North Sea (Arts et al., 2012). To ensure no faults are reactivated and transmit fluids, pore fluid pressures will have to remain <30 MPa. Faults studied here are highly segmented, and the locus of segment interaction can provide a suitable pathway for seal bypass.

CHAPTER FIVE

Differential compaction over Late Miocene submarine channels in SE Brazil: Implications for trap formation

An abridged version of this chapter has been published as:

Ward, N.I., Alves, T.M. and Blenkinsop, T.G., 2018. Differential compaction over Late Miocene submarine channels in SE Brazil: Implications for trap formation. *GSA Bulletin*, 130(1-2), pp.208-221.

Co-author contributions to the paper:

Tiago Alves – checked for grammatical errors, ensured the scientific content was accurate and appropriately presented.

Thomas Blenkinsop – checked for any errors in the theme of structural geology, provided feedback on paper.

5. Differential compaction over channel-fill deposits

5.1. Abstract

High-quality 3D seismic data are used to quantify the timing and magnitude of differential compaction over a Lower Miocene submarine channel complex in SE Brazil (Espírito Santo Basin). A thickness-relief method is applied to quantify the thickness variations in strata deposited over the channel complex. It was found that differential compaction started after the channel complex was buried by ~200 m of strata, as revealed by thinning horizons observed over a compaction-related anticline (anticline C^1). The size of anticline C^1 is greatest in the south of the study area, reaching heights of 41 ms (~50 m). Fluid expelled through faults on the margins of the channel complex formed large depressions. These depressions increased in size after deepwater currents removed the fluid-rich sediment filling them. Differential compaction also occurred over deposits downslope of knickpoints, reaching maximum heights of 29 ms (~35 m). Seismic reflections onlap the knickpoint face and are believed to comprise slumped strata and debrites. Two-way-time isochron and amplitude maps indicate that there is limited connectivity and lateral continuity of the coarse-grained units. Differential compaction over these deposits created anticlines with four-way dip closure. As a consequence, isolated reservoirs are closed vertically by the compaction anticlines and laterally by strata onlapping the knickpoint face. These unique reservoirs could have been charged by migration of hydrocarbons

along sands at the base of the channel complex. A fill-to-spill model is hypothesized using the above mechanism: once an isolated anticlinal trap has reached spill point, hydrocarbons migrate upslope into the next trap. Traps like these could form above submarine channels in similar basins around the world (e.g. Gulf of Mexico, west coast of Africa) after early burial.

5.2. Introduction

Compaction of sediments during the early stages of burial is closely related to lithology and water content (Athy, 1930, Trask, 1931). All porous sediments tend to compact under increasing burial depth, with the greatest amount of compaction occurring in intervals with the highest porosity (Perrier and Quiblier, 1974). Consequently, clays and shales compact more than sandstones and conglomerates, a phenomenon leading to differential compaction (Trask, 1931, Perrier and Quiblier, 1974, Clark and Pickering, 1996, Cosgrove and Hillier, 1999, Posamentier, 2003, Chopra and Marfurt, 2012). Structures associated with differential compaction commonly include anticlines over the less compacted lithology (Heritier et al., 1980, Cosgrove and Hillier, 1999, Posamentier, 2003, Alves, 2010, Chopra and Marfurt, 2012). This chapter examines compaction-related anticlines over a submarine channel complex, particularly those formed over coarse-grained sediment bodies deposited

downstream of knickpoints, where marked increases in the gradient of the channel complex are observed (Howard et al., 1994, Heiniö and Davies, 2007).

Positive relief structures that are concomitant with differential compaction over sandy intervals form very effective hydrocarbon traps. Many producing fields around the world present these types of feature, particularly in the North Sea (Heritier et al., 1980, Cosgrove and Hillier, 1999, Corcoran, 2006), Canada (Wood and Hopkins, 1989, Wood and Hopkins, 1992) and SE Brazil (Davison, 1999). Coarse-grained strata with high reservoir potential and low compaction rates are usually bounded laterally and vertically by less permeable, fine-grained sediment. This forms an effective seal for hydrocarbon reservoirs, which become stratigraphically and structurally trapped after compaction (Corcoran, 2006). However, a key problem faced when drilling compaction-related structures is the local development of overpressure in porous intervals. When compaction does not keep pace with sedimentation rate, fluids preferentially migrate towards permeable sands, creating local overpressure conditions (Osborne and Swarbrick, 1997). If pore pressure in the sand increases above the lithostatic pressure, the overburden fractures, allowing fluids to escape from potential reservoir intervals and migrate towards the surface (Gay et al., 2003, Davies, 2003).

Previous studies have focused on the seismic expression of differential compaction structures, their potential for forming hydrocarbon traps, and the

causes for overpressure and fluid expulsion (Gay et al., 2006a, Cosgrove and Hillier, 1999, Chopra and Marfurt, 2012, Corcoran, 2006, Xu et al., 2015). Most of these studies provide qualitative data on large, discrete structures. This chapter uses a 3D seismic data set from Espírito Santo Basin, SE Brazil, to quantify the magnitude and timing of differential compaction over a submarine channel complex, and over strata deposited downslope of knickpoints (Fig. 5.1). A thickness-relief method, modified by Alves and Cartwright (2010) from Perrier and Quiblier (1974), was used to quantify the topographic expression of compaction-related anticlines and assess when differential compaction was initiated. The findings were supported with variance, amplitude, and thickness maps (described in *section 3.1.3*). This chapter thus attempts to answer three key research questions:

a) What is the magnitude and timing of differential compaction over channel-fill deposits?

b) What are the main factors controlling differential compaction over the channel complex and knickpoints?

c) What effect does differential compaction have on trap formation?

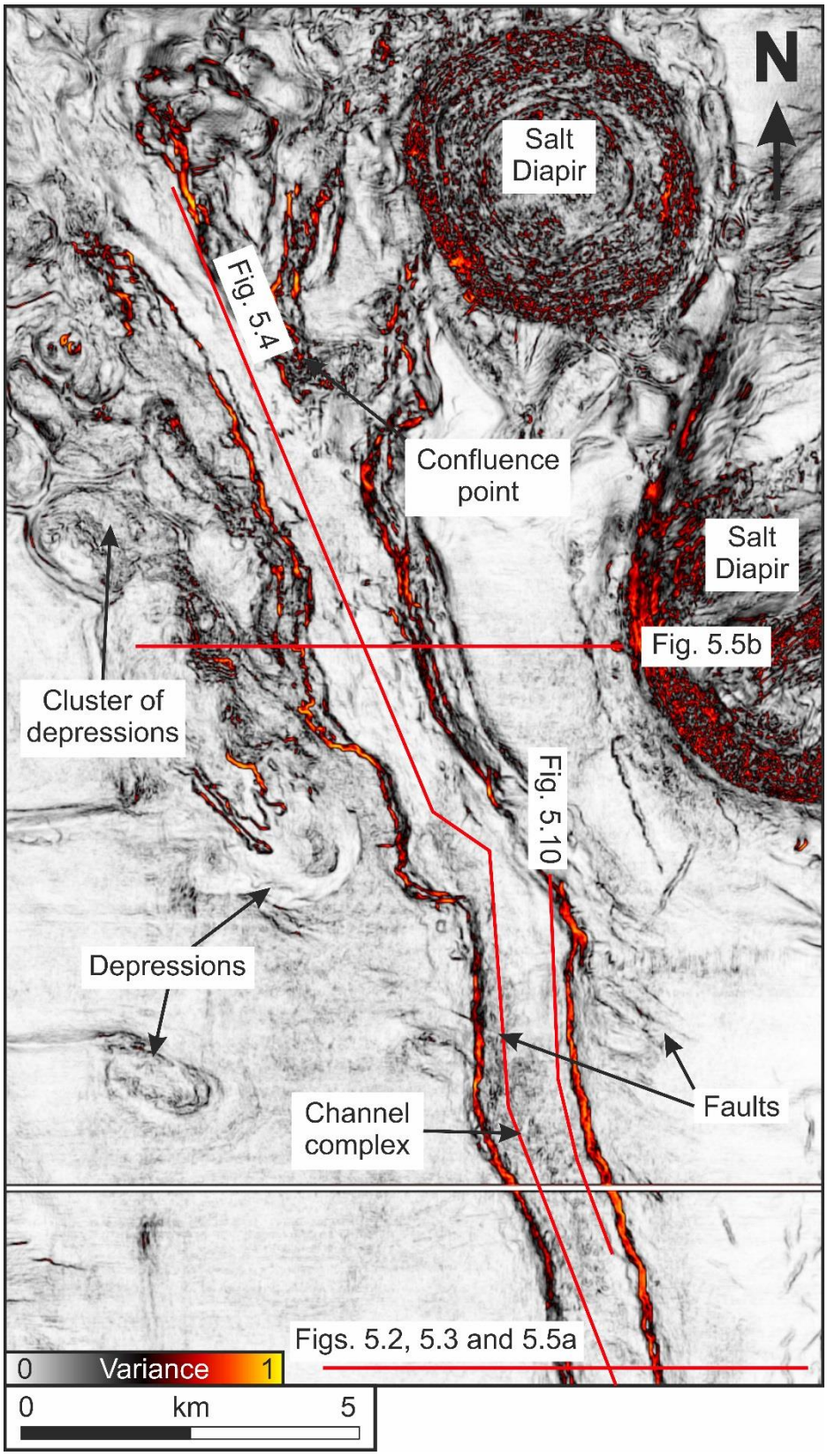

Fig. 5.1 Variance time-slice flattened along horizon D_1 so as to remove the gradient of the continental slope and visualise all key geological features. These features are identified by high variance contrasts and are duly labelled.

5.3. Chapter specific data, methods, and settings

The dataset used for this chapter is the BES-2 three-dimensional volume from the Espírito Santo Basin, SE Brazil. Full details of the acquisition and processing of the data can be found in *Chapter 3, section 3.1.1.2.* A detailed description of the seismic resolution is also provided.

Depth is measured as two-way time (TWT) in this data set. No accessible wells have been drilled in the study area, so any depth conversions are based on an average velocity due to abrupt changes in lithology both vertically and horizontally around the submarine channel complex (Figs. 2.5, 2.6 and 5.2).

The thickness-relief technique (described in *Chapter 3, section 3.3.2.*) is used to quantify the degree and relative timing of differential compaction over a submarine channel complex. Pitfalls in this method lie with inaccurate picking. Disrupted and transparent reflections (common among MTCs) lead to anomalous thickness measurements. Therefore, the method was conducted six times along the channel, using > 15,000 measurements each time. The 'D' value was also used to reduce the error of poorly-picked horizons (see *Chapter 3, section 3.3.2.*), which compares the measured thickness to the average thickness of that seismic reflection.

The mean thickness was calculated using up to 791 measurements of each horizon on a cross section of the channel complex. The measurements were taken 1400 m either side of the channel complex axis. By subtracting the mean thickness

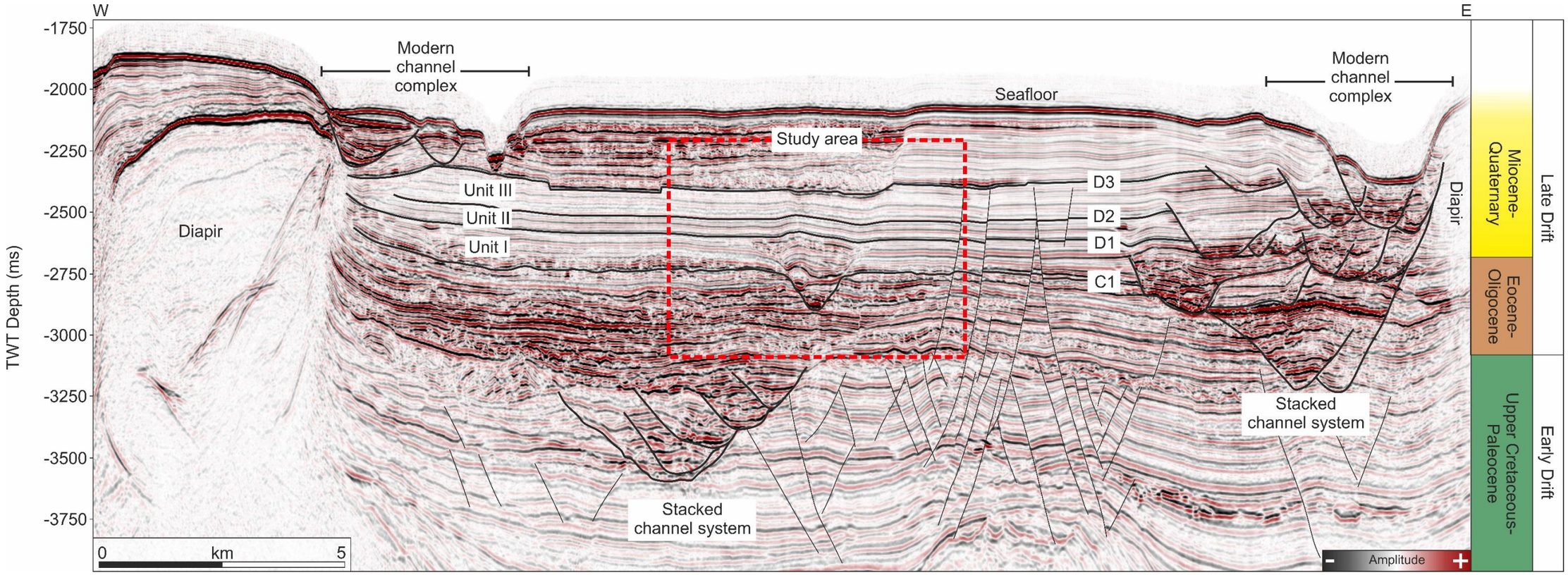

Fig. 5.2 Seismic profile of the BES-2 survey. The study area for this chapter is highlighted by the red box, and important horizons are labelled. Key stratigraphic markers on the seismic data were correlated with regional tectonic phases and with the chronostratigraphic column to the right of the figure. This was aided by the interpretations in França et al. (2007), Alves et al. (2009) and Gamboa & Alves (2015), as well as in Figure 2.5. The location of the seismic line is provided in Figure 5.1. TWT – two-way traveltime.

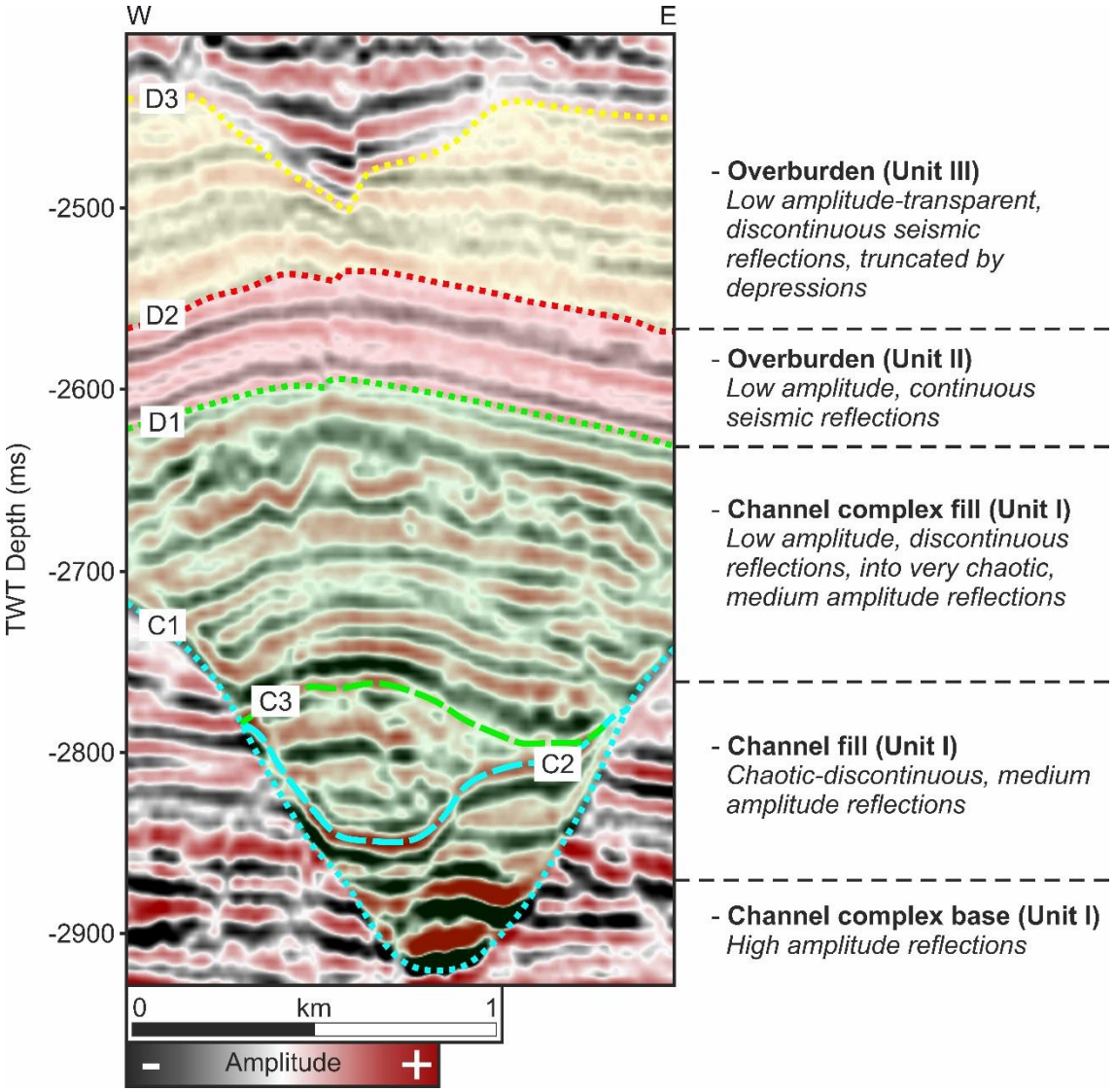

Fig. 5.3 Summary of the different seismic-stratigraphic units interpreted in this chapter. Each seismic-stratigraphic unit contains a description of seismic facies, and corresponding horizons at their tops and bases. These are: C_1 – base of the channel complex; C_2 – base of channels; C_3 – top of channel fill; D_1 – top of channel complex fill and top of Unit I; D_2 – top of Unit II where seismic reflections are still equal thickness; D_3 – top of Unit III where seismic reflections thin on the crest of anticline C^1. TWT – two-way travel time.

from the measured thickness on a single horizon, a direct comparison is made between units of different sizes. Interpretation of the graphs has been aided by dividing the channel complex into three different units (Fig. 5.3).

Vertical thickness maps were created in Schlumberger's Petrel© to compliment the analyses of differential compaction. The vertical thickness between successive reflections were calculated, displayed as red (thick) to purple (thin).

The study area is situated above the Rio Doce Canyon System (RDCS) on the southern bank of the Abrolhos Plateau (Fiduk et al., 2004) (Figs 2.4 and 2.5). The RDCS has been evolving since the Late Cretaceous and eight distinct episodes of canyon incision and deposition of mass-transport complexes (MTC's) have been identified (Alves et al., 2009, Fiduk et al., 2004). Canyon incision is believed to have been most active from the Late Eocene to the Oligocene, correlating with third-order lowstand system tracts (Alves et al., 2009). Two NNW-SSE oriented salt ridges have entrapped the RDCS, causing important mass-wasting events (Gamboa et al., 2011, Gamboa et al., 2010, Alves, 2010). These sandy turbidite fairways form potential reservoirs along the intermediate parts of the slope (Alves et al., 2009). This study focusses on a single channel complex cutting through early Miocene age hemipelagites, with differential compaction occurring above the channel sands (Fig. 5.1).

5.4. Internal character and geometries of channel and seal units

This chapter uses the hierarchal classifications for submarine channels described by Clark and Pickering (1996), Mayall et al. (2006), Di Celma et al. (2011), Abreu et al. (2003), McHargue et al. (2011), Gardner et al. (2003). Single channel-fill elements produced by incision and subsequent filling are referred to as 'channels'. Stacking of two or more channels with a similar architectural style and facies are called 'channel complexes'. Channels are bound by 4th or 5th order surfaces, whereas a channel complex is bound by 3rd order sequence boundaries (Mayall et al., 2006, Clark and Pickering, 1996). The interpreted channels have limited downslope connectivity and an irregular base (Fig. 5.4).

5.4.1. Miocene channel complex

The interpreted submarine channel complex trends north to south and has an average depth of 880 ms (approximately 800 m) below the sea floor. The maximum width of the channel complex is ~1650 m and its maximum vertical thickness is 376 ms (Fig. 5.5a-b). Amplitude extraction between horizons C_1 and D_1 (Unit I) highlights the main pathways of the channel complex (Fig. 5.6). The high amplitude indicates coarse-grain siliciclastics were deposited along its axis

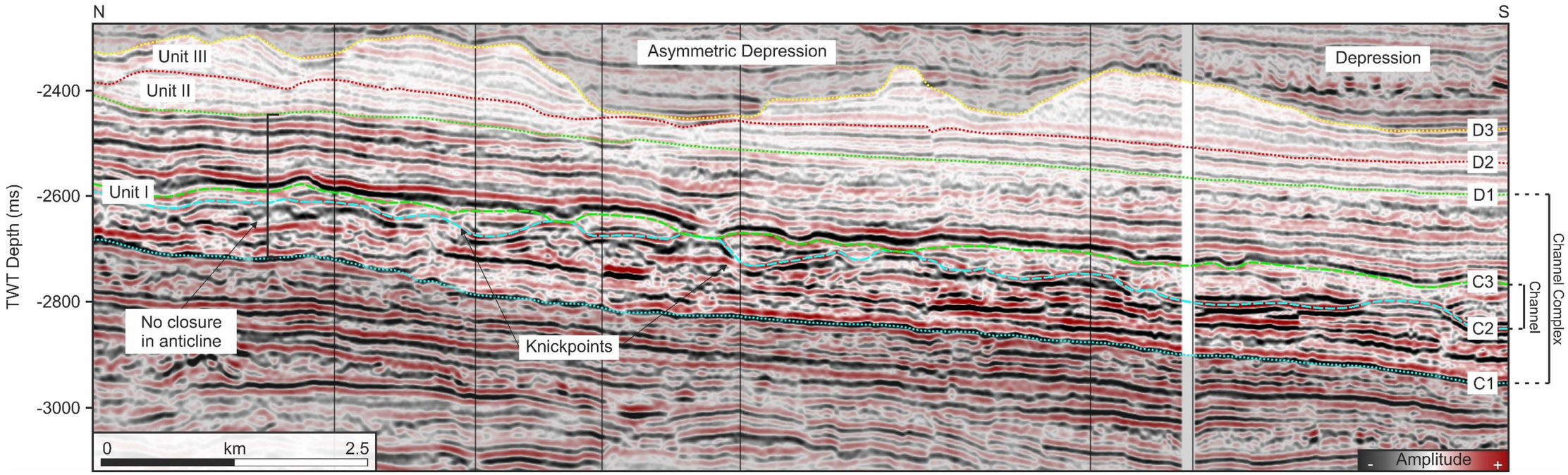

Fig. 5.4 Seismic profile along the axis of the submarine channel complex in the Espírito Santo Basin. Knickpoints along the base of the channels, and associated compaction anticlines, are highlighted. Asymmetric depressions are also apparent above unit III. The location of the seismic line is provided in Figure 5.1.

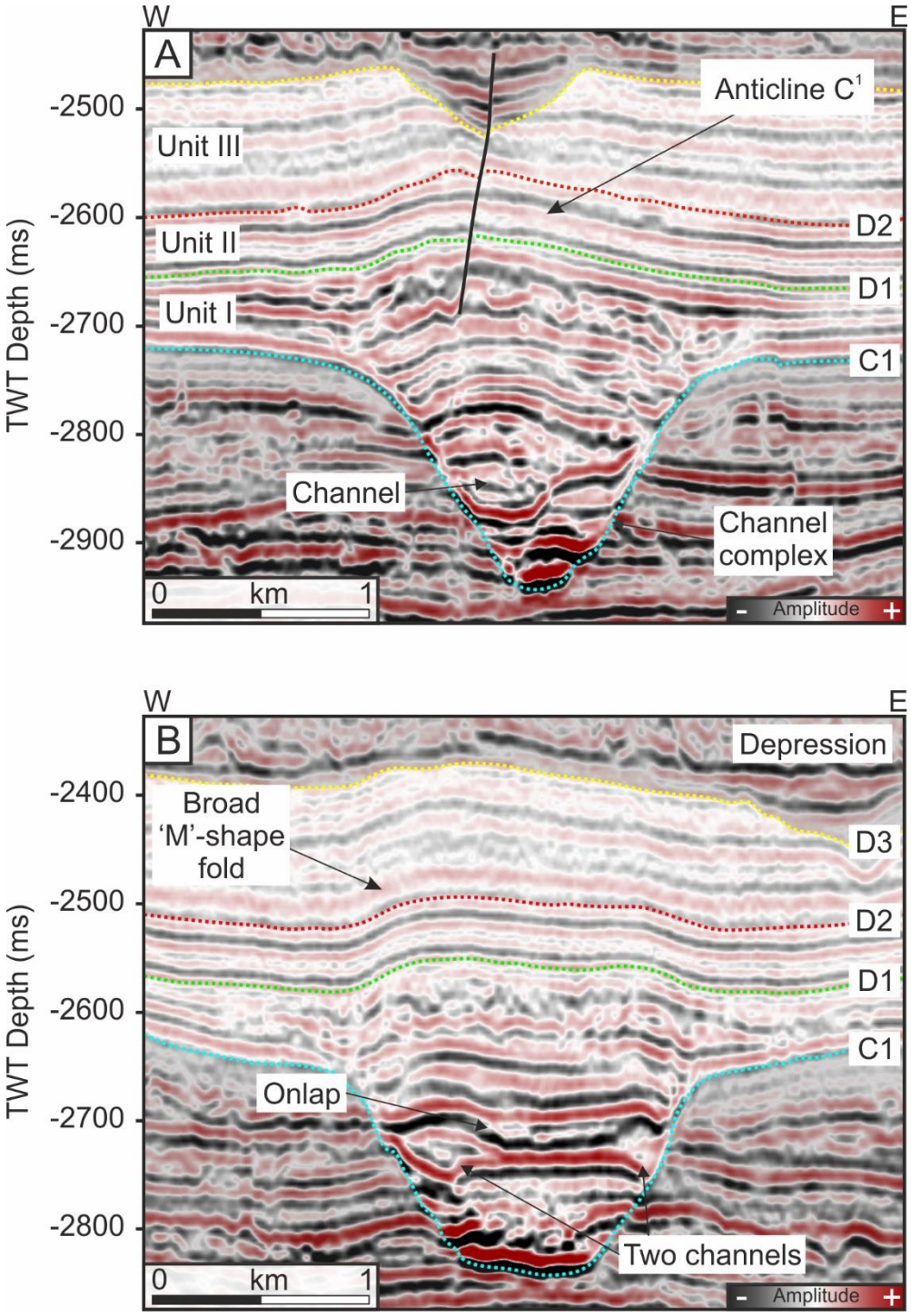

Fig. 5.5 a) Seismic profiles across the southern part of the channel complex in the Espírito Santo Basin, SE Brazil. Differential compaction is prominent here. A depression and associated fault cut through strata deposited over the channel complex. b) Seismic profile through the centre of the channel complex. Here, the smaller channels control differential compaction and a broad "M-shaped" fold has formed in anticline C^1. The locations of both seismic lines are provided in Figure 5.1.

(McHargue and Webb, 1986, McHargue et al., 2011, Posamentier, 2003). The channel complex is filled with low amplitude, discontinuous seismic reflections indicative of turbidite deposits (Fig. 5.3). Seismic reflections in the overbank units decrease in amplitude upwards, indicating a transition towards more homogeneous mud deposition as the levees were buried (Posamentier, 2003, McHargue and Webb, 1986). Unit I comprises the channel complex-fill described above. It is bounded at the base by horizon C_1 and at the top by horizon D_1, and increases in thickness towards the south of the study area (Figs. 5.3 and 5.7). Henceforth, the channel complex thickness is a measure of the vertical thickness of Unit I (Fig. 5.4).

5.4.2. Channels and knickpoints

Smaller channels are confined in the channel complex (Figs. 5.4 and 5.5). The channel thalwegs (ranging from 100 m – 400 m wide and up to 100 ms thick) follow the same path as the channel complex and occur close to the channel walls (Figs. 5.8 and 5.9). In cross-section, the channels are asymmetrical (steeper on the side closest to the channel complex margin), and do not exhibit stacking patterns (Figs. 5.5a and b). They are typically located down-dip of knickpoints (Figs. 5.4 and 5.10). Channel width is smallest at the knickpoint and increases downslope, where deposition occurs (Fig. 5.8). Gradients over the knickpoints reach 24°, contrasting with an average gradient along the base of the channels of <2° (Figs.

5.4 and 5.10). Immediately downslope of the knickpoints, seismic reflections are chaotic, reflecting the presence of MTCs (Alpak et al., 2013) (Fig. 5.10). They onlap the knickpoint face, and become more continuous downslope. Although chaotic, the channel fill downslope of the knickpoints have higher amplitudes than the surrounding material (Fig. 5.9). There is a lack of connectivity and lateral continuity between these sections of channel fill; isolated pods are therefore localized in areas of greatest incision and deposition (Heiniö and Davies, 2007) (Fig. 5.10).

5.4.3. Seal units

The top of the channel-fill deposits is represented by chaotic and discontinuous seismic reflections that pinch out laterally towards the margins of the channel complex (Figs. 5.3 and 5.5). The seismic reflections are convex-up and display evidence of differential compaction above the submarine channel complex (Fig. 5.5). The units above these chaotic seismic reflections are continuous and of low amplitude (Fig. 5.3). These low amplitude seismic reflections are thought to represent muds deposited uniformly over the whole channel complex. There is a change to more transparent, discontinuous reflections 65 ms above the channel complex, believed to be more homogeneous muds (Fig. 5.3). Unit II is measured from horizon D_1 to horizon D_2 (Fig. 5.2). Reflections in Unit II have the same amplitude, continuity and thickness as each

other. The boundary between the continuous and disrupted reflections (D_2) marks the transition from Unit II to Unit III.

5.5. Seismic geometries related to differential compaction

Convex-up structures (*e.g.* anticline C^1) occur within and above the studied submarine channel complex (Fig. 5.5). Observations made using the 3D seismic reflection data help explain the processes behind the formation of the anticlines and the relative timing of folding.

Fig. 5.6 (*next page*) Maximum-amplitude map of unit I (between horizons C_1 and D_1). The highest-amplitude reflections are located on the outer bends of the submarine channel complex. They are good indications of sand.

Fig. 5.7 (*in 2 pages*) Two-way traveltime (TWT) isochron map of the submarine channel complex between horizons C_1 and D_1. Thickness increases downslope along the channel complex.

Fig. 5.8 (*in 3 pages*) Two-way traveltime (TWT) isochron map between horizons C_2 and C_3. Submarine channels are easily recognisable due to their greater thickness. The thickest segments of the channels are located downslope of knickpoints in association with a sudden increase in channel gradient. The thickest parts of the channels are concomitant with the widest parts of the channels.

Fig. 5.9 (*in 4 pages*) Maximum-amplitude map of the interpreted submarine channels (between horizons C_2 and C_3). The highest amplitudes are in pods located in the southern part of the channel complex. High-amplitude pods have limited continuity and are not laterally connected.

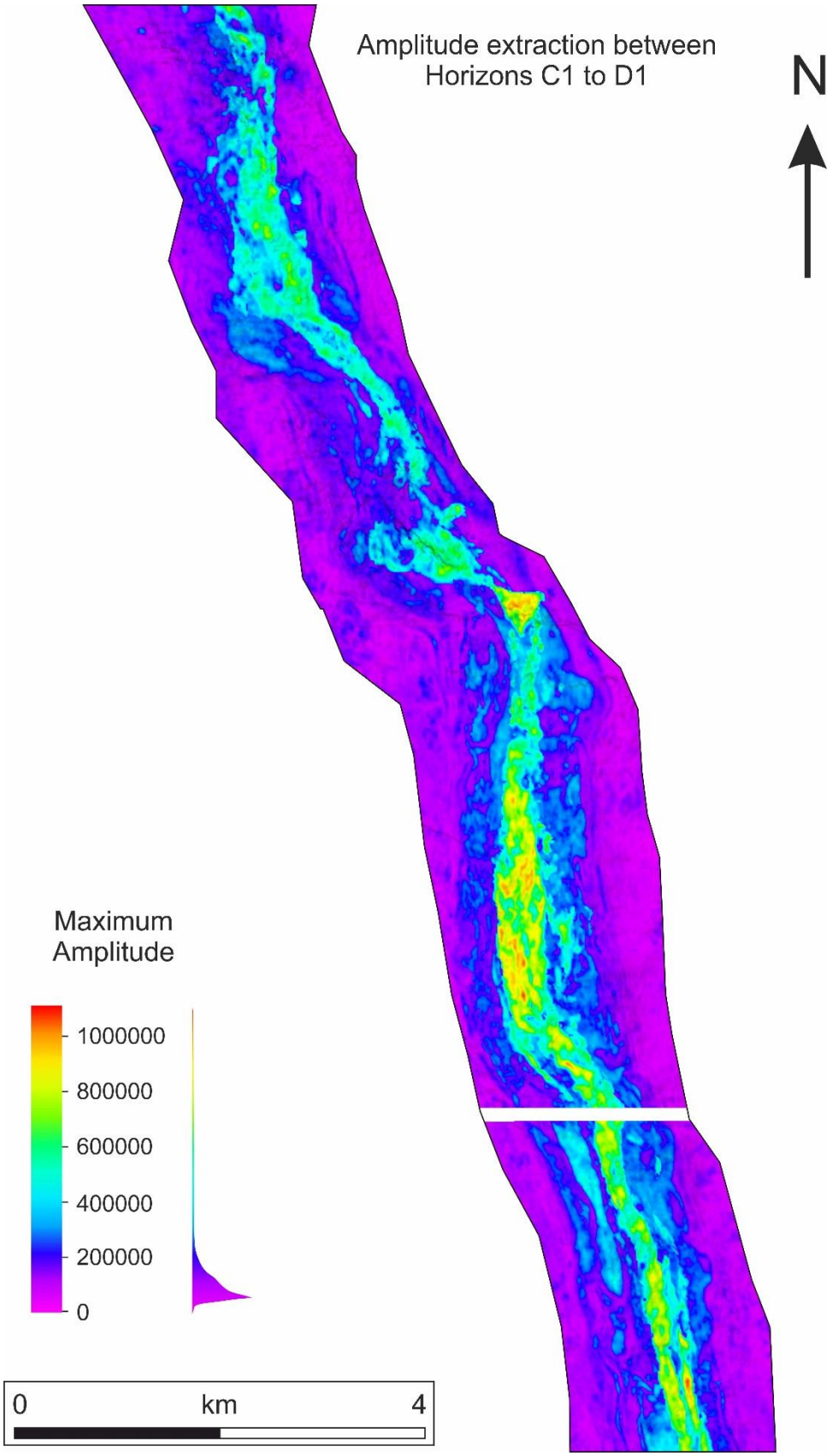
Amplitude extraction between
Horizons C1 to D1
N
Maximum
Amplitude
1000000
800000
600000
400000
200000
0
0
km
4

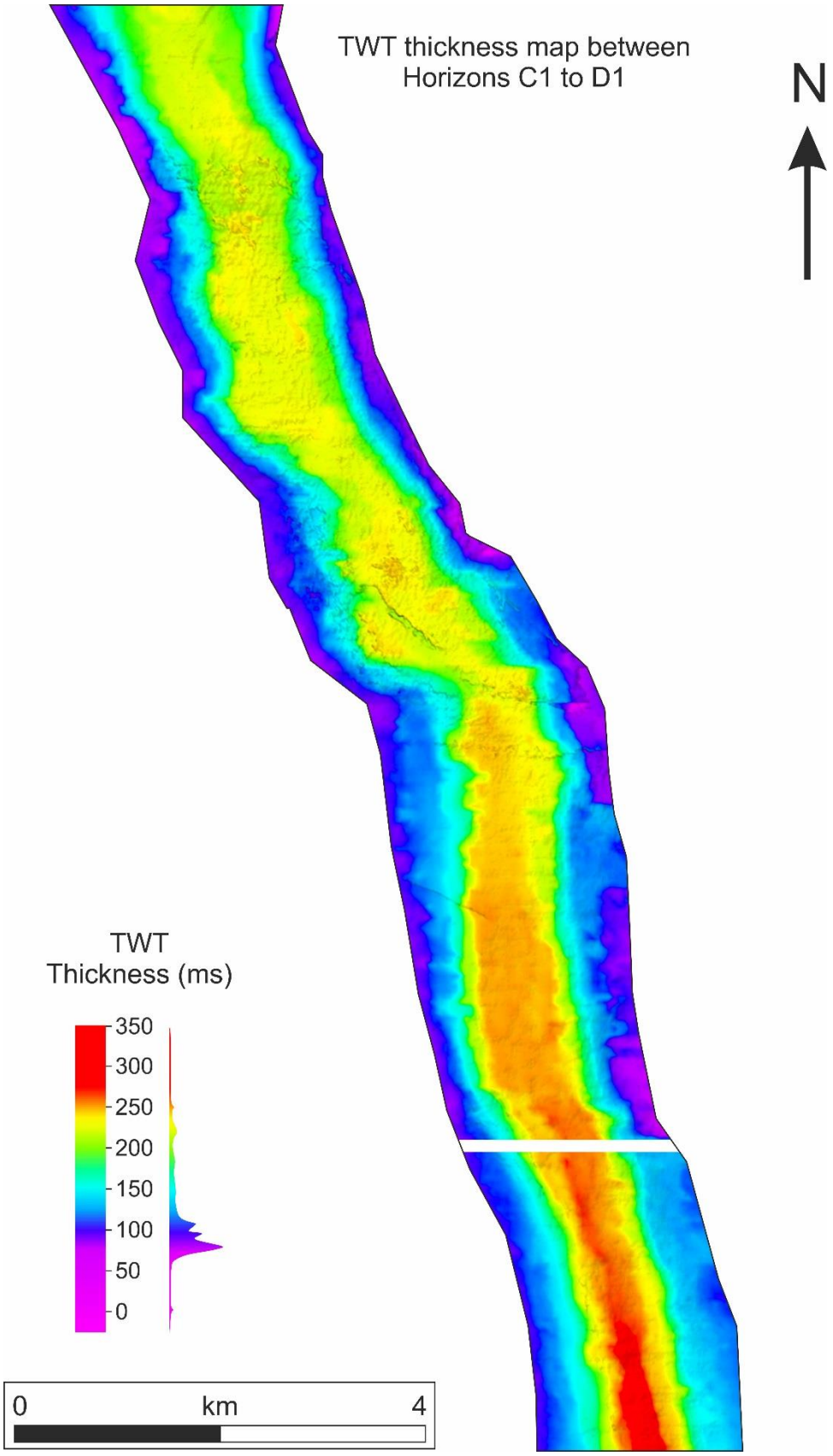
TWT thickness map between
Horizons C1 to D1
N
TWT
Thickness (ms)
350
300
250
200
150
100
50
0
0
km
4

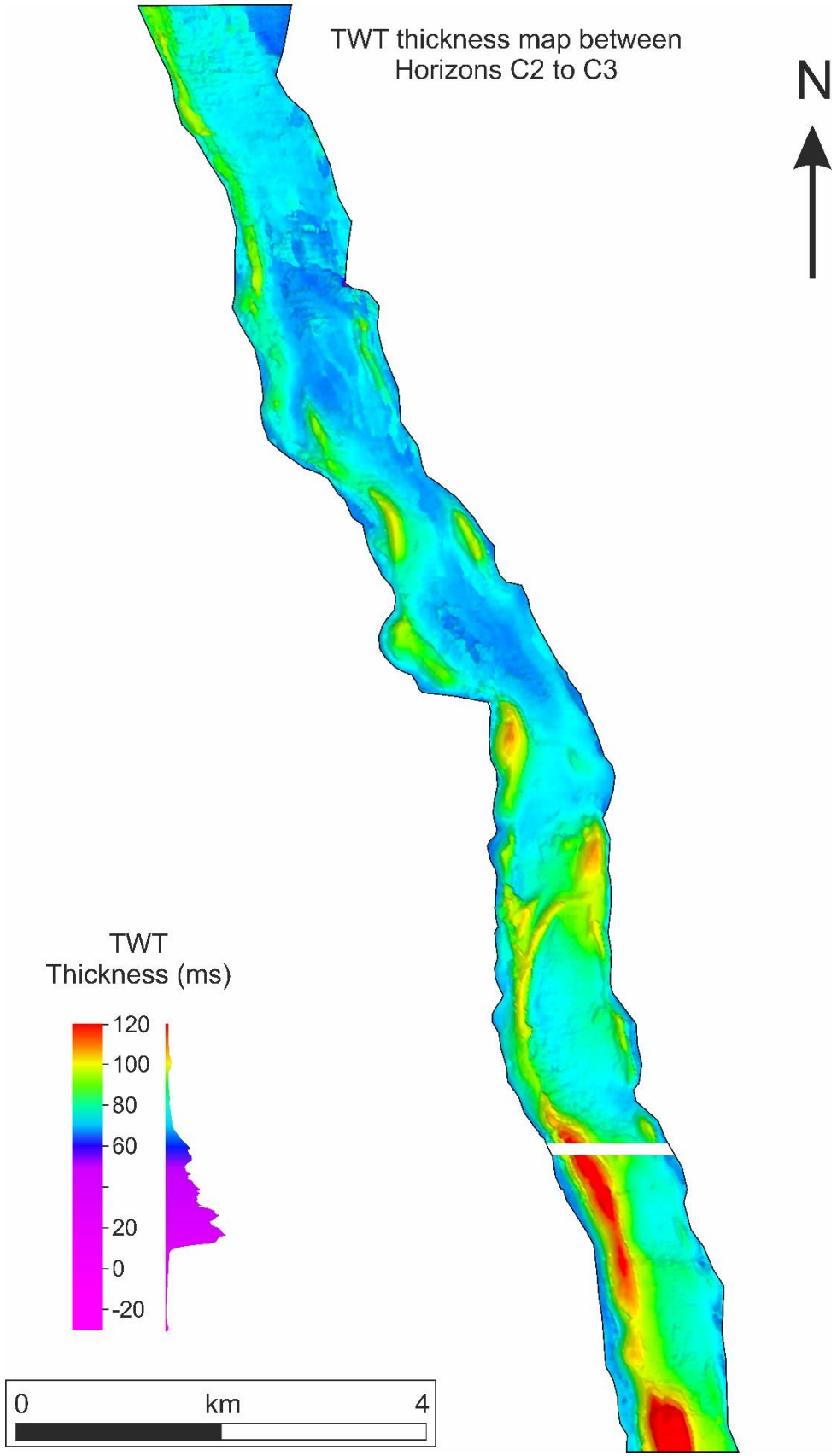
TWT thickness map between
Horizons C2 to C3
N
TWT
Thickness (ms)
120
100
80
60
20
0
-20
0
km
4

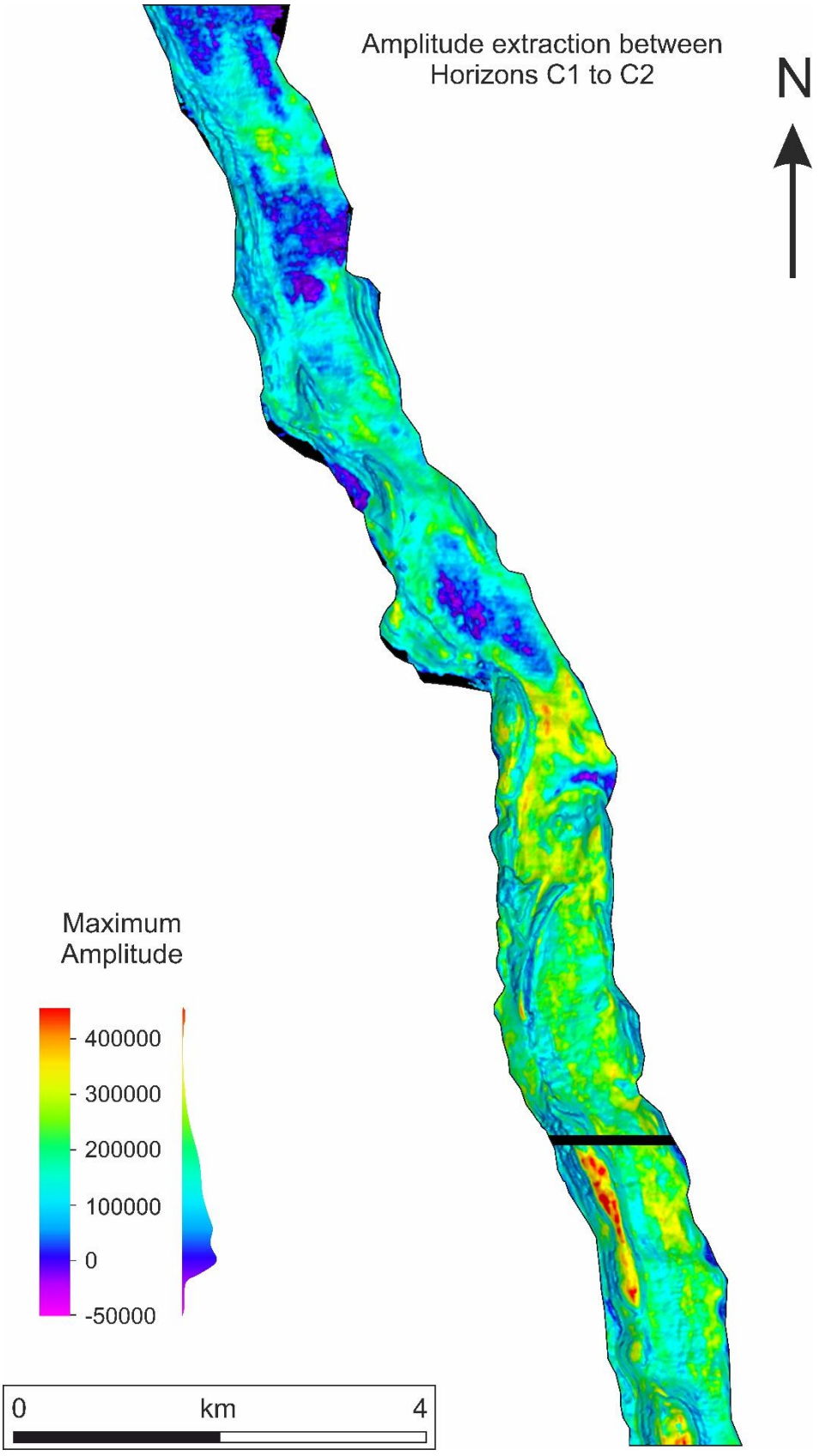
Amplitude extraction between
Horizons C1 to C2
N
Maximum
Amplitude
400000
300000
200000
100000
0
-50000
0
km
4

5.5.1. Compaction related traps

Two magnitudes of anticline are observed in the studied channel complex: a) at the scale of the channel complex forming in overburden strata (maximum height of anticline is 41 ms), b) at the scale of individual channels forming downslope of knickpoints (maximum height of anticline is 29 ms) (Fig. 5.5). The locations of the fold hinge in both examples suggests a close control of smaller channels on the loci of folding. Anticlines formed downslope of knickpoints have 4-way dip closures; they onlap C_2 both upslope and downslope of the channel fill, and also the margins of the channel complex (Figs. 5.5 and 5.10). Isolated 'pods' delineate the path of the channels within the channel complex (Fig. 5.8). The fold hinge of anticline C^1 lies directly above these pods. Seismic profiles show that the occurrence of channels either side of the channel complex gives anticline C^1 a broad 'M' shape, or a box fold (Fig. 5.5b), whereas a single channel, or pod, forms a single hinge in anticline C^1 (Fig. 5.4). Topographic expression of anticline C^1 must have occurred during early burial, as reflections within Unit I onlap anticline C^1 along horizon C_3 (Fig. 5.10). Accommodation space in the form of small depocentres, created by differential compaction, was later filled with sediment (Fig. 5.10). Seismic reflections within Units II and III are continuous along the fold axis, as there is no upslope or downslope closure (Fig. 5.4).

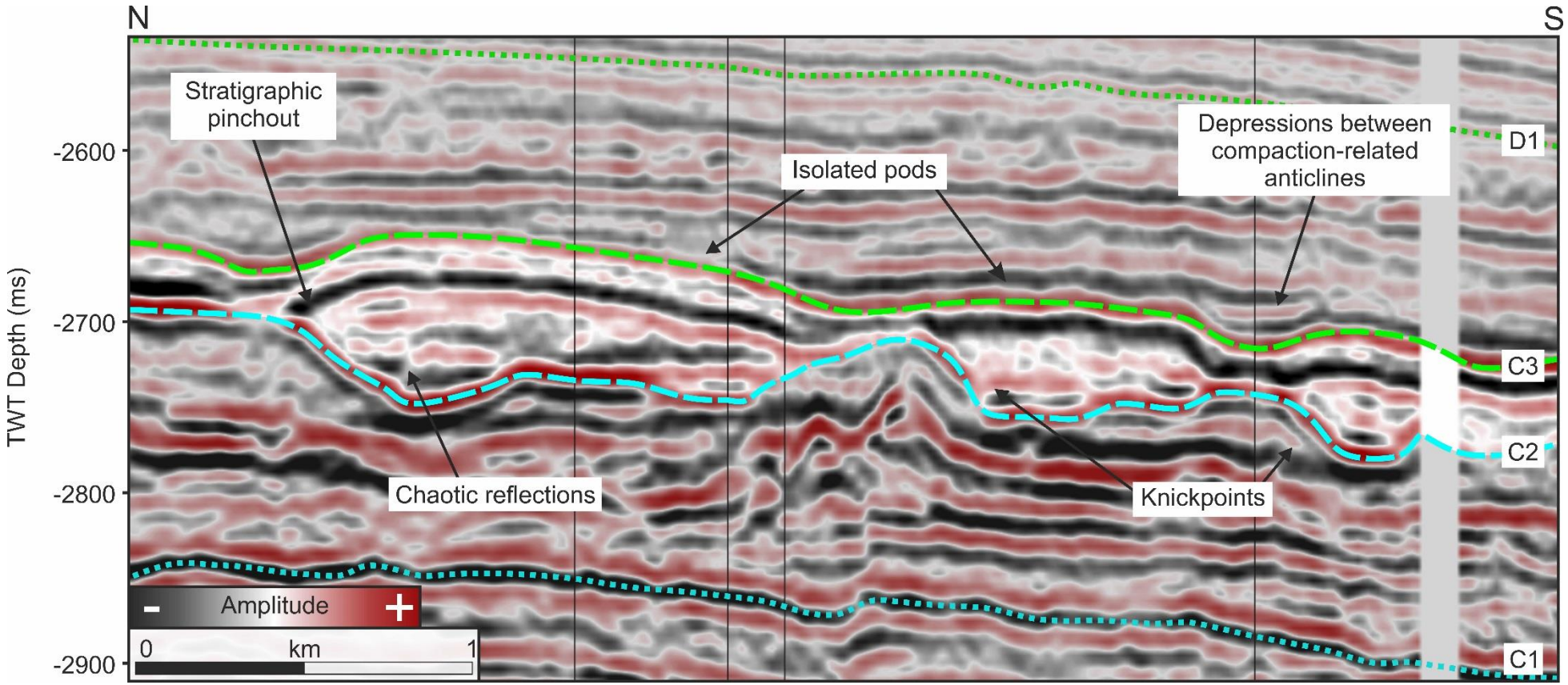

Fig. 5.10 Seismic line running along the axis of the submarine channel complex. This figure highlights the seismic facies typical of "pods" and the relationship among knickpoints, downslope deposits, and differential compaction.

5.5.2. Quantification of differential compaction

Using the thickness-relief method, graphs have been produced to compare thickness of Units I, II, and III (Figs. 5.11 – 5.13). Unit 1 thickens significantly towards the axis of the channel complex (Fig. 5.11). The D-value reaches a maximum of 27 ms. Above the margins of the channel, the D-value becomes negative, implying Unit I is thinner here (Fig. 5.11). This represents the boundary between more compactable mud in overbank deposits and less compactable sand in channel-fill deposits. Unit II has an equal thickness across the whole study area (~0 ms D-value) (Fig. 5.12). The only change is a decrease in thickness where erosional depressions occur in Unit II (Fig. 5.12). Analyses of differential compaction over Unit III were only conducted in the southern part of the study area. Towards the confluence point of the two tributaries, the unit has been eroded. The unit thins on the crest of anticline C^1 (up to 5 ms D-value), and increases in thickness away from the channel complex, reaching a maximum D-value of 4 ms (Fig. 5.13). Therefore, differential compaction initiated at the time Unit III was being deposited, and produced topographic relief on the seafloor. Sediment accumulated preferentially on the flanks of anticline C^1 where accommodation space had increased.

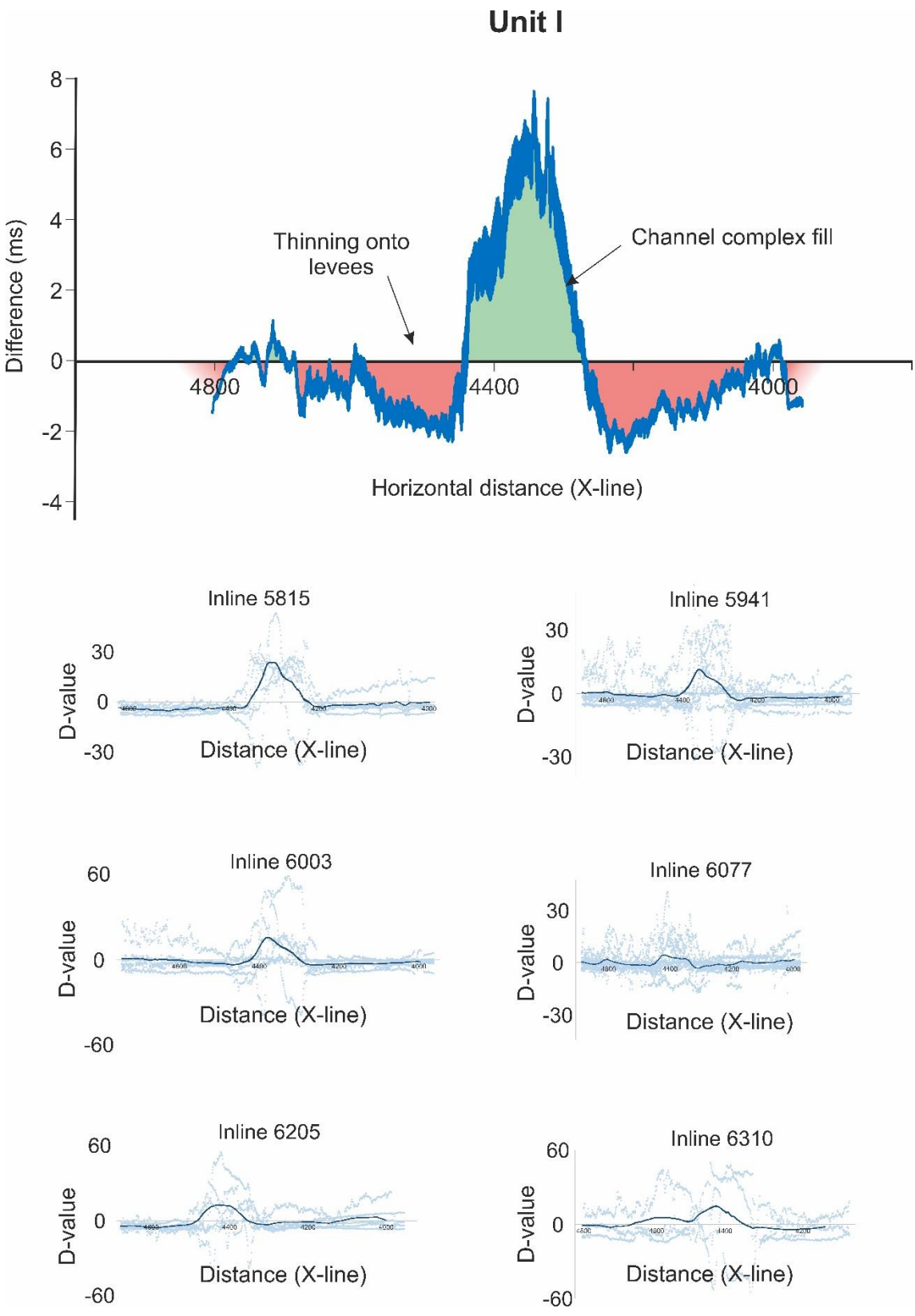

Fig. 5.11 Thickness-relief profile for unit I reflecting distance against the difference between the measured thickness and the mean thickness of a horizon (D-value). The maximum thickness is in the centre of the submarine channel complex in unit I. The channel complex is thinner on its margins. The graph at the top shows the average of all the other graphs below.

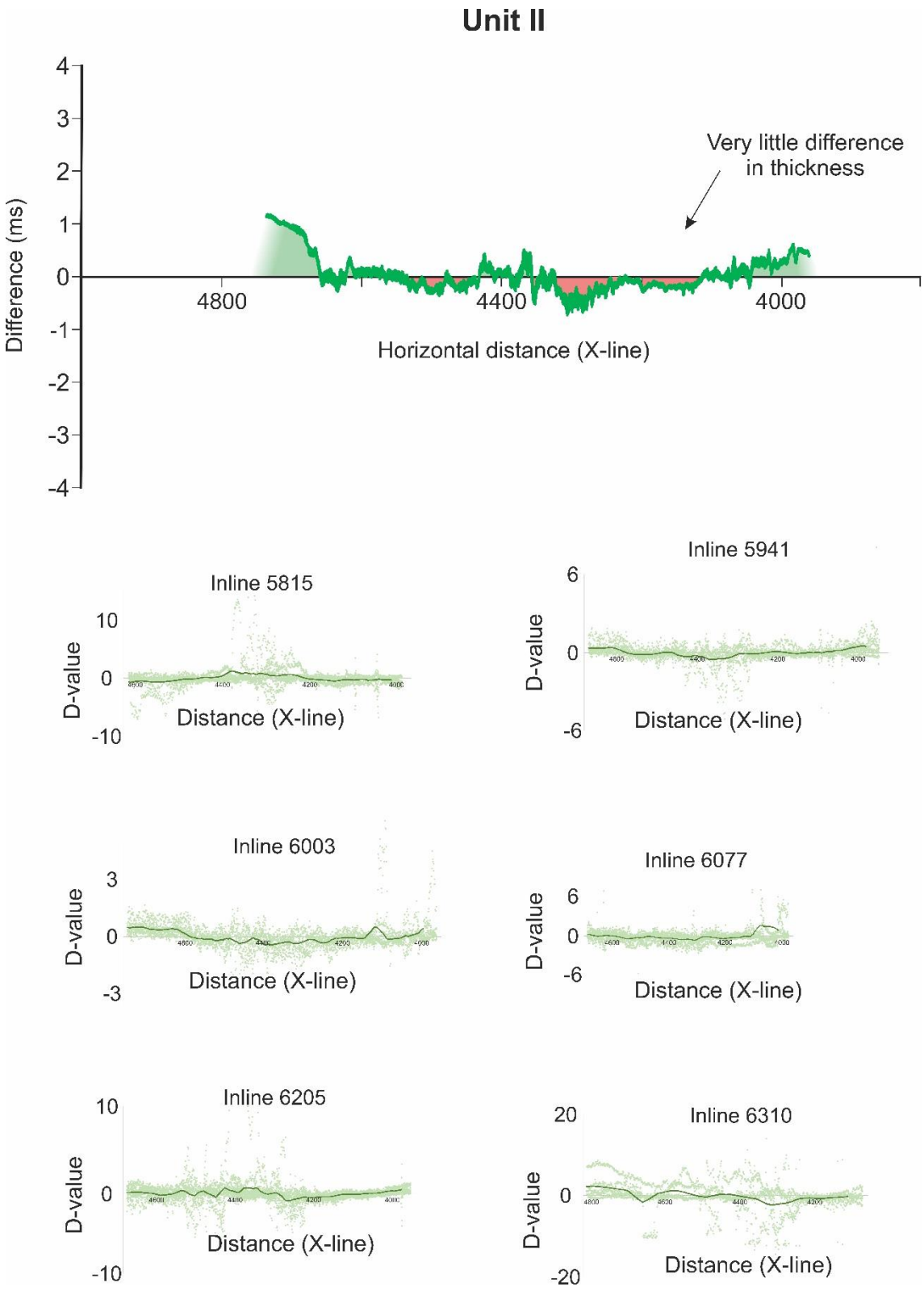

Fig. 5.12 Thickness-relief profiles for unit II. At this level, there is very little difference between the measured and mean thickness. The graph at the top shows the average of all the other graphs below.

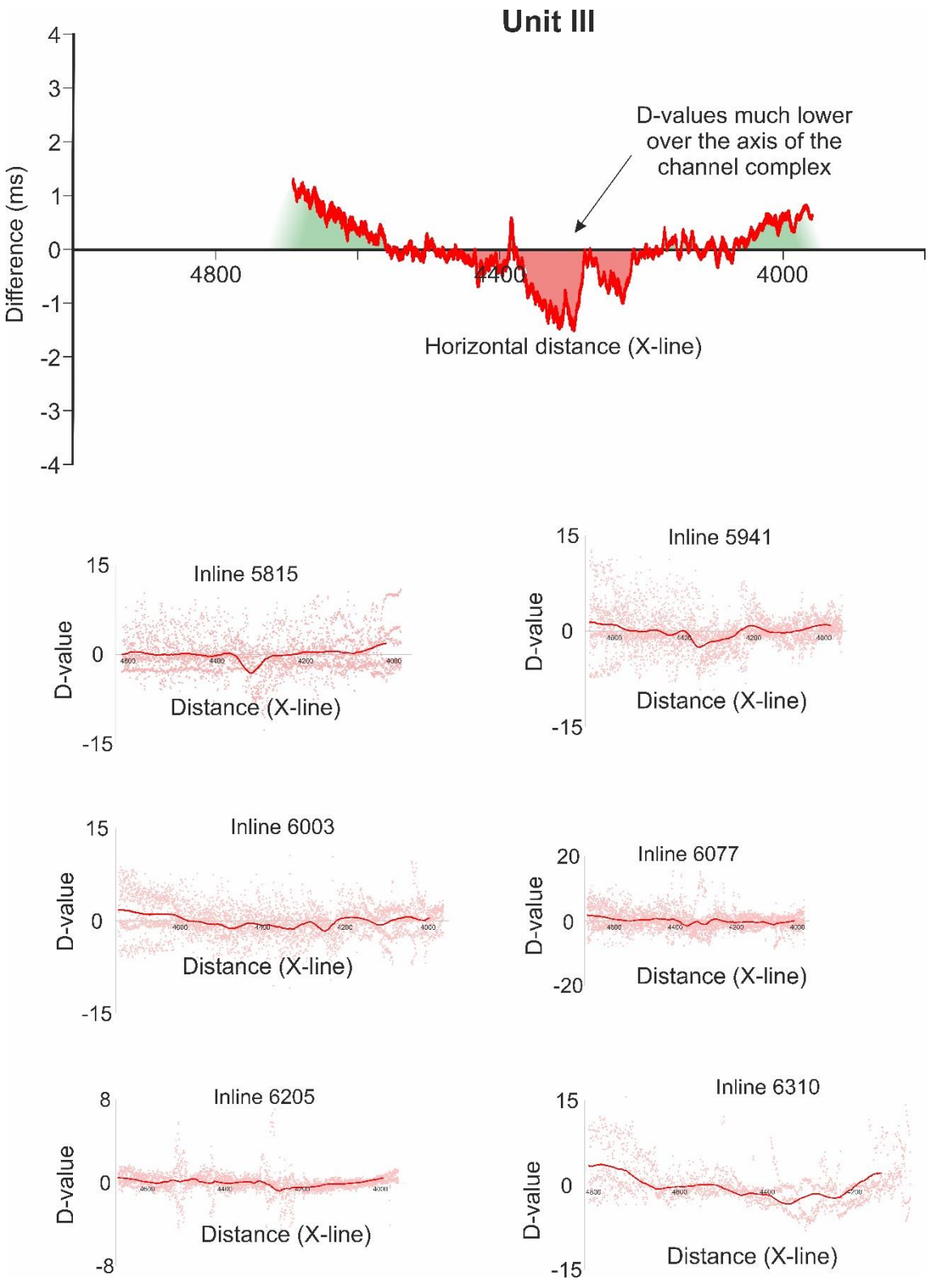

Fig. 5.13 Thickness-relief profile for unit III. Overburden strata show a lower measured thickness than the mean thickness (*i.e.* a lower D-value) over the crest of anticline C[1]. This indicates less deposition, and therefore topographic relief at the time of deposition. The graph at the top shows the average of all the other graphs below.

5.6. Structures associated with differential compaction

Differential compaction over the channel complex resulted in syn-/post-depositional structures forming in overlying strata, including anticlines, faults, and depressions. The mapped horizon in Figure 5.14 depicts the locations of linear and elliptical depressions running along the channel complex margins. Depressions are formed by the erosion of Units II and III (Fig. 5.15). Elliptical – circular depressions are closely spaced in the north of the study area, whereas linear depressions dominate the south of the study area. The long axis of each depression strikes WNW, parallel to faults below them. Widths range from ~350 m - 1150 m and lengths range from ~1725 m – 4250 m. Five elliptical - linear depressions are located along the margins of the channel complex (Fig. 5.14). Directly north of the central cluster of depressions is an abandoned channel tracing the east margin of anticline C^1, initiating north of the confluence zone and terminating in one of the central depressions (Fig. 5.14).

On 3D seismic data, the depressions have characteristic features: a) medium-/high-amplitude, semi-continuous basal reflections; b) they are convex downwards, similar to the base of the channel complex (Fig. 5.15); c) they have discontinuous, low amplitude reflections at the top, indicative of disrupted infill (Cole et al., 2000); d) they are asymmetric in cross section (Fig. 5.4). Seismic reflections within the depressions normally change laterally into more

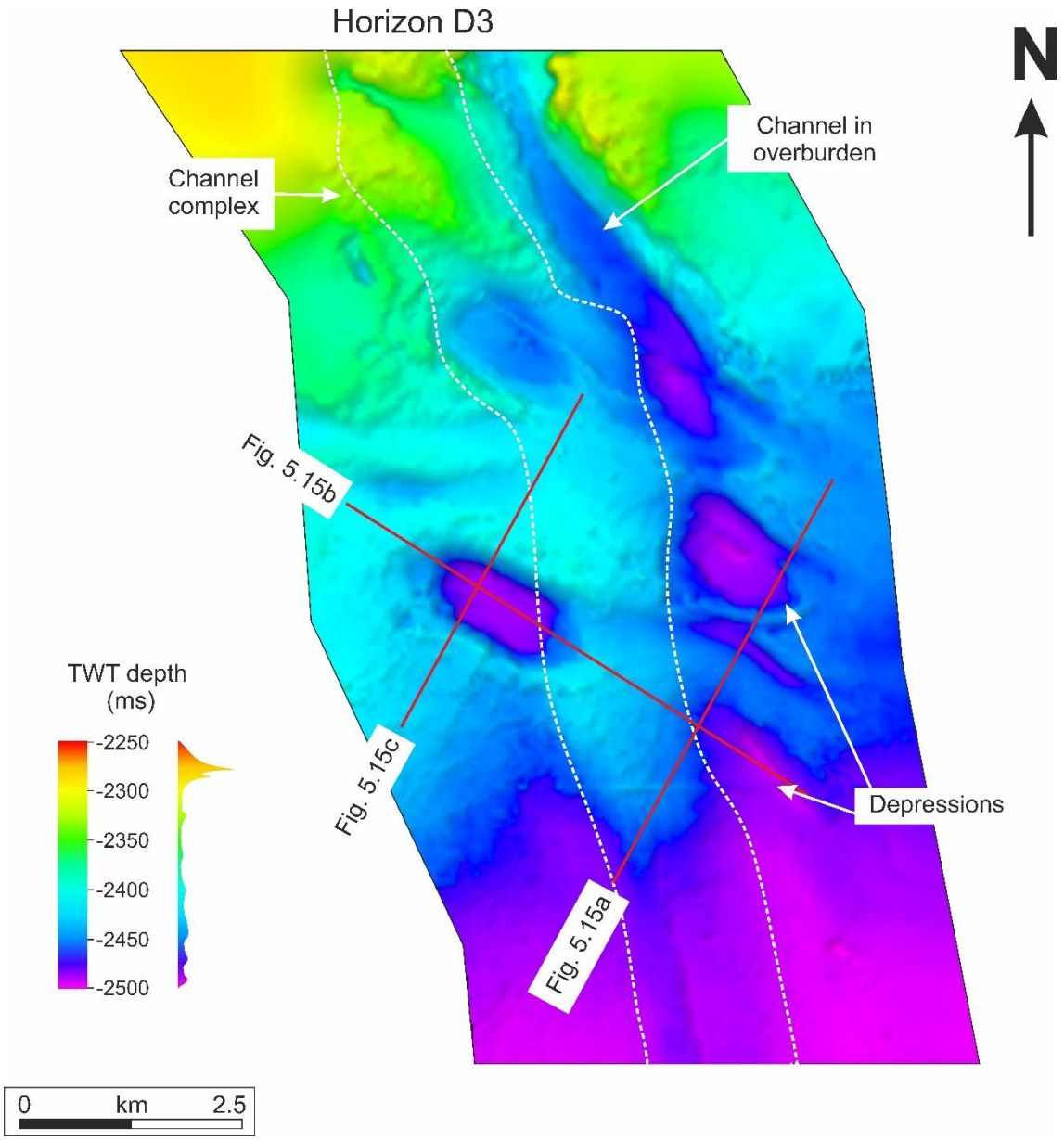

Fig. 5.14 Interpretation of horizon D_3. The submarine channel complex below this horizon is displayed as a white dashed line. Linear and elliptical depressions, and an abandoned channel, are dark blue/purple towards the north. Anticline C^1 is marked by lighter colours (shallower TWT depth) over the axis of the submarine channel complex. Locations for seismic lines in Figure 5.15 are also shown.

continuous, lower amplitude reflections, akin to more homogeneous sediments deposited in Units II and III (Fig. 5.15c).

5.7. Discussion

5.7.1. Magnitude and timing of differential compaction over channel-fill deposits

Thickness-relief plots help elucidate the timing of differential compaction. Sediment was deposited where accommodation space was created, i.e., it preferentially accumulated on the flanks of anticline C^1. This is portrayed on seismic data by reflections thinning over anticline C^1. Small scale variations in thickness that are lower than the resolution of the data are easier to identify with thickness-relief plots. Results show that Unit II has a constant D- value over the channel complex, whereas Unit III thins on the crest of anticline C^1 (Figs. 5.12 and 5.13). This suggests differential compaction over the channel complex produced anticline C^1 on the seafloor between the deposition of Unit II and Unit III.

As differential compaction is not uniform along the whole length of the channel complex, the variable magnitudes of differential compaction in the north and south can be explained by complex sedimentological and structural processes. It is predicted that differential compaction is greatest where sand is most abundant (Posamentier, 2003, Chopra and Marfurt, 2012). Figure 5.7 shows

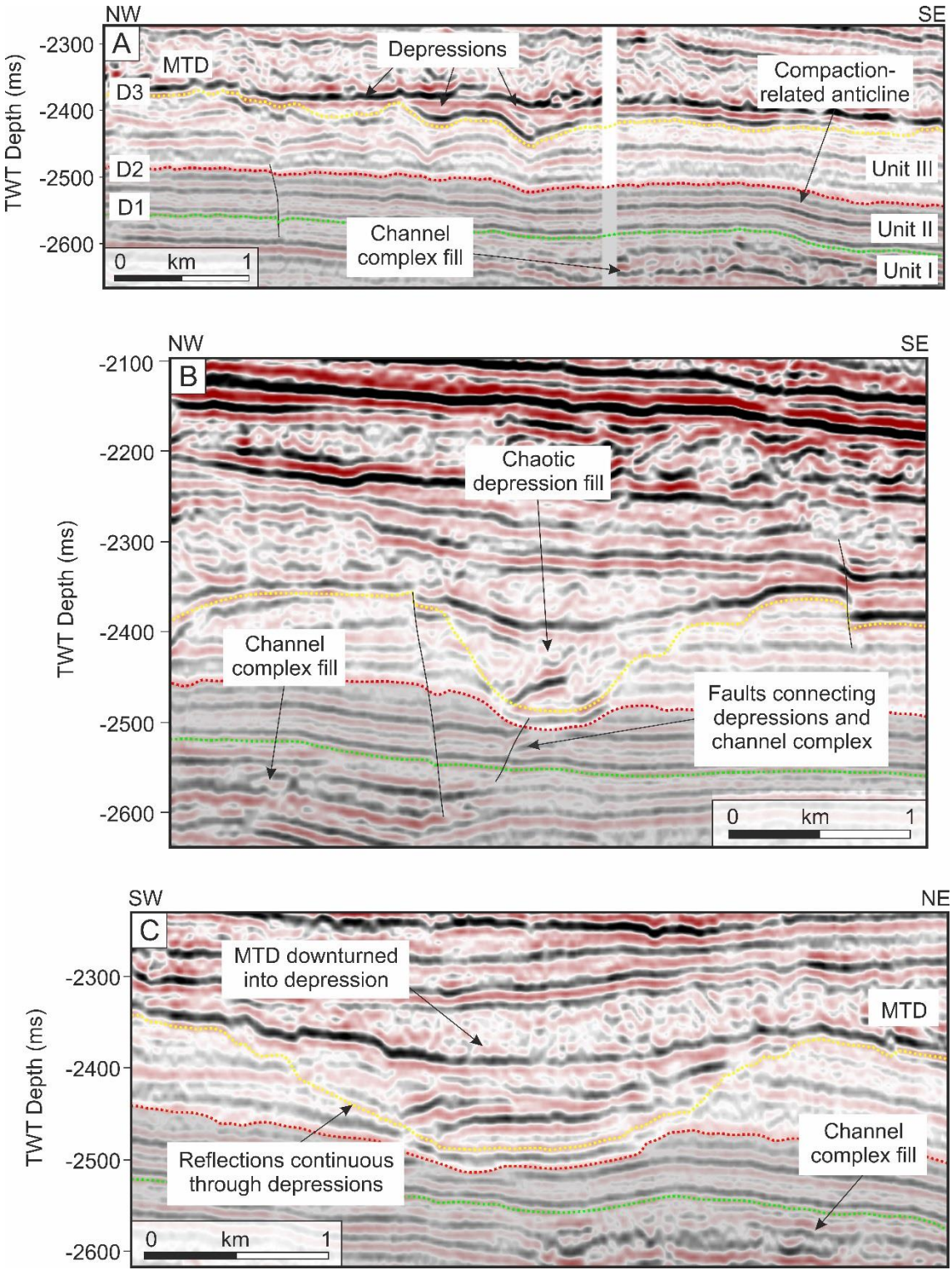

Fig. 5.15 a) Seismic profile through multiple depressions. b) Seismic profile through the long axis of a depression. A fault connects the depression to the submarine channel complex. The depression has a somewhat chaotic seismic character. c) Seismic profile through the short axis of the same depression in 5.15b. Seismic reflections above the depression are downwarped into its centre. Seismic reflections bounding the depressions continue through it with a lower amplitude. TWT – two-way traveltime; MTD – mass-transport deposit.

the thickness of channel-fill increases towards the south. The crest of anticline C^1 is spatially controlled by the size and location of the less compactable channels, which are also thicker in the south (Fig. 5.8).

A process that closely controlled differential compaction in the north was the expulsion of fluids. Hence, it was interpreted that depressions started to form as a result of fluid expulsion at the surface. The variance map in Figure 5.1 shows a dense cluster of stacked depressions in the north of the study area. This suggests that the depressions formed in multiple phases; pulses of fluid expulsion during compaction are thought to have discouraged differential compaction as sands are unable to retain pore fluids. At the time fluid was putatively expelled from the channel complex, there was very little overburden. Vertical stress was low and burial depths were not large enough to cause differential compaction.

Depressions above submarine turbidite channels have commonly been attributed to fluid expulsion and subsequent generation of pockmarks (Gay et al., 2003, Gay et al., 2006b, Cole et al., 2000, Davies, 2003). However, each of these studies provide evidence for fluid flow, e.g., fluid pipes or chimneys. There is no evidence for fluid migration at present in the study area, and the dimensions of the interpreted depressions are greater than the expected volume loss from the channelized reservoir. Faults connecting the channel complex with the

depressions may have acted as conduits for fluid flow, but were too small to expel enormous volumes of fluids (Bjørlykke and Høeg, 1997) (Fig. 5.15b).

The following theory has been proposed as the process for the formation of depressions. Sand-rich turbidite channels act as a linear, secondary reservoir for fluids to drain into during compaction (Gay et al., 2003, Davies, 2003). Rapid sedimentation and loading in the study area (>100 m my^{-1}) causes channel sands to become overpressured, a process enhanced by differential compaction of the sands and lateral overbank muds (Gay et al., 2003, Gay et al., 2006a). Rapidly deposited muds overlying the channel complex had low mechanical strength and small increases in pore pressure within the underlying sands were sufficient to fracture the rock and allow migration of fluids to the surface (Carver, 1968, Gay et al., 2006a, Davies, 2003). Fluid migration occurred if overpressure in the channel-fill was greater than the maximum horizontal stress and if the vertical stress was relatively low (Bjørlykke and Høeg, 1997). This would have formed pockmarks on the seafloor where sediment had become fluidized. The line of depressions seen on the structural map in Figure 5.14 are parallel with the buried channel complex and corresponding anticline C^1. They strike perpendicular to the predicted deep-water palaeocurrents along the Brazilian margin (Duarte and Viana, 2007). Therefore, localized erosion where pockmarks formed could have led to the large depressions seen in the seismic data (Viana, 2001). Figure 5.16 is a schematic diagram summarising the proposed mechanisms for trap formation, faulting and fluid expulsion, and the bottom current erosion of pockmarks.

5.7.2. Differential compaction as a process leading to trap formation over submarine channels

Coarse-grained channel turbidites in deep-water settings are common exploration targets in southeast Brazil (Gamboa and Alves, 2015a, Clark and Pickering, 1996, Mayall et al., 2006, Viana et al., 2003). Turbidite sands along channel axes have high porosity and permeability, permitting the migration of hydrocarbons (Clark and Pickering, 1996). Muds and shales draping the channel-fill and deposited within the channel complex may provide significant stratigraphic traps, though this heterogeneity in lithology can lead to major risks to exploration and recovery of hydrocarbons (Mayall et al., 2006, McHargue and Webb, 1986, Gamboa and Alves, 2015a). Amplitude maps are a good indication for the location of channel sands. Figure 5.6 shows high amplitudes (yellow-red) along the axis of the channel complex. There is continuity of the high amplitude along slope, indicating a possible pathway for hydrocarbons to migrate. Within many submarine turbidite systems, channels are stacked vertically and horizontally. This dramatically increases reservoir connectivity ensuring fluids migrate over long distances along multiple channel axes. The studied channel complex, however, is isolated and shows no evidence of channel migration or aggradation. Another caveat is the lack of upslope dip-closure of anticline C^1 (Fig. 5.4). The observed E-W closure of anticline C^1 over the flanks of the channel complex provides a suitable lateral trap, but hydrocarbons are likely to travel

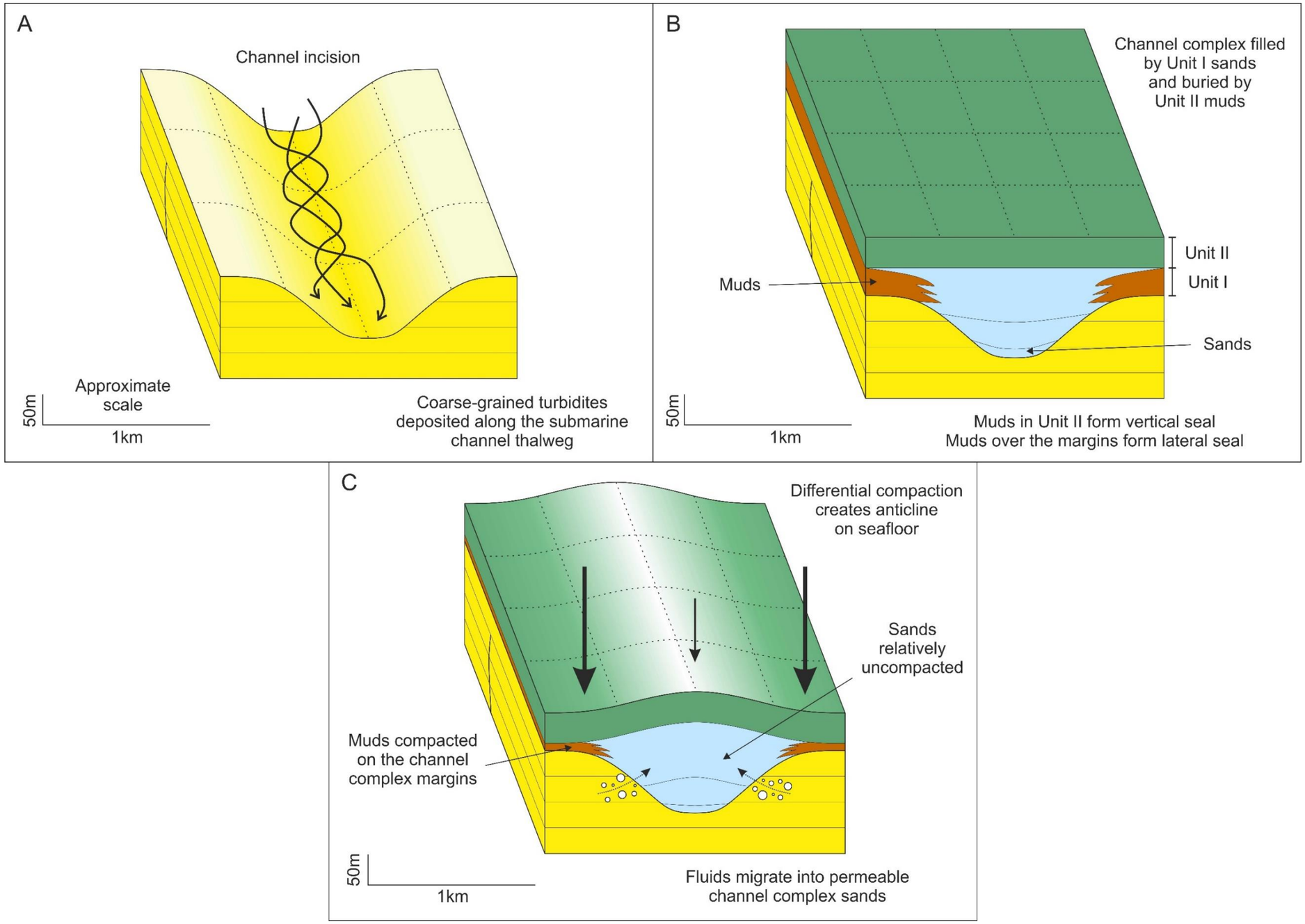

Fig. 5.16 (*continues on next page*) Schematic diagram summarising the evolution of differential compaction, the deposition of units I, II, and III, migration of fluids, and the formation of faults/depressions. a) The sea floor is incised by turbidity flows. b) The submarine channel complex is filled with sands and muds (unit I), and is subsequently overlain with mud from unit II. c) Differential compaction starts, and the channel complex margins compact more than channel-fill sands. Fluids then migrate into the sandy reservoir. d) *next page*; Unit III muds are deposited over the positive-relief seafloor structure. e) Overpressure in the reservoir leads to faulting of the overburden, transmitting fluids to the surface. f) Fluids weaken the rocks at the fault tips and form depressions that are enhanced by erosion due to seafloor currents. g) Sediment fills the depressions, and mass-transport deposits erode and bury unit III. MTC – mass-transport complex.

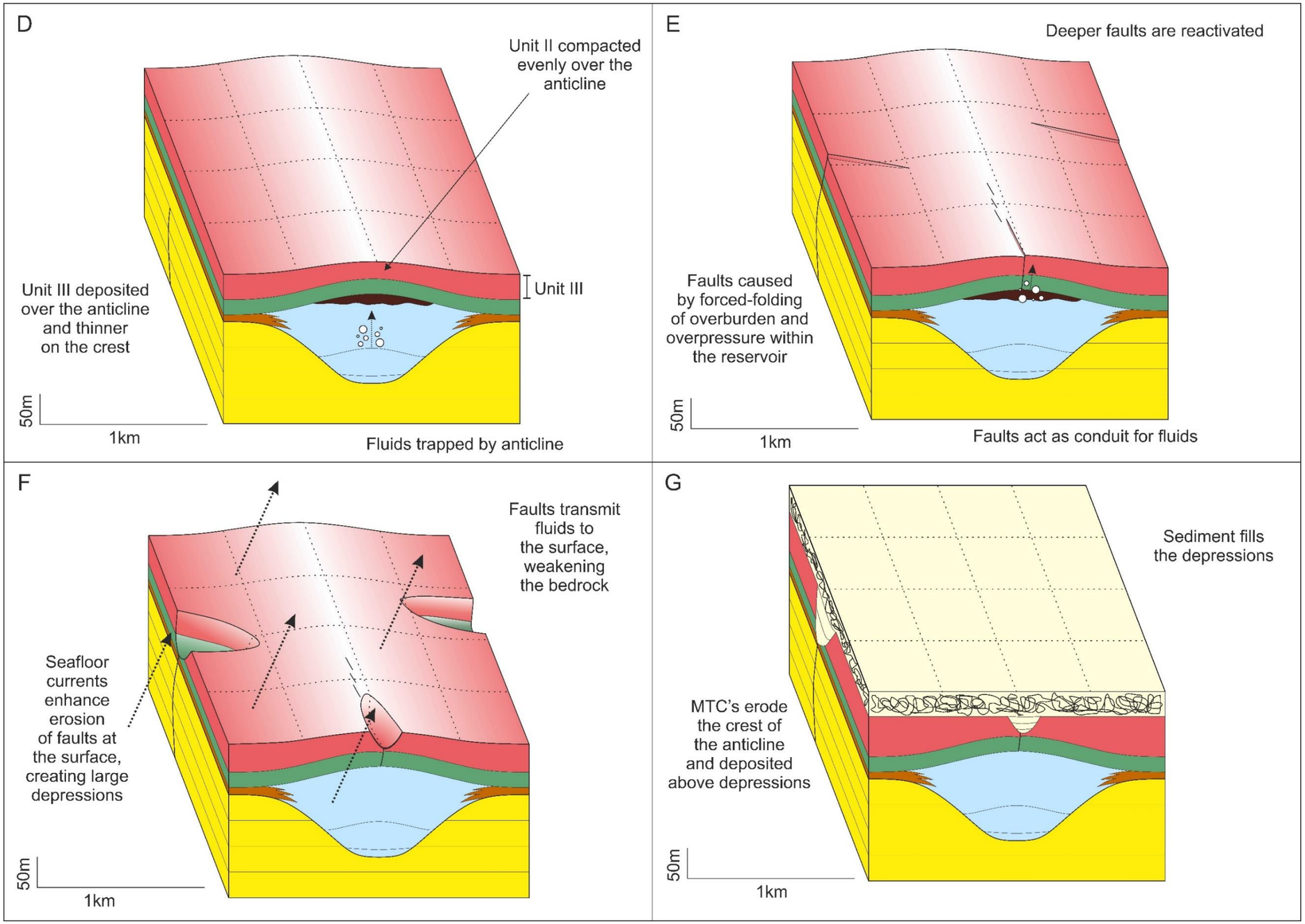
D
Unit II compacted evenly over the anticline
Unit III deposited over the anticline and thinner on the crest
Unit III
50m
1km
Fluids trapped by anticline
E
Deeper faults are reactivated
Faults caused by forced-folding of overburden and overpressure within the reservoir
50m
1km
Faults act as conduit for fluids
F
Faults transmit fluids to the surface, weakening the bedrock
Seafloor currents enhance erosion of faults at the surface, creating large depressions
50m
1km
G
Sediment fills the depressions
MTC's erode the crest of the anticline and deposited above depressions
50m
1km

upslope, where no evidence of trap closure is seen on the northern limit of the seismic data.

Due to the lack of well data in the study area, a tentative explanation of the hydrocarbon systems using evidence from this chapter is provided: deposition of coarse-sediment downslope of knickpoints enhances reservoir quality. The sudden decrease in gradient at the base of the knickpoints reduces flow velocity, so entrained coarse-sediment and MTCs are deposited (Alpak et al., 2013). Chaotic seismic reflections representing slumps and debrites onlap and pinchout onto the muddy slope drapes over the knickpoints (Prather, 2003). The muds act as a permeability barrier and form an updip stratigraphic trap. Differential compaction over the deposits downslope of the knickpoints creates anticlines with four-way dip closure. However, limited flow communication between the 'pods' compartmentalise these reservoirs. As the migration of hydrocarbons between isolated pods relies on a carrier bed – basal sands along the channel complex (Schowalter, 1979) - this scenario can lead to 'fill-to-spill' traps, where hydrocarbons fill a single pod or reservoir until it reaches a spill point (Fig. 5.17). The hydrocarbons travel upslope, along a permeable bed, and fill the next pod. For the example shown in Figure 5.17, fluids in two different phases will be differentially entrapped: the lightest, most buoyant fluid will be enclosed in the deepest pod. This is the most likely model for charging similar reservoirs to the study areas downslope of channel knickpoints.

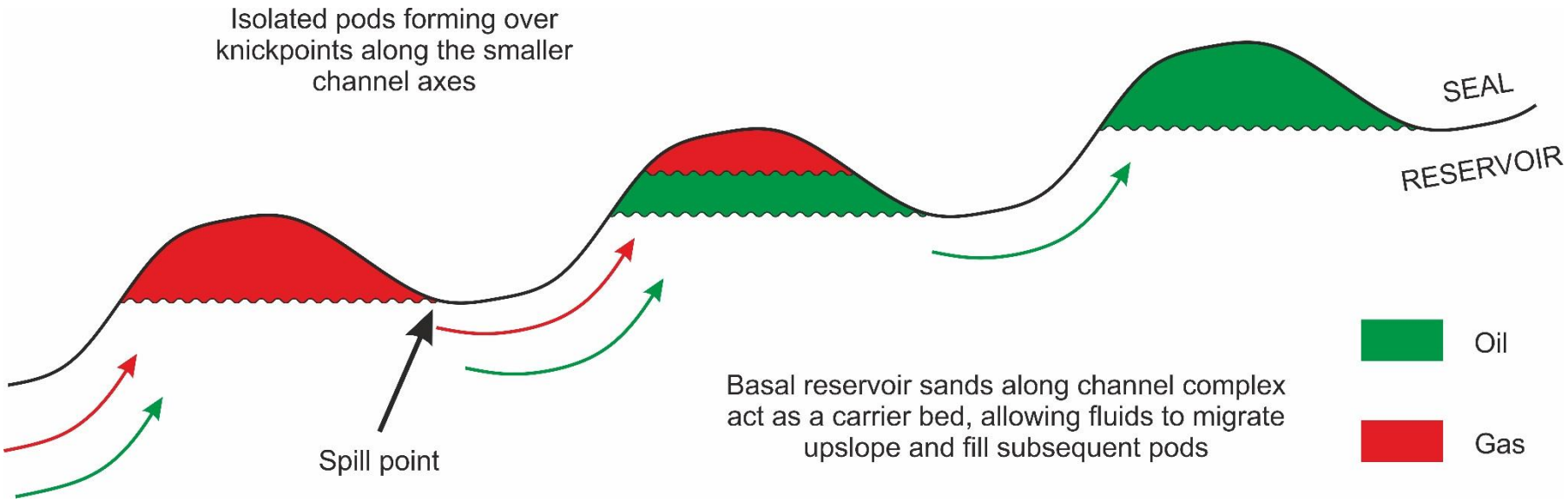

Fig. 5.17 "Fill-to-spill" trap scenario. Lighter fluids, e.g. gas, will be trapped downslope, whereas the heavier fluids will move upslope. *Modified from Schowalter (1979).*

In this chapter, the magnitudes of differential compaction were estimated in the time domain. In order to assess and understand the results and interpretations presented, the limitations of not converting the data into depth in metres needs to be considered. As there are no accessible wells drilled into the studied channel, the small scale changes in lithology, and therefore seismic velocity, are unknown. Seismic velocity through consolidated sands is greater than in shales and muds (Farmer and Jumikis, 1968). Taking this into account, it is expected that anticline C^1 is larger than that measured on the TWT seismic data used in this chapter.

5.8. Chapter specific summary

This chapter uses thickness-relief plots and seismic volume attributes to help understand how and when differential compaction occurred over a submarine channel complex in the Espírito Santo Basin, Brazil. Our results show:

- Differential compaction over the channel complex occurred during early burial. Results from the thickness-relief method indicate anticline C^1 was expressed on the surface after the channel was buried by ~200 m of sediment. The anticline reached a maximum magnitude of 41 ms (~37 m) in the south.

- Fluid expulsion limits differential compaction over the channel complex. Elliptical-linear depressions are observed on seismic data. Fluids from within the channel sands were transmitted to the seafloor by a set of faults on the channel complex margin. Deepwater palaeocurrents over the buried channel removed fluidized sediment and eroded the depressions. Subsequent scouring and collapse of the steep walls rapidly increased their size. There are more depressions in the north of the channel complex where differential compaction is not as prominent, due to the expulsion of larger volumes of fluid from the channel complex compared with the south.

- Knickpoints on submarine channels within the channel complex are associated with 'pods' of coarse-grained deposits, including slumps, slides, and debris flows. There is limited connectivity and lateral continuity of the pods. Differential compaction over the units downslope of knickpoints isolates the pods.

- Possible reservoir rocks are identified along the base of the channel complex, and pods downslope of knickpoints. The compaction-related anticline above the channel complex has no upslope closure; the trapping potential is limited. However, the isolated pods onlap

the knickpoint faces, indicating stratigraphic trapping potential, and have four-way dip closure above them.

- The identified petroleum system relies on hydrocarbon migration along the base of the channel complex. A fill-to-spill model is proposed to explain the process for charging these reservoirs, where the hydrocarbons migrate into a pod, and when the spill-point is reached, they migrate updip into the next pod along the channel complex.

These findings suggest suitable structural and stratigraphic traps form during early burial of a submarine channel. Analogues can be made to submarine channels in similar basins on passive margins, such as the Gulf of Mexico and the west coast of Africa.

CHAPTER SIX

Submarine sediment routing over a blocky mass-transport deposit in the Espírito Santo Basin, SE Brazil

An abridged version of this chapter has been published as:

Ward, N.I., Alves, T.M. and Blenkinsop, T.G., 2018. Submarine sediment routing over a blocky mass-transport deposit in the Espírito Santo Basin, SE Brazil. *Basin Research*, 30(4), pp.816-834.

Co-author contributions to the paper:

Tiago Alves – checked for grammatical errors, ensured the scientific content was accurate and appropriately presented.

Thomas Blenkinsop – checked for any errors in the theme of structural geology, provided feedback on paper.

6. Differential compaction over an MTD

6.1. Abstract

The control of slide blocks on slope depositional systems is investigated in a high-quality 3D seismic volume from the Espírito Santo Basin, SE Brazil. Seismic interpretation and statistical methods were used to understand the effect of differential compaction on strata proximal to the headwall of a blocky mass-transport deposit (MTD), where blocks are large and undisturbed (remnant), and in the distal part of this same deposit. The distal part contains smaller rafted blocks that moved and deformed with the MTD. Upon their emplacement, the positive topographic relief of blocks created a rugged seafloor, confining sediment pathways and creating accommodation space for slope sediment. In parallel, competent blocks resisted compaction more than the surrounding debrite matrix during early burial. This resulted in differential compaction between competent blocks and soft flanking strata, in a process that was able to maintain a rugged seafloor for >5 Ma after burial. Around the largest blocks, a cluster of striations associated with a submarine channel bypassed these obstructions on the slope and, as a result, reflects important deflection by blocks and compaction-related folds that were obstructing turbidite flows. Log-log graphs were made to compare the width and height of different stratigraphic elements; blocks, depocentres, and channels. There is a strong correlation between the sizes of each element, but with each subsequent stage (block –

depocentre – channel) displaying marked reductions in height. Blocky MTDs found on passive margins across the globe are likely to experience similar effects during early burial to those documented in this chapter.

6.2. Introduction

Mass-wasting can transport large volumes of sediment downslope and is one of the primary processes filling deep-water sedimentary basins around the world (Gee et al., 2006, Omosanya and Alves, 2013, Masson et al., 2006, Gamboa et al., 2010, Newton et al., 2004, Beaubouef and Abreu, 2010). On continental slopes, mass-wasting usually occurs in the form of recurrent (mass-transport complex) or discrete (mass-transport deposit) events, as documented in Pickering and Hiscott (2015). Both types of events can remobilise competent blocks ranging from boulders to large slide blocks of strata > 1 km in diameter, sometimes within a muddy, easily compactible debris-flow matrix (Armitage et al., 2009, Alves and Cartwright, 2010, Posamentier and Kolla, 2003, Hampton et al., 1996, Pickering and Corregidor, 2005, Masson et al., 2006). When containing large slide blocks thicker than the deposit, mass-transport deposits can generate topographic highs on the seafloor that enhance its roughness (Alves, 2010, Armitage et al., 2009). Subsequently, submarine channels and turbidity currents can be confined by these same unburied slide blocks (Gamboa et al., 2010, Pickering and Corregidor, 2005, McAdoo et al., 2004, Alves, 2010).

Lithological differences between slide blocks and surrounding strata can have a marked effect on the sea floor. After the blocks are completely buried by sediment, they can influence the degree of compaction of slope strata and, therefore, seafloor sediment distribution during early burial (Alves and Cartwright, 2010). Variations in compaction rate (differential compaction) can produce local topographic highs above the less compactible strata and increase accommodation space over the more compactible units (Hunt et al., 1996, Rusciadelli and Di Simone, 2007, Maillard et al., 2003). Such a phenomenon has a profound effect on the subsequent architecture of slope sediment; differential compaction over mud-rich deposits can lead to the development of both local and regional depocentres (Dykstra et al., 2011). In addition, compaction processes can induce important slope instability (Dugan and Flemings, 2000, Bjørlykke and Høeg, 1997, Stigall and Dugan, 2010).

In this chapter's study area, differential compaction is observed over competent slide blocks that constitute part of a Late Miocene mass-transport deposit (MTD A) that was triggered in association with gentle folding and faulting of the Espírito Santo continental slope (SE Brazil) (Figs. 2.3 and 6.1). A newly identified sediment fairway and its relationship with slide blocks in MTD A was analysed. Also discussed is the development of linear depocentres over MTD A. Statistical analyses were used to recognise any scaling relationships between stratigraphic features in the study area. Hence, this chapter addresses the following research questions:

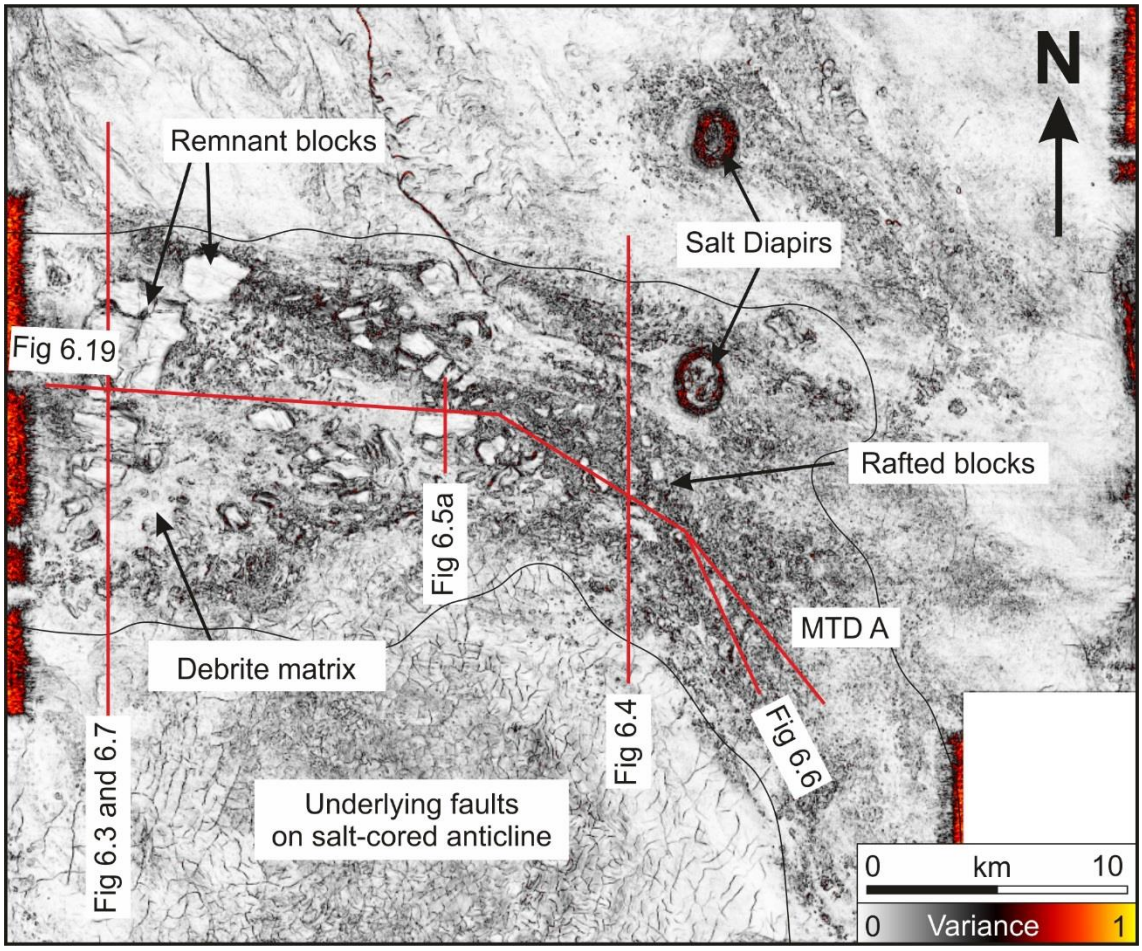

Fig. 6.1 Variance cube of the studied MTD A (SE Brazil), flattened at its base to show all relevant morphological features on the continental slope and the boundary of MTD A. *Modified from Alves and Cartwright (2010).*

- What process created seafloor depocentres after MTD A was buried?
- How did MTD A control the seafloor sediment distribution post-burial?
- What constraints do the slide blocks impose on the size and scale of overlying stratigraphic features?

New isochron maps, structural maps, and statistical data are presented to try to understand the relationship between MTD blocks and sediment distribution in younger strata offshore Espírito Santo (see *Chapter 3* for a full description of these methods). The impact of differential compaction on seafloor roughness is later discussed, focussing on the implications for submarine channel systems on continental slopes.

6.3. Chapter specific data and methods

This chapter uses interpretations of the BES-100 seismic volume from the Espírito Santo Basin, SE Brazil. For a full description of the data acquisition and processing, please see *Chapter 3, section 3.1.1.3*.

This chapter focusses on the strata overlying MTD A. Five horizons were mapped and analysed between the base of MTD A and the seafloor (e.g. Figs. 6.2 and 6.3). The upper and lower surfaces of mass-transport deposits are often irregular, which can lead to oversimplified structural maps being produced (*e.g.* Alves 2010). The picking accuracy is also hindered by terminations and limited continuity of seismic reflections within discrete sedimentary packages (Figs. 6.4 and 6.5). Detailed mapping was of vital importance to this study; structural maps for M_1, M_2, and M_4 were created using every inline and crossline, i.e. interpreted every 12.5 m. Consequently, metre-scale features were documented along the base of slope depocentres and channels, and the top surfaces of the MTD blocks were imaged at a resolution of <10 m (Fig. 6.2).

Variance data enabled us to investigate key structural and stratigraphic features on seismic data (Fig. 6.1). As the studied continental slope dips to the SE, the entire seismic cube was flattened to the base of MTD A (M_1) so that variance slices could be extracted through its full length. Isochron maps were also computed between the interpreted seismic horizons, a procedure that allowed us to visually compare features in MTD A with those of strata above it. Statistical data on imaged depocentres and slide blocks were compiled using direct measurements on vertical seismic profiles, converted to depth using an estimated seismic velocity of 1800 m/s.

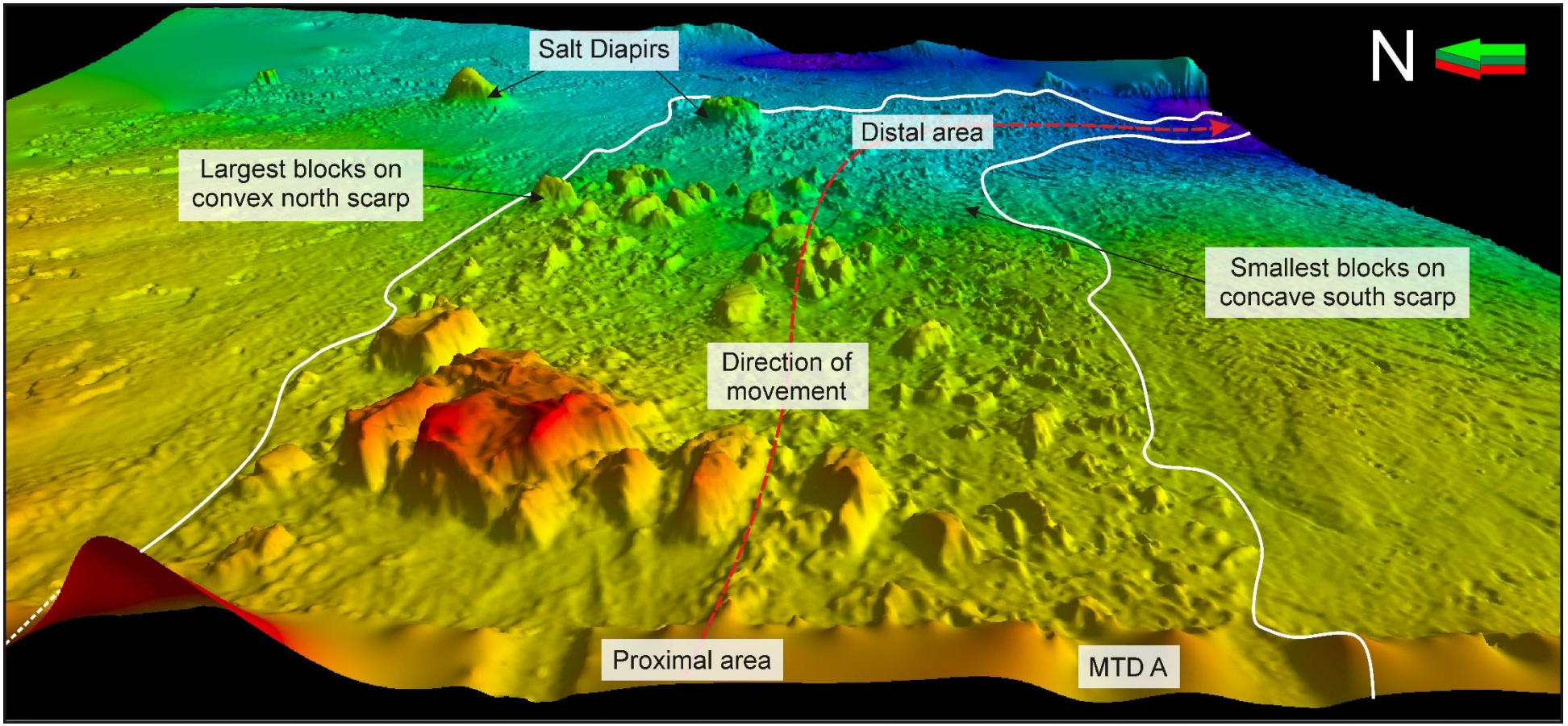

Fig. 6.2 3D window view of a map of horizon M_2, the top of MTD A. It highlights the downslope direction of flow within MTD A.

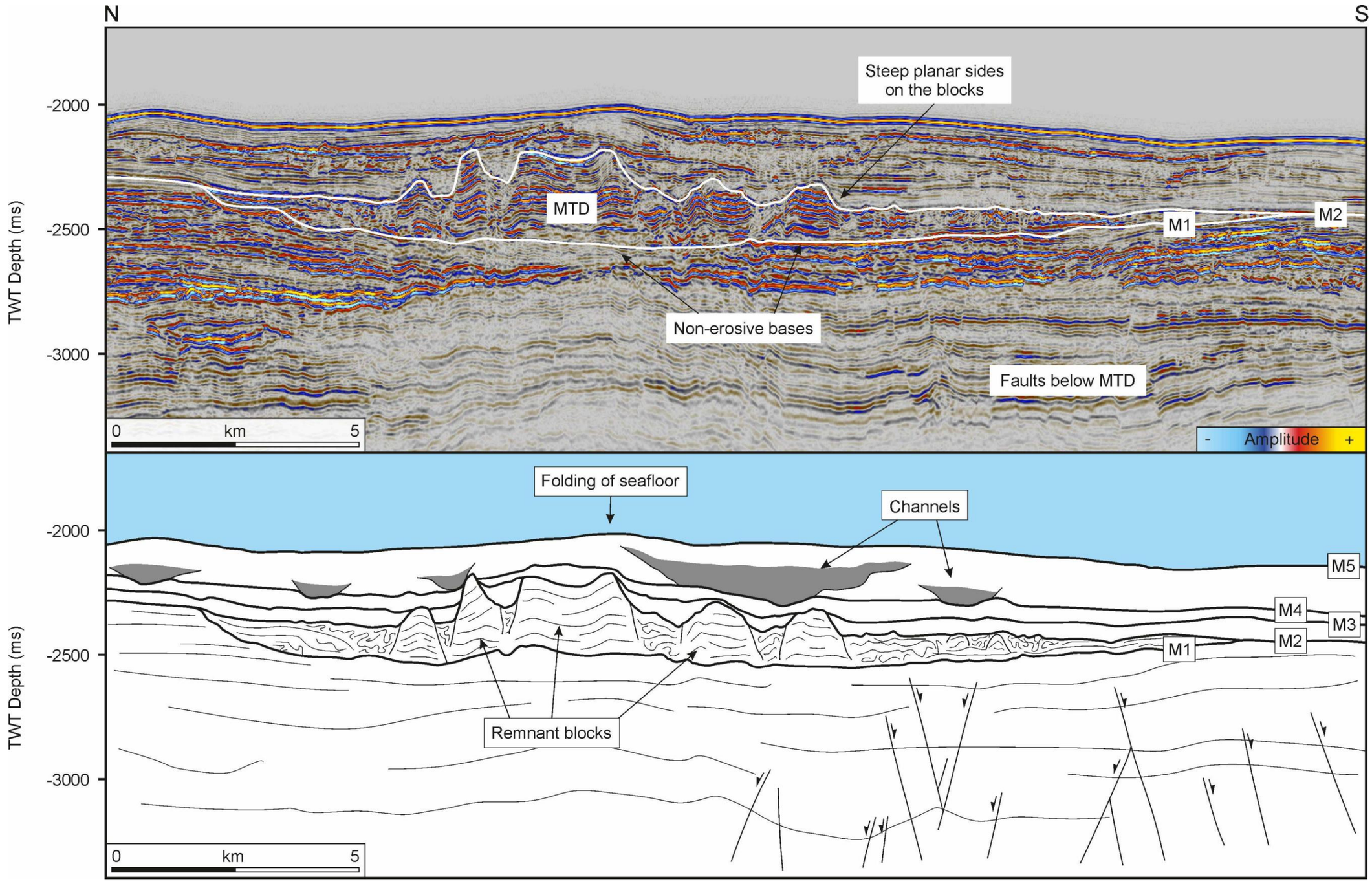

Fig. 6.3 Selected N-S seismic section through the largest blocks in MTD A, Espírito Santo Basin. Below is shown an interpretation of the seismic section. Key features studied include remnant blocks, channels, and folds over MTD A. Also highlighted are the interpreted seismic horizons M_1 to M_5. These represent: M_1 – the base of MTD A; M_2 – the top of MTD A; M_3 – moderately transparent reflections signalling a healing seafloor; M_4 – overburden affected by differential compaction over the small blocks; M_5 – present-day seafloor. Location of seismic line in Figure 6.1.

Width:height ratios were calculated in order to compute scaling relationships in depocentres and channels. Slide blocks were analysed by measuring their average width in plan view, and their height was recorded as the relief above debrites, i.e. from M_2 (top debrites) to the top of the block. Channel width was measured perpendicularly to its axis, and channel height was measured from the base of the channel to the top of the channel fill. Depocentres, represented on the plots as described in *section 6.5.1*, were measured similarly to the channels. As they lie perpendicular to the flow direction, width represents the depocentres' short axes. Only the linear-elliptical depocentres that formed in the distal parts of MTD A were measured for the width:height plots. In total, the width and height of 56 depocentres, 81 blocks, and 28 channels were measured and their ratios calculated (Table 6-1).

6.4. Seismic stratigraphy

6.4.1. MTD A (M_1-M_3)

MTD A is characterised by coherent and moderately deformed remnant blocks (Fig. 6.3). Highly deformed (rafted) blocks are also observed in debris-flow deposits, or debrites (Fig. 6.4). Using the classification scheme of Moscardelli and Wood (2008), the MTD has been interpreted as a 'slope-attached MTD'. Its surface area is ~440 km^2, it has a maximum width of <16 km, and is ~40 km in length. The

length:width ratio of the MTD is >2. The headwall of MTD A is not imaged on the seismic data. However, the presence of remnant blocks exceeding 5 km width in the proximal part of MTD A indicates the proximity of the headwall to the west of the study area. The largest blocks, both remnant and rafted, occupy the convex north scarp of MTD A, decreasing in size towards its concave south scarp (Figs. 6.1 and 6.2). This distribution also occurs from the proximal region to the distal region; as a result, the largest blocks lie in the head of MTD A, decreasing in size towards its toe (Fig. 6.1).

Remnant blocks, which are in general the largest blocks, comprise parallel, sub-horizontal, high amplitude seismic reflections representing relatively undeformed slide blocks (Fig. 6.5a). Their bases generally correlate with the base of MTD A (M_1), indicating they have experienced limited movement (Fig. 6.3). These blocks can range from >5 km to <1 km in width, >200 ms (~180 m) height (from the base to the top) and commonly have steep, planar sides (Fig. 6.5a). Conversely, rafted blocks are much smaller than remnant blocks; they are <500 m wide and show a similar height to the MTD itself (<100 ms or ~90 m). Internal seismic reflections are also parallel, but are rotated and the blocks are normally suspended within debrites in MTD A (Fig. 6.5b). Rafted blocks, therefore, were transported downslope during separate pulses of mass wasting, either sitting above previous debris flows, or having been covered by later debris flows during multiple failure events (Minisini et al., 2007).

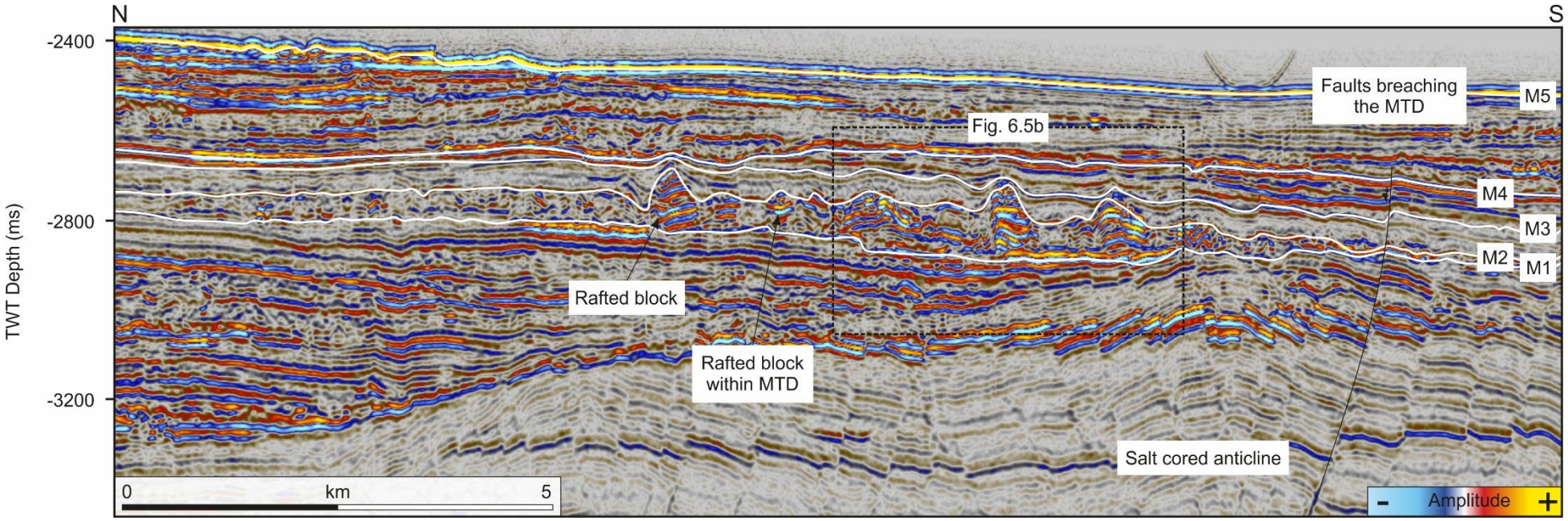

Fig. 6.4 Seismic profile crossing the rafted blocks in MTD A. From this seismic section, the 'ripple-like' morphology of the overburden indicates where the depocentres are located. Faults lying atop the salt-cored anticline occur below the MTD.

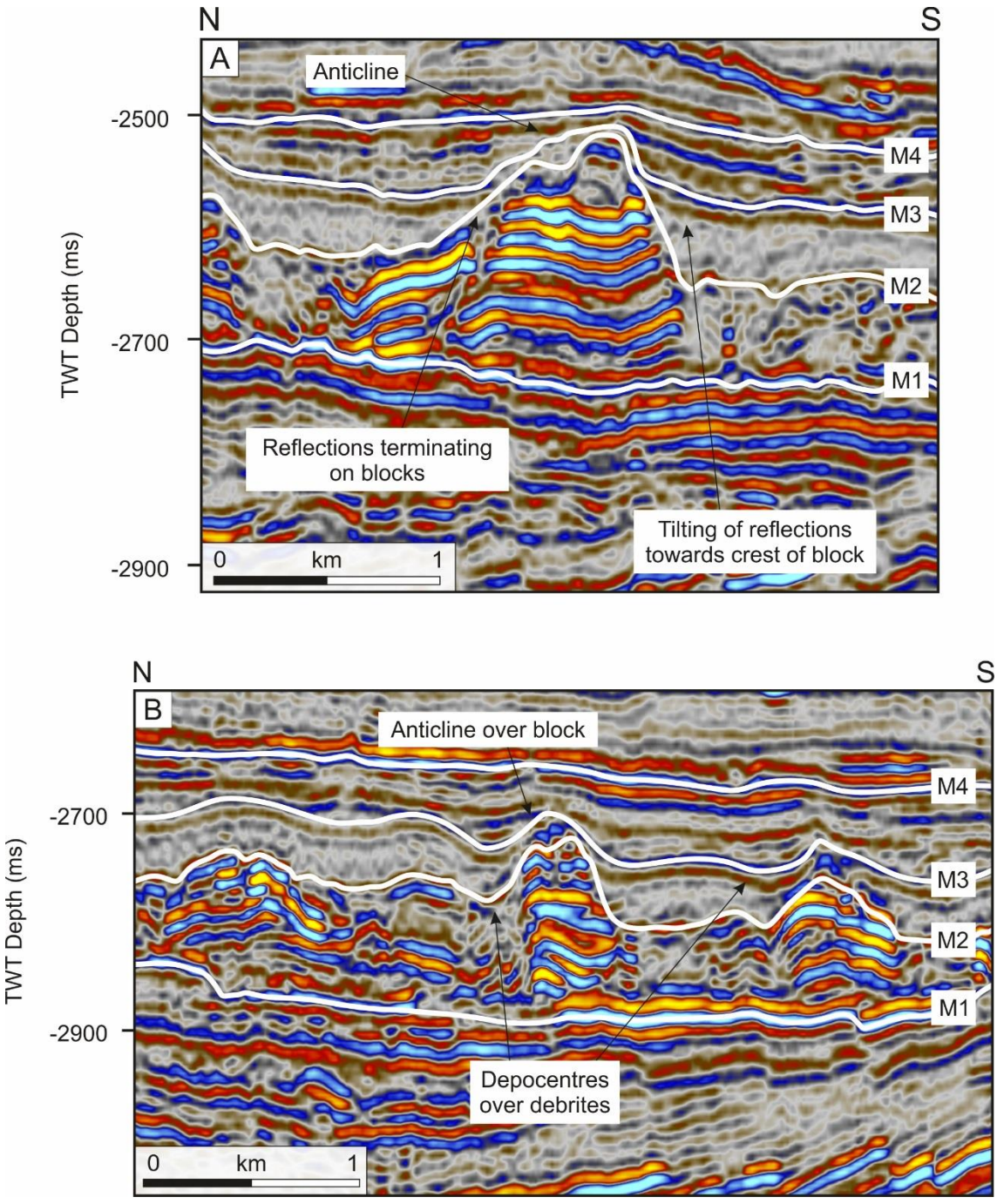

Fig. 6.5 Zoomed-in seismic profiles of the remnant and rafted blocks shown in Figures 6.3 and 6.4. a) A large remnant block is surrounded by debrites. These debrites tilt towards the crest of the block, an indication of differential compaction. b) Rafted blocks with depocentres formed between them and located over the debrites. Small anticlines over the blocks (as seen in Figure 6.4) are also a sign of differential compaction. Location of seismic profiles in Figure 6.1.

Based on their chaotic and relatively low amplitude character, strata between the blocks are interpreted as debrites (Fig. 6.3). The top surface of the debrites is marked by a continuous seismic reflection. This indicates the cessation of the mass movement and the initiation of normal sediment fallout. The height of the debrite unit increases towards some of the largest blocks (Fig. 6.5a).

Below MTD A, dense networks of faults deform a salt cored anticline (Fig. 6.3). These were formed during halokinesis by gentle folding of post-salt strata during the Miocene (Alves and Cartwright, 2010, Omosanya and Alves, 2013). In the proximal part of the MTD, faults rarely breach M_1 (Fig. 6.3). Downslope, the faults are closer to the surface and it is not uncommon for M_1 to be breached by vertically propagating faults, especially when MTD A is not present (Fig. 6.4).

6.4.2. Overburden (M_3-M_5)

Once MTD A was emplaced, the seafloor began to heal. The topographic lows that formed over the debrites and between the blocks were filled with relatively homogenous sediment, displaying low amplitude and semi-continuous seismic reflections (Fig. 6.5a). This low amplitude unit is less than 100 ms (~90 m) thick. It covers all of the smaller blocks, including all the rafted blocks in the distal part of MTD A, and is bounded by M_2 at its base and M_3 at its top (Fig. 6.6). However, remnant blocks taller than this unit were not buried and maintained their topographic relief on the seafloor. Seismic reflections onlapped

the sides of these exposed blocks and are folded upwards towards their crest (Fig. 6.5a). In comparison, seismic reflections that are continuous over the smaller blocks in MTD A (i.e. having buried the blocks) are folded, creating small anticlines and depocentres (Fig. 6.6).

Overlying the healed seafloor is a unit ~200 to 300 ms thick that includes all the strata from the top of MTD A (M_3) to the seafloor (M_5). Seismic reflections in this interval vary from very high amplitude to low amplitude, and are chaotic to semi-continuous (Fig. 6.7). Very few seismic reflections are completely continuous in this unit, owing to the large number of channels and scours truncating them (Fig. 6.7). These erosional features are orientated in a similar direction to MTD A; N-S cross sections across MTD A display the typical lenticular shape of the channels (Figs. 6.6 and 6.7). Each reflection is a constant amplitude in the direction of movement (Fig. 6.6), but changes amplitude across the width of MTD A (Fig. 6.7).

6.5. Evidence of deformation over MTD A

6.5.1. Early differential compaction over and around slide blocks

Differential compaction during early burial tends to occur in association to variations in lithology, which impose unequal rates of mechanical compaction

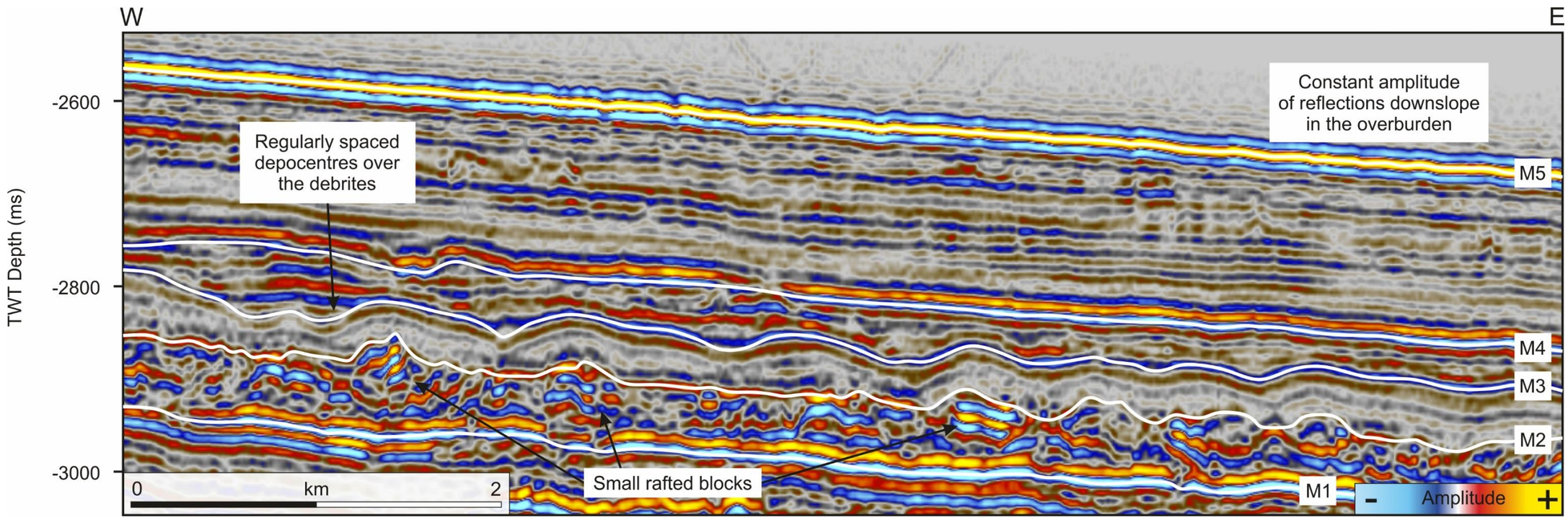

Fig. 6.6 Downslope seismic section showing regularly spaced depocentres formed over small rafted blocks entrained within a debrite matrix. Seismic reflections have a relatively constant amplitude downslope. Location of the seismic profile in Figure 6.1.

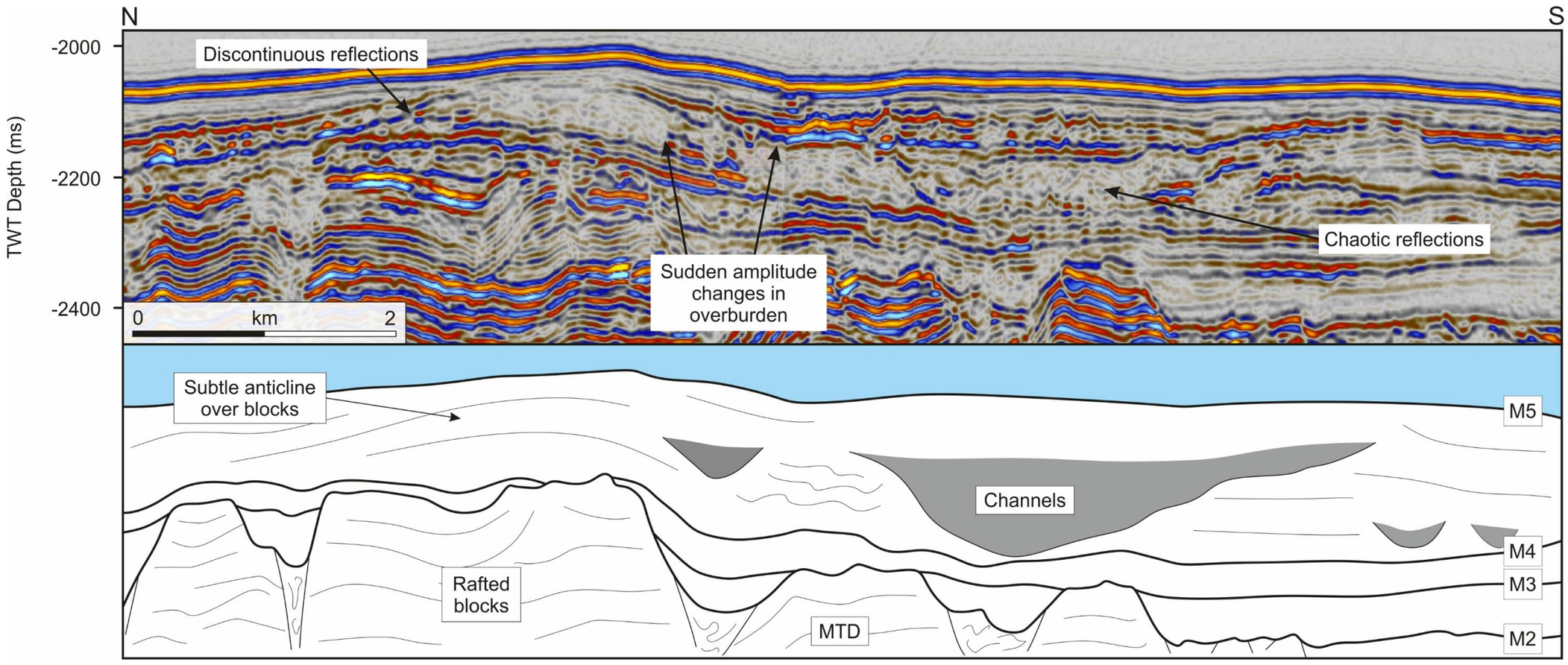

Fig. 6.7 Seismic section perpendicular to the flow direction of MTD A, highlighting the presence of submarine channels in the overburden, as well as their seismic character. Multiple discontinuous reflections are observed as the channels have eroded into the overburden. Seismic reflections range from chaotic to continuous, and transparent to opaque. It is hard to pick out deformation features in the overburden because of the complexity of seismic facies revealed at this place. Location of the seismic profile in Figure 6.1.

in strata (Trask, 1931, Weller, 1959). In the case of MTD A differential compaction is believed to have occurred over the blocks, i.e. under-consolidated debrites compacted more than relatively rigid carbonate blocks. This process therefore led to forced folding of strata over MTD A. Seismic reflection M_3 is continuous over the buried blocks and has a constant thickness (Fig. 6.4). Topographic highs developed along this horizon over the slide blocks, and local depocentres formed over the debrites, flanking the slide blocks (Fig. 6.5b). The depocentres were filled with sub-horizontal reflections, onlapping their inside walls.

As previously described, the largest blocks maintained their topographic relief on the seafloor after the deposition of M_3, and in some cases M_4 (Fig. 6.3). However, gentle folds are also observed over these blocks, although channels eroded a large proportion of the fold limbs, making the identification of their true shape difficult (Fig. 6.7). The smaller anticlines and depocentres (~1 km wide, ~30 ms thick) do not continue above M_4, as seismic reflections become flat. The larger anticlines in the proximal part of MTD A (<5km wide, ~100 ms thick) continue upwards over M_4 influencing the shape of the present-day seafloor (Fig. 6.7).

6.5.2. Sediment fairways over MTD A

Channels and scours predominate in the complex strata overlying MTD A (Fig. 6.8). Most are hard to distinguish from the surrounding material: they are low amplitude and filled with parallel horizontal seismic reflections, which are

truncated on the inner channel walls (Fig. 6.7). Other channels have slightly chaotic fill, which could be indicative of mass flows (Fig. 6.7). They range from <1 km to more than 3 km wide and are situated above the debrites, always marginal to the large blocks and seldom eroding horizon M_3. These channels differ from the depocentres that are observed over the distal parts of MTD A because they are orientated parallel to the direction of movement of the latter deposit (Fig. 6.8).

A TWT structural map of M_3 shows a series of elongated striations striking downslope (Figs. 6.8 and 6.9). This cluster of striations reaches a maximum width of 2.5 km, and they are continuous for at least 25 km (Fig. 6.8). At its greatest width, there are up to 12 striations side by side in the observed cluster. Towards the termination of the striations, the shape resembles that of a submarine fan as they splay out, almost doubling the width of the cluster (Fig. 6.9). Striations similar in size and geometry to those studied here are commonly associated with glacial movements (Rise et al., 2004, Dowdeswell et al., 2007), the base of submarine landslides (Gee et al., 2005), precursors to submarine channels (Gee et al., 2007), or below debris flows (Posamentier and Kolla, 2003). Directly above the

---

Fig. 6.8 (*next page*) TWT structural map of M_3 providing an overview of a sediment fairway. The boundary of MTD A is shown in white. The striated fairway appears to have moved downslope, along the margin of MTD A. An exposed block disrupts the pathway of the fairway, bifurcating it near its origin.

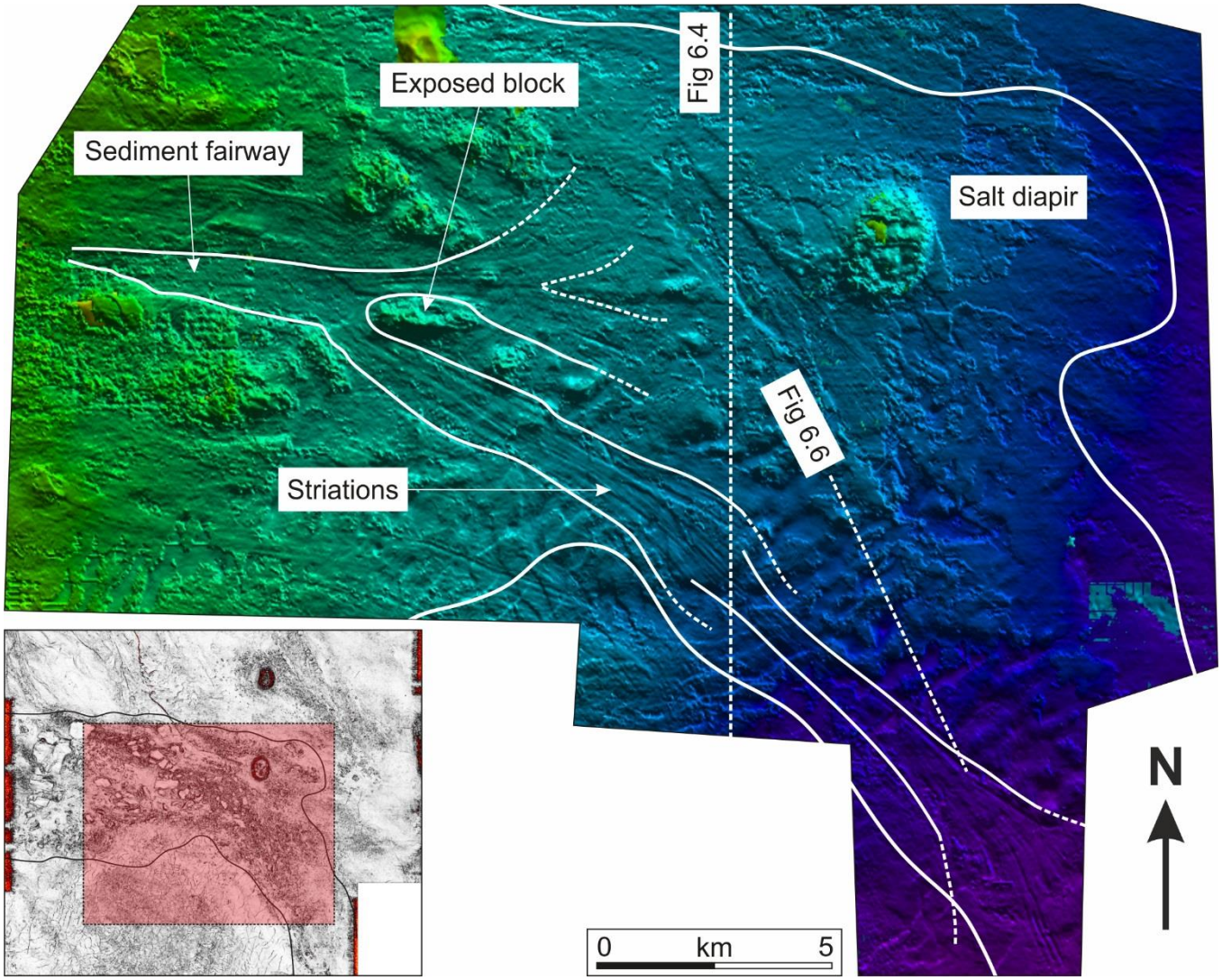
Exposed block
Fig 6.4
Sediment fairway
Salt diapir
Fig 6.6
Striations
N
0
km
5

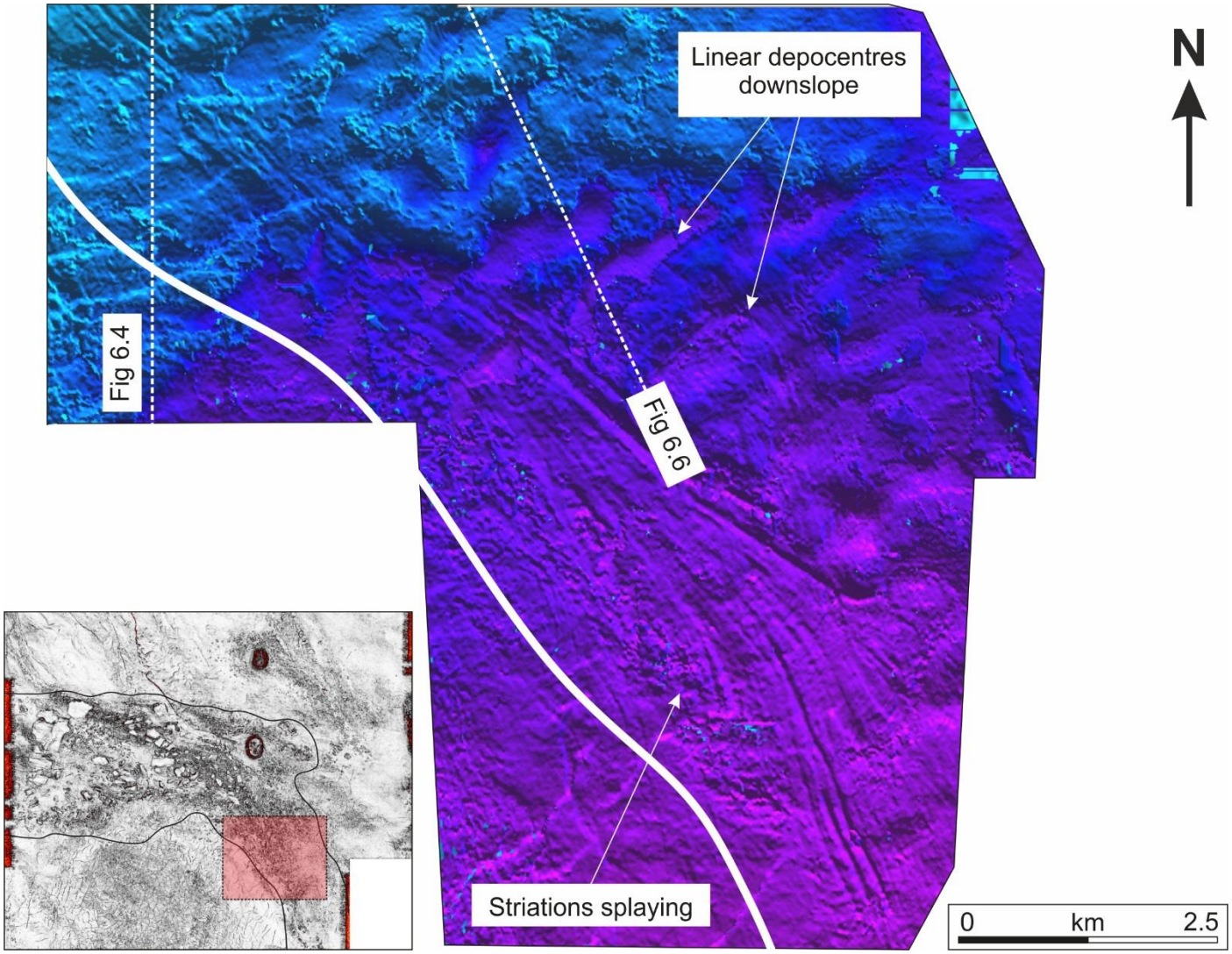
Linear depocentres downslope
N
Fig 6.4
Fig 6.6
Striations splaying
0 km 2.5

Fig. 6.9 (*previous page*) Close-up of the basal striations downslope (location shown on the map within the figure). The striations have a fan shape at their terminus. The fairway cuts through elliptical-linear depocentres, observed on its NE side.

striations lies a channel system (Figs. 6.10 and 6.11). It is unclear whether the striations were formed during the early growth of the channel, or if MTD processes created them, and the channel infilled the newly created space. Regardless of the timing, the channel is evidence for incision in the areas that lack large slide blocks.

6.6. Scaling relationships between slope stratigraphic elements

Statistical analyses were undertaken to record the scaling relationships between width and height of different stratigraphic elements, in this case the of depocentres, channels and blocks associated with MTD A (Gamboa and Alves, 2015a) (Table 6-1). Log-log plots were used to compare the width:height ratio between each of the elements (Figs. 6.12 – 6.16). Width:height ratios of the blocks range from three (3) to 15, and the mean is eight (8) (Fig. 6.12). Most of the blocks lie within a dense cluster of ratios varying from 6 to 10, as the standard deviation

Fig. 6.10 (*next page*) TWT structural map of the main submarine channel formed directly over the striations observed on Figure 6.8. The channel has a similar fan shape geometry at its terminus. The map of M_3 is included in grey, to distinguish the studied submarine channel.

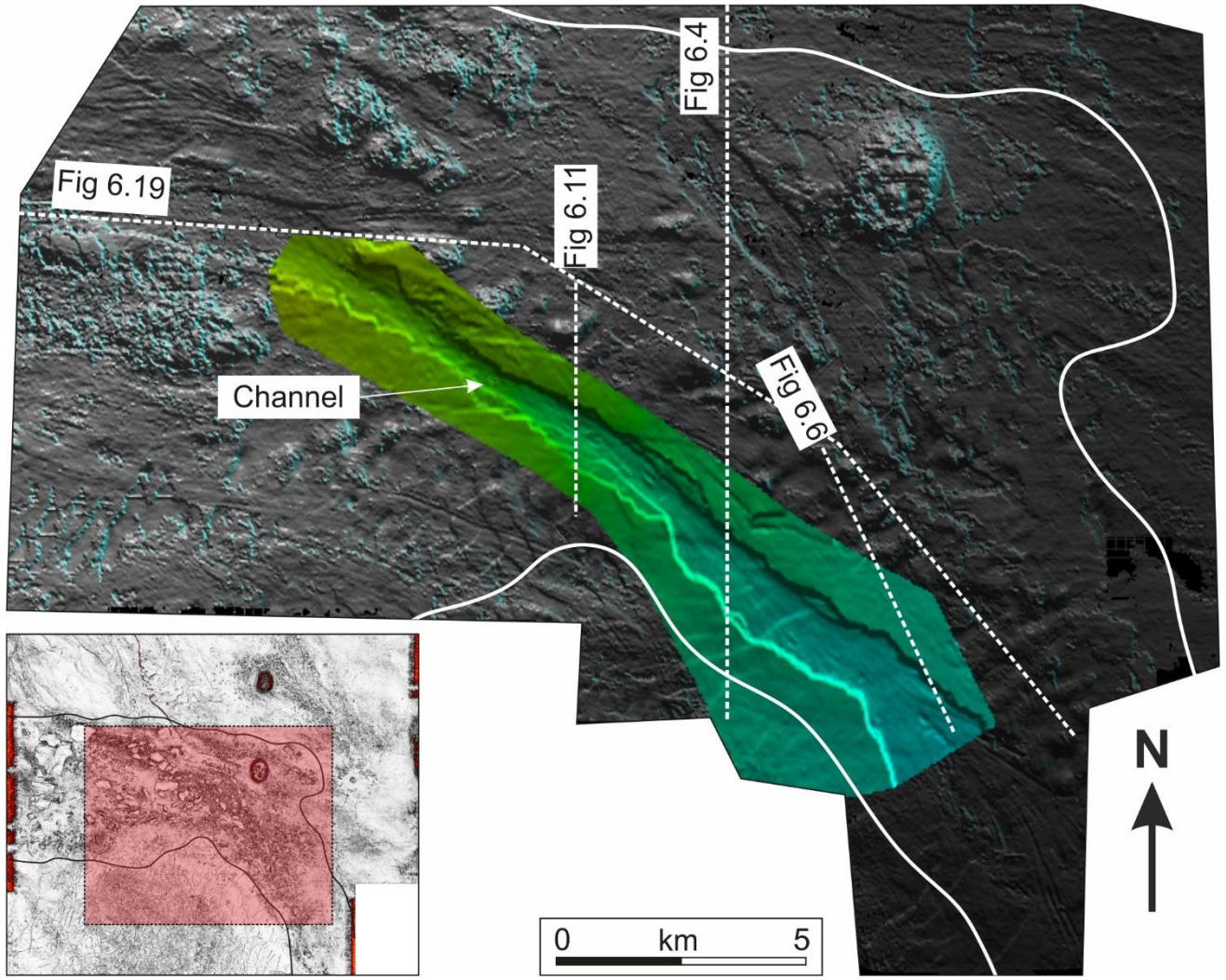
Fig 6.19
Fig 6.11
Fig 6.4
Fig 6.6
Channel
N
0
km
5

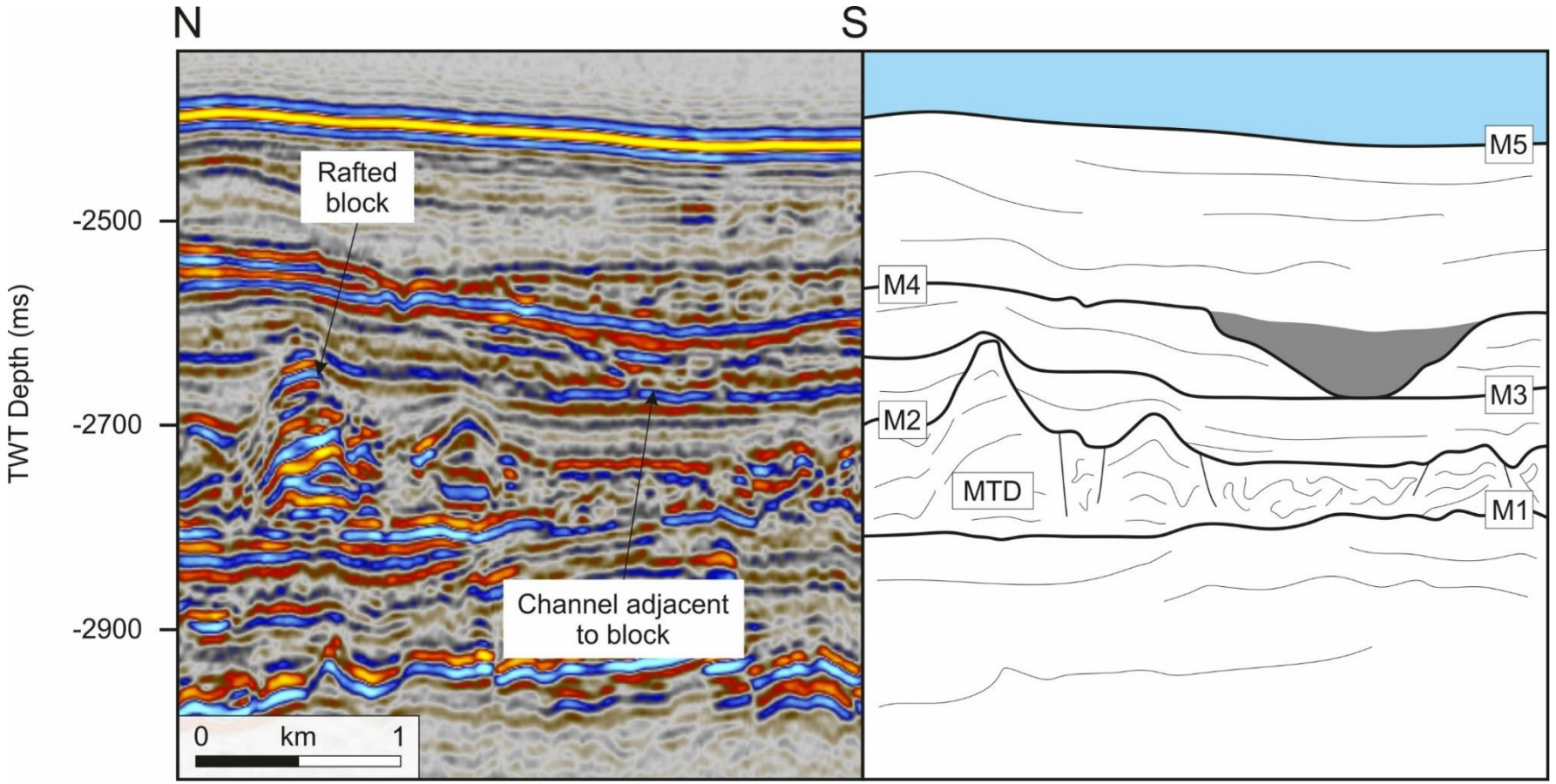

Fig. 6.11 Seismic cross-section through the submarine channel and blocks on its margins. The interpreted profile next to it highlights the key horizons and the morphology of the channel and blocks. The submarine channel is bound by M_3-M_4 and occurs directly over the debrites. A small anticline was formed over the rafted blocks along M_4. Location of the seismic profile is shown in Figure 6.10.

is two (2). The minimum and maximum ratios for the depocentres were seven (7) and 39 respectively, with a mean of 18 (Fig. 6.13). The standard deviation is six (6), so most of the depocentres lie within a ratio of 12-24. The submarine channels have higher width:height ratios, ranging from 17 to 30, with a mean of 23 and a standard deviation of 4 (Fig. 6.14). Figure 6.15 shows regions where values overlap in dark grey and similar ratios can be expected between channels and depocentres, and blocks and depocentres. Results show there is a linear scaling trend; the wider each element is, the taller it is expected to be. Although their trends are similar, there is an obvious decrease in width:height ratios when comparing the stratigraphic elements in the overburden (channels and depocentres), with those emplaced in MTD A (blocks) (Fig. 6.15).

These results are compared with width and height measurements from different stratigraphic elements in the literature. These include MTD blocks (Moscardelli and Wood, 2008, McHargue et al., 2011, Omosanya and Alves, 2014, Gamboa and Alves, 2015a), different elements from within a channel system (Clark and Pickering, 1996, Babonneau et al., 2002, Deptuck et al., 2007, Di Celma et al., 2011, Gamboa and Alves, 2015a, Qin et al., 2017, Gong et al., 2016), landslides, debris flows and MTDs (Hampton et al., 1996, Masson et al., 2006, Gamboa and Alves, 2015a), and plunge pools (Lee et al., 2002). All these data are compiled on a graph (Fig. 6.16). The data includes 140 measurements, ranging from scales of 10s of metres to 10s of kilometres, and there is a high density of

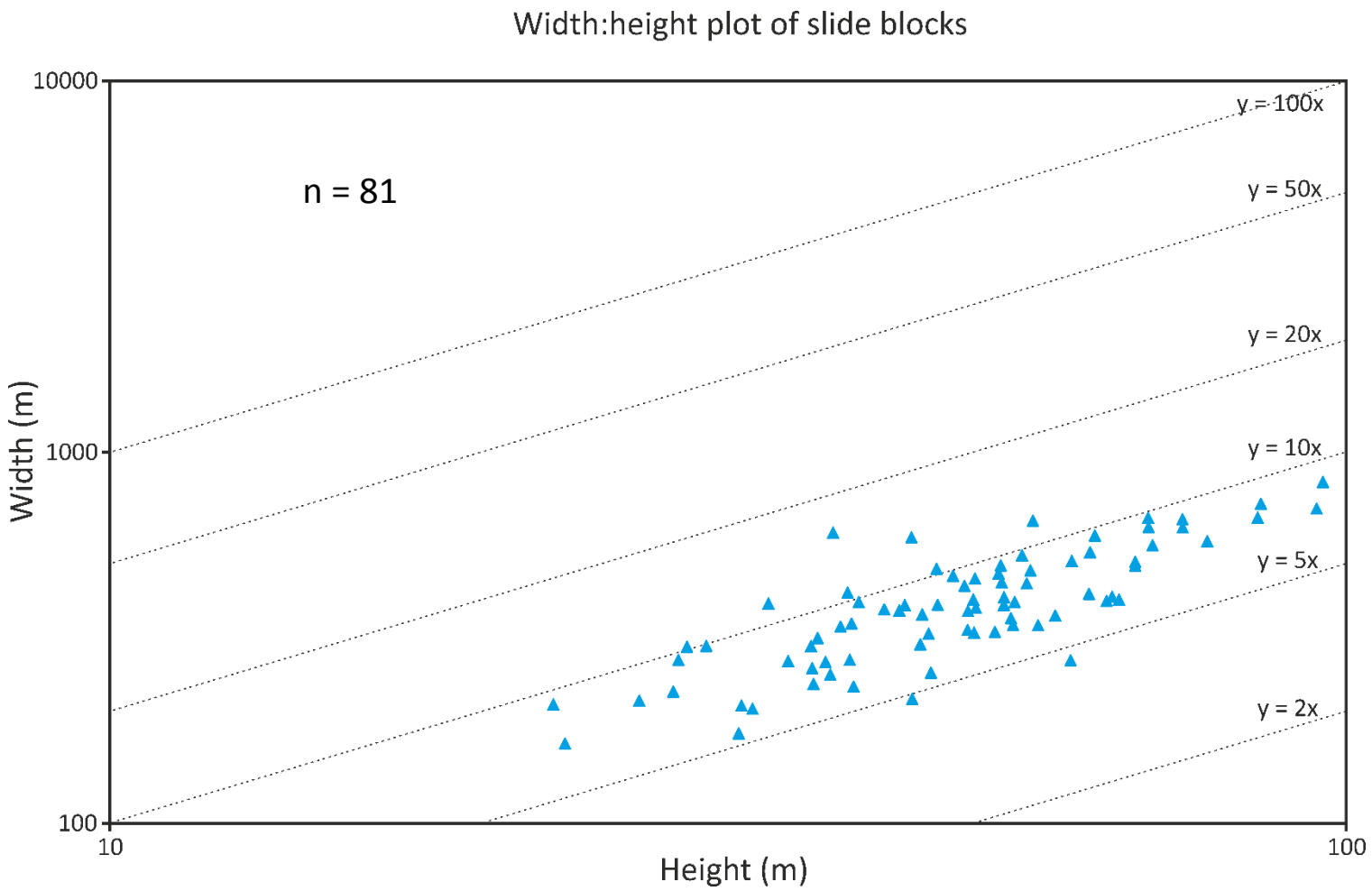

Fig. 6.12 Log-log plot of the width:height ratios of slide blocks within MTD A.

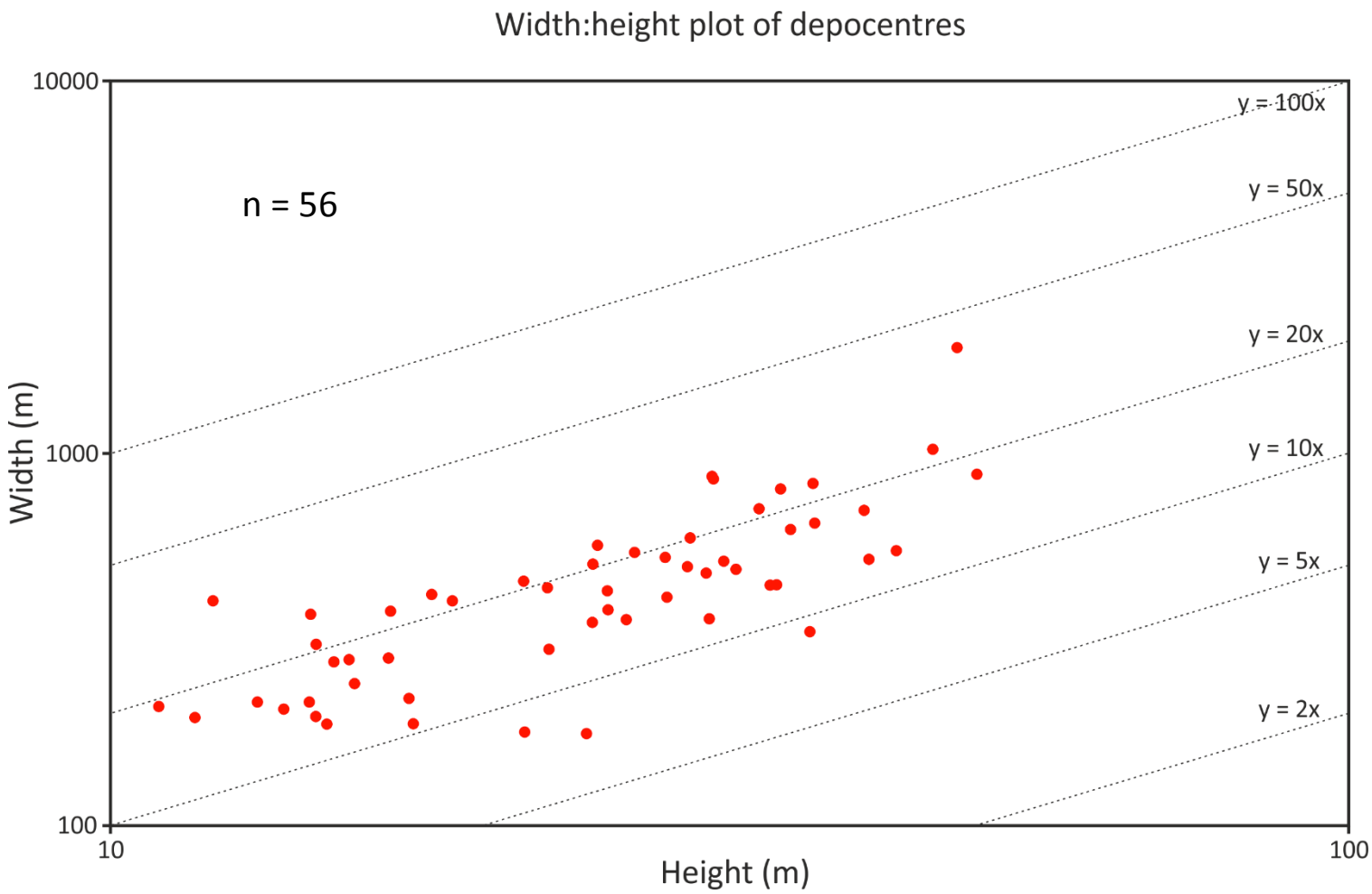

Fig. 6.13 Log-log plot of the width:height ratios of depocentres above MTD A, along horizon M_3.

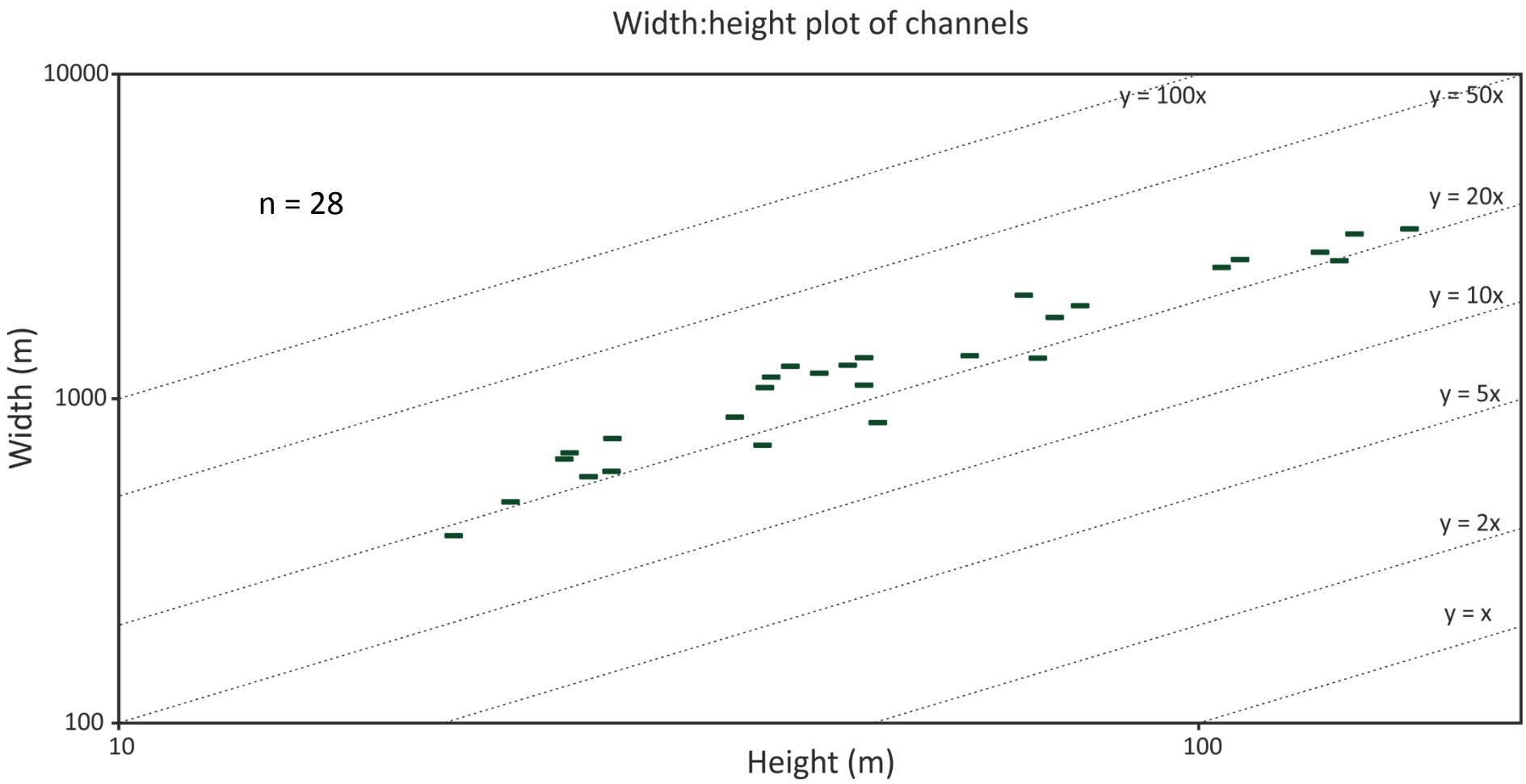

Fig. 6.14 Log-log plot of the width:height ratios of channels overlying MTD A.

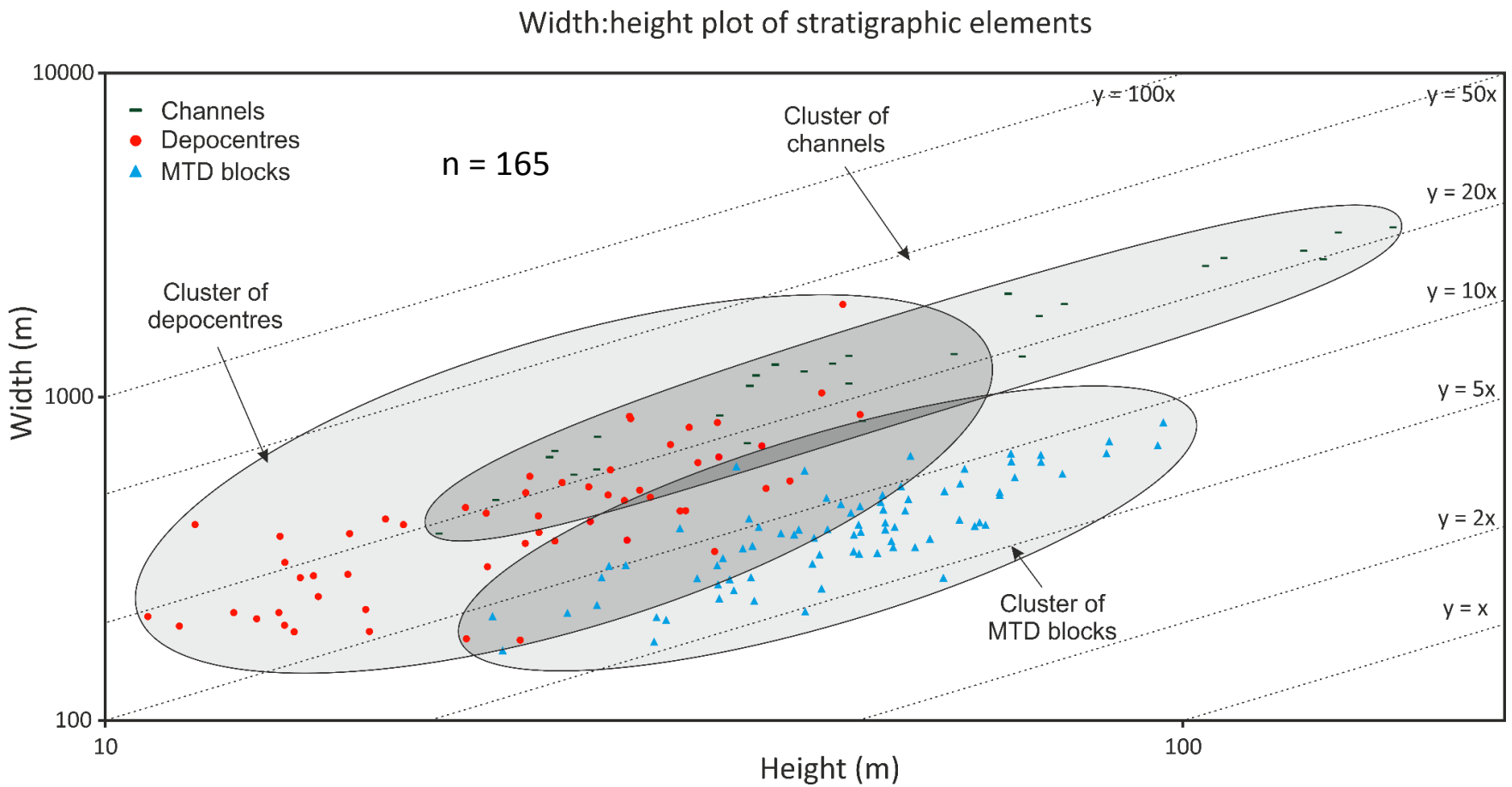

Fig. 6.15 Compilation of the log-log plots for each stratigraphic element in Figures 6.12 – 6.14. Ellipses have been drawn around all of the measurements for each discrete feature (MTD block, depocentre, and channel). The dark grey regions where they overlap are areas with similar ratios for different elements.

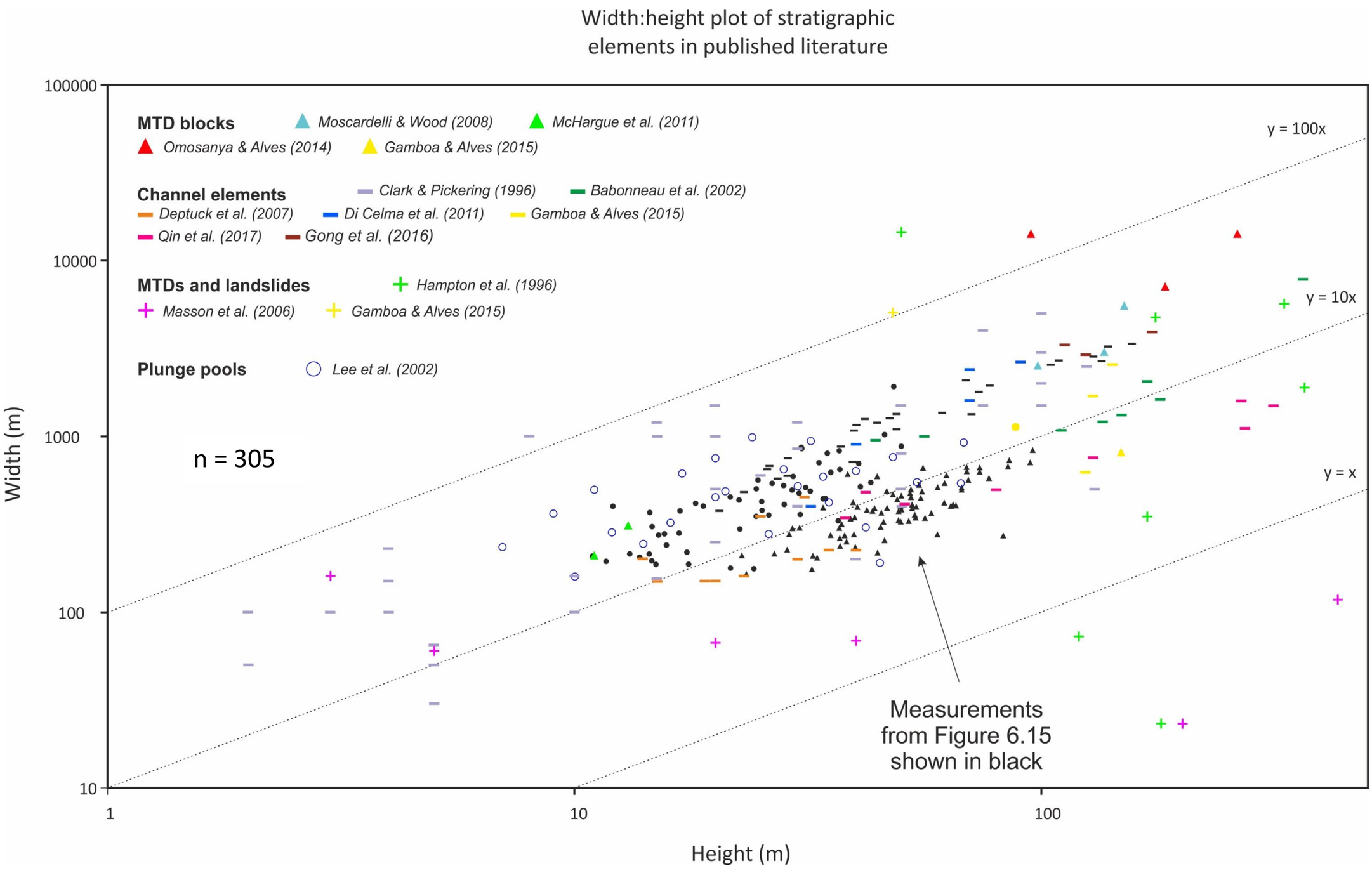

Fig. 6.16 Width:height plots comparing stratigraphic elements observed in this study with previous publications (*Clark and Pickering, 1996; Hampton et al., 1996; Babonneau et al., 2002; Masson et al., 2006; Deptuck et al., 2007; McHargue et al., 2011; Di Celma et al., 2011; Omosanya and Alves, 2014; Gamboa and Alves, 2015; Gong et al., 2016; Qin et al., 2017*). The measurements from this study are shown in black.

Measurements from this study

Element description	Number	Maximum width (m)	Minimum width (m)	Average width (m)	Maximum thickness (m)	Average thickness (m)	Average width:thickness
MTD blocks	81	1066	163	402	96	51	8
Depocentres above M_3	56	1783	136	851	50	26	18
Channels above M_3	28	3321	380	1450	156	62	23

Measurements from literature

Element description	Number	Maximum width (m)	Minimum width (m)	Average width (m)	Maximum thickness (m)	Average thickness (m)	Average width:thickness	Reference
Channel and thalweg elements	36	5000	30	950	130	37	31	*Clark & Pickering, 1996*
Submarine landslides	20	14545	1.36	2096	5000	1273	17.5	*Hampton et al., 1996*
Channels	10	11900	950	3593	1350	314	13.1	*Babonneau et al., 2002*
Plunge Pools	25	986	159	507	68	29.2	21.64	*Lee et al., 2002*
Debris flows	8	160	3	75	2000	338	8.9	*Masson et al., 2006*
Channel fill	11	450	150	219	40	24.3	9.44	*Deptuck et al., 2007*
Mass Transport Complex (MTC)	3	5500	2500	3667	150	128	28.1	*Moscardelli & Wood 2008*
Channel belt	5	2650	400	1690	90	60.4	24.3	*Di Celma et al., 2011*
MTDs	2	307	206	257	13	12	21.2	*McHargue et al., 2011*
MTDs	3	14000	7000	11667	263	181	80	*Omosanya & Alves, 2014*
Depressions, MTDs and canyons	6	5060	624	1978	148	113	27	*Gamboa & Alves, 2015*
Channel complex	3	3930	2920	3390	172	136	25.3	*Gong et al., 2016*
Channels and valleys	8	1602	345	839	314	149	7	*Qin et al., 2017*

Table 6-1 Summary table of the different measurements taken for each architectural element studied (Fig. 6.15), and the measurements from literature (Fig. 6.16).

measurements within the boundaries of those from this study. Scaling trends observed in data from this study are consistent with stratigraphic elements from literature. Mass-transport deposits and landslides occupy the lower width:height ratios, whereas channel elements have larger width:height values (Fig. 6.16). The blocks show a wider range in width:height values, though all are greater than the ones in MTD A. Strikingly, nearly all the data on the graph falls within width:height ratios between 5 and 35. This suggests that the scaling trend observed between blocks, channels, and depocentres can be applied to a variety of other stratigraphic elements on continental margins. However, caution needs to be taken when comparing stratigraphic elements in different settings. Without knowing the stratigraphic and structural relationships between individual elements and completing detailed analyses of the features (as performed in this study), scaling trends would render meaningless.

Isochron maps were created for different units in this study area by Alves (2010), Alves and Cartwright (2010), Omosanya and Alves (2013), Gamboa and Alves (2016), Gamboa et al. (2010), but none of the maps produced have been high enough quality to resolve smaller features such as the linear depocentres on the margins of MTD A. Isochron maps were used to help understand the size, geometry and timing of creation of depocentres above this same MTD (Figs. 6.17 and 6.18). Figure 6.17 represents the thickness between M_3 and M_4. It shows the linear depocentres that formed above M_3 along the southern margin and the distal parts of MTD A (Fig. 6.17). It also highlights the thickness increase

downslope along the axis of MTD A. Post-MTD A deposition was concentrated above the MTD itself, away from the slide blocks. In similarity to Figure 6.17, an increase in thickness downslope suggests accommodation space was still present after MTD A was buried by, at least, horizon M_4 (Fig. 6.18). Sediment fairways are displayed on the isochron map as dark purple, i.e. the thickest sediment packages (Fig. 6.17). These are relatively linear features orientated along the flow direction of MTD A. Each channel overlies the debrites and flowed through the chasms between blocks. Blocks that were still exposed on the seafloor at the time of M_4 deposition are red. Blocks highlighted in yellow were buried and structural relief over them was created by differential compaction.

Figure 6.18 is an overlay of two separate maps: a) TWT structural map of the seafloor, b) an isochron map of the overburden (M_2-M_5). Blocks within MTD A are easily identifiable because they were positive topographic features and have less strata overlying them than surrounding debrites. The boundaries of MTD A correlate with a thicker sediment package in the overburden (red colour). This represents the folding of the seafloor over MTD A (Fig. 6.3). One final feature of interest is the location of a channel on the present-day seafloor over MTD A (Fig. 6.18). The anticline has created an irregular seafloor, causing the channel to form along its axis. Like the channel investigated in Figure 6.10, this one flows between the largest blocks and over the debrites. Therefore, the blocks are still impacting the distribution of sediments on the present-day seafloor.

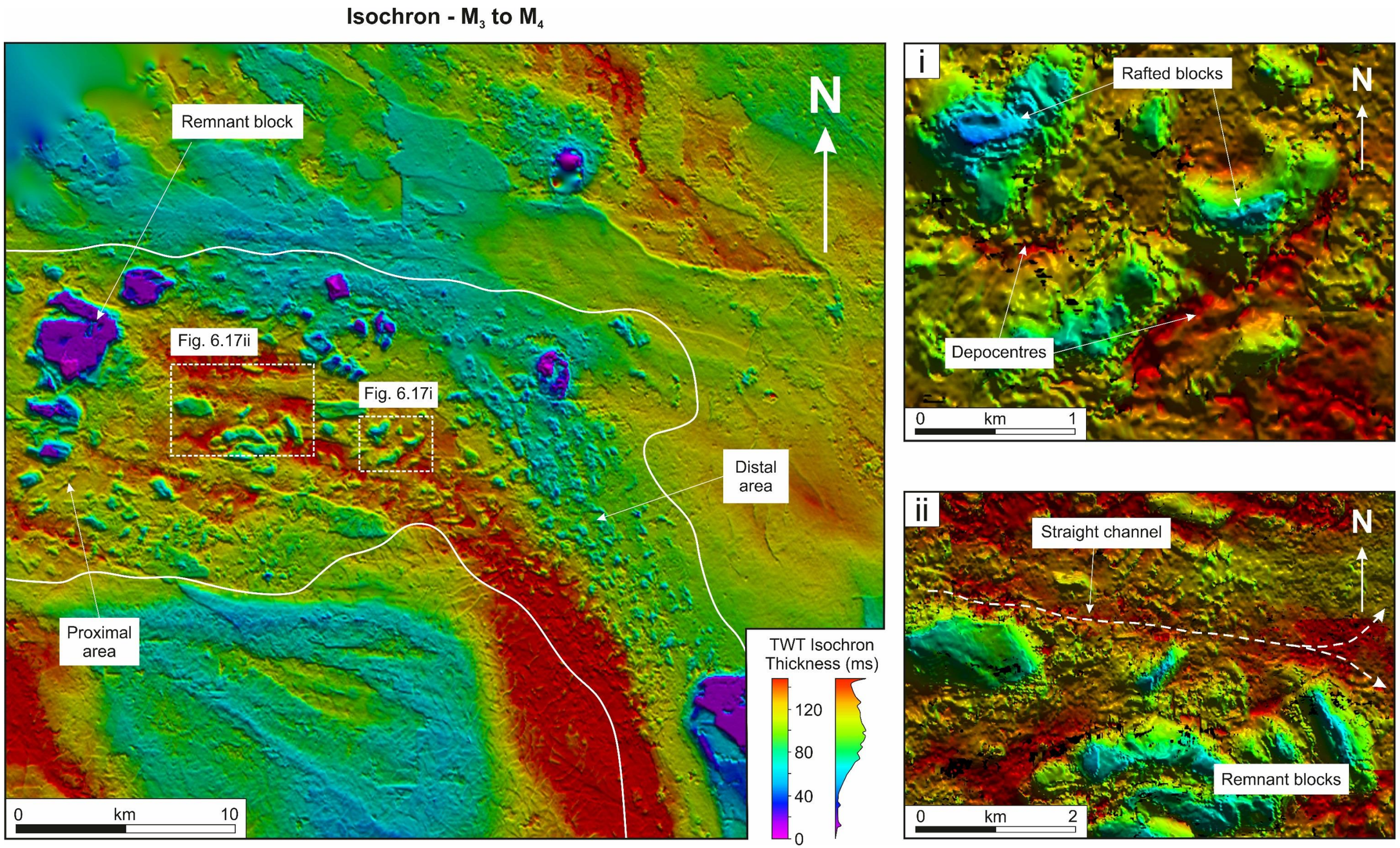

Fig. 6.17 Isochron map between M_3 and M_4 projected onto Horizon M_3. Key characteristics are highlighted in Figures 6.17i and 6.17ii: (i) depocentres and ridges are formed over rafted blocks; (ii) submarine channel in overburden units.

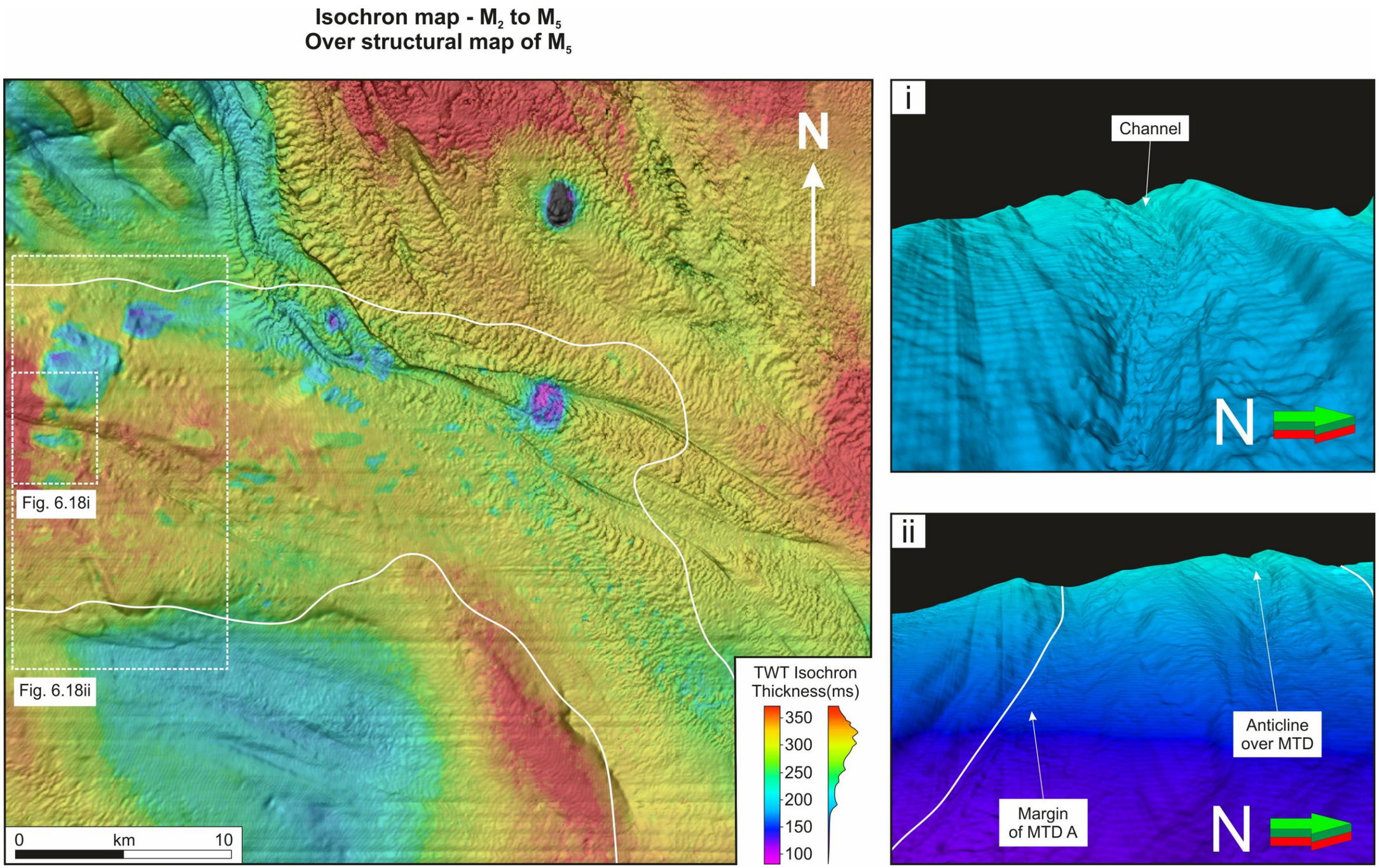

Fig. 6.18 Composite map showing an **i**sochron map of M_2 to M_5, overlying a structural map of the seafloor. This map shows the thickness of the overburden strata relative to MTD A and the features on the present-day seafloor that resulted from differential compaction: (i) channel over the axis of MTD A flowing over a chasm separating two distinct blocks; (ii) anticline formed over MTD A.

6.7. Discussion

6.7.1. Processes generating seafloor depocentres offshore Espírito Santo

The results obtained from seismic interpretation show a relationship between blocks within the MTD and overlying depocentres. As previously suggested, only those blocks that were positive relief structures after emplacement have anticlines situated over them, flanked on each side by depocentres. This is evidence for the control of the blocks within the MTD on the evolution and spatial distribution of depocentres. As the seafloor healed, accommodation space between the blocks was reduced (Prather, 2003, Armitage et al., 2009, Shultz et al., 2005, Kneller et al., 2016). The blocks were subsequently buried. Timing of burial is directly related to the size of blocks and position on the slope. Smaller blocks at the toe of the MTD (downslope) were completely buried before M_3 was deposited (Fig. 6.19), whereas larger blocks in the proximal region of MTD A (upslope) still had topographic relief until after the deposition of M_4 (Fig. 6.19). This difference in timing could become an important control on the compaction history, as smaller blocks within the same mass-transport deposit will have undergone differential compaction before the largest blocks.

Near the headwall, the largest blocks in MTD A were still positive-relief structures until after the deposition of M_4 (Fig. 6.19). Loading of the debrites

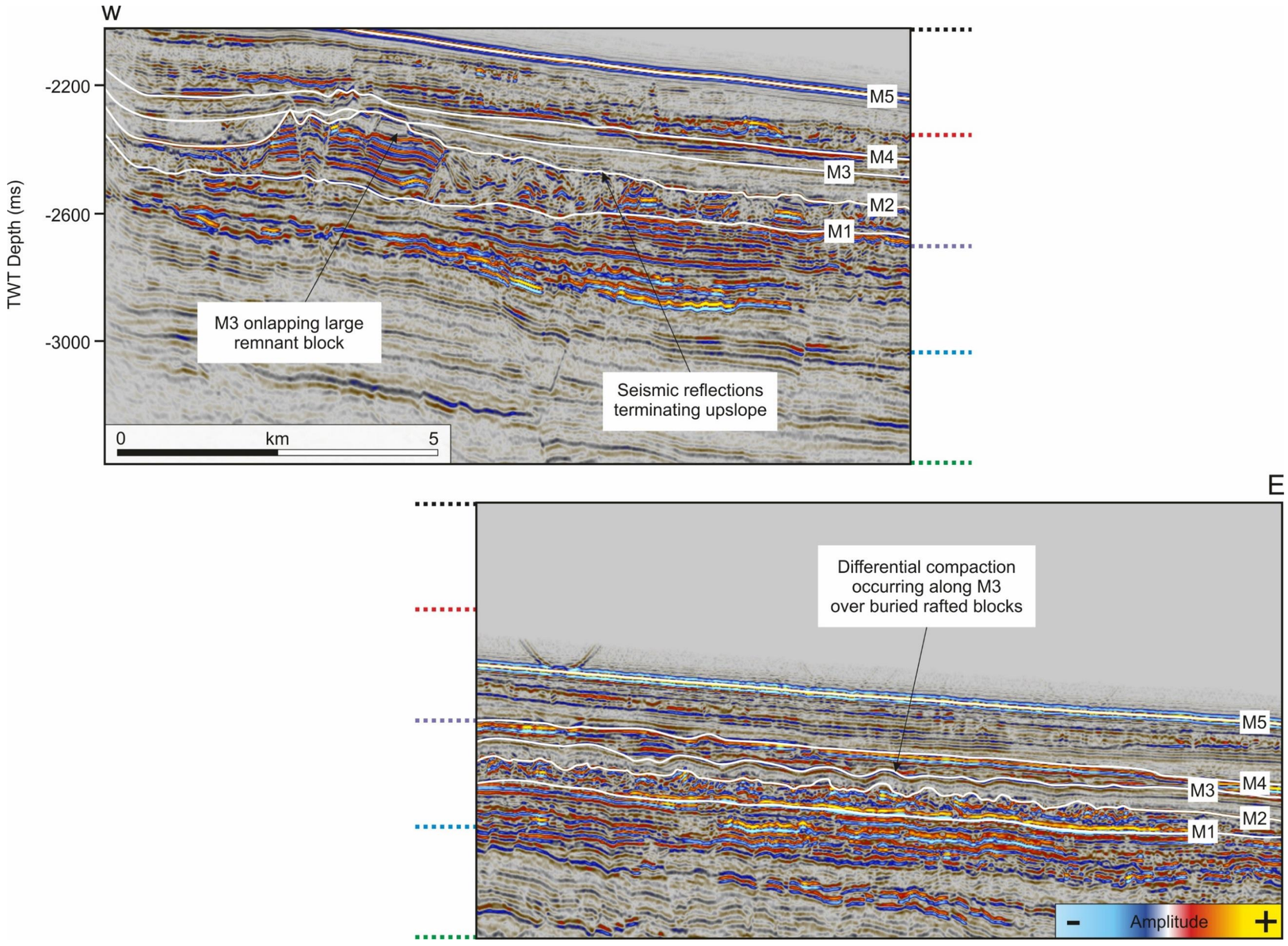

Fig. 6.19 Downslope seismic section showing the main differences in overburden geometry above large remnant blocks and smaller rafted blocks. Seismic reflections in the proximal area (top left box) are relatively flat. Below M_4, they onlap the flanks of the imaged block, or terminate upslope onto MTD A. Downslope (bottom right box), the seismic reflections are folded over the rafted blocks at the level of M_3, but return to almost flat by the time M_4 was deposited. This indicates that differential compaction between the debrites and blocks occurred early in the burial history of such sediment. Dashed coloured lines outside the boxes represents missing seismic data and connect the two seismic lines. Location of seismic line in Figure 6.10.

between the blocks would cause them to start compacting before the blocks were buried. Evidence for this process can be seen in Figure 6.5a. Horizon M_3 is the top of the healed stratal package between the blocks and onlaps the sloping edge of a large block. This horizon is tilted towards the top surface of the block, due to the compaction of debrites (Fig. 6.5a). This same geometry is replicated in the seismic reflections above M_3. Subtle anticlines fold over the top of these blocks, dipping towards the accommodation space created by the compacting debrites on both sides. The creation of accommodation space from differential compaction enhanced the size of depocentres over the debrites, even after the blocks were completely buried.

In the distal parts of MTD A, the blocks were completely buried with >50 ms (45 m) of sediment prior to the deposition of M_3 (Fig. 6.4). Continuous seismic reflections over the MTD in this area corroborate this interpretation. Here, the seafloor had completely healed prior to compaction (Armitage et al., 2009). However, as seen in the seismic data (Fig. 6.5b) and the structural map of M_3 (Fig. 6.20), there are elliptical depocentres spaced at regular intervals in the strata immediately above the blocks (M_3-M_4). Two geological features may explain the evolution of the depocentres that dominate the distal part of MTD A: a) smaller rafted blocks that rise above the debrites (Fig. 6.21a), and b) faults related to the underlying salt structures (Fig. 6.21b). The faults in this region deform rocks below MTD A, rarely displacing strata above M_1. This has been attributed to the upper tip of the faults being eroded as MTD A was emplaced (Alves et al., 2009,

Omosanya and Alves, 2013). Were the faults to propagate through MTD A, the depocentres could be linked to fault-related folds as there are mechanical contrasts between the MTD and its cover (Hardy and McClay, 1999). However, there is an obvious orientation to these structures, and fault scarps are easily discernible. These fault scarps occur south east of the margins of MTD A (Fig. 6.20). In contrast, the plan view geometry of depocentres is much more elliptical than the fault-related folds and they are also symmetrical in cross section (Fig. 6.21). Between each of the depocentres there are a series of small rafted blocks. Horizon M_3 folds over the top of these blocks, creating gentle anticlines (Fig. 6.20).

Because of the continuous seismic reflections over the blocks and the spatial relationship between the blocks and depocentres, it is thought that the depocentres were enhanced (if not formed) by differential compaction: a larger load over the debrites led to greater compaction than the relatively small load over the rigid carbonate blocks. This work attributes the evolution of depocentres to differential compaction, but faults are known to produce similar features (Sharp et al., 2000, Corfield and Sharp, 2000, Cosgrove and Ameen, 1999). It is therefore important to discuss the differences between the deformation caused by faults and differential compaction in this study, especially as the depocentres are relatively linear, evenly spaced features, and orientated in the same direction as the underlying faults. Primarily, seismic reflections along M_3 deformed by the faults have distinctly different seismic characteristics to the depocentres formed

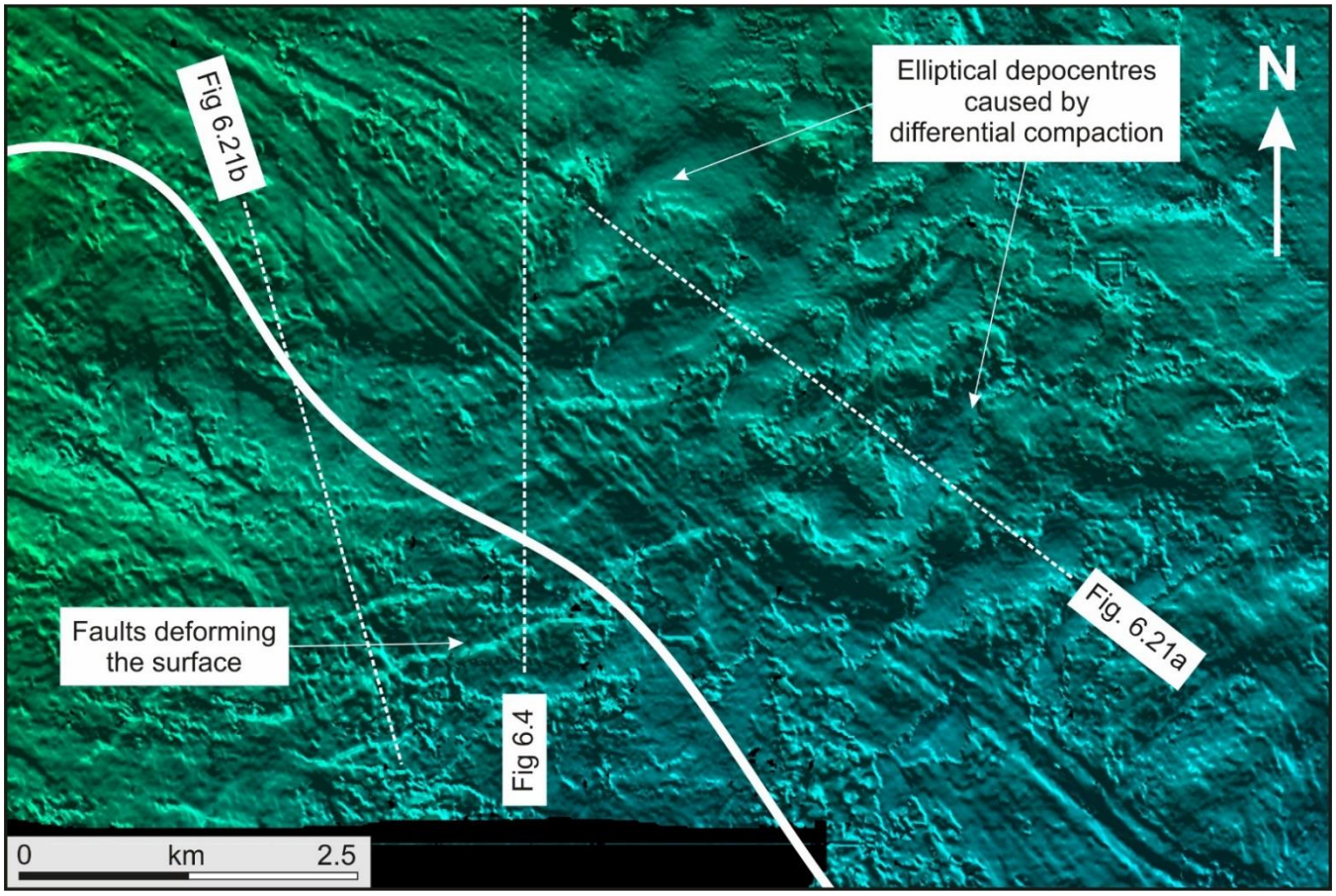

Fig. 6.20 TWT structural map of Horizon M_3 taken further upslope than the map in Figure 6.9. The boundary of the MTD is represented by the white line in the figure. Northwest of the boundary (over MTD A), the sea floor has elliptical-linear depocentres that are regularly spaced and lie perpendicularly to the flow direction of MTD A.

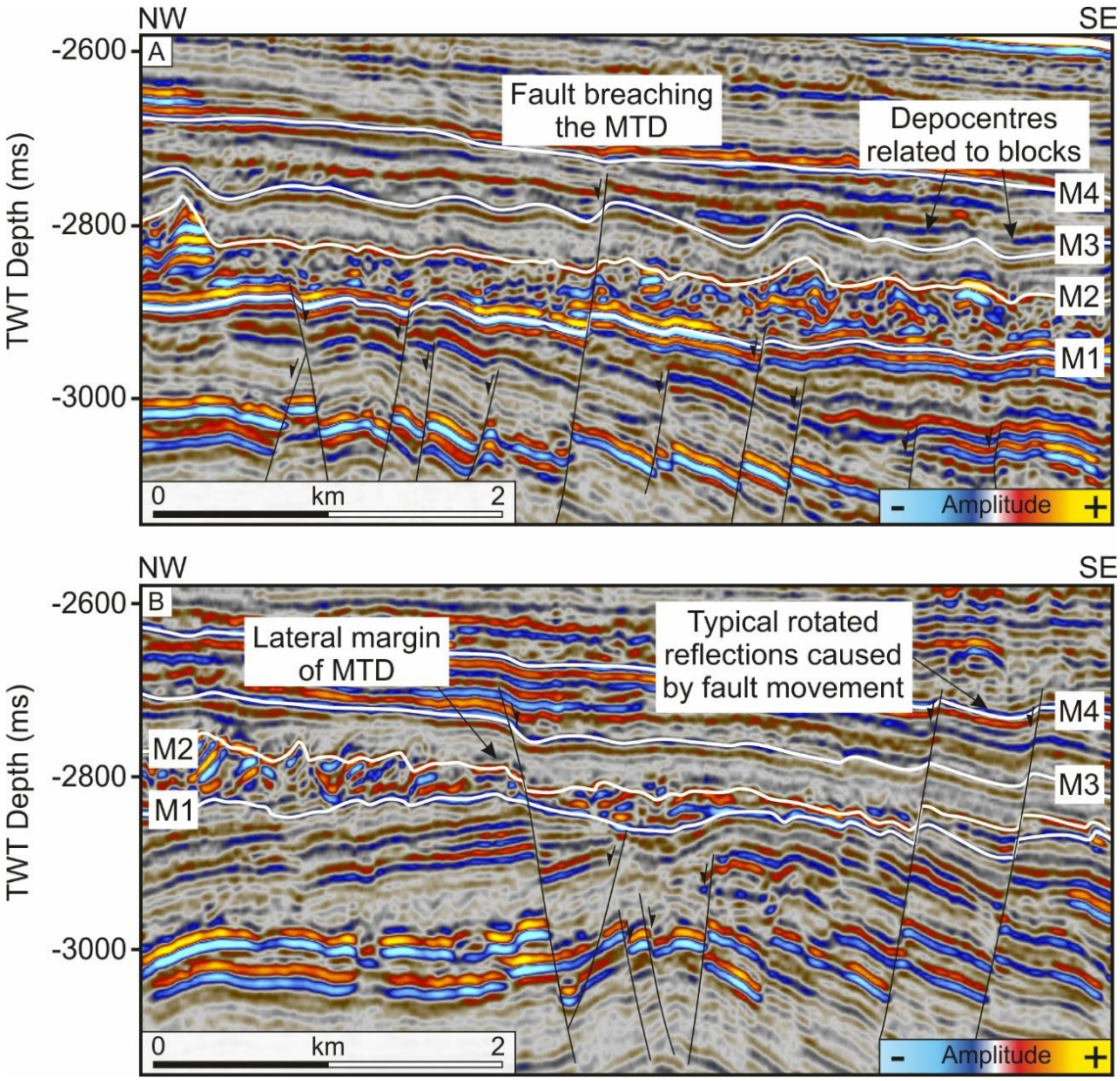

Fig. 6.21 Seismic profiles highlighting the differences between fault-controlled depocentres and block-controlled depocentres. a) The faults do not breach MTD A. It is therefore believed that these relatively symmetrical depocentres were influenced by differential compaction. A single fault passes through MTD A, affecting the overburden in a typical 'rotated-block' deformation style, *i.e.* the downthrown side rotates towards the fault surface. To the southwest of where MTD A pinches out, linear features are interpreted as faults. (c) The seismic line shows the imaged faults deforming strata in which MTD A is not present, therefore forming asymmetrical depocentres.

over blocks in the same horizon. Most significantly, the faults create asymmetrical depocentres as the downthrown footwall rotates towards the fault scarp (Fig. 6.21b). The depocentres over the blocks are symmetrical in cross section and the lowest point is directly above the debrites (Fig. 6.21a). In addition, the hanging wall of some of the faults breaching M_1 lie beneath the middle of the depocentres (Fig. 6.21a). This contradicts the typical model of normal faults, where the hanging wall is up thrown. Also, the change in style between compaction-related depocentres and fault-related depocentres seems to be concurrent with the presence of MTD A, which prevents most faults from propagating through and above it (Fig. 6.21).

6.7.2. Impact of seafloor roughness created by MTD A

Once MTD A was emplaced, there were sharp topographic variations on the seafloor between the blocks and surrounding debrites. Some blocks protruded >50 m above the height of the debrites (Fig. 6.3). This seafloor roughness likely controlled subsequent sediment distribution (McAdoo et al., 2004, Armitage et al., 2009, Alves, 2010, Kneller et al., 2016). Chasms between the blocks, ranging from 100 m – 1 km wide, confined sediment fairways, as turbidity currents bypassed them downslope (Armitage et al., 2009). Due to their varying heights, the tops of some blocks were still exposed after others had been buried. This is most prominent when comparing the distal blocks to the proximal blocks;

there was >100 ms of sediment deposited over the distal blocks before the proximal blocks were buried (Fig. 6.19). Differential compaction over smaller blocks maintained seafloor roughness shortly after burial. It was therefore possible that large, exposed blocks confined sediment fairways in the proximal area, whilst the same sediment fairway was confined by compaction-related anticlines over the smaller blocks in the distal area.

The striations found within the map of M_3 demonstrate the influence the blocks exert on sediment fairways (Fig. 6.8). As suggested by Gee et al. (2005) and Posamentier (2003), striations can represent sediment pathways. On the map, the sediment fairway is bisected by a slide block; the striations split and divert around the north and south of it (Fig. 6.8). Directly overlying this fairway is a channel confined by compaction-related anticlines and large blocks in MTD A (Fig. 6.11). The base of these channel lies on horizon M_3 and the upper surface is interpreted as M_4 (Fig. 6.11). Few blocks were actually exposed on the seafloor at the time M_4 was deposited, but the compaction-related anticlines were still affecting the seafloor topography. We interpret these anticlines to be responsible for confining the channel. Other channels are observed on the interpreted seismic volume (without the striated bases), and they all seem to lie lateral to the blocks (Fig. 6.7).

The isochron maps agree with the channels seen on seismic sections (Figs. 6.7, 6.17 and 6.18). Channels overly the debrites, forming linear features parallel

to the flow direction of MTD A. Also, the thickest packages initiate upslope from chasms between the largest blocks (Fig. 6.17). Topographic expression of blocks on the seafloor in the proximal parts of MTD A confined downslope flows, synchronous with compaction-related anticlines over the blocks confining sediments in the distal part. This whole process is summarised on a block diagram in Figure 6.22.

Trends observed in the width:height graph provide scaling relationships between the stratigraphic elements. The oldest elements (MTD blocks) have the lowest width:height ratio. Younger elements width:height ratios increase (Figs. 6.15 and 6.16). Thus, during progressive burial, the influence slide blocks have on the size of stratigraphic elements diminishes. This is an important conclusion: the interpreted slide blocks can control the dimensions and location of younger, overlying stratigraphic elements, but will only create stratigraphic elements with relatively higher width:height ratios.

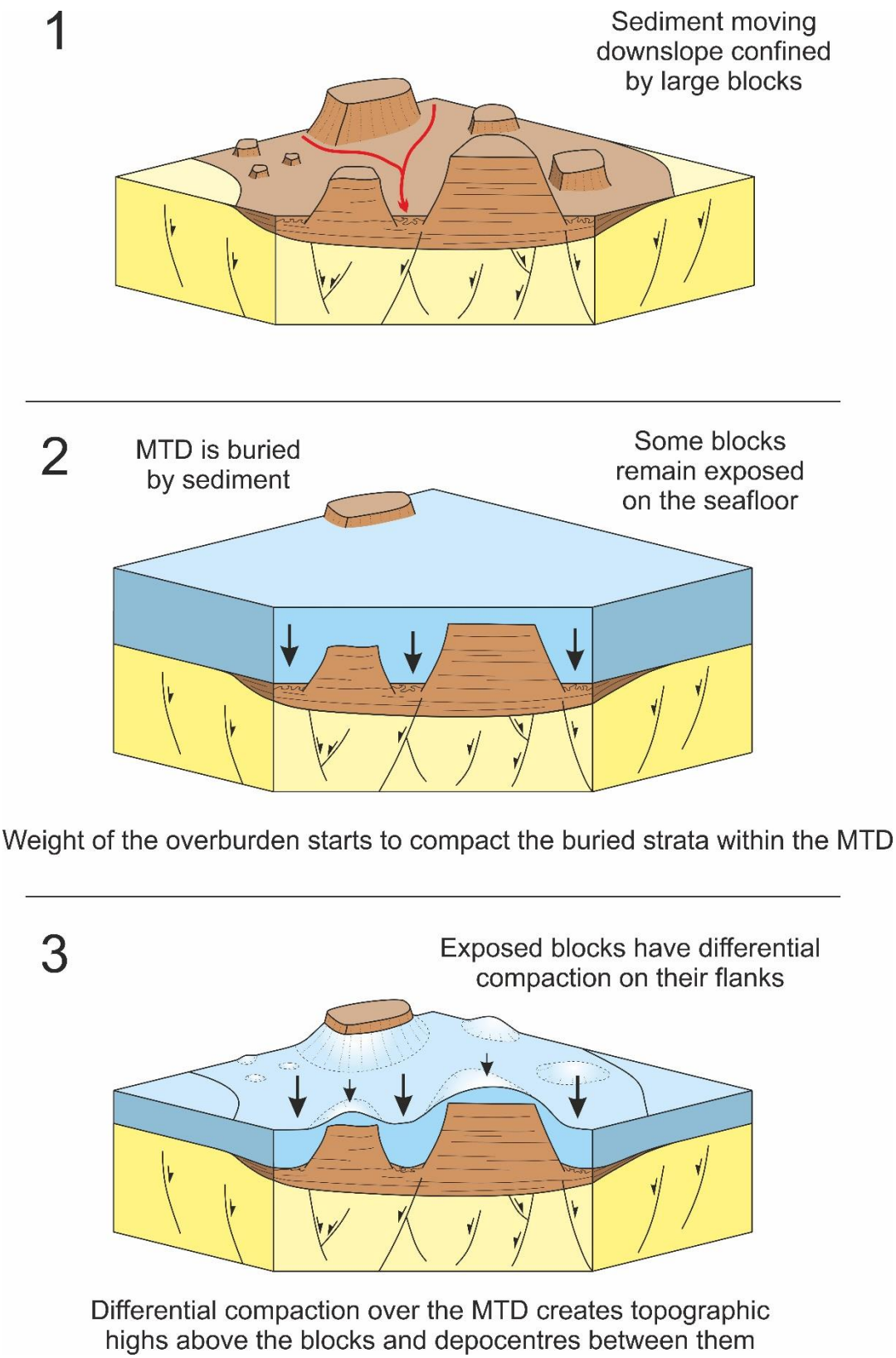

Fig. 6. 22 (*continues next page*) Block diagrams showing the evolution of sediment distribution pathways influenced by differential compaction above MTD A. Stages 1-5 represent important controls on sediment distribution.

4

Turbidites are deposited between the anticlines

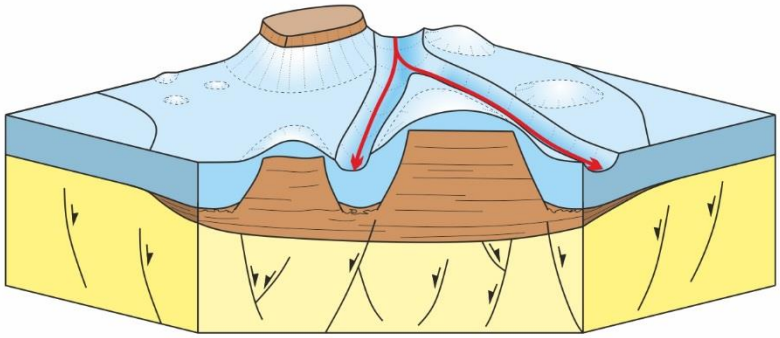

Channels cut down in the overburden and are bifurcated by the anticlines over the blocks caused by differential compaction

5

Channels formed in the overburden are buried

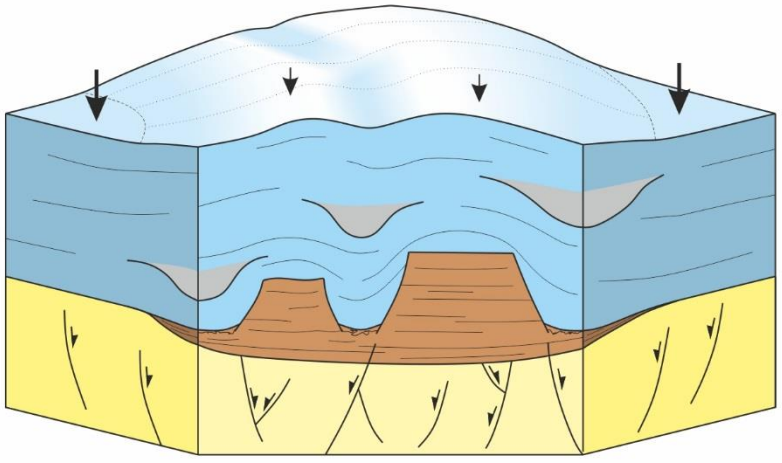

Differential compaction continues to control present day seafloor topography

6.8. Chapter specific summary

This chapter investigated the effects of differential compaction over remnant and rafted blocks within an MTD. In particular, it focused on the evolution and effects of differential compaction on sediment distribution after MTD A was buried. The conclusions are:

- Differential compaction occurred after the rafted and remnant blocks had been buried by at least 50 ms (~45 m) of sediment, i.e. after the deposition of horizon M_3. We interpret this as the result of lithological contrasts between calcareous blocks from the Caravelas Formation and surrounding debrites.
- Post burial, differential compaction led to the formation of anticlines and associated depocentres over MTD A. Present-day strata is still deforming over the largest blocks located in the proximal area of MTD A.
- Differential compaction was not synchronous across the whole of MTD A. Some blocks were still exposed in the proximal areas after others in the distal areas had been buried by >100 ms (~90 m) of sediment.
- Slide blocks controlled sediment distribution over MTD A: sediment fairways were confined to the areas between the blocks.

After differential compaction had occurred, the compaction-related anticlines continued to control sediment distribution downslope. This maintained the seafloor roughness for >5 Ma after MTD A was buried. Figure 6.10 shows an example of this.

- Log-log plots of width and height prove that there is a relationship between the size of slide blocks and depocentres. Large blocks can influence the formation of stratigraphic elements in the overburden, which tend to have higher width:height ratios than the blocks. Understanding these relationships can help predict the effects of differential compaction over shallow MTDs in similar passive margins, and where depocentres are likely to form.

We have shown one example of the impact that differential compaction, promoted by a blocky MTD, can have on the seafloor topography and sediment distribution. Seafloor roughness, originally created by the blocks, will be maintained over topographic features if differential compaction occurs after burial. This can potentially confine flows and channels. Smaller depocentres can potentially pond significant volumes of sediment travelling downslope as the channels pass through them.

CHAPTER SEVEN

General summary of findings and discussion of results

7. Summary and Discussion

7.1. Preamble

Each of the chapters in this thesis discusses the influence of local structures on the development of subtle traps and how significant they are to petroleum systems. This chapter initially summarises the main findings of this thesis (Fig. 7.1). It then re-examines the seismic data to evaluate new subtle traps. In addition to the analyses based on seismic volumes from the Broad Fourteens and Espírito Santo basins, a seismic volume from the Taranaki Basin (New Zealand) is introduced in this chapter. With a more complete analysis of subtle traps in multiple geological settings and geographic locations, a classification scheme is proposed for subtle traps associated with differential compaction.

As previously mentioned in *section 1.1*, subtle traps comprise true stratigraphic traps (a lateral change in facies or reservoir properties), palaeogeomorphic traps (shape of the land or seabed surface), or combinations of both (Martin, 1966, Halbouty, 1969, Gabrielsen et al., 1995). Understanding subtle stratigraphic traps requires a detailed knowledge of subsurface lithologies, primarily those acquired from borehole data. Palaeogeomorphic traps, in contrast, demand the knowledge of subsurface structures on seismic data. The analyses undertaken in *Chapters 5* and *6* lack systematic borehole data, but some degree of lithological context exists. Their results focus on subtle structural traps,

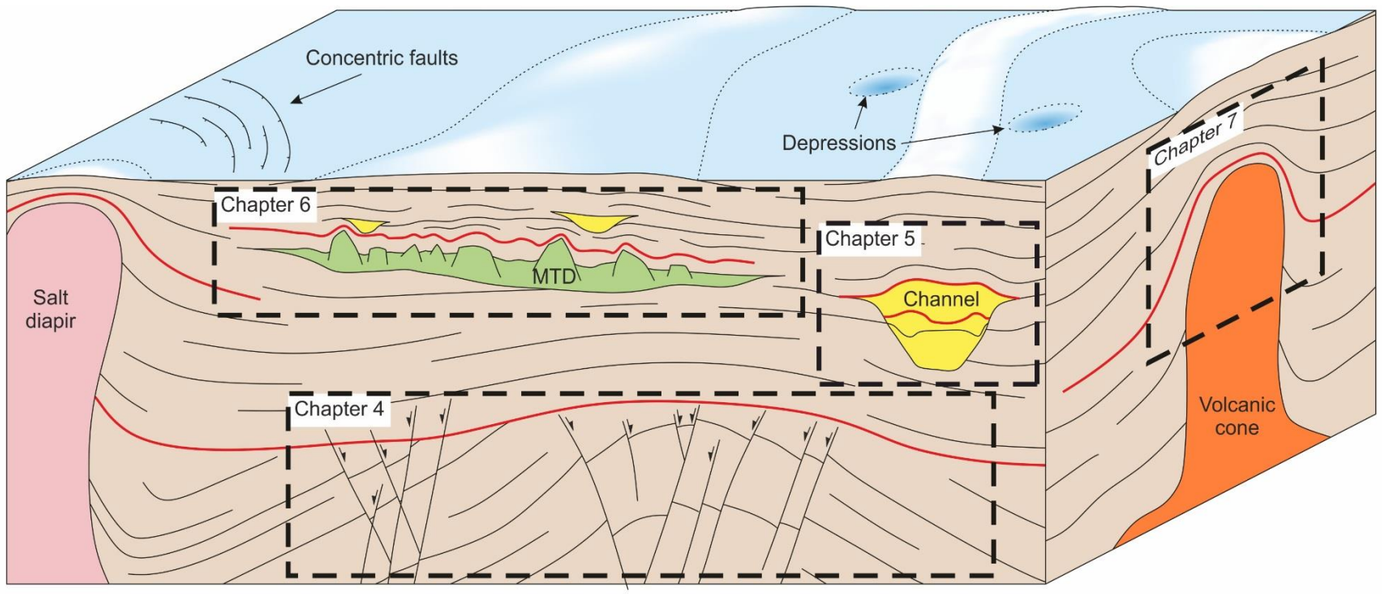

Fig. 7.1 Schematic representation of all the results in this thesis in the form of on one geological block diagram. The seismic surveys used in this work are highlighted on the maps.

using high quality 3D seismic data. *Chapter 4* uses robust well constraints within the seismic volume, and these constraints are used to help ground-truth the structural analyses undertaken in the chapter. In essence, the subtle traps investigated in this thesis formed in response to either differential subsidence (*Chapter 4*), or differential compaction (*Chapters 5 and 6*). These processes are considered on different scales in their corresponding chapters; from km-long faults and folds in a salt withdrawal basin (*Chapter 4;* Broad Fourteens Basin), to forced folds over submarine channels that are hundreds of metres wide (*Chapter 5*; Espírito Santo Basin), and depressions reaching tens of metres above a blocky MTD (*Chapter 6*; Espírito Santo Basin).

7.2. Summary of technical results

7.2.1. Chapter 4: Concentric faults and fluid flow

Chapter 4 uses 3D seismic data from the Broad Fourteens Basin, Southern North Sea, to understand the causes and evolution of three families of concentric faults (Fig. 7.1). These faults were formed in a salt withdrawal basin, on the crest of an inverted anticline (anticline α), and bounding large rafts (Fig. 4.7). Though initially thought to have formed by forced folding, throw-depth and throw-distance plots revealed complex reactivation and linkage histories along these same faults (Figs. 4.13 and 4.14). After careful interpretation and attribute

mapping, it was concluded that the concentric faults were formed in response to local subsidence during the development of a salt withdrawal basin throughout the Cretaceous. Concentric faults in this ~5 km wide salt withdrawal basin accommodated extension promoted by the removal of Zechstein salt during halokinesis and salt diapirism. As the diapir was a circular body, the salt was withdrawn from its periphery and resulting faults were circular in plan view. In contrast, the set of faults on anticline α were created due to extension over the footwall block of a large raft below. Lateral linkage of fault segments over anticline α led to their characteristic curvature as the faults propagated laterally towards each other and became hard-linked (Fig. 4.14).

These observations were used later to model how the faults would react to relative increases in pore-fluid pressure, simulating the typical conditions of CO_2 injection during carbon capture and storage (CCS) (Arts et al., 2012). Carbon capture and storage involves capturing CO_2 from the atmosphere, fossil-fuelled power plants, or industrial processes, returning it into oil-, gas-, and water-bearing geological formations in the subsurface (Rackley, 2017). Commonly, these formations contain faults that are similar to the study area in *Chapter 4* (Fig. 4.9). Slip tendency analyses highlighted the portions of the interpreted faults that are optimally oriented for reactivation (Figs. 4.17 – 4.20). Leakage factors indicated which parts of the faults are likely to leak gas. Importantly, vertical patches of high slip tendency values roughly correspond to the presence of large fluid escape features that formed during the Late Jurassic (Figs. 4.13 and 4.16).

This is an important discovery; the presence of faults can compartmentalise a reservoir, but it is obvious that by increasing the pore fluid pressure of certain rock types, these fault segments can be reactivated to vertically expel fluid towards the sea floor. Also in *Chapter 4*, Mohr circles were created for different lithologies (representing the average lithology for each rock unit intersected by faults), and the results in this thesis indicate that CCS techniques are viable in the Broad Fourteens Basin if pore fluid pressure within the rocks remains below 30 MPa, at the depth in which the faults are observed. Similar pore fluid pressures are being used at present to store CO_2 in other parts of the Southern North Sea (Arts et al., 2012).

7.2.2. Chapter 5: Differential compaction over channel-fill deposits

The 3D seismic data used in *Chapters 5* and *6* was acquired in the Espírito Santo Basin, offshore SE Brazil (Fig. 2.4). *Chapter 5* focusses on a kilometre-wide anticline (anticline C^1) over buried channel-fill deposits (Fig. 5.2). Anticline C^1 is direct evidence for differential compaction; coarser-grained strata within the main channel complex compacted less than the fine-grained material around it (Fig. 5.3). As a result, the strata overlying the sides of the channel complex subsided more than the strata over its axis, folding these rocks to produce anticline C^1.

An adaptation of the thickness-relief method of Perrier and Quiblier (1974), also used by Alves and Cartwright (2010), proved that differential compaction had started during early burial of the channel complex (Figs. 5.11, 5.12, and 5.13). The method revealed that topographic relief was generated on the sea floor by the channel-fill units at burial depths of less than 200 m. Isochron thickness maps, together with thickness-relief plots, showed that differential compaction varies by up to 80 m from north to south along the channels (Fig. 5.7). Above the channels, large elongate depressions (<1.15 km wide) erode into unit II. They are connected to the channel fill (unit I) by faults with small throws (Fig. 5.15b). The formation of the depressions is attributed to fluid expulsion during compaction: fluids migrated through faults on the channel margins, breaching the sea floor and creating pockmarks. More pockmarks occurred in the north where the magnitude of differential compaction was smaller than in the south. Large pockmarks were observed in the central area of the channel complex (Fig. 5.14*)*. The size of these pockmarks was enhanced by local currents, which removed liquefied sediment from the sea floor (Fig. 5.16).

Within the channel complex per se, differential compaction created smaller anticlines over individual channels (Figs. 5.5 and 5.8). Furthermore, compaction-related anticlines were most developed downslope of knickpoints, where coarse-grained sediment is predicted to have been deposited. These strata onlap the knickpoint face, creating an effective stratigraphic trap (Fig. 5.10). Four-way dip closure of the smaller anticlines isolated the coarse-grained sediment

downslope of the knickpoints, forming 'pods'. Hydrocarbons were putatively able to build up beneath these stratigraphic trap, obeying a 'fill-to-spill' model (*cf*. Schowalter 1979), where the fluids relied on the basal sands of the channel complex to migrate up-dip into the next pod.

7.2.3. Chapter 6: Differential compaction over an MTD

Slope depositional systems above a mass-transport deposit (MTD A) were investigated in *Chapter 6* using a different 3D seismic volume to *Chapter 5*, but also from the Espírito Santo Basin (Fig. 2.4). MTD A comprises slide blocks that were entrained and surrounded by debrites (Fig. 6.3). Proximal to the headwall of MTD A, the blocks are large (up to 5 km wide and 200 ms high) and relatively undisturbed (*i.e.* remnant blocks). Towards the distal region of MTD A, the blocks moved and were deformed (*i.e.* rafted blocks), being much smaller (less than 500 m wide and 100 ms high) - some no thicker than MTD A (Fig. 6.4). Positive topographic relief created by the blocks resulted in a rugged sea floor. Sediment pathways were subsequently confined by remnant and rafted blocks and accommodation space was filled between them. Once the sea floor healed, the blocks were buried (Fig. 6.5).

As the vertical load increased over MTD A, differential compaction took place between the debrites and the blocks, *i.e*. unconsolidated rocks within the debrites compacted more than the rigid blocks. This occurred after ~50 ms (45 m)

of sediment was deposited over MTD A. Compaction-related anticlines were produced over the blocks, which were bounded by depocentres (Fig. 6.5b). Importantly, differential compaction was not synchronous across the whole MTD; remnant blocks in the proximal region were still exposed well after >100 ms (90 m) of sediment had been deposited over rafted blocks in the distal region (Fig. 6.19).

A series of striations lying between exposed remnant blocks and compaction-related anticlines over rafted blocks - along horizon M_3 - represent a sediment transport system (Figs. 6.8 and 6.9). A single cluster of striations marks the base of a submarine channel formed after MTD A was deposited in the Late Miocene (Fig. 6.10). This channel was confined by large, exposed blocks in the proximal region, and by the compaction-related anticlines in the distal region. A block in the centre of MTD A bifurcated the channel, one resulting segment of this latter continuing east, the other deflected south (Fig. 6.8). In the distal region, the channel bypasses a system of elliptical anticlines separated by similarly shaped elliptical depocentres (Fig. 6.9). These small depocentres, less than 1 km wide and 30 ms thick, were a product of differential compaction during very early burial, and thus did not continue vertically above M_4. Nevertheless, these small depocentres may have ponded significant volumes of sediment travelling along the channels.

In Figure 6.15 a log:log graph for the width and height of various stratigraphic elements (blocks, depocentres, channels) associated with MTD A is shown. The relationship between the trend lines for the different elements was analysed in this thesis. All the trends have a similar gradient, but their average width:height ratio is variable. Younger elements have a higher width:height ratio than older elements. This suggests blocks controlled the sizes of depocentres and channels, which are wider and shorter than the former underlying features (*i.e.* MTD A). Therefore, the size of blocks can be used as a predictive tool for the size of overlying stratigraphic features with reservoir potential, such as the depocentres and channels.

7.3. Classification of subtle traps resulting from differential compaction

Different processes can generate prominent folds within a basin; lateral tectonic compression, mass failure, fault propagation, fault drag, igneous intrusions, salt and mud diapirism (Erslev, 1991, Suppe and Medwedeff, 1990, Mitra, 1990, Schlische, 1995, Suppe, 1983, Grasemann et al., 2005, Woodcock, 1976, Cloetingh et al., 1999, Ziegler et al., 1995, Trude et al., 2003, Magee et al., 2013, Hansen and Cartwright, 2006, Davison et al., 2000a, Stewart, 2006). Likewise, differential compaction has been shown to produce folds that are

geometrically similar to those described in *Chapters 5 and 6*. One key difference is the size of the folds created by a passive process such as differential compaction - they have much smaller amplitudes relative to their widths when compared with other types of folds (*e.g.* tectonic or related to magmatism). These low amplitude anticlines and synclines have been previously identified, but no literature has tried to classify them. In part, this is due to the fact that differential compaction often occurs in areas where active tectonics can overprint early deformation during burial, making it hard to distinguish what is purely compaction-related folding from tectonic folding and deformation related to magmatism (De Lugt et al., 2003, Gómez and Vergés, 2005).

This section presents a classification scheme for subtle structural traps formed by differential compaction. Each feature described relates to early mechanical compaction rather than chemical compaction, as this scheme solely accounts for the generation of subtle structural traps. Fresh interpretations from the Broad Fourteens Basin dataset are presented here, and they identify differential compaction over: 1) anticline α (*i.e.* anticline α^1 in the Lower North Sea Group) and, 2) a topographic step on the flanks of anticline α, at the level of the Base Tertiary Unconformity (Fig. 7.2). In parallel, new data from the Taranaki Basin are used to analyse differential compaction over a large volcano near the Parihaka Fault (Fig. 7.2). The classification of subtle traps from *Chapters 5* and *6*, as well as from these new data, will be complemented by a thorough review of

traps documented in the literature that fit into each of the proposed classes (Table 7-1 and Fig. 7.3).

Once the classification scheme is fully developed and explained, the relative scales and sizes of each compaction feature are compared and contrasted to draw any obvious relationships between them. This approach provides a suitable method to discern structures related to differential compaction from those formed by salt withdrawal, regional tectonics and subsidence. Finally, the application of this classification scheme will be discussed in relation to the hydrocarbon industry, focussing on the known petroleum systems in the three study areas.

Table 7-1 Table summarising all the studied examples of differential compaction creating subtle structural traps. Where possible, measurements of the trap have been provided, either given in the published literature, or measured from the published figures. The traps analysed in this thesis are also included.

Example	Subtle trap type	Location	Lithological description	Additional processes	Estimated size of trap		Reference and figure
					Width (m)	Height (m) or (ms)	
Volcano	Type A	Taranaki Basin, New Zealand	Differential compaction occurs over a volcano (part of the Mohakatino Volcanic Centre) within the Giant Foresets Formation. Siliciclastics making up the foresets compact significantly more than the almost incompactible volcano.		9200 m	130 ms	This thesis (*Chapter 7*) **Figure 7.2a**
Anticline	Type A	Broad Fourteens Basin, Dutch North Sea	An angular unconformity truncating an inverted anticline juxtaposes different lithologies against the overlying strata. Chalks on the flanks of the inverted anticline compact more than sandstones and limestones in the core, forming a Type A trap in the overlying strata. This is enhanced by tectonic compression.	Tectonic compression	> 7500 m	140 ms	This thesis (*Chapter 7*) **Figure 7.2b**
Dome	Type A	Vøring Basin, mid-Norwegian Atlantic Margin	Helland Hansen Arch and the Vema Dome grew via a mixture of differential compaction and tectonic folding. A prograding clastic wedge led to differential compaction, but an overlying clastic wedge subsequently reduced the amplitude of the folds.	Tectonic compression	25,000 m	600 m	*Gómez & Vergés 2005* **Figure 7.3a**
Impact Crater	Type A	Utopia Planitia, Mars	Drape folds over the margins of a buried crater produces Type A folds in the overburden. The folds are asymmetric, with compaction greatest on the interior crater wall, less over the exterior crater wall, and very little compaction over the crater wall itself. Compaction, coeval with volumetric shrinkage, creates double-ringed grabens on the inside and outside of the crater rim.	Volumetric shrinkage	2500 m	70 m	*Buczkowski & Cooke 2004* **Figure 7.3b**
Salt Diapir	Type A	Sørvestsnaget Basin, SW Barents Sea	Differential compaction over a salt diapir creates a crestal horst in the thick overburden. The salt is incompressible, whereas adjacent sediments are normally pressured and compacted. Rising of the salt diapir enhances the height of the horst.	Diapiric rise due to gravitational gliding	9300 m	350 ms	*Perez-Garcia 2013* **Figure 7.3c**

Isolated carbonate platform	Type A	Offshore Philippines	Well-cemented brittle carbonate strata formed a structural buttress, leading to strain and differential compaction in siliciclastic strata around it. This produced four-way closures over the carbonate reef. Strata has been tilted, reducing the impact of vertical stress on the Type A trap.		2800 m	70 ms	*Burgess et al. 2013*
Submarine channel complex	Type B	Espirito Santo Basin, SE Brazil	Differential compaction occurred over a channel complex, as well as individual channels. The channel complex resisted compaction more than the surrounding muds, creating an elongated, two-way dipping anticline than continues over the length of the axis. Smaller anticlines over the individual channels have four-way dip closure, and are contained within the channel complex.		2200 m	50 ms	This thesis (*Chapter 5*); *Ward et al. 2018* **Figure 7.2c**
Submarine channel					740 m	25 ms	
Submarine channel-fan complex	Type B	UK Central North Sea	This trap formed over Tertiary deep-marine channel-fan complexes. The example provided is the Gannet East Field: Eocene Tay Sandstone Member is the reservoir for this unit, and resisted compaction more than the surrounding muds.		5000 m	150 ms	*Armstrong 1987; Lynn et al. 2015*
Submarine channel	Type B	Outer Moray Firth, UKCS	A forced fold was developed in response to differential compaction over deep-marine channel sandstones. The sandstones are part of the Eocene Brodie Sandstone Formation, and the trap created has been drilled as part of the Alba Field. Post-depositional fluidisation and remobilisation of sandstones towards the crest of the fold increased its amplitude.	Sandstone injection	<3000 m	<100 ms	*Newton & Flanagan 1993; Cosgrove & Hillier 2000* **Figure 7.3d**
Deep-water turbidites	Type B	UKCNS	Differential compaction induced four-way dip closure over a mounded channel. Examples include the West Brae and Frigg fields. These are referred to as one-seal traps.	Depositional mounding	<5000 m	<150 m	*Milton & Bertram 1992; Corcoran 2006*

Submarine channel	Type B	Western Canadian Sedimentary Basin	Differential compaction creates both negative and positive relief structures over the submarine channels. Mud-rich channels with sand-rich levees create a syncline over its axis, whereas sand-rich channels create an anticline. The positive relief structures over the sand-rich channels, and to a lesser extent the sand-rich levees, are the Type B traps.		450 m	n/a	*Chopra & Marfut 2012* **Figure 7.3e**
Turbiditic channel	Type B	Lower Congo Basin	Sand-rich turbiditic palaeochannels are stacked vertically. Differential compaction over these stacked channels produces large-amplitude anticlines, which are faulted at their crest as fluids are driven upwards during burial.		4700 m	110 ms	*Gay et al. 2006* **Figure 7.3f**
Canyon	Type B	Mauritanian Continental Margin	On the seismic data provided, differential compaction is observed over the large canyon in the south of the study area. This process is also attributed to the formation of axis parallel faults, dipping towards the centre of the canyon.	Opal A to C/T transition	6000 m	120 ms	*Ireland et al. 2011*
MTD	Type B	Espirito Santo Basin, SE Brazil	A broad anticline along the present-day seafloor represents differential compaction over the whole mass-transport deposit. It overprints the effects of the Type C traps formed over the individual blocks.		7000 m	140 ms	This thesis (*Chapter 6*) **Figure7.2d**
MTD blocks	Type C	Espirito Santo Basin, SE Brazil	Strata over individual carbonate blocks entrained within the MTD underwent differential compaction; the debrites surrounding the blocks were compacted more than the blocks themselves. Depocentres formed over the debrites, anticlines formed over the blocks. The sizes of depocentres and anticlines were dependant on the size of blocks.		100 - 1000 m	10 - 50 ms	This thesis (*Chapter 6*) **Figure 7.2e**
Topographic scarp	Type C	Broad Fourteens Basin, Dutch North Sea	Differential compaction occurred over a topographic scarp along the Base Tertiary Unconformity. Softer chalks were eroded more than harder cemented limestones and sandstones. Once buried, the chalk compacted more than the scarp, resulting in a compaction-fold within the Lower North Sea Group strata.		1000 m	75 ms	This thesis (*Chapter 7*) **Figure 7.2f**

Basement highs	Type C	Manitoulin Island, Ontario, Canada	Precambrian quartz arenite inliers, part of the Lorrain Formation and Bar River Formation, form resistant basement highs. Differential compaction is observed via bed thickening of overlying dolostone down-dip of the highs. The size of the Type C traps over the top is not quantified, but the height of the quartz arenite inliers is recorded. The Type C traps will therefore be less than these folds.	Mg-rich fluid alterations at base	<2000 m	<250 m	*Corcoran 2008* **Figure 7.3g**
Isolated carbonate platform	Type C	Central Appenines, Italy	Strata was tilted onto the flanks of an isolated carbonate platform due to differential compaction. Once buried, rocks were then folded over the crest of the carbonate platform, leading to four-way closure. The study area had incurred severe tectonic compression, but the folds are retrodeformed to remove these effects allowing the amount of differential compaction to be modelled. There are no measured heights to the folds produced by differential compaction.	Tectonic compression	<1000 m	n/a	*Carminati & Santantonio 2005*
Carbonate platform margin	Type C	Central Appenines, Italy	Differential compaction folded strata over the Maiella platform margin. Field observations show basinward divergence and thickening of strata, updip pinch-out of packages, and an anticlinal hinge. Differential compaction was controlled by highly compactable basin fill deposits and a high-relief cemented carbonate platform.		1000 m	50 m	*Rusciadelli & Di Simone 2007* **Figure 7.3h**
Carbonate concretions	Type D	Holzmaden, Southern Germany	Concretions grew within a concretionary limestone bed just below the sediment-water interface. Differential compaction occurred between the concretions and the surrounding black shales within the first meter of burial. No measurements of the folds were provided.		n/a	n/a	*Savrda & Bottjer 1988*
Carbonate concretions	Type D	Western NY State Appalachian Plateau	Early diagenetic growth in unconsolidated sediment formed carbonate concretions. This allowed differential compaction to occur in black shales surrounding the concretions.		1.5 m	0.2 m	*Lash & Blood 2004* **Figure 7.3i**

Sandstone injectite	Type D	West Canyon, Utah/Arizona Border	Sandstone was remobilised and injected into a bed of laminated carbonates in the first meter of burial. The Type D trap developed over the sandstone injectite, as differential compaction folded the strata over it, and the weight of the injectite folded the strata below it. Only an estimate of the size of injection is provided.	<1 m	<0.1 m	*Bryant & Miall 2010* **Figure 7.3j**
Boulders in conglomerate	Type D	Manitoulin Island, Ontario Canada	Individual boulders entrained in a shoreface conglomerate comprise quartz arenite fragments from the Lorrain Formation and Bar River Formation. These rocks resist compaction more than the surrounding matrix and the overlying dolostone matrix folds over the top of the blocks, thickening away from them.	<15 m	<1 m	*Corcoran 2008*
Dolomite-pseudomorphed nodule	Type D	Onega Lake Region, Fennoscandia	Thin section shows plastically deforming sulphate-red mud laminations folding around a dolomite-pseudomorphed nodule. There is also bending of laminations below the nodule, suggesting it formed during early diagenesis.	0.06 m	0.02 m	*Melezhik et al. 2005*

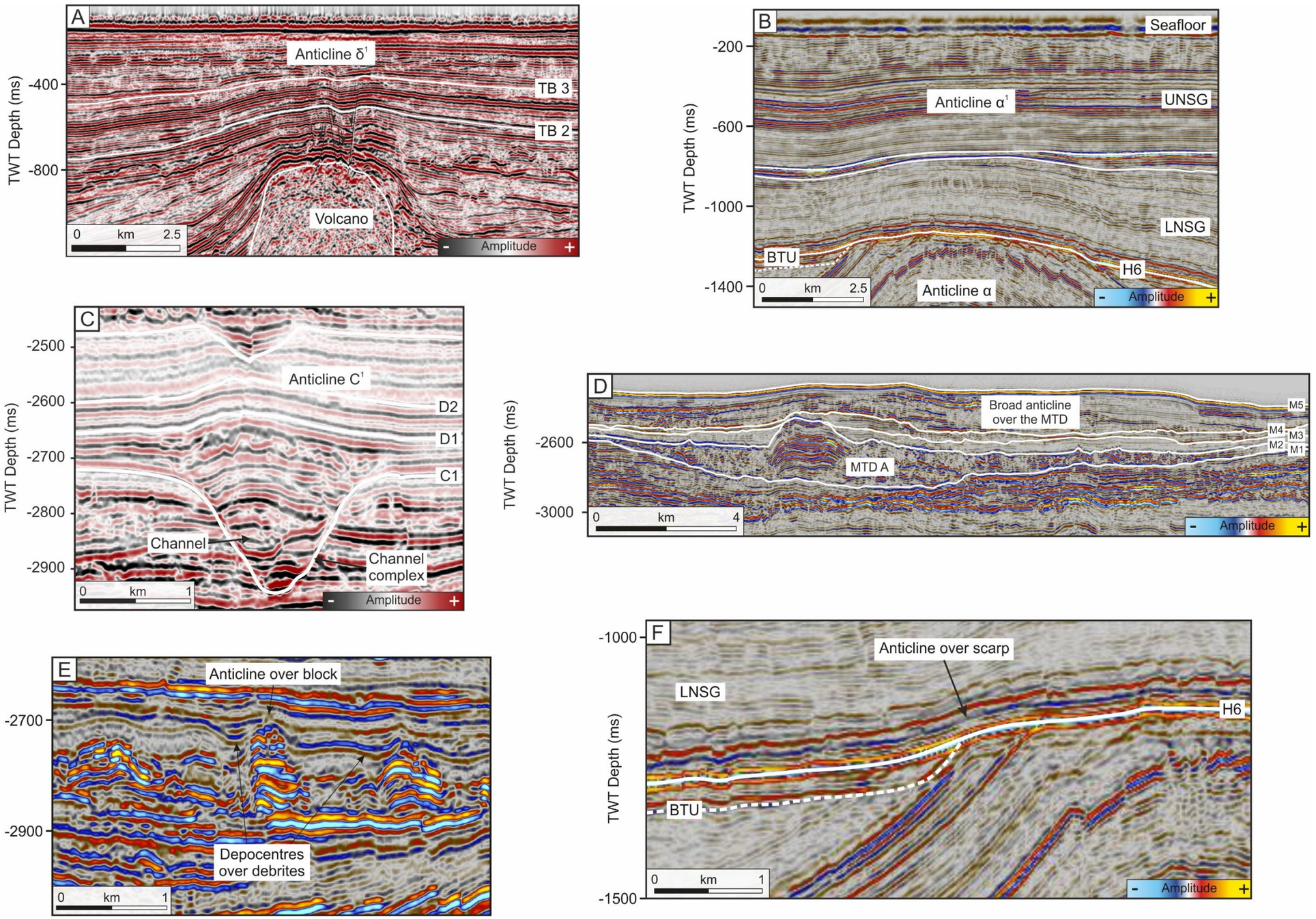

Fig. 7.2 Examples of differential compaction over key features discussed in this thesis: a) Parihaka volcano, New Zealand (*Chapter 7*); b) inverted anticline, Broad Fourteens Basin (*Chapter 4*); c) submarine channel complex, Espírito Santo Basin (*Chapter 5*); d) mass-transport deposit, Espírito Santo Basin (*Chapter 6*); rafted blocks, Espírito Santo Basin (*Chapter 6*); f) topographic scarp, Broad Fourteens Basin (*Chapter 4*). The character of these features is summarised in Table 7-1

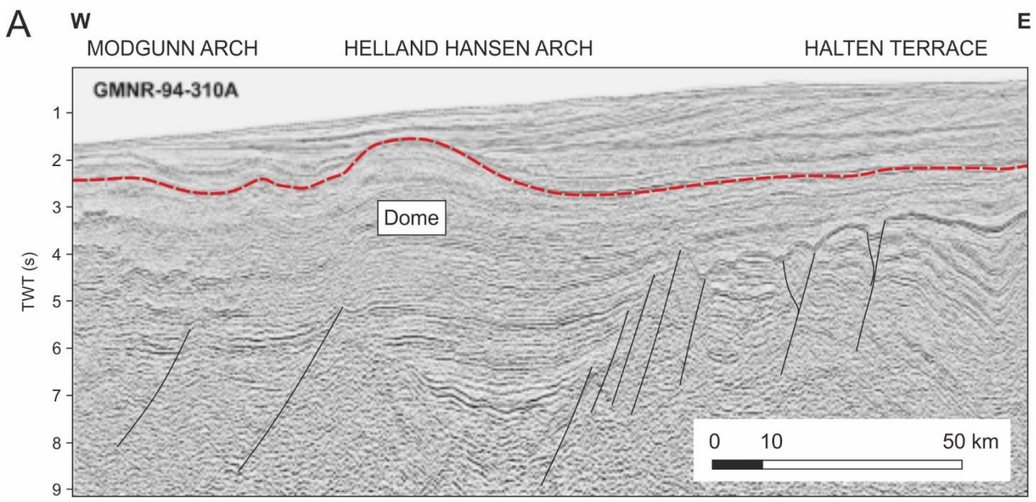
A
W
E
MODGUNN ARCH
HELLAND HANSEN ARCH
HALTEN TERRACE
GMNR-94-310A
Dome
TWT (s)
1
2
3
4
5
6
7
8
9
0 10 50 km

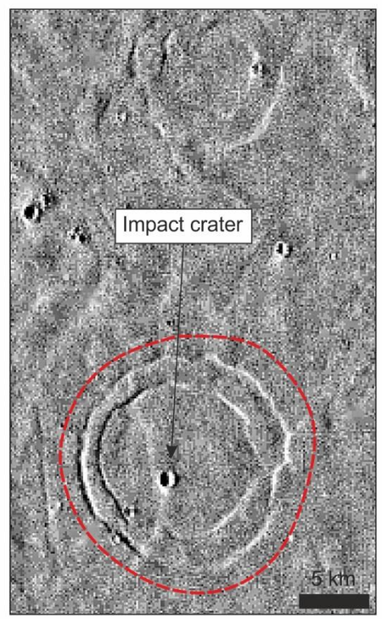
B
Impact crater
5 km

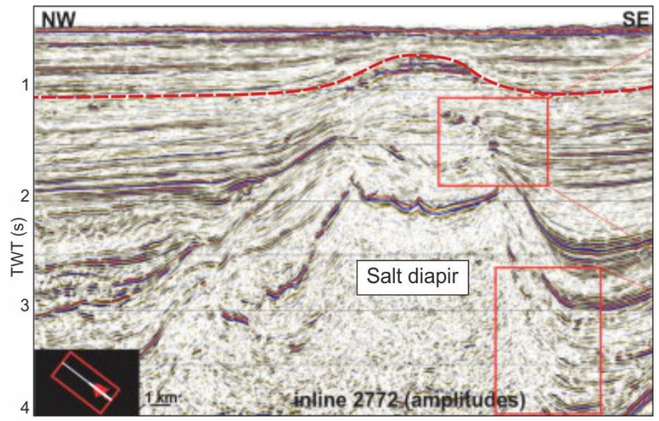
C
NW
SE
TWT (s)
1
2
3
4
Salt diapir
1 km
inline 2772 (amplitudes)

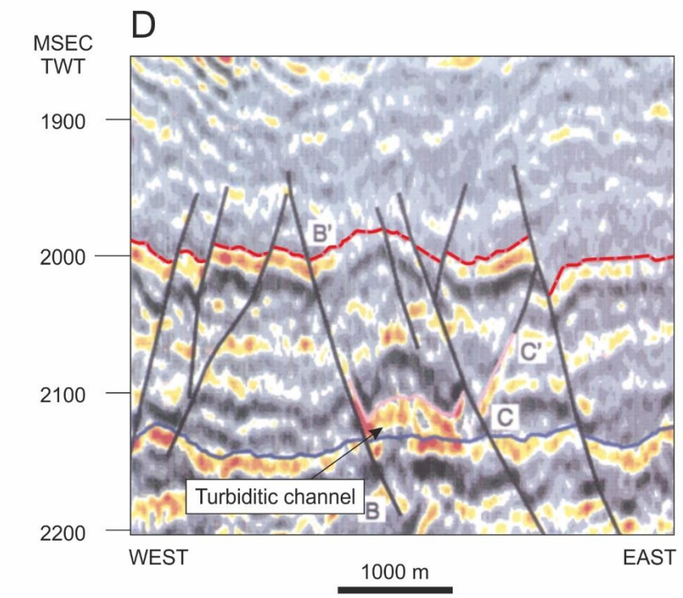
D
MSEC
TWT
1900
2000
2100
2200
B'
C'
C
B
Turbiditic channel
WEST
EAST
1000 m

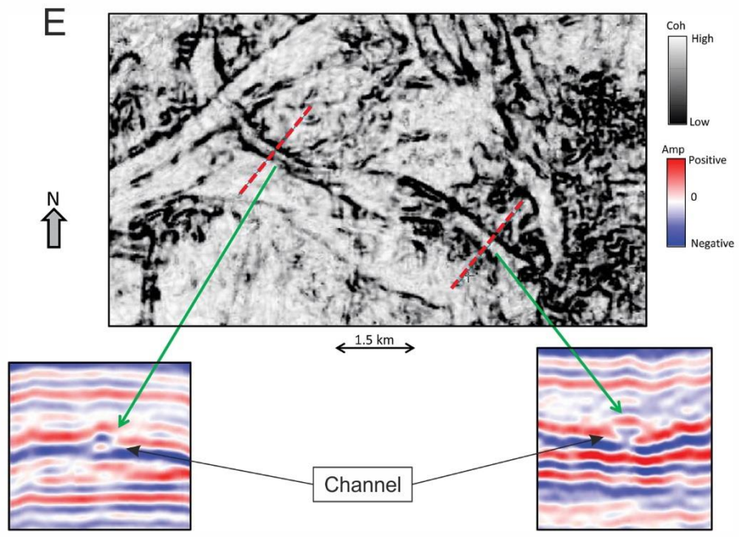
E
N
Coh
High
Low
Amp
Positive
0
Negative
1.5 km
Channel

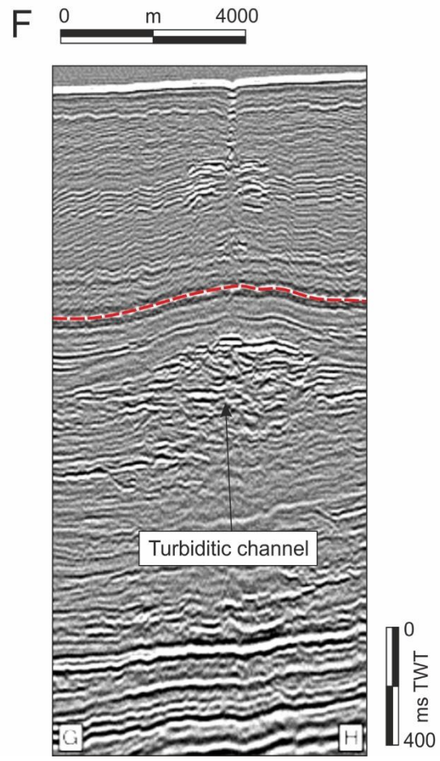
F
0
m
4000
Turbiditic channel
G
H
0
ms TWT
400

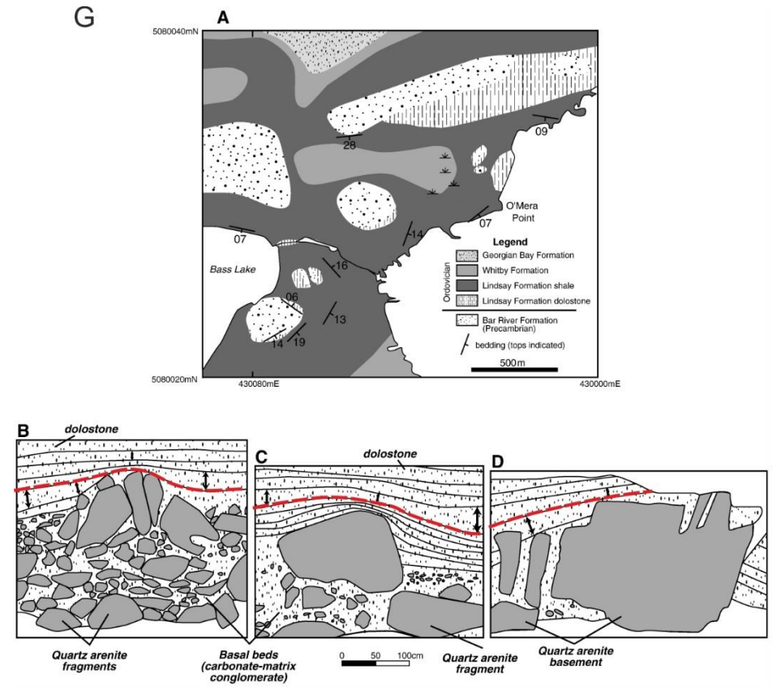

Fig. 7.3 (*including previous page*) Examples of differential compaction taken from the published literature: a) structural dome, *Gómez & Vergés (2005)*; b) impact crater, *Buczkowski & Cooke (2004)*; c) salt diapir, *Perez-Garcia et al. (2013)*; d) submarine channel, *Cosgrove & Hillier (2000)*; e) submarine channel, *Chopra & Marfut (2012)*; f) turbiditic channel, *Gay et al. (2006)*; g) basement highs, *Corcoran (2008)*; h) carbonate platform margin, *Rusciadelli & Di Simone (2007)*; i) carbonate concretion, *Lash & Blood (2004)*; j) sandstone injectite, *Bryant & Miall (2010)*. Strata revealing differential compaction are highlighted with a red line. All the features are summarised in Table 7-1.

7.3.1. Description of new compaction features in the Broad Fourteens Basin

The analysis of the Broad Fourteens Basin (*Chapter 4*) considered the evolution of faults below the Base Tertiary Unconformity, i.e. crossing Triassic-Cretaceous units. Deformation in these units resulted from basin inversion, raft movement, differential subsidence over the rafts, and halokinesis (De Lugt et al., 2003, Oudmayer and De Jager, 1993, Coward and Stewart, 1995, Nalpas et al., 1995). Above the Base Tertiary Unconformity lies the North Sea Supergroup (Fig. 3.5). This thick sequence was not analysed in *Chapter 4* and will be re-examined in this section to identify and describe subtle structural closures formed over previously documented geological features.

7.3.1.1. Lower North Sea Group

Prior to the deposition of the North Sea Supergroup, the Laramide and Pyrenean Orogenies imposed moderate tectonic inversion in the Broad Fourteens Basin, leading to the removal of large volumes of Late Cretaceous and Early Cenozoic strata. Erosion was concentrated on the apex of inverted anticlines (Oudmayer and De Jager, 1993, Verweij and Simmelink, 2002) (Fig. 4.9). The onset of regional subsidence and high sedimentation rates that occurred after tectonic inversion ceased, creating an angular unconformity – the Base Tertiary

Unconformity (Nalpas et al., 1995, De Lugt et al., 2003, Duin et al., 2006) (Figs. 7.4 - 7.6). Different stratigraphic units and, therefore, different lithologies, were later deposited and draped against the older Triassic-Cretaceous structures (Fig. 4.10).

After the Laramide inversion, the onset of tectonic quiescence in the Broad Fourteens Basin led to the deposition of horizontal strata healing the seafloor topography (Nalpas et al., 1995, Van Wijhe, 1987). On seismic data, these parallel reflections (of equal thickness) overly the Base Tertiary Unconformity and have subsequently been deformed and folded (Figs. 7.4 – 7.6). A structural map of the Base Tertiary reveals three subtle structural highs in the Lower North Sea Group (Fig. 7.7): 1) directly above the anticline α – anticline α^1 (Fig. 7.4), 2) over the smaller anticline β northwest of anticline α – anticline β^1 (Fig. 7.5), and 3) over a collapsed salt diapir located to the west of the other two anticlines – anticline γ^1 (Fig. 7.6). The geometry of the subtle structures in the Lower North Sea Group directly matches the underlying features. However, few faults penetrated the Base Tertiary Unconformity, indicating the most intense phase of inversion pre-dated the deposition of the Lower North Sea Group (Fig. 7.6). This is also a key characteristic of anticline α. Accordingly, there must have been a later post-depositional process that folded the Lower North Sea Group. Pyrenean compression occurred between the Late Eocene-Oligocene, and was responsible for up to 500 m of erosion on major structural highs in the southern North Sea, adjacently to main graben structures (Van Wijhe, 1987, Nalpas et al., 1995). This

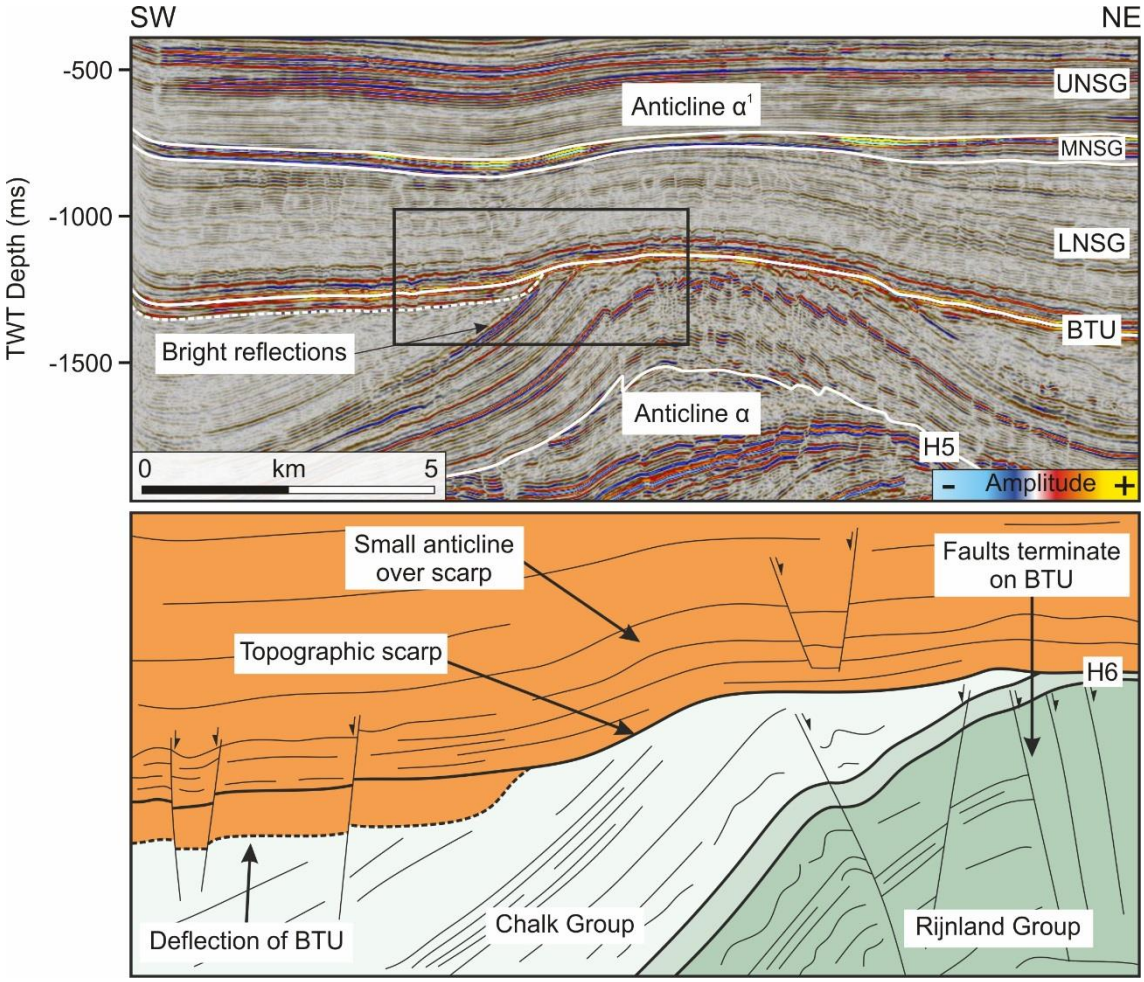

Fig. 7.4 Seismic profile of anticlines α and α^1, including a zoomed in section of the subtle trap over the topographic scarp along the Base Tertiary Unconformity. BTU – Base Tertiary Unconformity; LNSG – Lower North Sea Group; MNSG – Middle North Sea Group; UNSG – Upper North Sea Group.

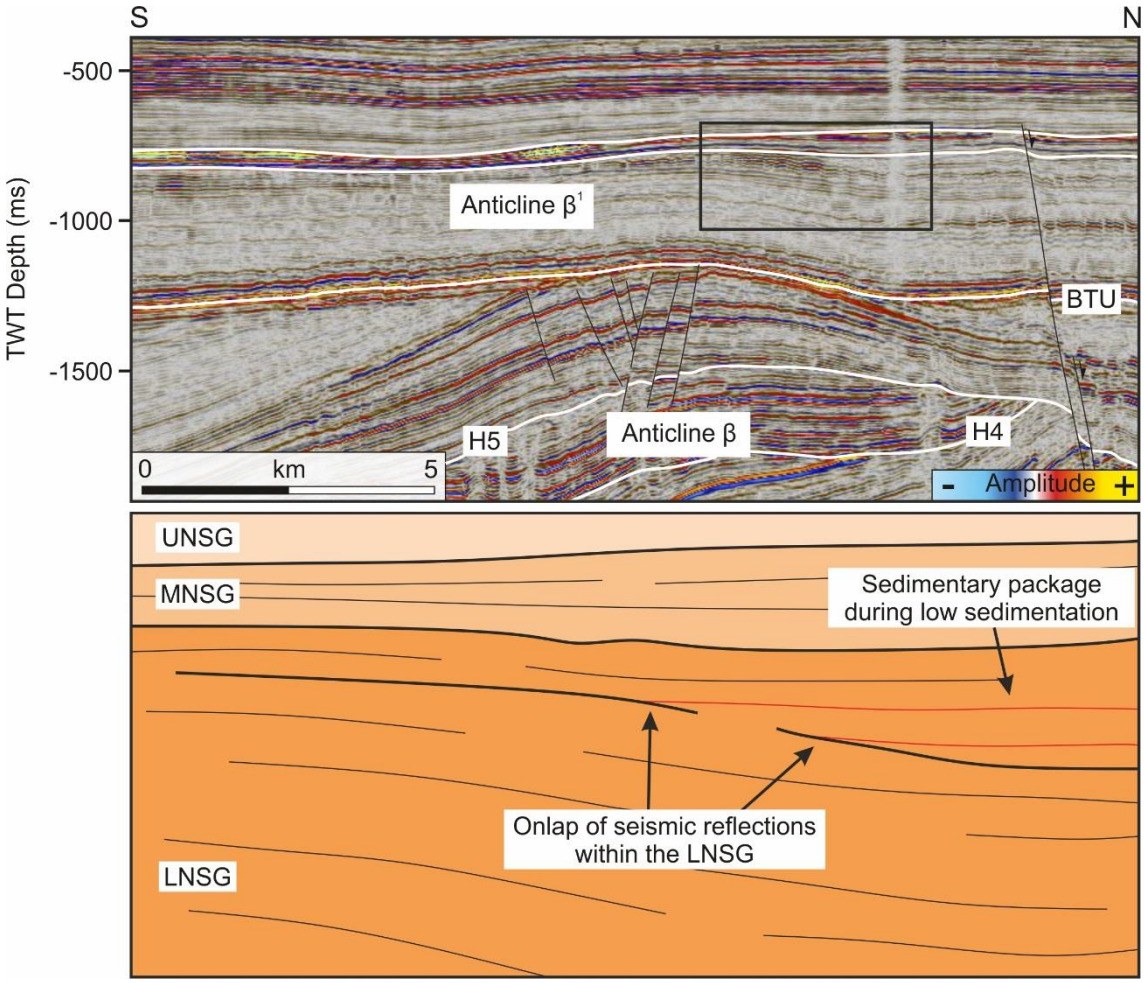

Fig. 7.5 Seismic profile of anticlines β and β^1, including a zoomed in section of the condensed sedimentary package onlapping anticline β^1 in the LNSG. BTU – Base Tertiary Unconformity; LNSG – Lower North Sea Group; MNSG – Middle North Sea Group; UNSG – Upper North Sea Group.

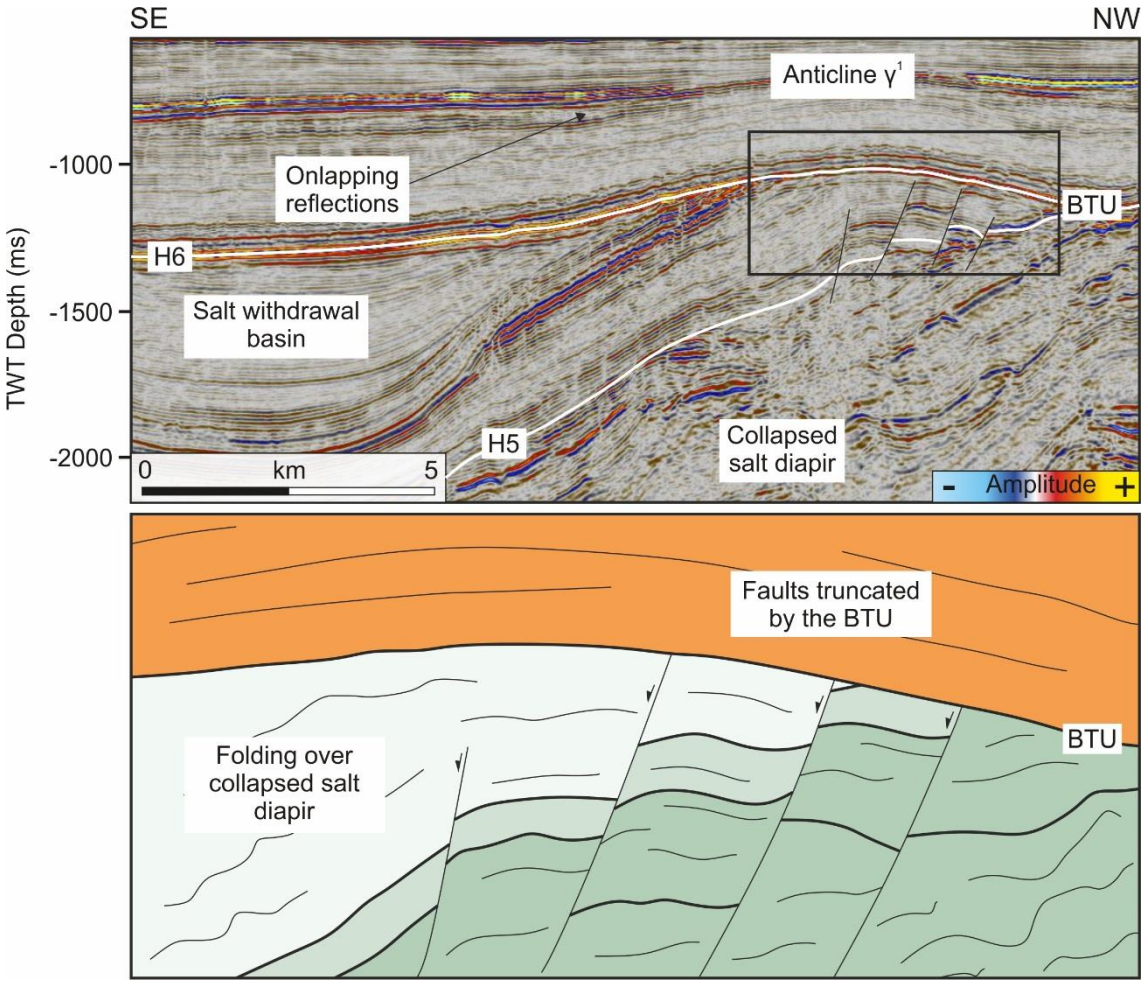

Fig. 7.6 Seismic profile of anticline γ^1 overlying a collapsed salt diapir. A zoomed-in section shows large Mesozoic faults truncated at the Base Tertiary Unconformity. BTU – Base Tertiary Unconformity.

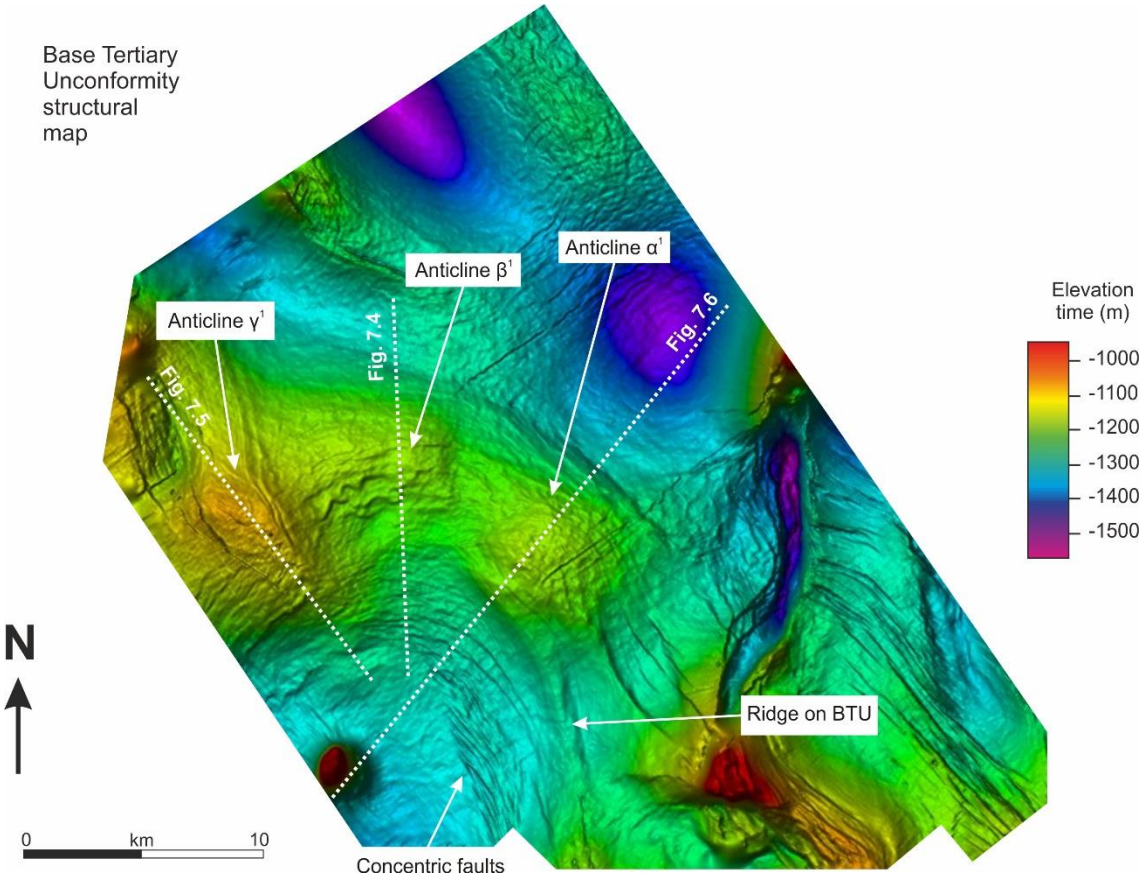

Fig. 7.7 Structural map of the Base Tertiary Unconformity in the study area of the Broad Fourteens Basin, Southern North Sea. Subtle traps are highlighted, as well as a smaller subtle trap over the main ridge. Locations of seismic lines in Figures 7.4, 7.5, and 7.6. BTU – Base Tertiary Unconformity.

inversion episode is believed to have been responsible for at least part of the folding in the Lower North Sea Group (*see also* De Lugt et al. 2003).

Alternatively, differential compaction of strata over the Mesozoic anticlines α and β enhanced the size of the Lower North Sea Group folds. Gradual development of these subtle compaction-related anticlines (α^1, β^1, and γ^1) is associated to burial and compaction of strata below. Clearly, the subtle anticline decreases in amplitude vertically, becoming almost unrecognisable in the Middle North Sea Group (Figs. 7.4 - 7.6). In addition, sediment deposition struggled to keep up with local folding, creating packages of strata that onlap the developing (subtle) anticline (Fig. 7.5). These packages were preferentially deposited over the flanks of the Mesozoic anticlines α and β, where accommodation space was greatest. The thickness map in Figure 7.8 shows that the thickest parts of the Lower North Sea Group match the latter observation; warmer colours (representing larger thicknesses) are located away from the crests of the Mesozoic and Tertiary anticlines.

The interpreted data from the Espírito Santo Basin in *Chapters 5* and *6* have eluded to differential compaction occurring over discrete stratigraphic elements with varying physical and lithological properties. However, borehole data was not available for the Espírito Santo Basin datasets. In contrast, subtle closures analysed in the Broad Fourteens Basin have well-data <2 km from their crests (Fig. 4.1). Wells K15-07 and K15-02 show significant changes in gamma ray

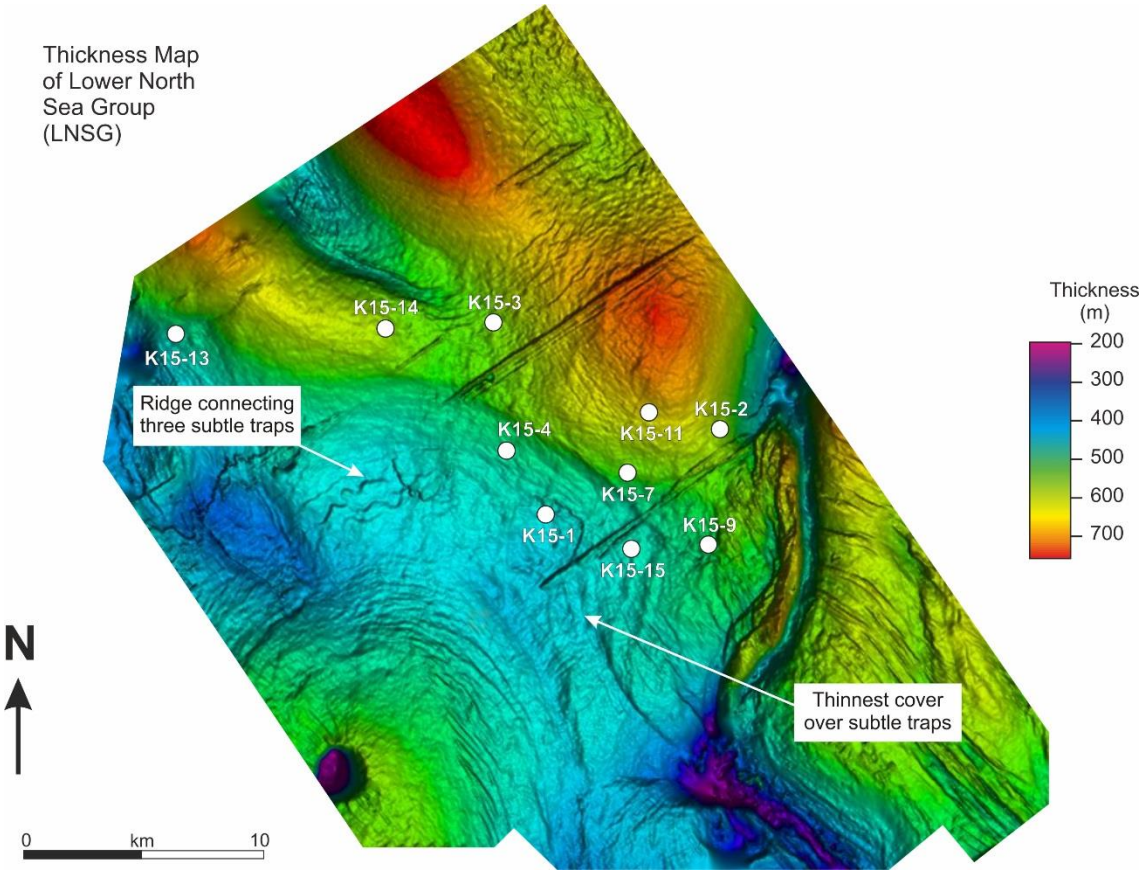

Fig. 7.8 Thickness map of the Lower North Sea Group overlaid on a structural map of the Base Tertiary Unconformity (BTU). The map images strata between the Base Tertiary Unconformity and the top of the Lower North Sea Group. Areas that are blue-purple highlight the thinnest parts of the unit. These thinner strata coincide with the ridge joining the top of the three subtle traps. Sediment was predominantly deposited over the flanks of the anticlines, as indicated by the reds and yellows.

values from the flanks of anticline α to its crest (Fig. 4.2). The local stratigraphy of the two wells is shown in Figure 7.9, and concentrates on the Ommelanden Formation and Texel Formation (Chalk Group), as well as on the Rijnland Group below and the Lower North Sea Group above. This change in lithology dictates the location of anticlines α^1 and β^1.

7.3.1.2. Base Tertiary Unconformity

A second feature not discussed in *Chapter 4*, but clearly observed on the structural maps concerning Horizon H_6, is a linear ridge running parallel to concentric faults in the salt withdrawal basin (Fig. 7.7). The ridge lies between the salt withdrawal basin and the inversion crest, separating the two (Fig. 7.7). Mirroring the shape of the salt withdrawal basin, the ridge is observed on the southwest side of anticline α, striking approximately NW-SE. It is deformed along its axis, with its concave side facing the salt withdrawal basin in the southwest (Fig. 7.7). The ridge is ~10 km long, <1 km wide, and <75 ms high.

The ridge lies along the Base Tertiary Unconformity at a depth ranging from ~1250 ms to 1350 ms (Fig. 7.4). The Base Tertiary Unconformity is discernible as a very high amplitude seismic reflection above dipping strata and has been mapped accordingly. In Figure 7.4, the unconformity forms the bright reflection on the crest of anticline α. On the southwest flank of anticline α (SW half of the seismic line in Figure 7.4), there are parallel seismic reflections below

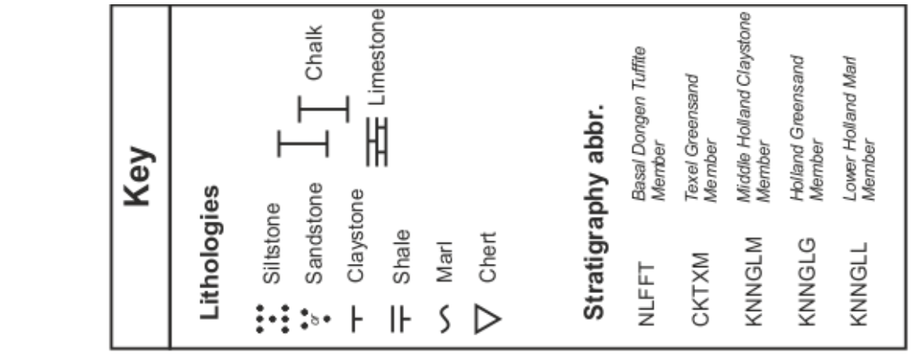

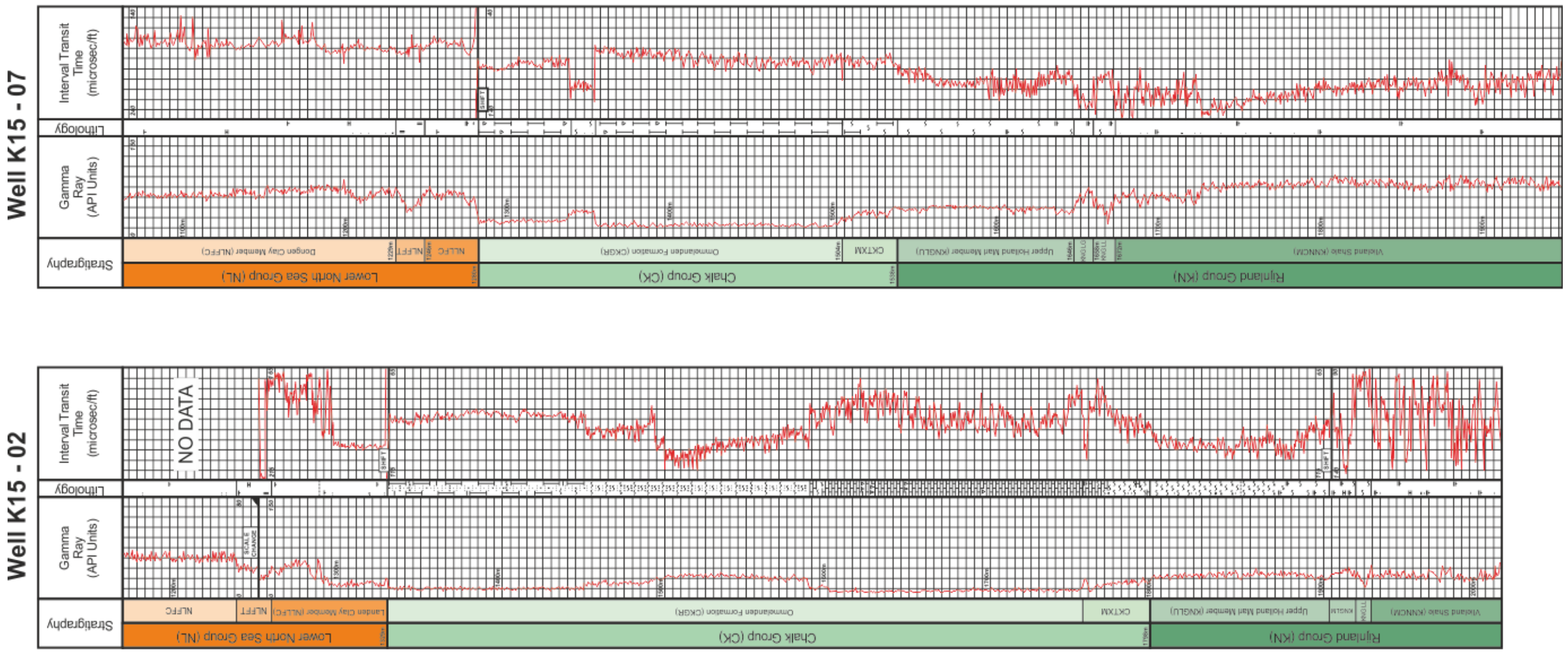

Fig. 7.9 Wireline logs from wells K15-02 and K15-07 in the Broad Fourteens Basin, Southern North Sea. Stratigraphy, gamma-ray log, lithological interpretation from cores, and interval transit time are all provided. This is a selected section from the same logs used in Figure 3.5. The logs are used to help tying the seismic data to true subsurface lithologies and are provided as open access files from NLOG's online database. The locations of the wells are shown in Figure 7.8.

the mapped unconformity. These are of lower amplitude than the Base Tertiary Unconformity (Fig. 7.4). Seismic reflections under the Base Tertiary Unconformity also onlap the side of anticline α (Fig. 7.4).

It is assumed, therefore, that a prominent scarp existed on the sea floor at the time the Lower North Sea Group was deposited. After significant erosion of the Mesozoic strata, the earliest sediments filled minibasins adjacent to the scarps, *i.e.* formed by remnant topography (Nalpas et al., 1995, De Lugt et al., 2003, Oudmayer and De Jager, 1993, Verweij and Simmelink, 2002). The small ridge over Horizon H_6 was created after the onset of deposition in the Lower North Sea Group, as demonstrated by the marked continuity of seismic reflections over it (Figs. 7.4 – 7.6).

7.3.2. Description of a new dataset from New Zealand

To complement the results from the Broad Fourteens and Espírito Santo Basins, a new 3D seismic cube from the Taranaki Basin, New Zealand was interpreted (Fig. 2.9). This dataset images an andesitic volcano (Parihaka Volcano) associated with the Late Miocene Mohakatino Volcanic Centre (Hansen and Kamp, 2004, Stagpoole and Funnell, 2001, Stagpoole, 1999, Salazar et al., 2016). The Parihaka volcano is up to 10 km wide and is situated in the southwest quadrant of the interpreted seismic cube (Fig. 7.10). When viewed in cross-section, the Parihaka volcano is obvious; its internal seismic character has

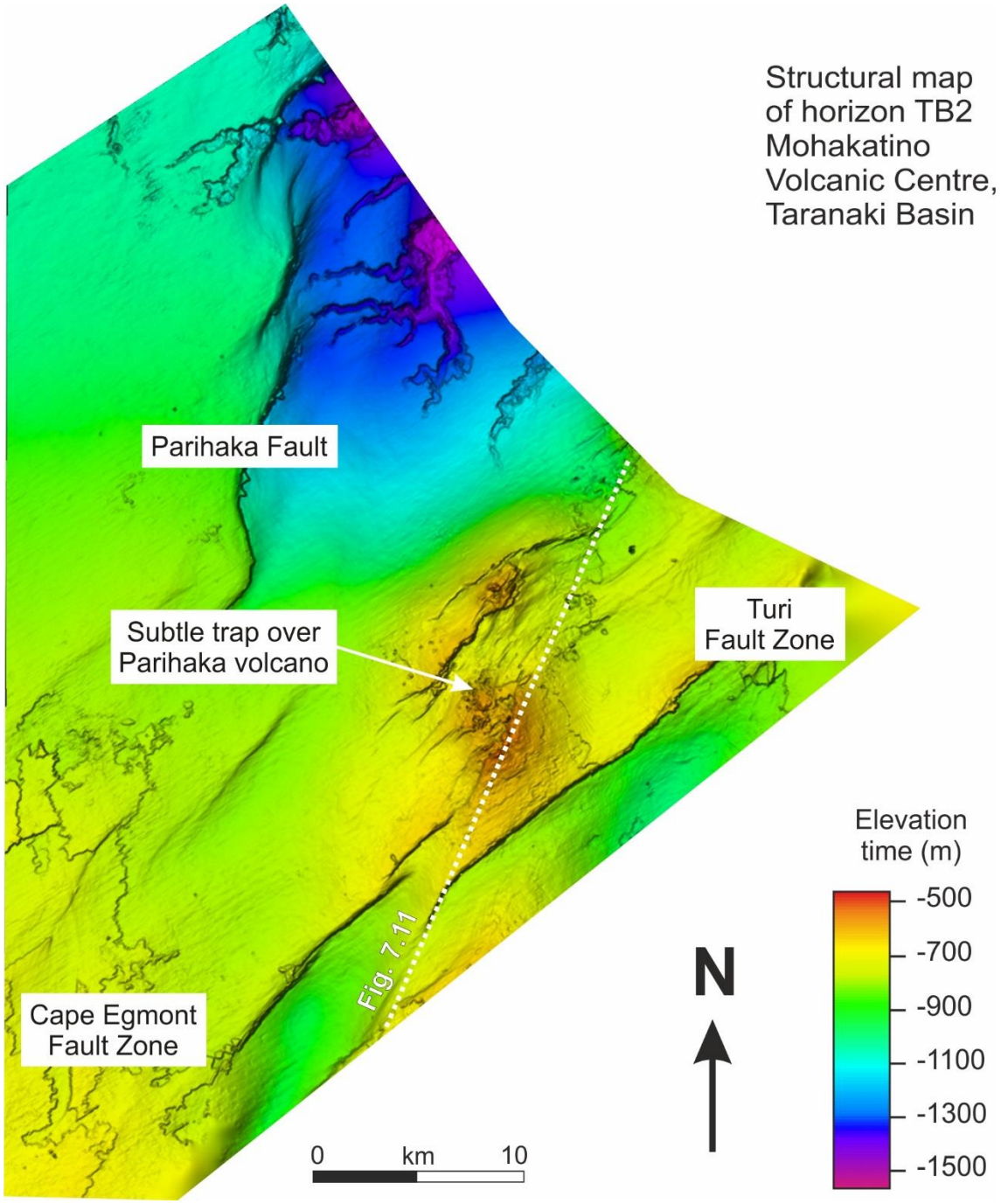

Fig. 7.10 Structural map of Horizon TB_2 showing the Mohakatino Volcanic Centre, Taranaki Basin, New Zealand. The volcanic centre shows a subtle trap over the crest of the Parihaka volcano, towards the east of the study area. Large, through-going faults from the Turi Fault Zone dissect it. The Parihaka Fault Zone is to the north, running N-S, and is associated with a channel system in the Northern Graben.

a marked change from continuous, bright seismic reflections surrounding it, to chaotic reflections typical of hard, unstratified rock, within the volcano (Hansen and Kamp, 2006) (Fig. 7.11).

Contiguous to the top half of the Parihaka volcano, and overlying it, is the Giant Foresets Formation described by Salazar et al. (2016) (Fig. 7.11). It comprises fine-grained marine sediments rapidly deposited downslope of the Taranaki continental shelf (Hayward et al., 2001, Salazar et al., 2016, King and Thrasher, 1996, Hansen and Kamp, 2004). Such a rapid deposition indicates that little to moderate erosion occurred on top of the volcanic edifices forming the Mohakatino Volcanic Centre (Stagpoole, 1999). Consequently, the Giant Foresets Formation reaches thicknesses of ~2000 m in the study area, with individual clinoforms reaching heights ~1500 m. These clinoforms thin significantly to less than 700 m on the crest of the Parihaka volcano (Helland-Hansen and Hampson, 2009, Salazar et al., 2016).

A thickness map was produced for the section of Giant Foresets Formation overlying the Parihaka volcano to reveal significant thinning over the crest of the volcano (Fig. 7.12). In the lowermost Giant Foresets Formation, seismic reflections onlap the side of the Parihaka volcano (Fig. 7.11). Over the crest, seismic reflections are continuous and warp upwards. A subtle anticline (anticline δ^1) lies over the Parihaka volcano, decreasing in amplitude towards the sea floor. Due to the large throws observed in the NE-trending Turi Fault

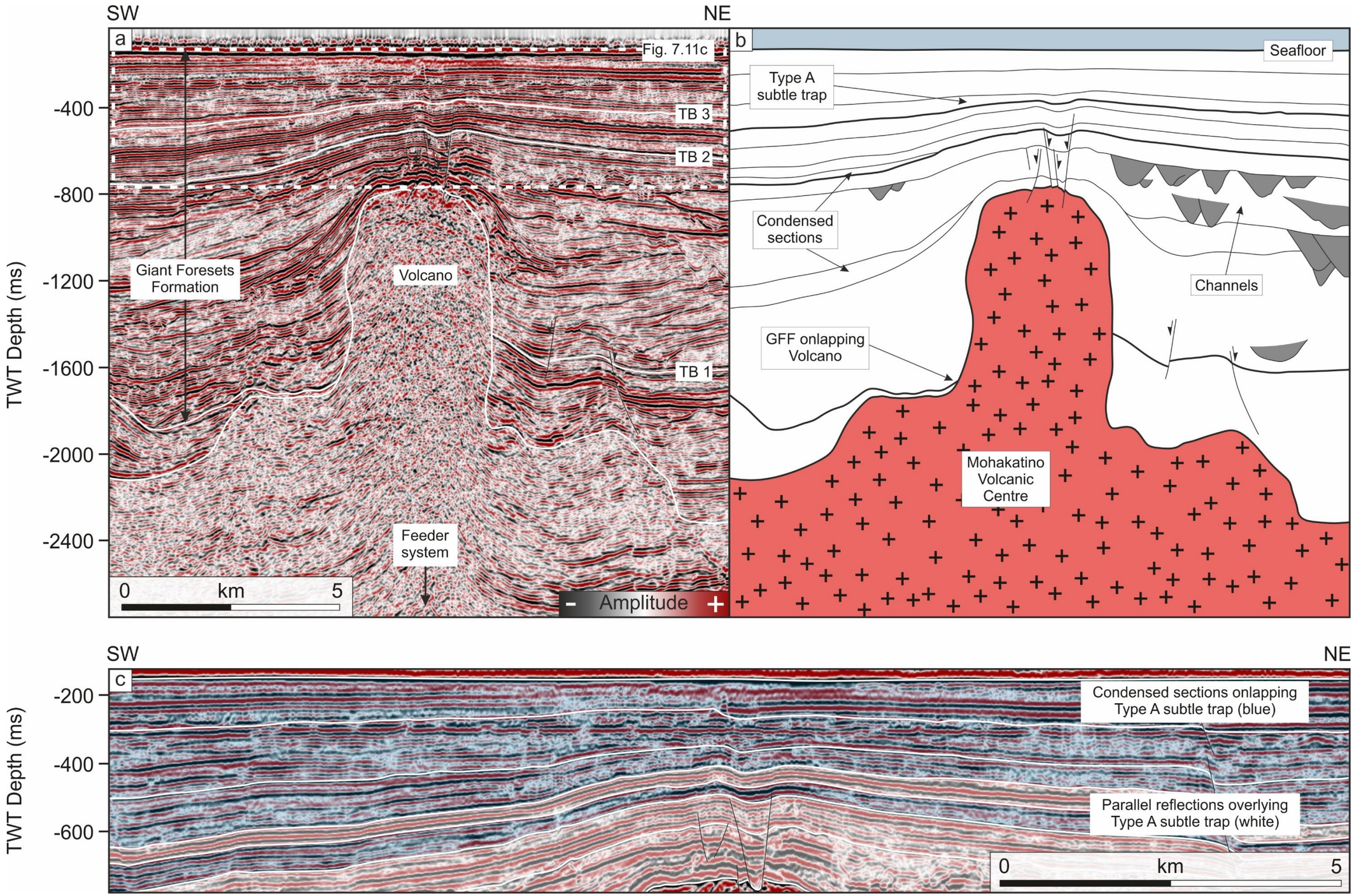

Fig. 7.11 a) Seismic profile of the Mohakatino Volcanic Centre, showing the extent of the Giant Foresets Formation that overlie the Parihaka volcano. The acoustic character of the volcano is markedly different from the surrounding Giant Foresets Formation. b) intepretation of the seismic profile from a), illustrating a subtle trap over Parihaka volcano, the condensed sections onlapping the subtle fold, and the Giant Foresets Formation onlapping the volcano. c) Close up seismic profile from a) showing condensed sedimentary packages in blue. The seismic line is shown in Figure 7.10.

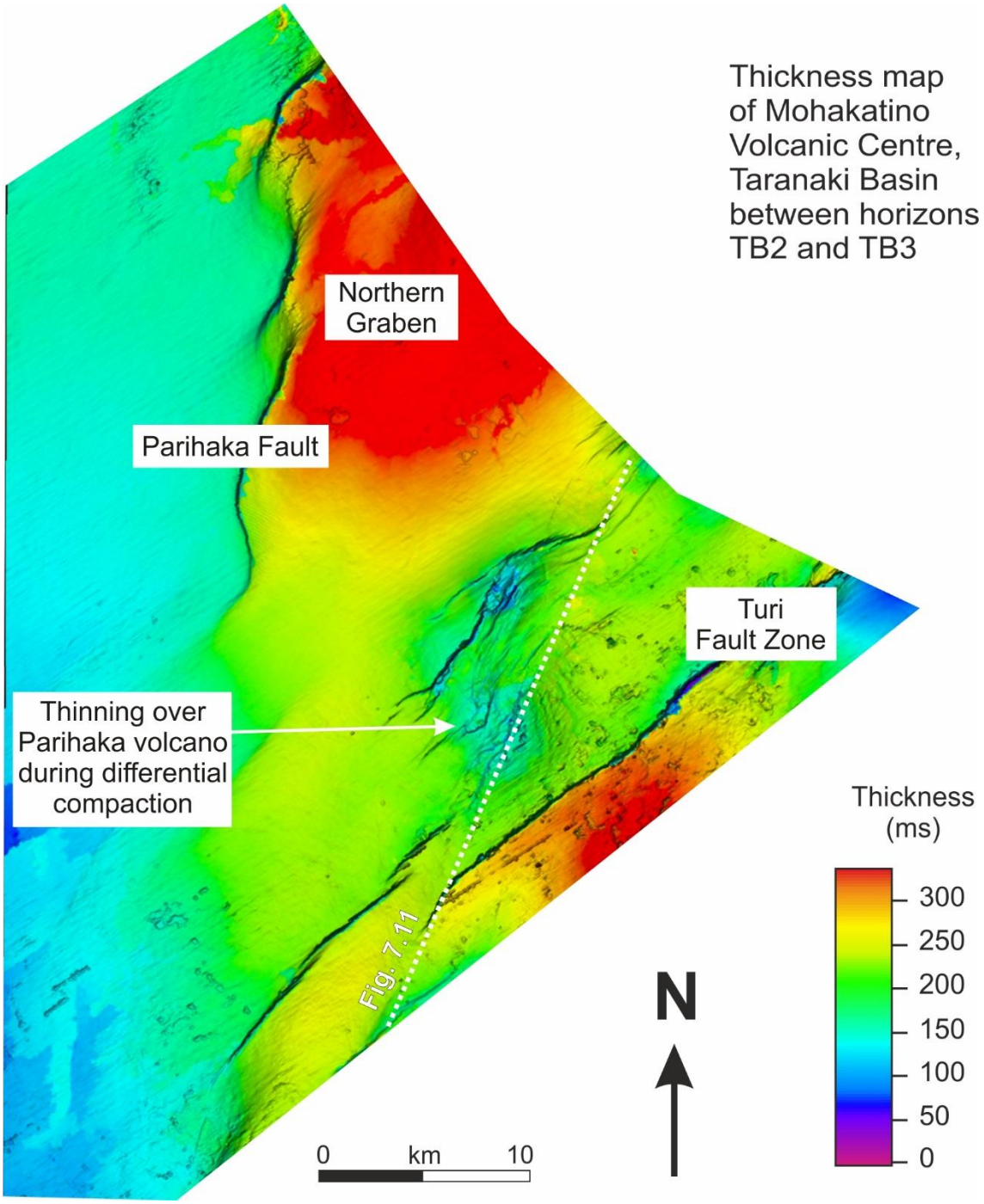

Fig. 7.12 Thickness map of the units overlying the Mohakatino Volcanic Centre (Taranaki Basin), over a structural map of TB_2. The map was created between horizons TB_3 and TB_2, which are both part of the Giant Foresets Formation. The thinnest areas correspond to the strata overlying the Parihaka volcano, *i.e.* the crest of the subtle fold.

Zone, anticline δ^1 is only clear in transects that run parallel to the faults, i.e. NE-SW (Fig. 7.10). Small packages of strata onlap the flanks of anticline δ^1 (Fig. 7.11a). These packages are similar to those observed in the Lower North Sea Group folds (anticlines α^1, β^1, and γ^1) in *section 7.3.1.1.1*. They are a product of the slow sedimentation rates recorded during active periods of differential compaction (Hansen and Kamp, 2004, Hansen and Cartwright, 2006) (Fig. 7.11c).

7.3.3. Classification scheme

A classification scheme was developed in this section to help characterise subtle structural traps associated with differential compaction (Table 7-1). Using the interpretations from previous chapters, the scheme was also developed to group other subtle traps identified in the published literature (Gómez and Vergés, 2005, Buczkowski and Cooke, 2004, Burgess et al., 2013, Ward et al., 2018, Armstrong et al., 1987, Perez-Garcia et al., 2013, Lynn et al., 2015, Cosgrove and Hillier, 1999, Newton and Flanagan, 1993, Corcoran, 2006, Milton and Bertram, 1992, Chopra and Marfurt, 2012, Gay et al., 2006b, Ireland et al., 2011, Corcoran, 2008, Carminati and Santantonio, 2005, Savrda and Bottjer, 1988, Lash and Blood, 2004, Bryant and Miall, 2010, Alves, 2010, Melezhik et al., 2005). It provides a clear and concise method to describe subtle structural traps formed at different locations, but with similar morphologies and evolutions. Two characteristic features of compaction-related folds are used to categorise each of the given

examples: 1) the type of underlying feature associated with the fold, and 2) their dimensions (*i.e.* width and height as in Figure 7.13). This approach is partly qualitative, and other examples were assessed on 3D seismic data to obtain the most accurate measurements and understand the extent of the compaction-related folds in the three-dimensional space. Some subtle traps are difficult to define; they show the characteristic features of one class, but fit into the size limits of other classes. Ideally, the subtle structural traps are first classified by what geological feature they forms over, then by their dimensions.

This thesis defines four classes of subtle traps: Types A to D (Table 7-1). Type A traps are the largest of the three types. They occur over tectonic structures and are of basin scale (>2 km). Type B traps occur over sedimentary packages with widths ranging from 500 metres to 5 km, in locations where there are distinct lithological changes. Type C traps comprise small scale compaction-related folds at the limit of seismic resolution and are formed in response to differential compaction over local topographic features. These can range from 20 m to more than 2 km in width. A tentative class (Type D) representing outcrop-scale features is also discussed. Although no fieldwork was completed in this thesis, sub-seismic/outcrop scale (<20 m) compaction-related folds have been discussed in published literature and are incorporated in the proposed classification scheme.

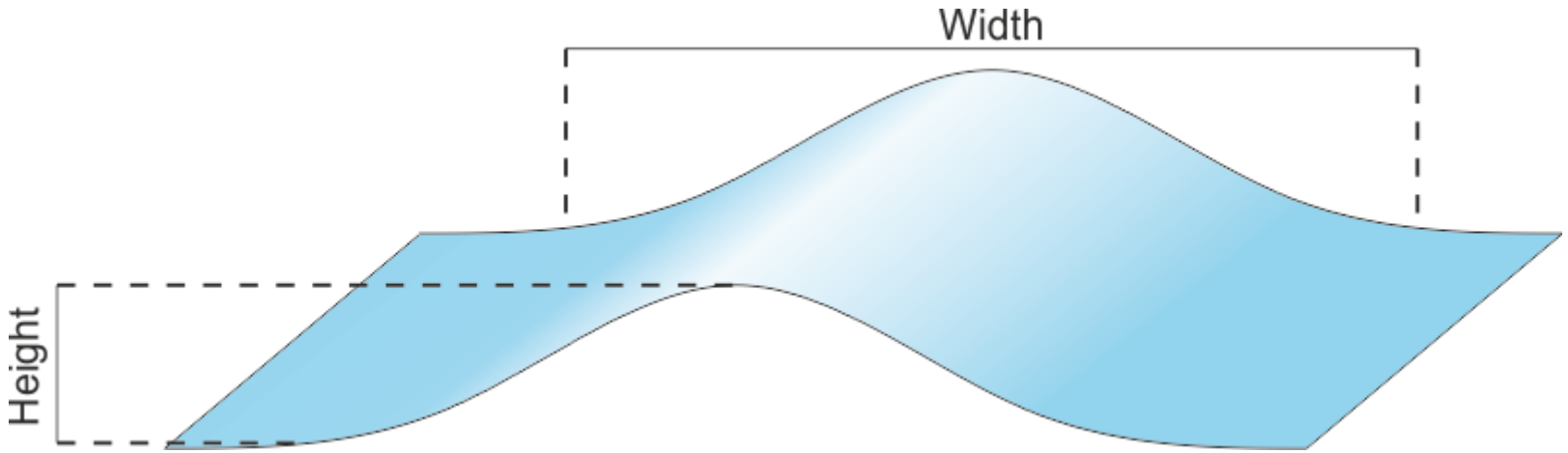

Fig. 7.13 Diagram illustrating how the geometry (width and height) of subtle traps were measured in this thesis.

7.3.3.1. Type A: Compaction over tectonic structures

The largest subtle traps, Type A, comprise features that can be easily detected on regional seismic data or basin maps. They form significant anticlines and are capable of subdividing basins into minibasins. It is difficult to unequivocally attribute Type A traps to differential compaction at first, as they show similar scales to tectonic folds related to crustal and halokinesis (Colman-Sadd, 1978, Cloetingh et al., 1999, Rowan and Vendeville, 2006, Gonzalez-Mieres and Suppe, 2006). Two examples of Type A traps are explored in the 3D seismic data in this thesis; the subtle anticline over the inverted Triassic-Cretaceous strata in the Broad Fourteens Basin, and the subtle anticline over the Parihaka volcano, Taranaki Basin (Fig. 7.2a and b, and Table 7-1).

In the Lower North Sea Group of the Broad Fourteens Basin, three separate structures are joined by a broad fold (Fig. 7.7). Each of these three structures are similar in size. The first, anticline α^1, is 7.9 x 6.9 km wide, showing a maximum relief of ~95 ms (Fig. 7.4). The second, anticline β^1, is 7.4 x 6.5 km wide, with a maximum relief of ~137 ms (Fig. 7.5). The final structure, anticline γ^1, is located above a heavily deformed crest of a collapsed salt diapir. Here, anticline γ^1 has a surface area of 6.0 x 5.3 km, and a maximum topographic relief of ~121 ms (Fig. 7.6).

On seismic data, alternating high- and low-amplitude intervals mark important lithological variations in the Broad Fourteens Basin (Figs. 4.2 and 4.9).

The core of anticline α contains high-amplitude seismic reflections along the boundary between the Chalk and Rijnland Groups. This boundary generally occurs less than 50 ms below the Base Tertiary Unconformity (Fig. 7.4). Of all the Chalk Group subdivisions the Ommelanden Formation, composed of fine-grained limestones and occasional tongues of sandstone, is by far the most widespread, laterally continuous and thickest (van Gent et al., 2010, Van Adrichem Boogaert and Kouwe, 1994-1997). Near the base of this formation, parallel transparent reflections transition downwards into bright, high-amplitude seismic reflections (Fig. 7.4). This character is only observed on the flanks of anticline α. Complementing this, gamma ray profiles from boreholes K15-07 and K15-02 allude to strong lithological variations within the Chalk Group (Fig. 4.2 and 7.9).

The key lithological difference in Mesozoic strata directly below the Base Tertiary Unconformity is the presence of silty marl, which appears on the flanks but is absent on the crest (Fig. 7.9). It correlates to the low-amplitude, semi continuous seismic reflections in Figure 7.4. This interval is up to 600 ms thick on the southwest flank of anticline α, and has compacted more than strata on the crest where carbonates predominate (Lowest Chalk and Rijnland Groups). Well K15-02, located on the NE flank of anticline α, crossed cemented limestones, whereas well K15-07, located closer to the crest of anticline α, crossed a thick chalk interval (Fig. 7.9). Either way, both gamma ray profiles are very low (deflected to the left), and the interval transit time (μs/ft), or acoustic slowness, is

lower than the silt. This indicates the limestones have had a greater porosity reduction than the silts during compaction, as these units have been buried to a great depth already (Mallon and Swarbrick, 2002, Hillis, 1995)

A burial history model for anticline α in the Broad Fourteens Basin was created by Verweij et al. (2012). Strata in the Chalk and Rijnland Groups are expected to obey the normal compaction trends estimated for North Sea sediments. The subsequent erosion of more than 1 km of strata above returned them to hydrostatic conditions (Verweij et al., 2012, Hillis, 1995). In Figure 7.14, Cretaceous rocks (i.e. Chalk and Rijnland Groups) reached peak burial depths of ~2000 m. Prior to inversion, the overlying stratal package solely comprised Cretaceous rocks (Verweij et al., 2012, Hillis, 1995). Using data compiled by Van Der Molen (2004), regional porosity-depth curves for the Chalk Group strata in different locations were compared. Average porosity for the Chalk Group was ~70% at the surface, and decreased to ~15 – 30% after being buried to ~2000 m (Hillis, 1995, Scholle, 1977, Mallon and Swarbrick, 2002, Japsen, 1998). The rocks in the centre of anticline α were therefore compacted to a large degree and, accordingly, resisted secondary compaction in a more effective way than its flanking strata after being returned to the surface during the Laramide inversion. As depth-controlled compaction in chalks is largely irreversible, any rock uplifted during regional tectonic inversion may record compaction values higher than those estimated at present day depths, forming overcompacted intervals

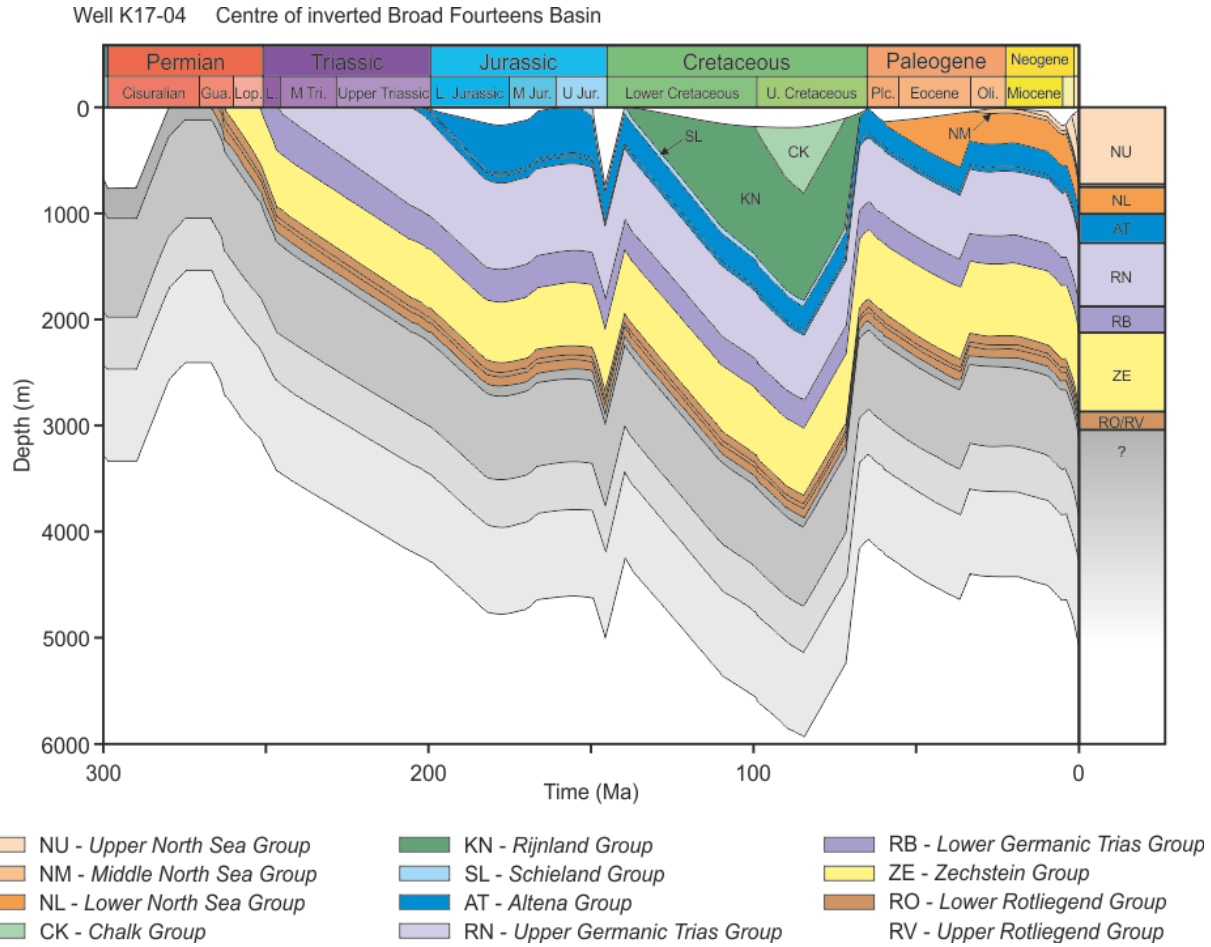

Fig. 7.14 Basin model at the centre of the Broad Fourteens Basin, showing the burial history of the rocks in the study area. The units were correlated to well K17-04, revealing slightly greater erosion of Cretaceous Units than in block K15. *Modified from Verweij et al. (2012).*

(Japsen, 1998, Hillis, 1995). In addition, absolute rock properties and depth estimates can be affected by diagenesis, by the development of overpressures, or by entrained hydrocarbons preventing cementation of grains (Avseth et al., 2003, Worum and van Wees, 2017, Hillis, 1995, Scholle, 1977). All this led to differential compaction and the formation of the Type A traps in the Lower North Sea Group (anticlines α^1, β^1, and γ^1) (Fig. 7.4).

The Type A trap in the Taranaki Basin (anticline δ^1) formed in sediments surrounding the Parihaka volcano (Fig. 7.11). Until the Late Pliocene, volcanoes belonging to the Mohakatino volcanic arc remained exposed at the surface (Hansen and Kamp, 2002). When active, they comprised submarine andesitic stratavolcanoes fed from a magma chamber with a large intrusive complex below. Volcanic activity stopped between 4.8 and 6 Ma b.p. (Chenrai and Huuse, 2017). As such, the volcanic cone has a very thin sedimentary cover (Fig. 7.11). In contrast, rapid deposition in the basin continued around the flanks of the Parihaka volcano during the Pliocene (Hansen and Kamp, 2002). The Giant Foresets Formation, surrounding the top of the Parihaka volcano, largely consists of fine-grained muds. Numerous channels eroded the base of the unit, and occasional volcaniclastics and coarser-grained siliciclastics are interbedded with these muds (Hansen and Kamp, 2002, Hansen and Kamp, 2004).

Comparable to the Lower North Sea Group example, the lithological and rheological differences between the Parihaka volcano and the Giant Foresets

Formation led to differences in their compaction rates. Whereas the Parihaka volcano resisted compaction, the surrounding fine-grained material likely compacted significantly (Chenrai and Huuse, 2017, Reynolds et al., 1991, Anell and Midtkandal, 2017). Chenrai and Huuse (2017) predicted compaction within the Giant Foresets Formation to be as great as 70% in some areas, after noticing pockmarks associated with fluid expulsion during sediment loading in the north of the study area. The amount of compaction in the fluid-filled units studied by Chenrai and Huuse (2017) is comparable with the value calculated by Reynolds et al. (1991). In stark contrast, Anell and Midtkandal (2017) expected the 'average clinoform' in the Giant Foresets Formation to compact as little as 12%. Although this is a much lower figure when compared to a buried volcano that does not compact, a volume reduction of 12% within each clinoform is significant enough to produce the subtle traps observed in the Taranaki Basin. Using the seismic data, compaction of the Giant Foresets Formation was estimated in this thesis to reach values of ~50 to 60% away from the Parihaka volcano (Fig. 7.11).

The Taranaki Basin example (anticline δ^1) contrasts with the Lower North Sea Group folds (anticlines α^1, β^1, and γ^1) in terms of its evolution. In the Broad Fourteens Basin, the Lower North Sea Group strata was deposited on a relatively flat topography; differential compaction occurred in response to varying rheological properties of the buried rocks. The Taranaki Basin example focusses on a large volcano that remained exposed on the seafloor for up to 8 Myrs (Hansen and Kamp, 2004). The Giant Foresets Formation was continually

deposited around the Parihaka volcano until it was buried in the Late Pliocene (Hansen and Kamp, 2002) (Fig. 7.11). As a result, a very thick, fine-grained sedimentary succession sits adjacently to a rigid, lithified volcanic complex. Under its own weight, the Giant Foresets Formation started compacting before the Parihaka volcano was buried (Reynolds et al., 1991). Paradoxically, this created more accommodation space for oncoming sediment. The tilting of seismic reflections away from the Parihaka volcano provides the strongest evidence for compaction within the Giant Foresets Formation (Fig. 7.11). Even after the complete burial of the Parihaka volcano, the sedimentary pile was still compacting at a much greater rate than the (uncompactable) volcano, producing the Type A trap documented in this discussion.

In the published literature, Type A traps have been documented over structural highs. Gómez and Vergés (2005) studied differential compaction over basement highs in the Mid-Norwegian extensional margin. They immediately differentiated between anticlines formed during tectonic compression, and anticlines generated by differential compaction (Fig. 7.3a). During compression, anticlines form over structural lows, whereas during differential compaction anticlines form over structural highs (Fig. 1.5a). This character is similar to the Type A traps in the Broad Fourteens and Taranaki basins (Figs. 7.4 and 7.11). Tectonic compression was calculated to be responsible for at least a third of the height of the anticline in the Mid-Norwegian study, but was considerably enhanced by differential compaction (Gómez and Vergés, 2005).

Buczkowski and Cooke (2004) studied 'drape folding' in circular grabens over buried impact craters (Fig. 7.3b). Although the formation of the drape fold (anticline over the impact structure) resulted largely from differential compaction, there was an added contribution of horizontal volumetric compaction. As wet soils started to dry during vertical compaction, the surface tension of the water pulled the grains towards each other, shrinking the rock mass (Buczkowski and Cooke, 2004). Many other studies have associated anticlines with differential compaction over positive basement topography or isolated stratigraphic packages, e.g. carbonate platforms (Williams, 1987, Carminati and Santantonio, 2005, Maillard et al., 2003, Collette and Rutten, 1970, Perez-Garcia et al., 2013, Xu et al., 2015).

Similarly to the Taranaki dataset, each of the examples above suggests that differential compaction occurs over a single, discrete lithological package, whether it is a basement high (Gómez and Vergés, 2005, Collette and Rutten, 1970, Williams, 1987, Maillard et al., 2003), a carbonate platform (Carminati and Santantonio, 2005), salt diapir (Perez-Garcia et al., 2013), or sandstone bodies (Xu et al., 2015). While there are parallels between anticlines α^1, β^1, and γ^1 in the Broad Fourteens Basin and those researched in the literature, there are also significant differences. Anticline α^1 in the Broad Fourteens Basin occurs over different lithologies; the core of anticline α contains cemented limestone, siltstone, marl, and sandstone belonging to the Rijnland and Chalk Group's (Figs. 4.2. and 7.9). The flanks are largely dominated by chalk and it was the mechanical properties

of the chalk (the more compactible unit), not its lithological character, that allowed differential compaction to occur. In the centre of anticline α, rocks were buried to greater depths than on the flanks, increasing the amount of compaction during initial burial and before tectonic inversion (Verweij et al., 2012).

Another key difference between the subtle anticlines in this work and those from the literature is the input of other geological processes. The studies from Gómez and Vergés (2005) and Buczkowski and Cooke (2004) emphasise the importance of non-compaction related factors to the generation of Type A traps. Both tectonic compression and volumetric contraction occurred in parallel with differential compaction to produce the topographic features in Gómez and Vergés (2005) and Buczkowski and Cooke (2004) respectively. No evidence for active tectonic compression can be seen in the Taranaki Basin dataset. In the Broad Fourteens Basin dataset, tectonic inversion did contribute to the formation of a Type A trap, although differential compaction enhanced the size of this trap significantly. In addition, there are no large faults associated with intense tectonic inversion within the Tertiary strata. Instead, polygonal faults are pervasive in the Lower North Sea Group, hinting at significant compaction and volume loss (Fig. 7.4).

Following the postulate in Cartwright (1994), polygonal faults in this unit may relate to episodic dewatering of shales after a critical load was reached. Similarly to the faults over the impact crater presented in Buczkowski and Cooke

(2004), volumetric contraction can lead to the formation of polygonal faults during early burial (Lonergan and Cartwright, 1999). The faults are concentrated in the centre of anticline α^1, decreasing in number on its flanks (Fig. 7.4). Obeying the processes denoted by Cartwright (1994), Lonergan and Cartwright (1999), and Buczkowski and Cooke (2004), maximum volumetric reduction of the rocks occurs on the crest of the compaction-related anticline. A prerequisite for volumetric contraction from polygonal faulting is a large vertical load over the whole rock unit. Differential compaction would have occurred as the vertical load increased, meaning anticlines α^1, β^1, and γ^1 must have been formed prior to their volume reduction. This reduced the height of the Type A traps.

7.3.3.2. Type B: Compaction over discrete sediment packages

Type B traps comprise compaction-related anticlines formed over isolated sediment packages or pathways. As such, the material underlying Type B traps tends to be coarse-grained, having been deposited there during high energy events (Ritchie et al., 1999). One Type B trap has already been discussed in detail in *Chapter 5*: a buried Late Miocene channel complex in the Espírito Santo Basin is observed below a ridge-like anticline (anticline C^1) (Fig. 7.2c and Table 7-1). In essence, Type B traps are much smaller than their Type A counterparts, generally between 500 m and 5 km wide, and are a consequence of sedimentary processes rather than tectonic, igneous, or halokinetic phenomena (Table 7-1).

In a dataset that is dominated by vertically stacked erosional channels, it is unusual to see the impact a channel complex has on overlying strata (Fig. 5.2). However, the studied channel complex from the Espírito Santo Basin was isolated, overlain by a thick unit of homogeneous, fine-grained material (Fig. 5.3). Consequently, deformation was preserved in overburden strata. Differential compaction produced an anticline (anticline C^1) after the channel complex was buried to a depth exceeding 200 m (*see Chapter 5* - Fig. 5.3). Within the isolated channel complex, individual channels are also characterised by smaller compaction-related anticlines formed directly over them (Fig. 5.5).

As ascertained in *section 5.7.2*, the scarce well data in the Espírito Santo Basin means it is difficult to predict the true lithologies in and around the channel complex. This is a real caveat for accurate measurements and modelling of differential compaction, as lithological contrasts are the key control in this process (Schultz et al., 2010, Aplin et al., 1995, Yang and Aplin, 1998). However, knowledge of other similar features in different localities provides vital information to predict the lithologies associated with the channel complex. In *Chapter 5* it was concluded that the compaction-related anticlines with the greatest relief corresponded to parts of the channel complex with the largest volumes of coarse-grained material. With the aid of descriptions from literature (below), Type B traps can be used as a diagnostic feature of sand fairways, *i.e.* submarine channels and fans, and of the lithologies filling them.

If most Type B traps are in fact related to sediment (sand) pathways, their global importance, and partly the reason they have been ascribed their own class, is down to their greater potential for being effective hydrocarbon traps. Closure of low-permeability strata over coarse-grained intervals creates perfect conditions for sealing hydrocarbons. Type B traps have historically been explored and some are being produced from at present (Corcoran, 2006, Cosgrove and Hillier, 1999, Armstrong et al., 1987). They are not limited to channels; Type B traps also form over submarine fans, unconfined terminal lobes, isolated turbidites and mounded channels (Corcoran, 2006). Each of these examples can show structural closures that form in response to stratigraphic and lithological changes. Coarse-grained material is deposited in the thalweg of the sediment pathway and subsequently resists compaction more than a surrounding material, creating the compaction-related anticline (Figs. 7.2c and 7.3d-f).

The contrast in the initial porosity between channel-fill and overbank deposits allows the surrounding fine-grained material to compact much more than the channelized coarse-grained material (Athy, 1930, Perrier and Quiblier, 1974, Weller, 1959, Corcoran, 2008). The initial rates at which porosity diminishes within fine-grained shales are much greater than those of an average sandstone (Perrier and Quiblier, 1974) (Fig. 1.4). However, once the rocks reach a certain depth, estimated to be between 100 m and 1000 m (Perrier and Quiblier, 1974), porosity losses in sandstone are enhanced until the porosity of both sandstone

and shale has been reduced to ~ 0%. In this case, beyond a certain depth Type B, traps can reduce in size, as the sandstone starts to compact at a faster rate than the surrounding shale (Fig. 1.4). The amount of folding caused by differential compaction will therefore be underestimated with increasing depth. In contrast, if fluids are not expelled from the sandstones because of the permeability contrast of surrounding muds, porosity can be retained at depth and the sandstones would become overpressured.

In the Espírito Santo Basin, overpressure led to failure of the overlying rock unit, permitting fluids to migrate towards the surface (*section 5.7.1*). A similar process has been observed by Gay et al. (2006b) and Xu et al. (2015), where faulting along compaction-related anticlines has led to catastrophic fluid release. As Type B traps are the only traps associated with the presence of coarse-grained sediment and the possible development of overpressures, they are the most likely type of trap to fail from faulting.

Compared with Type A, C and D subtle traps, Type B traps are unique. They form over depositional packages that are normally elongate, which leads to two-way dip closure. The strata below are often reservoir type coarse-grained deposits (Corcoran, 2006, Armstrong et al., 1987). They are also the hardest to predict. While it is easy to draw a model of a Type A trap forming over a tectonic, halokinetic or volcanic feature, the lithological, petrophysical and hydrological factors associated with Type B traps can be so variable that two identical looking

channels may show compaction-related anticlines of unequal sizes. To identify the full geological parameters, and to fully understand its effectiveness as a hydrocarbon play, it is necessary to have an integration of well logs, 3D seismic data, and core data. However, it is possible to gain a detailed understanding by first identifying the compaction-related trap, and thus classifying it on 3D seismic data, then working backwards. Once located on seismic data, volume and attribute analyses can be used in conjunction with the classification scheme to identify areas that could have either coarse-grained reservoir quality strata, or high pore-fluid pressures (Chopra and Marfurt, 2012).

7.3.3.3. Type C: Compaction over local topographic features

Type C subtle traps include some of the smallest seismically resolvable compaction-related anticlines. They form over local topographic features generally created by erosion of the seafloor. Once buried, the topographic features resist compaction more than the surrounding sediments, generating Type C subtle traps over them. Both the mass-transport deposit (MTD A) from *Chapter 6* (Espírito Santo Basin) and the scarp along the Base Tertiary Unconformity in this chapter (Broad Fourteens Basin) belong in this class (Figs. 7.2e-f, and Table 7-1). While these two subtle traps have been identified on 3D seismic data, many examples of Type C traps in the published literature rely on outcrop descriptions. The identification of Type C traps also depends on the

resolution of seismic data, but for this classification scheme they comprise features larger than ~20 m (Table 7-1).

Chapter 6 investigated a mass transport deposit in the Espírito Santo Basin. A crucial interpretation was the formation of compaction-related anticlines over lithified remnant and rafted carbonate blocks entrained within a debris flow. The bulk of the chapter focussed on the development of depocentres over the debrites, which are ~140 to 1800 m wide (Table 6-1). Type C traps separate each of the seafloor depocentres, mimicking the geometry of the underlying blocks and ranging in width from ~100 m to 1100 m (Figs. 6.3 and 6.4). The high density and large surface area of blocks entrained in MTD A make Type C traps very different from Types A and B. Rather than producing a single fold, interlinking anticline-depocentre-anticline features creates a downslope 'ripple-like' morphology (Fig. 6.6). Indeed, it is the location of the depocentres between Type C traps that controls the sediment distribution post-compaction. Differential compaction occurred during the very early burial stages of MTD A, as portrayed by seismic reflections onlapping the sides of the depocentres (Fig. 6.21a).

Such a high density of blocks in MTD A enables a detailed description of Type C traps. The most obvious characteristic of these traps is how the shape of the imaged blocks determines the shape and size of overlying folds. Blocks with a wide, flat upper surface create broad, shallow anticlines; tall blocks with a pointed surface create much more tightly folded, thinner anticlines (Figs. 6.3 and

6.4). Above the blocks irregular top surfaces, the folds produced are rounded. Even the largest blocks containing steps and very irregular surfaces produce rounded Type C traps (Fig. 6.3 and 6.4). Folds produced by differential compaction are therefore dependent on scaling laws. Small scale lithological variations such as sub-seismic bedding may well induce differential compaction, yet the large scale lithological variations will supersede this and overwrite the imprint of smaller features. This process is not limited to debrites compacting more than blocks in MTD A. In fact, it can be seen in all the previously described categories. The Type A traps formed in the Lower North Sea Group (anticlines α^1, β^1, and γ^1) responds to the broad lithological changes between the core of anticline α and its flanks, ignoring the lithological variations within this unit (Fig. 7.4). The Type B trap in the Espírito Santo Basin (anticline C^1) responds to gross lithological changes; a single anticline is produced over the channel complex axis, even with the inconsistent presence of smaller channels (Fig. 7.2c).

This process is again shown by the Base Tertiary Unconformity example described in *section 7.3.1.1.2*. A subtle anticline was formed over a topographic scarp that remained on the sea floor after the erosion of hundreds of metres of Mesozoic strata during inversion (Verweij and Simmelink, 2002, De Lugt et al., 2003). Once the sea floor healed and sediment filled the minibasin adjacent to the topographic scarp, its burial caused the sediment to compact more than the lithified rocks on the scarp (Fig. 7.4). A Type C trap was formed in strata <150 ms

above the scarp, and follows the whole north-eastern rim of the salt withdrawal basin/southwest rim of anticline α (Fig. 7.7).

The lack of wells on the southwest quadrant of the seismic data renders it impossible to determine the absolute lithology of the topographic scarp below the Type C trap. However, it is clearly marked across its entire extent as a set of high-amplitude seismic reflections (Fig. 7.4 - 7.6). A maximum amplitude map shows the ridge by a set of two high amplitude bands (red-yellow) separated by a low amplitude band (blue) (Fig. 7.15). This dictates a sudden lithological contrast from the salt withdrawal basin to the edge of anticline α. These bright reflections can be correlated to the other side of anticline α to predict their lithology (Fig. 4.2). Well K15-07 penetrates the set of bright reflections and attributes them to sands and marls (Fig. 7.9). This unit (Ommelanden Formation) is described as containing tongues of sandstone (Van Adrichem Boogaert and Kouwe, 1994-1997). Bounding the sandy interval are chalks and limestones. Preferential erosion of the chalks could have formed the prominent ridge of sandstone, which had previously been buried to a significant depth, to become compacted and cemented (Verweij et al., 2012) (Fig. 7.14).

Differential compaction has been observed above quartz arenite basement highs (Corcoran, 2008). This later study provided an example where overlying

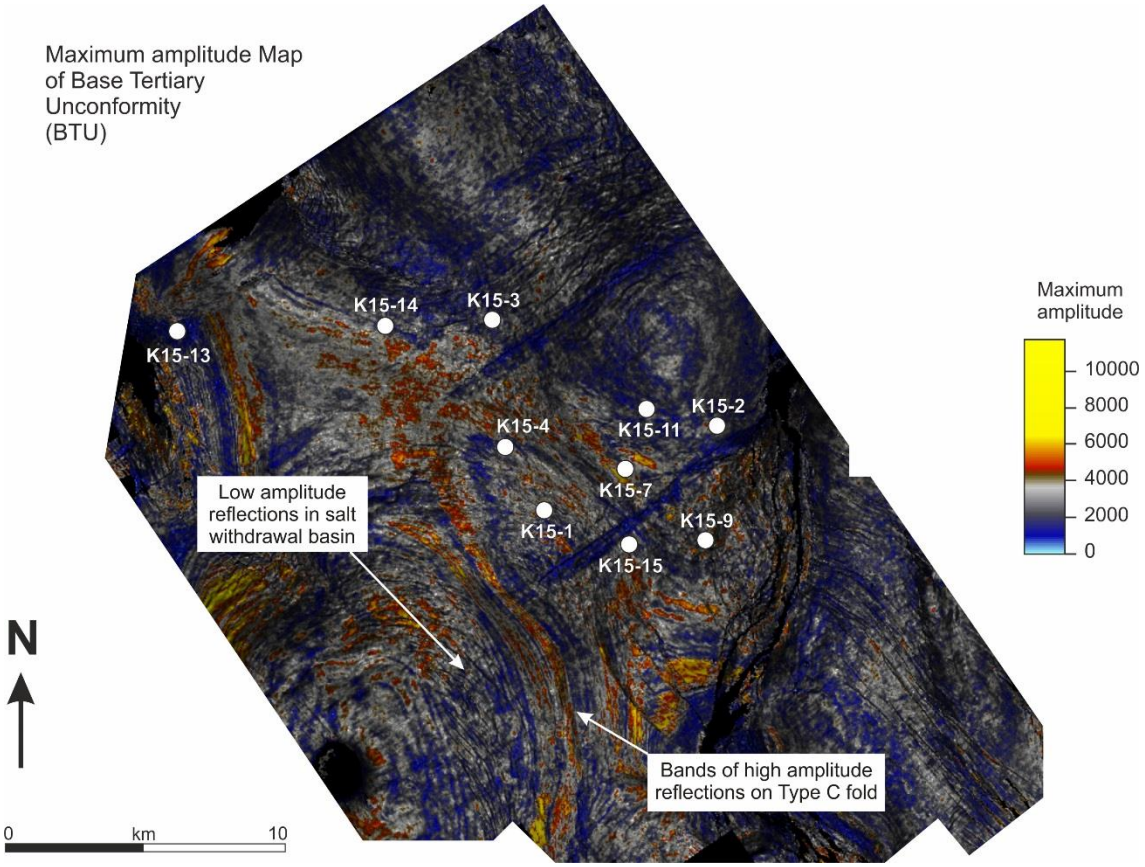

Fig. 7.15 Maximum amplitude attribute map of the Base Tertiary Unconformity, including 20 ms below the interpreted Horizon H_6. The high amplitude reflections in the Ommelanden Formation, associated with the Type C fold, enclose the salt withdrawal basin in the southwest.

dolostone thickened down-dip of basement highs (Fig. 7.3g). The stratigraphic sequence in Corcoran (2008) represented a transgressive sequence (dolostone) deposited over a coastal shoreface (basement highs). Dolostone deposited along the flanks of the basement highs actually preserved some of the original topographic dip, although differential compaction subsequently enhanced it. Along the shoreface, basement fragments (from 2.5 m boulders to 4.5 m blocks) created smaller topographic variations (Fig. 7.3g). Differential compaction was also observed over these basement fragments, but the resulting folds are too small to be classified as Type C traps. As discussed in Corcoran (2008), small scale variations in lithology between the eroded basement fragments and carbonate matrix did not control the Type C trap over the basement highs. Instead a broad, rounded anticline (~25 m) was formed over a conglomerate sequence (Fig. 7.3g).

7.3.3.4. Type D: Compaction at outcrop

If smaller than ~20 m, geological structures become very difficult, if not impossible, to resolve on industry seismic data, and to thus truly understand. Features with smaller scales can be identified and analysed in much greater detail in outcrop. Type D traps incorporate any compaction-related anticlines that form over features <20 m. No fieldwork was conducted in this study, but features that can be classed as Type D traps have been identified in the literature (Table 7-1).

Differential compaction over a basement high was described in *section 7.3.2.3* as a Type C trap. In the same study, Corcoran (2008) described differential compaction over the fragments of quartz arenite basement blocks and boulders. Beds thickened down-dip of boulder flanks creating depocentres reminiscent of those seen over MTD A (*Chapter 6*). The folds continue vertically for less than a metre and are very small in comparison to the Type C folds. Nonetheless, they comprise very comparable features; they produce rounded folds, the shape of the block is inherited in the overlying fold, and the density of blocks can create anticline-depocentre-anticline 'ripples'. Because these compaction-related anticlines are so small, their influence on post-compaction sediment distribution is also moderate, especially in comparison to Type A, B, and even C traps. One does not expect to see deposition of alternate material within depocentres associated with Type D, as shown by the continual deposition of dolostone above the quartz arenite blocks in Corcoran (2008) (Fig. 7.3g).

One of the most widely documented examples of differential compaction at outcrop is that involving carbonate concretions. They regularly form within shale sequences during early diagenesis, and often prior to significant compaction (Savrda and Bottjer, 1988, Melezhik et al., 2005). Concretions are much more competent than the surrounding shale and will therefore resist compaction (Fig. 7.3i). Differential compaction around the concretion will occur during very early burial and produce significant folds within the shale layer (Savrda and Bottjer, 1988, Lash and Blood, 2004). Forming on such a small scale,

it is the only type of fold that will occur in the first few metres of burial (Savrda and Bottjer, 1988).

While the previous example pertained differential compaction to the highly competent carbonate concretion within shale, Bryant and Miall (2010) identified differential compaction between a laminated carbonate and sandstone injectite. At an outcrop in West Canyon, Utah/Arizona border, a laminated carbonate compacts more than a sandstone injectite (Fig. 7.3j). The outcrop in question is ~0.5 m high, with the sandstone injectite roughly half that height. Injection of the sandstone, and subsequent differential compaction, are believed to also have occurred during very early burial.

In both the concretion and the injectite, the more compactable strata completely surrounded the less compactable strata. Not only was a Type D trap produced over the competent features, bedding was deflected downwards, underneath it. As the concretion and injectite were emplaced near to the surface, the weight of the body must have forced down the surrounding strata. This is not observed in any other types of fold. Types A, B, and C form over the top of contrasting lithologies, and the deformation is observed only in overlying units. The two Type D traps just described occur within a single sedimentary package (Fig. 7.3i).

7.3.4. Overlapping trap types

The classification in this thesis is based on interpreted 3D seismic data and geological features described in the published literature. It is a classification scheme that enables immediate assessment of subtle traps. Other structures formed by differential compaction also produce deformation and topographic variations, but are systematically different to the subtle traps documented here. Sandstone wedges, for example, will produce a monocline over buried sandstones and will pinch out laterally into mudstones and shales (Carver, 1968) (Fig. 1.5c). Even though the fold is created by differential compaction, it does not exhibit more than one-way dip closure, so it cannot be classified as a structural trap. The same can be ascribed to differential compaction over basement steps, prograding carbonate platforms, and differential sediment loading over shales (Nunn, 1985, Maillard et al., 2003, Saller, 1996, Xu et al., 2015, Rusciadelli and Di Simone, 2007, Verwer et al., 2009, Hunt et al., 1996). However, there are some examples in the literature that span two different classes, and some geological features that vary so greatly in size and geometry that different examples of such features fit into different classes. Figure 7.16 is a summary graph of all the measured examples from Table 7-1, showing the division and overlap between different trap classes.

As seems to be the case in all matters of sedimentology, carbonates are the hardest rock to classify. This is largely down to compositional heterogeneities,

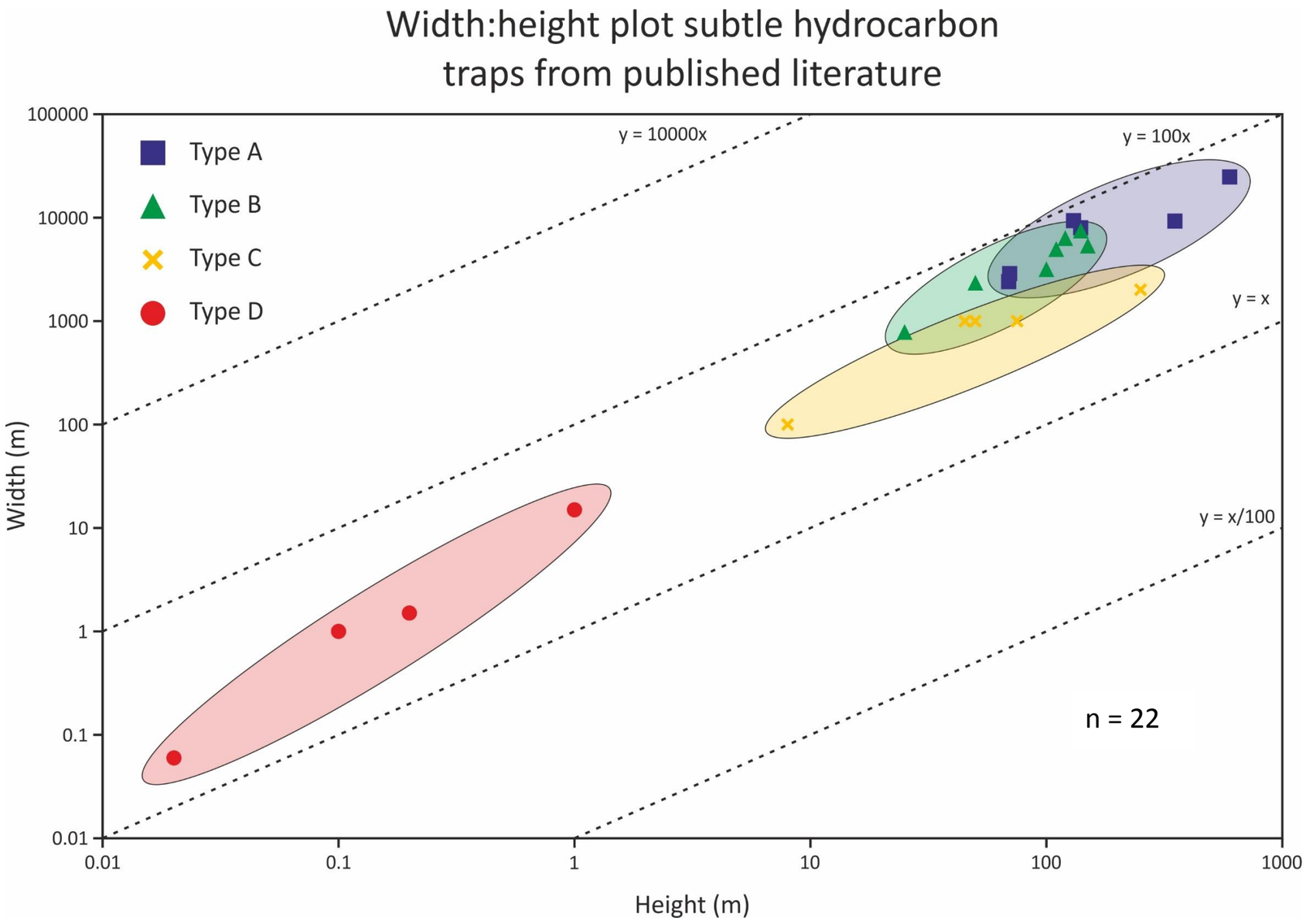

Fig. 7.16 Log:log graph of all the examples of differential compaction taken from the published literature (see Table 7-1). Type A traps are shown in blue, Type B traps are shown in green, Type C traps are shown in yellow, and Type D traps are shown in red. There is clearly some overlap between the different subtle traps when comparing their sizes, especially Type A, B, and C.

the chemical reactivity of carbonate minerals, and porosity/permeability variations within carbonate rocks (Choquette and Pray, 1970, Anselmetti et al., 1998, Ehrenberg and Nadeau, 2005, Dunham, 1962). Of particular interest to this classification scheme, buried isolated carbonate platforms can have subtle traps over them (Fig. 7.3h). They are often composed of hard, well-cemented substrate that compacts less than the surrounding muds. The confusion in classification comes primarily down to the size of the platforms. Clearly, carbonate platforms are not related to sediment transport, rather building up *in situ* and do not fit into the Type B traps. However, studies have been conducted on isolated carbonate platforms ranging from <1 km (Carminati and Santantonio, 2005, Elvebakk et al., 2002) to >10 km (Belde et al., 2017, Burgess et al., 2013), which show descriptions of differential compaction occurring over these same build ups. Because of their size range, they can fit into both Type A and C (Fig. 7.3h). Individual carbonate build ups would need careful assessment before being classified as one of the two types.

Another ambiguous geological feature are MTDs. In *section 7.3.2.3* MTD A was given as an example of a Type C trap (Fig. 7.2d-e and Table 7-1). Even though some blocks were very large, they were topographic features on the seafloor, and indeed acted like Type C traps. In *Chapter 6*, a thickness map showed a broad anticline close to the headwall over the width of MTD A (Fig. 6.9b). The anticline is ~10 km wide and therefore fits in the realms of a Type B trap. Using the same dataset, Alves (2010) noticed this broad fold. As MTD A represents a sediment

transport system, this fold can be classified as Type B. It is also noticed that this large fold does not follow the geometry of the blocks, overprinting the Type C traps previously described. In summary, some geological features can contain multiple types of subtle traps at different scales, with the larger traps often overprinting the smaller ones.

7.4. Exploration potential of subtle hydrocarbon traps

As mentioned in *section 1.1* subtle traps (stratigraphic and palaeogeomorphic) are well documented features in the subsurface (Gabrielsen et al., 1995, Li et al., 1982). Halbouty (1969) explained the necessity of discovering subtle traps even before the great drive for exploration of the North Sea in the 1970's. Now, more than ever, subtle traps can provide sufficient hydrocarbon resources to keep mature basins, such as the North Sea, actively producing (Verweij et al., 2012). The previous sections (*7.3 and 7.4*) provide a classification scheme for subtle structural traps; those that are characterised by two-way or four-way dip closures resulting from differential compaction. This type of subtle trap is rarely considered in the typical classification highlighted by Gabrielsen et al. (1995). They have been called many different names in published literature, including forced-folds (*e.g.* Cosgrove and Hillier 1999), drape-folds (*e.g.* Biddle and Wielchowsky 1994) and plain-type folds (*e.g.* Merriam 2005). Table 7-1 summarises many of these subtle structural traps. However, missing from the

classification scheme is its importance of these structures for hydrocarbon exploration.

One of the key features of traps is that they are only considered traps if they are associated with a reservoir (Biddle and Wielchowsky, 1994). It is essential in trap evaluation for both the seal and reservoir to be analysed. For example, the Type B traps form over sediment pathways. In most cases, differential compaction will create positive relief structures when sediment pathways, such as submarine channels and fans, contain coarser-grained material than their flanks (Cosgrove and Hillier, 1999, Chopra and Marfurt, 2012, Corcoran, 2006, Posamentier, 2003, Mayall et al., 2006). The coarse-grained strata acts as the reservoir, with the Type B trap overlying it. The deformed rocks displaying the subtle structural traps tend to be homogeneous and fine-grained, with limited lateral variation (*i.e.* mudstones). Hence, muds act as a permeability barrier and form a seal within the trap, necessary to prevent further migration of hydrocarbons. It is thus true that differential compaction is intrinsically linked to variations in the petrophysical properties of different rocks – *i.e.* porosity and permeability (Trask, 1931, Perrier and Quiblier, 1974, Aplin et al., 1995, Snarskiy, 1961). As well as forming over reservoir intervals, topographic relief of these subtle features can redirect sediment on the sea floor (Alves and Cartwright, 2010). In *Chapter 6*, depocentres formed between Type C traps, and depocentres may hold large volumes of reservoir rocks that are sealed vertically by overlying muds, and laterally by the Type C traps also containing mud. Multiple sediment-

routing events, confined by subtle-structural traps, can produce a series of isolated hydrocarbon systems over large stratigraphic features. Exploration in mature basins, such as the North Sea, would do well focussing on smaller, more subtle features away from the apex of typical large structural closures.

Another vital aspect of the traps that needs careful consideration is the timing of their formation (Selley and Sonnenberg, 2014). For a reservoir to retain hydrocarbons, the trap and seal must be in place prior to the migration of hydrocarbons. Evidence from *Chapters 5* and *6* suggests that trap formation occurred after <200 m of sediment had been deposited over the channel complex and MTD A (Figs. 5.11 – 5.13). Forming the trap after such limited burial increases the chances of it being present before a source rock reaches maturity and expels hydrocarbons. Source rock maturation is so heavily dependent on kerogen types, burial rates, subsidence, and the thermal gradient of a basin, that no exact number can be provided for the temperature or depths at which it will mature (Tissot and Welte, 1984).

A possible caveat to this rule is the effect increasing burial depth has on structures related to differential compaction. Perrier and Quiblier (1974) modelled the compaction curves for sandstone and mudstone with increasing depth. According to their figure (Figure 1.4 in this thesis), sandstones start to rapidly lose porosity at ~250 m below the sea floor. After a couple of kilometres of burial, the sandstones have a similar porosity to the shales. The variation in

compaction rates with depth is not limited to sands and muds (Perrier and Quiblier, 1974). In addition, chemical compaction (*e.g.* diagenesis) will alter the compaction rates of different lithologies. This is a crucial aspect when analysing subtle structural traps. Continual burial may increase, or alternatively decrease, the amplitude of the fold depending on which lithologies are being compacted. This could result in an over-/under-estimation of the traps' dimensions. However, as the compaction rates of different lithologies do not change on an exploration timescale (Meckel et al., 2007), this will not be a concern if thorough analyses of the trap are conducted using a combination of modern seismic data and borehole data. It will only be problematic when estimating trap size using limited datasets.

7.5. Impact of faulting

During the processes forming subtle traps from differential compaction, catastrophic failure in the overburden can hinder petroleum prospects (Xu et al., 2015, Cosgrove and Hillier, 1999, Osborne and Swarbrick, 1997). Fractures and faults act either as conduits for fluid flow, releasing fluids from the reservoir or bypassing the seal, or as a seal, segmenting and compartmentalising a reservoir (Bjørlykke and Høeg, 1997, Cartwright et al., 2007, Stewart, 2006). Fractures and faults related to differential compaction form in two ways: 1) a build-up of overpressure in the reservoir (Bjørlykke and Høeg, 1997, Cosgrove and Hillier,

1999, Osborne and Swarbrick, 1997); 2) bending of material over a lithological boundary or along a neutral surface (Carver, 1968, Xu et al., 2015, Stewart, 2006). In the first process, overpressured conditions are created in the reservoir when fluids flow into the reservoir at higher rates than they escape, *i.e.* the pore fluid pressure in the reservoir is greater than the hydrostatic gradient at that depth (Osborne and Swarbrick, 1997). It is necessary to have an impermeable sealing surface for this to take place. As the reservoir is buried to greater depth, the vertical stress increases, whilst the effective stress remains low, as the stress is transferred from the rock grains to the pore fluids. At the point when the pore pressure exceeds the tensile strength of the rock, hydraulic fracturing produces faults, leading to catastrophic fluid release (Osborne and Swarbrick, 1997). An example of this style of fracturing is seen in the Type B trap over the submarine channel complex in *Chapter 5*.

The second process involves the failure of strata as it is bent during differential compaction. Lithological variations in the underlying rock layers, inducing differential compaction, cause faults to be oriented either perpendicular or parallel to the lithological boundary (Xu et al., 2015). These faults represent simple shear in the compacting rock mass: differential subsidence between the more compactable strata compared to the less compactable strata induces brittle failure (Carver, 1968). This occurred in the Broad Fourteens salt withdrawal basin in *Chapter 4* (Figs. 4.9 and 4.20). Although the studied concentric faults represent

differential subsidence of the salt withdrawal basin, they are a direct analogue to the type of faults produced during differential compaction.

Most of the faults discussed here are related to differential compaction. *Chapter 4* analyses a set of faults that developed below the anticline α^1 in the Broad Fourteens Basin (Fig. 4.9). Faults cross-cutting anticline α chiefly terminate at the Base Tertiary Unconformity; only a couple propagate into the Lower North Sea Group (Fig. 7.4). Slip tendency analyses were conducted on all interpreted faults to understand how they would react to an increase in pore fluid pressures during the injection of CO_2 into the reservoirs within anticline α (Figs. 4.17 – 4.20). Were these faults to act as conduits for fluid flow, carbon capture and storage would not be possible in this area (*see sections 4.7 and 4.8.3*). However, anticline α^1 (Type A trap) was not considered in *Chapter 4*. Flow along the faults would permit fluids to charge reservoirs at the base of anticline α^1. In the case of the Broad Fourteens Basin, strata at the base of the Lower North Sea Group consists of sands, fining upwards into clays (Van Adrichem Boogaert and Kouwe, 1994-1997) (Fig. 7.9). Therefore, a suitable reservoir exists, making Type A traps similar to this one (with underlying, fluid transmitting faults) viable exploration prospects in the Dutch North Sea.

In many explored differential compaction-related traps, hydrocarbons migrate from rocks with lower porosity and permeability, into rocks which are more porous and permeable, *e.g.* mudstones into sandstones (Magara, 1968,

Magara, 1976, Gay et al., 2006a, Gay et al., 2003, Davies, 2003). For example, *Chapter 5* discusses the migration of fluids from overbank muds into a large channel complex in SE Brazil (Fig. 5.16). This migration between strata is not a primary or secondary migration route, as is the case with the faults below anticline α^1 in the Broad Fourteens Basin. The pressure increase from fluids forced into reservoir intervals in the submarine channel complex facilitates overpressured conditions (Bjørlykke, 1999, Osborne and Swarbrick, 1997). Brittle failure occurs when the pressure within the reservoir exceeds the fracture pressure (Osborne and Swarbrick, 1997). These faults occur on the crest of the trap and cross-cut the seal, transmitting fluids vertically. Reservoirs may lose all their hydrocarbons in this process (Gay et al., 2006b). If the faulting occurs during early burial, a large volume of the fluids entrained within the channel will be released to the sea floor (Fig. 5.15). Fortunately, the channel complex from *Chapter 5* would not have reached a sufficient depth to contain volumes of non-biodegraded (or even thermogenic) hydrocarbons. However, were failure to occur during deeper burial, hydrocarbons could escape through the seal, towards the surface (Xu et al., 2015). Anticline α^1 in the Broad Fourteens Basin (*Chapter 4*) may not have experienced overpressure, but a dense set of polygonal faults cross cuts the Lower North Sea Group seal unit (Fig. 7.4). They are considered to have formed from horizontal contraction during dewatering (Lonergan and Cartwright, 1999). Triple-junctions of polygonal faults can provide active fluid

migration pathways, allowing fluids to bypass heavily fractured seal units (Gay et al., 2004, Hustoft et al., 2007).

Contrasting with seal-bypassing faults, a large proportion of faults can act as barriers to fluid flow and compartmentalise a reservoir (Smith, 1966). Sealing faults cutting through the subtle traps can form from bending during differential compaction, or possible reactivation of underlying faults. On the crest of structures, significantly large compartments may form (Cartwright, 2007). In the Taranaki Basin (*section 7.3.1.2*), the Parihaka Fault system cuts through anticline δ^1 (Type A trap) overlying the Parihaka volcano (Fig. 7.10). This has the potential to split the subtle trap into hydrocarbon-filled and water-filled compartments. Similarly, radial faults on the crest of diapirs are known to compartmentalise reservoirs (Davison et al., 2000b, Scott et al., 2010).

Another important style of failure in a compacting rock mass are deformation bands. These are zones of small faults, with millimetre offsets and 10's meters length, that have no discrete surface of discontinuity, making them impossible to identify on 3D seismic data (Aydin, 1978, Ogilvie and Glover, 2001, Aydin and Johnson, 1978, Antonellini et al., 1994). They roughly occupy tabular zones of deformation where grain reorganisation occurs via sliding, rotation, fracturing, shearing and compaction (Fossen et al., 2007, Fortin et al., 2006, Aydin, 2000). Effectively, they reflect a process of porosity loss during compaction and loading, where there is a reduction in grain size and sorting aided by increased

confining pressures. This type of deformation band is known as cataclastic deformation (Ogilvie and Glover, 2001, Knipe, 1997, Antonellini et al., 1994).

Single deformation bands tend to be characterised by strain-hardening, resulting in an abrupt "lock-up" of the band (Davis, 1999, Antonellini et al., 1994, Fortin et al., 2006). Stress is subsequently concentrated on the first band, localising other deformation bands in proximity to the first (Davis, 1999). Gradually, zones of deformation bands form, which leads to discrete slip surfaces, *i.e.* the initial stages of fault planes (Aydin, 1978, Antonellini et al., 1994, Davis, 1999). The creation of bands is strongly dependent on the host rocks' porosity, grain size, lithification, the depth of burial and the confining stresses (Fossen et al., 2007). For example, large porosity and permeability reductions can occur along deformation bands in porous-granular materials with a high percentage of sands, whereas a clay-rich host rock will have a similar porosity and permeability to a deformation band formed within it (Ogilvie and Glover, 2001). For that reason, deformation bands play a significant role in the hydrodynamics of a reservoir. In a porous sandstone, it is common to find the permeability of a deformation band to be two to four orders of magnitude less than the host rock (Aydin, 2000, Ogilvie and Glover, 2001, Fortin et al., 2006, Antonellini et al., 1994). Adequately large zones of deformation bands can act as effective seals, compartmentalising reservoirs without being detected on seismic data (Aydin, 2000, Antonellini et al., 1999) (Fig. 7.17).

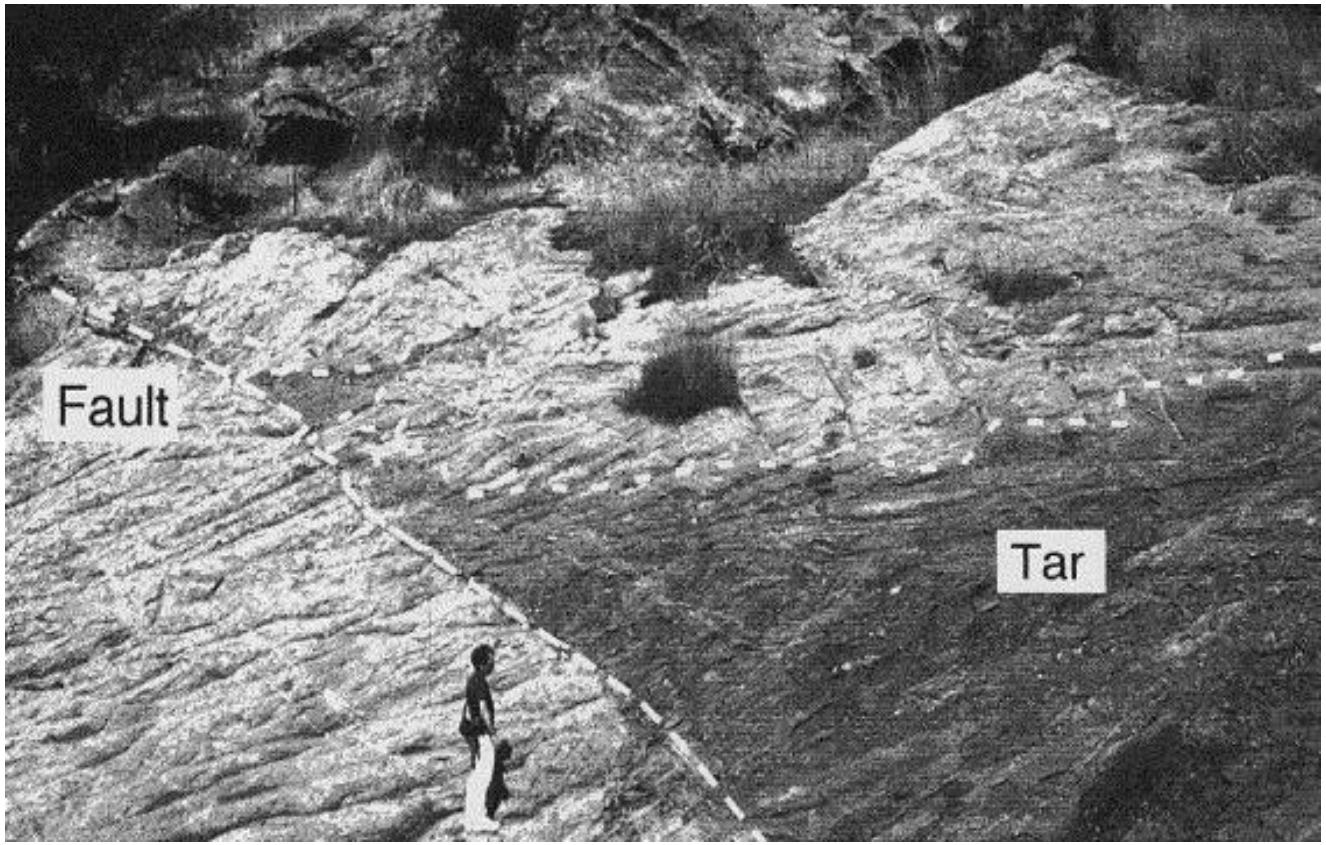

Fig. 7.17 Photograph showing the permeability contrast either side of a deformation band. The sandstones on the right of the photo are impregnated by oil (part of the Arroyo Grande oil field, central California). The oil containing sandstones are compartmentalised by the deformation band faults. *From Antonellini et al. (1999) and Aydin (2000).*

True analyses of a reservoir would therefore require detailed microstructural analyses from borehole data (Knipe et al., 1998). This has important implications to the results from this thesis. Deformation bands cannot be identified on the 3D seismic data provided - without borehole data, they will be completely missed. Formation of these deformation bands requires high confining pressures. In the Espírito Santo Basin, vertical loading is high enough to produce compaction-related structures and occasionally create overpressured reservoirs (*see Chapter 5*). Faults are observed in anticline C^1, over the channel in the Espírito Santo Basin (*Chapter 5*), and as outlined, deformation bands are precursors to faulting. Therefore, the reservoirs below the subtle structural traps are predicted to be – at least partly – compartmentalised by these zones of deformation bands.

7.6. Limitations of this research

This thesis scrutinises differential compaction and subtle structural traps in different geological settings (Figs. 7.2 – 7.3 and Table 7-1). High resolution three-dimensional seismic data was used, allowing reconstructions and analyses of subsurface palaeotopography. The effects of differential compaction could be seen to almost meter scale, yet the resolution of data is still a hindering factor in this work, as revealed by the lack of data for Type D subtle traps. There is a dearth of research crossing between the two; many structures either form on the scale of

seismic data or on the scale of outcrops. The new classification scheme provided was based on published literature to describe the Type D and some of the Type C traps, but primary fieldwork considering the compaction-related anticlines would have helped the classification greatly. Fieldwork was attempted in West Wales, where thick shale sequences were found surrounding sandstone and carbonate blocks. However, all the features were resolved in only two dimensions. The trapping styles requires knowledge of features in three dimensions. As such, these types of analyses (*e.g.* thickness-relief plots) are only possible at the scale provided by the seismic data.

A common theme residing in studies associated with oil and gas, or using seismic data, is the lack of accessible borehole data. In the Espírito Santo Basin, no boreholes were accessible in the study area, meaning true lithological identification was impossible. Additionally, the resolution of seismic data means that each seismic reflection is a gross estimate of the true subsurface geology. One seismic reflection may consist of multiple beds. An attempt to correlate the lithologies with boreholes from other basins or areas was made, but this was a far from perfect solution as the geological features concerned were discrete local features that could not be correlated. In the Broad Fourteens Basin, boreholes were provided, but were only drilled on the northeast of the study area, yet the focus was on the southwest. As differential compaction (the ongoing theme of the thesis) is so strongly dependent on the porosity and grain texture of rocks, the interpretations would have been much more accurate with lithological

context. All the explanations for the causes of differential compaction in this work are, in part, speculative.

Well logs from boreholes can also be used to convert time into depth. Data from the Broad Fourteens Basin was converted into depth, so measurements are all in the depth domain, but the Espírito Santo Basin was not converted to depth, so remained as two-way time. This is fundamentally important when measuring structures over different lithologies. As the acoustic waves pass into a different lithology, their velocity changes. Therefore, structures may appear larger or smaller on seismic data. It is important to stress, however, that the increase in velocity through the channel sands should create a structure that is smaller on seismic data than in reality (*Chapter 5*).

7.7. Further work

Four volumes of seismic data were used in this thesis. Accessibility to this many pieces of data is a privilege. Nonetheless, only a couple of each trap types were analysed. New seismic data, from different basins and regions, would allow identification of more compaction-related features, adding rigour to the classification scheme. It would be necessary to correlate the seismic data with borehole information. In turn, this will be used to determine the down-well stress variations and lithological controls on differential compaction. It would be

interesting to see whether differential compaction also occurs in active margins, and how it affects the sediment distribution of overlying units.

Stress calculations were used in *Chapter 4* to model carbon capture and storage and the effect it would have on concentric faults. These stress values could also be used to estimate the vertical load being applied to the compaction-related structures. An important conclusion was the evolution of the structures during burial; they were caused by increasing vertical load and compaction with depth (Fig. 1.4). Each of the features were analysed on 3D seismic data – differential subsidence in the Broad Fourteens Basin and Type A, B, and C traps in the Broad Fourteens, Espírito Santo, and Taranaki Basins. No estimates or calculations were provided for how these features would evolve (increase or decrease in size) with increasing burial. There is an obvious depth control on compaction; the deeper a rock is buried, there greater the vertical stress. But no work has been published on how compaction-related anticlines would evolve with continual depth. Would porosity loss also occur in the less-compactable unit, reducing the size of the subtle trap? These processes work in geological time, the types of traps analysed do not form in our lifespan. Therefore, the only way this can be understood is if a model was created to show the impact of an increasing vertical load on compaction-related structures. A sandbox model would be an ideal tool, where the compaction-related anticline is already formed, and then sediment is placed on top at stepped intervals. It can be expected that after a large amount of time, or when the underlying stratigraphic feature is

completely incompressible, the sea floor will heal and there will be no anticline. But the small changes in shape over slightly compressible units may provide analogues for deeply buried subtle structural traps.

As discussed in *section 7.6*, field work would aid the classification scheme, providing stronger evidence for Type D traps. If compaction-related features were exposed on the surface (perhaps over shallow carbonate concretions), Type D traps could be analysed in three dimensions.

One of the final, and most challenging, pieces of work to be conducted in the future, is the mechanics behind differential compaction on an inclined surface. Most estimates of differential compaction, and all provided in this study, have occurred on a planar, horizontal surface. Vertical compaction due to loading is therefore normal to the bedding plane. However, if compaction was to occur on an inclined surface, how would the rock react? Computer based modelling could answer this question. Not only would there be an element of normal stress, there would also be tangential stress acting on the compacting strata. This would hopefully shed light on whether failure is more likely to occur during compaction on an inclined surface.

CHAPTER EIGHT

Conclusions of this thesis

8. Conclusions

This thesis provides a very detailed analysis of subtle structural traps related to both differential compaction and differential subsidence. Below is a summary of the main conclusions from this extensive work:

8.1. Conclusions of Chapter 4

- Concentric faults formed during a period of regional compression, although they exhibit normal offset. The faults formed in response to differential subsidence: salt withdrawal and movement of large raft bounding faults caused overlying strata to fold and buckle.
- The curvature of the faults are in part due to the circular nature of salt withdrawal. In addition, they have very complex growth histories, including multiple phases of reactivation, vertical linkage and horizontal linkage. The horizontal linkage in particular can increase the curvature of the faults as the segment propagates towards a larger fault.
- Parts of the faults are optimally oriented for reactivation with regards to the present day stress field. Slip tendency analyses highlight sub-vertical patches where slip is more likely. These are associated with vertical fluid-escape features.

- The heterogeneities of the rocks which are cross-cut by concentric faults means detailed analyses of each segment is necessary. For example, at <30 MPa fluid pressures, fault segments in the Vlieland Sandstone reservoir are unlikely to reactivate, whereas they may reactivate in the chalk seal above. This could have strong implications for seal bypass.
- Carbon capture and storage is therefore possible in this study area if pore fluid pressures remain below <30 MPa. This is a similar value to the fluid pressures already being implemented in the Southern North Sea.

8.2. Conclusions of Chapter 5

- A thickness-relief method was used to calculate when differential compaction occurred over a submarine channel complex. It was shown that after ~200 m of burial, an anticline was produced on the seafloor, reaching magnitudes of ~37 m.
- Differential compaction was limited by fluid expulsion. Faults transmitted fluids from the channel complex to the seafloor after the channel sands became overpressured. The subsequent

pockmark was eroded by deep-water currents and the size of it was further enhanced from scouring and collapse of the steep walls.

- Smaller submarine channels are located within the channel complex. Knickpoints along the base of the channels were associated with pods of coarse-grained deposits, which resisted compaction more than surrounding muds. Differential compaction produced anticlines with four-way dip closure over these pods.

- The pods were sealed by surrounding muds, but had limited lateral and vertical connectivity. They therefore rely on hydrocarbon migration along the base of the channel complex for them to be effective reservoirs. A fill-to-spill model is proposed, suggesting once each pod reaches spill point, hydrocarbons migrate to the next pod upslope, leading to a reverse hydrocarbon gradient (oil found further upslope than gas).

8.3. Conclusions of Chapter 6

- Differential compaction over an MTD occurred after very little burial (~45 m). Compaction was controlled by the lithological contrasts between competent carbonate blocks and surrounding debrites.

- Anticlines formed over individual blocks, and are associated with depocentres between each one. Deformation is still occurring on the present day seafloor, as the whole MTD resists compaction.

- Downslope, rafted blocks have travelled much further, and are therefore smaller. Differential compaction produced anticlines over these small blocks before the larger blocks in the proximal region were buried. In fact, some blocks were still exposed after the rafted blocks had been buried by ~90 m of sediment.

- Sediment transport was confined by the slide blocks. Confinement continued after the blocks were buried, caused by the anticlines on the seafloor. Sediment distribution was controlled for over 5 Ma after MTD A was buried, as the seafloor maintained its roughness.

- Log:log plots helped understand the correlation between the size of slide blocks and the stratigraphic elements associated with them. Overlying elements tend to have a higher width:height ratio. This can help predict how differential compaction may affect seafloor sediment distribution in similar areas.

REFERENCES

References

ABREU, V., SULLIVAN, M., PIRMEZ, C. & MOHRIG, D. 2003. Lateral accretion packages (LAPs): an important reservoir element in deep water sinuous channels. *Marine and Petroleum Geology,* 20**,** 631-648.

AIZEBEOKHAI, A. & OLAYINKA, I. 2011. Structural and stratigraphic mapping of Emi field, offshore Niger Delta. *Journal of Geology and mining Research,* 3**,** 25-38.

ALPAK, F. O., BARTON, M. D. & NARUK, S. J. 2013. The impact of fine-scale turbidite channel architecture on deep-water reservoir performance. *AAPG bulletin,* 97**,** 251-284.

ALSOP, G. I. 1996. Physical modelling of fold and fracture geometries associated with salt diapirism. *Geological Society, London, Special Publications,* 100**,** 227-241.

ALVES, T. M. 2010. 3D Seismic examples of differential compaction in mass-transport deposits and their effect on post-failure strata. *Marine Geology,* 271**,** 212-224.

ALVES, T. M. 2012. Scale-relationships and geometry of normal faults reactivated during gravitational gliding of Albian rafts (Espírito Santo Basin, SE Brazil). *Earth and Planetary Science Letters,* 331**,** 80-96.

ALVES, T. M., CARTWRIGHT, J. & DAVIES, R. J. 2009. Faulting of salt-withdrawal basins during early halokinesis: effects on the Paleogene Rio Doce Canyon system (Espírito Santo Basin, Brazil). *AAPG bulletin,* 93**,** 617-652.

ALVES, T. M. & CARTWRIGHT, J. A. 2010. The effect of mass-transport deposits on the younger slope morphology, offshore Brazil. *Marine and Petroleum Geology,* 27**,** 2027-2036.

ALVES, T. M. & ELLIOTT, C. 2014. Fluid flow during early compartmentalisation of rafts: A North Sea analogue for divergent continental margins. *Tectonophysics,* 634**,** 91-96.

ALVES, T. M., ELLIOTT, C. 2014. Fluid flow during early compartmentalisation of rafts: A North Sea analogue for divergent continental margins. *Tectonophysics,* 634**,** 91-96.

ANDERSON, E. M. 1905. The Dynamics of Faulting. *Edinburgh Geological Society Transactions,* 8**,** 393-402.

ANDERSON, E. M. 1951. The Dynamics of Faulting, 1951. *Oliver and Boyd, Edinburgh*.

ANDERSON, N. & FRANSEEN, E. K. 1991. Differential compaction of Winnipegosis reefs: A seismic perspective. *Geophysics,* 56**,** 142-147.

ANDRESEN, K. J. & HUUSE, M. 2011. 'Bulls-eye'pockmarks and polygonal faulting in the Lower Congo Basin: relative timing and implications for fluid expulsion during shallow burial. *Marine Geology,* 279**,** 111-127.

ANELL, I. & MIDTKANDAL, I. 2017. The quantifiable clinothem–types, shapes and geometric relationships in the Plio-Pleistocene Giant Foresets Formation, Taranaki Basin, New Zealand. *Basin Research,* 29**,** 277-297.

ANSELMETTI, F. S., LUTHI, S. & EBERLI, G. P. 1998. Quantitative characterization of carbonate pore systems by digital image analysis. *AAPG bulletin,* 82**,** 1815-1836.

ANTONELLINI, M., AYDIN, A. & ORR, L. 1999. Outcrop-Aided Characterization of a Faulted Hydrocarbon Reservoir: Arroyo Grande Oil Field, California, USA. *Faults and subsurface fluid flow in the shallow crust*, 7-26.

ANTONELLINI, M. A., AYDIN, A. & POLLARD, D. D. 1994. Microstructure of deformation bands in porous sandstones at Arches National Park, Utah. *Journal of structural geology,* 16**,** 941-959.

APLIN, A. C., YANG, Y. & HANSEN, S. 1995. Assessment of β the compression coefficient of mudstones and its relationship with detailed lithology. *Marine and Petroleum Geology,* 12**,** 955-963.

ARMITAGE, D. A., ROMANS, B. W., COVAULT, J. A. & GRAHAM, S. A. 2009. The influence of mass-transport-deposit surface topography on the evolution of turbidite architecture: the Sierra Contreras, Tres Pasos formation (Cretaceous), southern Chile. *Journal of Sedimentary Research,* 79**,** 287-301.

ARMSTRONG, L., TEN HAVE, A. & JOHNSON, H. 1987. The geology of the Gannet fields, central North Sea, UK sector. *Petroleum Geology of North West Europe. Graham & Trotman, London,* 533**,** 548.

ARMSTRONG, P. A., CHAPMAN, D. S., FUNNELL, R. H., ALLIS, R. G. & KAMP, P. J. 1996. Thermal modeling and hydrocarbon generation in an active-margin basin: Taranaki Basin, New Zealand. *Aapg Bulletin,* 80**,** 1216-1241.

ARTS, R., EIKEN, O., CHADWICK, A., ZWEIGEL, P., VAN DER MEER, B. & KIRBY, G. 2004. Seismic monitoring at the Sleipner underground CO_2 storage site (North Sea). *Geological Society, London, Special Publications,* 233**,** 181-191.

ARTS, R., VANDEWEIJER, V., HOFSTEE, C., PLUYMAEKERS, M., LOEVE, D., KOPP, A. & PLUG, W. 2012. The feasibility of CO_2 storage in the depleted P18-4 gas field offshore the Netherlands (the ROAD project). *International Journal of Greenhouse Gas Control,* 11**,** S10-S20.

ATHY, L. F. 1930. Density, porosity, and compaction of sedimentary rocks. *AAPG Bulletin,* 14**,** 1-24.

AVSETH, P., FLESCHE, H. & VAN WIJNGAARDEN, A.-J. 2003. AVO classification of lithology and pore fluids constrained by rock physics depth trends. *The Leading Edge,* 22**,** 1004-1011.

AYDIN, A. 1978. Small faults formed as deformation bands in sandstone. *Rock Friction and Earthquake Prediction.* Springer.

AYDIN, A. 2000. Fractures, faults, and hydrocarbon entrapment, migration and flow. *Marine and petroleum geology,* 17**,** 797-814.

AYDIN, A. & JOHNSON, A. M. 1978. Development of faults as zones of deformation bands and as slip surfaces in sandstone. *Pure and applied Geophysics,* 116**,** 931-942.

BAARS, D. & STEVENSON, G. 1982. Subtle stratigraphic traps in Paleozoic rocks of Paradox basin.

BABONNEAU, N., SAVOYE, B., CREMER, M. & KLEIN, B. 2002. Morphology and architecture of the present canyon and channel system of the Zaire deep-sea fan. *Marine and Petroleum Geology,* 19**,** 445-467.

BACON, M., SIMM, R. & REDSHAW, T. 2007. *3-D seismic interpretation*, Cambridge University Press.

BARKER, P. 1983. Tectonic evolution and subsidence history of the Rio-Grande Rise. *Initial Reports of the Deep Sea Drilling Project,* 72**,** 953-976.

BARKER, P., BUFFLER, R. & GAMBÔA, L. 1983. A seismic-reflection study of the Rio-Grande Rise. *Initial Reports of the Deep Sea Drilling Project,* 72**,** 499-517.

BARTON, N. 1973. Review of a new shear-strength criterion for rock joints. *Engineering geology,* 7**,** 287-332.

BAUDON, C. & CARTWRIGHT, J. 2008. The kinematics of reactivation of normal faults using high resolution throw mapping. *Journal of Structural Geology,* 30**,** 1072-1084.

BEAUBOUEF, R. & ABREU, V. 2010. MTCs of the Brazos-Trinity slope system; thoughts on the sequence stratigraphy of MTCs and their possible roles in shaping hydrocarbon traps. *Submarine Mass Movements and Their Consequences.* Springer.

BEGLINGER, S. E., DOUST, H. & CLOETINGH, S. 2012. Relating petroleum system and play development to basin evolution: Brazilian South Atlantic margin. *Petroleum Geoscience,* 18**,** 315-336.

BELDE, J., BACK, S., BOURGET, J. & REUNING, L. 2017. Oligocene and Miocene Carbonate Platform Development In the Browse Basin, Australian Northwest Shelf. *Journal of Sedimentary Research,* 87**,** 795-816.

BENTHAM, M., GREEN, A. & GAMMER, D. 2013. The occurrence of faults in the Bunter Sandstone Formation of the UK sector of the Southern North Sea and the potential impact on storage capacity. *Energy Procedia,* 37**,** 5101-5109.

BERG, O. R. 1982. Seismic detection and evaluation of delta and turbidite sequences: their application to the exploration for the subtle trap.

BERTONI, C. & CARTWRIGHT, J. A. 2005. 3D seismic analysis of circular evaporite dissolution structures, Eastern Mediterranean. *Journal of the Geological Society,* 162**,** 909-926.

BIDDLE, K. T. & WIELCHOWSKY, C. C. 1994. Hydrocarbon Traps, *in* L. B. Magoon and W. G. Dow, eds., The petroleum system - From source to trap. *AAPG Memoir,* 60**,** 219-235.

BIONDI, B. 2006. *3D seismic imaging*, Society of Exploration Geophysicists Tulsa.

BJØRLYKKE, K. 1999. Principal aspects of compaction and fluid flow in mudstones. *Geological Society, London, Special Publications,* 158**,** 73-78.

BJØRLYKKE, K. 2014. Relationships between depositional environments, burial history and rock properties. Some principal aspects of diagenetic process in sedimentary basins. *Sedimentary Geology,* 301**,** 1-14.

BJØRLYKKE, K. & HØEG, K. 1997. Effects of burial diagenesis on stresses, compaction and fluid flow in sedimentary basins. *Marine and Petroleum Geology,* 14**,** 267-276.

BLENKINSOP, T. G. 2004. Orebody geometry in lode gold deposits from Zimbabwe: implications for fluid flow, deformation and mineralization. *Journal of structural geology,* 26**,** 1293-1301.

BOLDY, S. & FRASER, S. Introduction and review. Geological Society, London, Petroleum Geology Conference series, 1999. Geological Society of London, 825-826.

BOTT, M. H. P. 1959. The mechanics of Oblique Slip Faulting. *Geological Magazine,* 96**,** 109-117.

BOUW, L. & ESSINK, G. 2003. Fluid flow in the northern Broad Fourteens Basin during Late Cretaceous inversion. *Netherlands Journal of Geosciences/Geologie en Mijnbouw,* 82**,** 55-69.

BRAMWELL, N., CAILLET, G., MECIANI, L., JUDGE, N., GREEN, M. & ADAM, P. Chalk exploration, the search for a subtle trap. Geological Society, London, Petroleum Geology Conference series, 1999. Geological Society of London, 911-937.

BROWN, A. R. 2004. *Interpretation of three-dimensional seismic data*, American Association of Petroleum Geologists Tulsa.

BRUHN, C. H., PINTO, A. C., JOHANN, P. R., BRANCO, C., SALOMÃO, M. C. & FREIRE, E. B. Campos and Santos Basins: 40 Years of Reservoir Characterization and Management of Shallow-to Ultra-Deep Water, Post- and Pre-Salt Reservoirs-Historical Overview and Future Challenges. OTC Brasil, 2017. Offshore Technology Conference.

BRUHN, C. H. & WALKER, R. G. 1997. Internal architecture and sedimentary evolution of coarse-grained, turbidite channel-levee complexes, Early Eocene Regencia Canyon, Espirito Santo Basin, Brazil. *Sedimentology,* 44**,** 17-46.

BRUIJN, A. N. 1996. De Wijk gas field (Netherlands): reservoir mapping with amplitude anomalies. *Geology of Gas and Oil under the Netherlands.* Springer.

BRYANT, G. & MIALL, A. 2010. Diverse products of near-surface sediment mobilization in an ancient eolianite: outcrop features of the early Jurassic Navajo Sandstone. *Basin Research,* 22**,** 578-590.

BUCZKOWSKI, D. L. & COOKE, M. L. 2004. Formation of double-ring circular grabens due to volumetric compaction over buried impact craters: Implications for thickness and nature of cover material in Utopia Planitia, Mars. *Journal of Geophysical Research: Planets,* 109.

BULL, S., CARTWRIGHT, J. & HUUSE, M. 2009. A review of kinematic indicators from mass-transport complexes using 3D seismic data. *Marine and Petroleum Geology,* 26**,** 1132-1151.

BULLING, T. & BREYER, J. 1989. Exploring for subtle traps with high-resolution paleogeographic maps: Reklaw 1 interval (Eocene), South Texas. *AAPG Bulletin,* 73**,** 24-39.

BURGESS, P. M., WINEFIELD, P., MINZONI, M. & ELDERS, C. 2013. Methods for identification of isolated carbonate buildups from seismic reflection data. *AAPG bulletin,* 97**,** 1071-1098.

BYERLEE, J. 1978. Friction of rocks. *Pure and applied geophysics,* 116**,** 615-626.

CAMP, W. K. 2008. Basin-centered gas or subtle conventional traps?

CARMINATI, E. & SANTANTONIO, M. 2005. Control of differential compaction on the geometry of sediments onlapping paleoescarpments: Insights from field geology (Central Apennines, Italy) and numerical modeling. *Geology,* 33**,** 353-356.

CARMINATTI, M., WOLFF, B. & GAMBOA, L. New exploratory frontiers in Brazil. 19th World Petroleum Congress, 2008. World Petroleum Congress.

CARTER, R. T. & NORRIS, R. 1976. Cainozoic history of southern New Zealand: an accord between geological observations and plate-tectonic predictions. *Earth and planetary science letters,* 31**,** 85-94.

CARTWRIGHT, J. 2007. The impact of 3D seismic data on the understanding of compaction, fluid flow and diagenesis in sedimentary basins. *Journal of the Geological Society,* 164**,** 881-893.

CARTWRIGHT, J., HUUSE, M. & APLIN, A. 2007. Seal bypass systems. *AAPG bulletin,* 91**,** 1141-1166.

CARTWRIGHT, J. & SANTAMARINA, C. 2015. Seismic characteristics of fluid escape pipes in sedimentary basins: Implications for pipe genesis. *Marine and Petroleum Geology,* 65**,** 126-140.

CARTWRIGHT, J., STEWART, S. & CLARK, J. 2001. Salt dissolution and salt-related deformation of the Forth Approaches Basin, UK North Sea. *Marine and petroleum geology,* 18**,** 757-778.

CARTWRIGHT, J. A. 1994. Episodic basin-wide fluid expulsion from geopressured shale sequences in the North Sea basin. *Geology,* 22**,** 447-450.

CARTWRIGHT, J. A., TRUDGILL, B. D. & MANSFIELD, C. S. 1995. Fault growth by segment linkage: an explanation for scatter in maximum displacement and trace length data from the Canyonlands Grabens of SE Utah. *Journal of Structural Geology,* 17**,** 1319-1326.

CARVER, R. E. 1968. Differential compaction as a cause of regional contemporaneous faults. *AAPG Bulletin,* 52**,** 414-419.

CATHLES, L., SU, Z. & CHEN, D. 2010. The physics of gas chimney and pockmark formation, with implications for assessment of seafloor hazards and gas sequestration. *Marine and Petroleum Geology,* 27**,** 82-91.

CAWLEY, S., SAUNDERS, M., LE GALLO, Y., CARPENTIER, B., HOLLOWAY, S., KIRBY, G., BENNISON, T., WICKENS, L., WICKRAMARATNA, R. & BIDSTRUP, T. 2015. The NGCAS project—assessing the potential for EOR and CO_2 storage at the Forties Oilfield, Offshore UK. *Carbon dioxide capture for storage in deep geologic formations—results from the CO,* 2**,** 713-750.

CHANG, H. K., KOWSMANN, R. O., FIGUEIREDO, A. M. F. & BENDER, A. 1992. Tectonics and stratigraphy of the East Brazil Rift system: an overview. *Tectonophysics,* 213**,** 97-138.

CHENRAI, P. & HUUSE, M. 2017. Pockmark formation by porewater expulsion during rapid progradation in the offshore Taranaki Basin, New Zealand. *Marine and Petroleum Geology,* 82**,** 399-413.

CHILDS, C., NICOL, A., WALSH, J. J. & WATTERSON, J. 1996. Growth of vertically segmented normal faults. *Journal of Structural Geology,* 18**,** 1389-1397.

CHILDS, C., NICOL, A., WALSH, J. J. & WATTERSON, J. 2003. The growth and propagation of synsedimentary faults. *Journal of Structural Geology,* 25**,** 633-648.

CHOPRA, S. & MARFURT, K. J. 2012. Seismic attribute expression of differential compaction. *The Leading Edge,* 31**,** 1418-1422.

CHOQUETTE, P. W. & PRAY, L. C. 1970. Geologic nomenclature and classification of porosity in sedimentary carbonates. *AAPG bulletin,* 54**,** 207-250.

CLARK, J. D. & PICKERING, K. T. 1996. Architectural elements and growth patterns of submarine channels: application to hydrocarbon exploration. *AAPG bulletin,* 80**,** 194-220.

CLOETINGH, S., BUROV, E. & POLIAKOV, A. 1999. Lithosphere folding: Primary response to compression? (from central Asia to Paris basin). *Tectonics,* 18**,** 1064-1083.

COLE, D., STEWART, S. & CARTWRIGHT, J. 2000. Giant irregular pockmark craters in the Palaeogene of the outer Moray Firth basin, UK North Sea. *Marine and Petroleum Geology,* 17**,** 563-577.

COLLETTE, B. & RUTTEN, K. 1970. Differential compaction vs. diapirism in abyssal plains. *Marine Geophysical Research,* 1**,** 104-107.

COLMAN-SADD, S. 1978. Fold development in Zagros simply folded belt, Southwest Iran. *AAPG Bulletin,* 62**,** 984-1003.

CORCORAN, J. 2006. Application of a sealing surface classification for stratigraphic related traps in the UK Central North Sea. *Geological Society, London, Special Publications,* 254**,** 207-223.

CORCORAN, P. 2008. Ordovician paleotopography as evidenced from original dips and differential compaction of dolostone and shale unconformably overlying Precambrian basement on Manitoulin Island, Canada. *Sedimentary Geology,* 207**,** 22-33.

CORFIELD, S. & SHARP, I. 2000. Structural style and stratigraphic architecture of fault propagation folding in extensional settings: a seismic example from the Smørbukk area, Halten Terrace, Mid-Norway. *Basin Research,* 12**,** 329-341.

COSGROVE, J. & AMEEN, M. 1999. A comparison of the geometry, spatial organization and fracture patterns associated with forced folds and buckle folds. *Geological Society, London, Special Publications,* 169**,** 7-21.

COSGROVE, J. W. & HILLIER, R. D. 1999. Forced-fold development within Tertiary sediments of the Alba Field, UKCS: evidence of differential compaction and post-depositional sandstone remobilization. *Geological Society, London, Special Publications,* 169**,** 61-71.

COWARD, M. 1995. Structural and tectonic setting of the Permo-Triassic basins of northwest Europe. *Geological Society, London, Special Publications,* 91**,** 7-39.

COWARD, M. & STEWART, S. 1995. Salt-influenced structures in the Mesozoic-Tertiary cover of the southern North Sea, UK.

COWIE, P. A. & SCHOLZ, C. H. 1992. Physical explanation for the displacement-length relationship of faults using a post-yield fracture mechanics model. *Journal of Structural Geology,* 14**,** 1133-1148.

CRIDER, J. G. 2001. Oblique slip and the geometry of normal-fault linkage: mechanics and a case study from the Basin and Range in Oregon. *Journal of Structural Geology,* 23**,** 1997-2009.

CUREWITZ, D. & KARSON, J. A. 1997. Structural settings of hydrothermal outflow: fracture permeability maintained by fault propagation and interaction. *Journal of Volcanology and Geothermal Research,* 79**,** 149-168.

DAVIES, R., IRELAND, M. & CARTWRIGHT, J. 2009. Differential compaction due to the irregular topology of a diagenetic reaction boundary: a new mechanism for the formation of polygonal faults. *Basin Research,* 21**,** 354-359.

DAVIES, R. J. 2003. Kilometer-scale fluidization structures formed during early burial of a deep-water slope channel on the Niger Delta. *Geology,* 31**,** 949-952.

DAVIES, R. J. 2005. Differential compaction and subsidence in sedimentary basins due to silica diagenesis: A case study. *Geological Society of America Bulletin,* 117**,** 1146-1155.

DAVIS, G. H. 1999. *Structural geology of the Colorado Plateau region of southern Utah, with special emphasis on deformation bands*, Geological Society of America.

DAVISON, I. 1999. Tectonics and hydrocarbon distribution along the Brazilian South Atlantic margin. *Geological Society, London, Special Publications,* 153**,** 133-151.

DAVISON, I. 2007. Geology and tectonics of the South Atlantic Brazilian salt basins. *Geological Society, London, Special Publications,* 272**,** 345-359.

DAVISON, I., ALSOP, G., EVANS, N. & SAFARICZ, M. 2000a. Overburden deformation patterns and mechanisms of salt diapir penetration in the Central Graben, North Sea. *Marine and Petroleum Geology,* 17**,** 601-618.

DAVISON, I., ALSOP, I., BIRCH, P., ELDERS, C., EVANS, N., NICHOLSON, H., RORISON, P., WADE, D., WOODWARD, J. & YOUNG, M. 2000b. Geometry and late-stage structural evolution of Central Graben salt diapirs, North Sea. *Marine and Petroleum Geology,* 17**,** 499-522.

DAWERS, N. H. & ANDERS, M. H. 1995. Displacement-length scaling and fault linkage. *Journal of Structural Geology,* 17**,** 607-614.

DE JAGER, J., DOYLE, M., GRANTHAM, P. & MABILLARD, J. 1996. Hydrocarbon habitat of the West Netherlands Basin. *Geology of Gas and Oil under the Netherlands.* Springer.

DE LUGT, I. R., VAN WEES, J. D. & WONG, T. E. 2003. The tectonic evolution of the southern Dutch North Sea during the Palaeogene: basin inversion in distinct pulses. *Tectonophysics,* 373**,** 141-159.

DEMERCIAN, S., SZATMARI, P. & COBBOLD, P. 1993. Style and pattern of salt diapirs due to thin-skinned gravitational gliding, Campos and Santos basins, offshore Brazil. *Tectonophysics,* 228**,** 393-433.

DEPTUCK, M. E., SYLVESTER, Z., PIRMEZ, C. & O'BYRNE, C. 2007. Migration–aggradation history and 3-D seismic geomorphology of submarine channels in the Pleistocene Benin-major Canyon, western Niger Delta slope. *Marine and Petroleum Geology,* 24**,** 406-433.

DEWERS, T. & ORTOLEVA, P. 1990. A coupled reaction/transport/mechanical model for intergranular pressure solution, stylolites, and differential compaction and cementation in clean sandstones. *Geochimica et Cosmochimica Acta,* 54**,** 1609-1625.

DI CELMA, C. N., BRUNT, R. L., HODGSON, D. M., FLINT, S. S. & KAVANAGH, J. P. 2011. Spatial and temporal evolution of a Permian

submarine slope channel–levee system, Karoo Basin, South Africa. *Journal of Sedimentary Research,* 81**,** 579-599.

DOWDESWELL, J. A., OTTESEN, D., RISE, L. & CRAIG, J. 2007. Identification and preservation of landforms diagnostic of past ice-sheet activity on continental shelves from three-dimensional seismic evidence. *Geology,* 35**,** 359-362.

DUARTE, C. S. & VIANA, A. R. 2007. Santos Drift System: stratigraphic organization and implications for late Cenozoic palaeocirculation in the Santos Basin, SW Atlantic Ocean. *Geological Society, London, Special Publications,* 276**,** 171-198.

DUFRÉCHOU, G., ODONNE, F. & VIOLA, G. 2011. Analogue models of second-order faults genetically linked to a circular strike-slip system. *Journal of Structural Geology,* 33**,** 1193-1205.

DUGAN, B. & FLEMINGS, P. B. 2000. Overpressure and fluid flow in the New Jersey continental slope: implications for slope failure and cold seeps. *Science,* 289**,** 288-291.

DUIN, E., DOORNENBAL, J., RIJKERS, R., VERBEEK, J. & WONG, T. E. 2006. Subsurface structure of the Netherlands-results of recent onshore and offshore mapping. *Netherlands Journal of Geosciences,* 85**,** 245.

DUNHAM, R. J. 1962. Classification of carbonate rocks according to depositional textures, *in* Ham W.E. ed., Classification of carbonate rocks: Americaion Association of Petroleum Geologists, Memoir. *AAPG Bulletin,* 1**,** 108-121.

DYKSTRA, M., GARYFALOU, K., KERTZNUS, V., KNELLER, B., MILANA, J., MOLINARO, M., SZUMAN, M. & THOMPSON, P. 2011. Mass-transport deposits: combining outcrop studies and seismic forward modeling to understand lithofacies distributions, deformation, and their seismic expression. *Mass-transport Deposits in Deepwater Settings. SEPM, Special Publication,* 96**,** 293-310.

EHRENBERG, S. & NADEAU, P. 2005. Sandstone vs. carbonate petroleum reservoirs: A global perspective on porosity-depth and porosity-permeability relationships. *AAPG bulletin,* 89**,** 435-445.

ELVEBAKK, G., HUNT, D. W. & STEMMERIK, L. 2002. From isolated buildups to buildup mosaics: 3D seismic sheds new light on Upper Carboniferous–

Permian fault controlled carbonate buildups, Norwegian Barents Sea. *Sedimentary Geology,* 152**,** 7-17.

ERSLEV, E. A. 1991. Trishear fault-propagation folding. *Geology,* 19**,** 617-620.

ESTRELLA, G., MELLO, M. R., GAGLIANONE, P., AZEVEDO, R., TSUBONE, K., ROSSETTI, E., CONCHA, J. & BRUNING, I. 1984. The Espirito Santo Basin (Brazil) source rock characterization and petroleum habitat.

FARMER, I. W. & JUMIKIS, A. R. 1968. *Engineering Properties of Rocks,* 11 New Fetter Lane, London E.C.4, E. & F. N. Spon Limited.

FERRILL, D. A., STAMATAKOS, J. A. & SIMS, D. 1999. Normal fault corrugation: implications for growth and seismicity of active normal faults. *Journal of Structural Geology,* 21**,** 1027-1038.

FIDUK, J. C., BRUSH, E. R., ANDERSON, L. E., GIBBS, P. B. & ROWAN, M. G. Salt deformation, magmatism, and hydrocarbon prospectivity in the Espirito Santo Basin, offshore Brazil. Salt-sediment interactions and hydrocarbon prospectivity: Concepts, applications, and case studies for the 21st century: Proceedings of Gulf Coast Section SEPM Foundation Bob F. Perkins Research Conference, 2004. SEPM, 370-392.

FORTIN, J., STANCHITS, S., DRESEN, G. & GUÉGUEN, Y. 2006. Acoustic emission and velocities associated with the formation of compaction bands in sandstone. *Journal of Geophysical Research: Solid Earth,* 111.

FOSSEN, H., SCHULTZ, R. A., SHIPTON, Z. K. & MAIR, K. 2007. Deformation bands in sandstone: a review. *Journal of the Geological Society,* 164**,** 755-769.

FRANÇA, R. L., DEL REY, A. C., TAGLIARI, C. V., BRANDÃO, J. R. & FONTANELLI, P. D. R. 2007. Bacia do Espírito Santo. *Boletim de Geociencias da PETROBRAS,* 15**,** 501-509.

FREY-MARTINEZ, J., CARTWRIGHT, J., HALL, B. & HUUSE, M. 2007. Clastic intrusion at the base of deep-water sands: A trap-forming mechanism in the eastern Mediterranean.

FRIKKEN, H. W. 1999. *Reservoir-geological aspects of productivity and connectivity of gasfields in the Netherlands.* PhD Thesis, TU Delft, Delft University of Technology.

GAARENSTROOM, L., TROMP, R. & BRANDENBURG, A. Overpressures in the Central North Sea: implications for trap integrity and drilling safety.

Geological Society, London, Petroleum Geology Conference series, 1993. Geological Society of London, 1305-1313.

GABRIELSEN, R. H., STEEL, R. J. & NOTTVEDT, A. 1995. Subtle traps in extensional terranes; a model with reference to the North Sea. *Petroleum Geoscience,* 1**,** 223-235.

GAMBOA, D., ALVES, T. & CARTWRIGHT, J. 2011. Distribution and characterization of failed (mega) blocks along salt ridges, southeast Brazil: Implications for vertical fluid flow on continental margins. *Journal of Geophysical Research: Solid Earth (1978–2012),* 116.

GAMBOA, D., ALVES, T., CARTWRIGHT, J. & TERRINHA, P. 2010. MTD distribution on a 'passive'continental margin: the Espírito Santo Basin (SE Brazil) during the Palaeogene. *Marine and Petroleum Geology,* 27**,** 1311-1324.

GAMBOA, D. & ALVES, T. M. 2015a. Spatial and dimensional relationships of submarine slope architectural elements: A seismic-scale analysis from the Espírito Santo Basin (SE Brazil). *Marine and Petroleum Geology,* 64**,** 43-57.

GAMBOA, D. & ALVES, T. M. 2015b. Three-dimensional fault meshes and multi-layer shear in mass-transport blocks: Implications for fluid flow on continental margins. *Tectonophysics,* 647**,** 21-32.

GAMBOA, D. & ALVES, T. M. 2016. Bi-modal deformation styles in confined mass-transport deposits: Examples from a salt minibasin in SE Brazil. *Marine Geology,* 379**,** 176-193.

GARDNER, M. H., BORER, J. M., MELICK, J. J., MAVILLA, N., DECHESNE, M. & WAGERLE, R. N. 2003. Stratigraphic process-response model for submarine channels and related features from studies of Permian Brushy Canyon outcrops, West Texas. *Marine and Petroleum Geology,* 20**,** 757-787.

GAY, A., LOPEZ, M., BERNDT, C. & SERANNE, M. 2007. Geological controls on focused fluid flow associated with seafloor seeps in the Lower Congo Basin. *Marine Geology,* 244**,** 68-92.

GAY, A., LOPEZ, M., COCHONAT, P., LEVACHÉ, D., SERMONDADAZ, G. & SERANNE, M. 2006a. Evidences of early to late fluid migration from an upper Miocene turbiditic channel revealed by 3D seismic coupled to geochemical sampling within seafloor pockmarks, Lower Congo Basin. *Marine and Petroleum Geology,* 23**,** 387-399.

GAY, A., LOPEZ, M., COCHONAT, P., SÉRANNE, M., LEVACHÉ, D. & SERMONDADAZ, G. 2006b. Isolated seafloor pockmarks linked to BSRs, fluid chimneys, polygonal faults and stacked Oligocene–Miocene turbiditic palaeochannels in the Lower Congo Basin. *Marine Geology,* 226**,** 25-40.

GAY, A., LOPEZ, M., COCHONAT, P. & SERMONDADAZ, G. 2004. Polygonal faults-furrows system related to early stages of compaction–upper Miocene to recent sediments of the Lower Congo Basin. *Basin Research,* 16**,** 101-116.

GAY, A., LOPEZ, M., COCHONAT, P., SULTAN, N., CAUQUIL, E. & BRIGAUD, F. 2003. Sinuous pockmark belt as indicator of a shallow buried turbiditic channel on the lower slope of the Congo Basin, West African Margin. *Geological Society, London, Special Publications,* 216**,** 173-189.

GE, H. & JACKSON, M. P. 1998. Physical modeling of structures formed by salt withdrawal: Implications for deformation caused by salt dissolution. *AAPG bulletin,* 82**,** 228-250.

GEE, M., GAWTHORPE, R., BAKKE, K. & FRIEDMANN, S. 2007. Seismic geomorphology and evolution of submarine channels from the Angolan continental margin. *Journal of Sedimentary Research,* 77**,** 433-446.

GEE, M., GAWTHORPE, R. & FRIEDMANN, J. 2005. Giant striations at the base of a submarine landslide. *Marine Geology,* 214**,** 287-294.

GEE, M., GAWTHORPE, R. & FRIEDMANN, S. 2006. Triggering and evolution of a giant submarine landslide, offshore Angola, revealed by 3D seismic stratigraphy and geomorphology. *Journal of Sedimentary Research,* 76**,** 9-19.

GERLING, P., GELUK, M., KOCKEL, F., LOKHORST, A., LOTT, G. & NICHOLSON, R. 'NW European Gas Atlas'–new implications for the Carboniferous gas plays in the western part of the Southern Permian Basin. Geological Society, London, Petroleum Geology Conference series, 1999. Geological Society of London, 799-808.

GIBA, M., NICOL, A. & WALSH, J. 2010. Evolution of faulting and volcanism in a back-arc basin and its implications for subduction processes. *Tectonics,* 29.

GIBBS, P. B., BRUSH, E. R. & FIDUK, J. C. The evolution of the syn rift and transition phases of the central/southern Brazilian and W. African conjugate margins: the implications for source rock distribution in time and space, and their recognition on seismic data. 8th International Congress of the Brazilian Geophysical Society, September 14-18 2003 Brazil.

GILLESPIE, P., WALSH, J. T. & WATTERSON, J. 1992. Limitations of dimension and displacement data from single faults and the consequences for data analysis and interpretation. *Journal of Structural Geology,* 14**,** 1157-1172.

GLENNIE, K. 1997. History of exploration in the southern North Sea. *Geological Society, London, Special Publications,* 123**,** 5-16.

GLENNIE, K. & PROVAN, D. 1990. Lower Permian Rotliegend reservoir of the southern North Sea gas province. *Geological Society, London, Special Publications,* 50**,** 399-416.

GLUYAS, J. & SWARBRICK, R. 2013. *Petroleum geoscience*, John Wiley & Sons.

GÓMEZ, M. & VERGÉS, J. 2005. Quantifying the contribution of tectonics vs. differential compaction in the development of domes along the mid-Norwegian Atlantic margin. *Basin Research,* 17**,** 289-310.

GONG, C., WANG, Y., STEEL, R. J., PEAKALL, J., ZHAO, X. & SUN, Q. 2016. Flow processes and sedimentation in unidirectionally migrating deep-water channels: From a three-dimensional seismic perspective. *Sedimentology,* 63**,** 645-661.

GONZALEZ-MIERES, R. & SUPPE, J. 2006. Relief and shortening in detachment folds. *Journal of Structural Geology,* 28**,** 1785-1807.

GRASEMANN, B., MARTEL, S. & PASSCHIER, C. 2005. Reverse and normal drag along a fault. *Journal of Structural Geology,* 27**,** 999-1010.

GROLLIMUND, B., ZOBACK, M. D., WIPRUT, D. J. & ARNESEN, L. 2001. Stress orientation, pore pressure and least principal stress in the Norwegian sector of the North Sea. *Petroleum Geoscience,* 7**,** 173-180.

GUPTA, A. & SCHOLZ, C. H. 2000. A model of normal fault interaction based on observations and theory. *Journal of Structural Geology,* 22**,** 865-879.

GUPTA, S., COWIE, P. A., DAWERS, N. H. & UNDERHILL, J. R. 1998. A mechanism to explain rift-basin subsidence and stratigraphic patterns through fault-array evolution. *Geology,* 26**,** 595-598.

HALBOUTY, M. T. 1969. Hidden trends and subtle traps in Gulf Coast. *AAPG Bulletin,* 53**,** 3-29.

HAMPTON, M. A., LEE, H. J. & LOCAT, J. 1996. Submarine landslides. *Reviews of geophysics,* 34**,** 33-59.

HANDIN, J., HAGER JR, R. V., FRIEDMAN, M. & FEATHER, J. N. 1963. Experimental deformation of sedimentary rocks under confining pressure: pore pressure tests. *AAPG Bulletin,* 47**,** 717-755.

HANSEN, D. M. & CARTWRIGHT, J. 2006. The three-dimensional geometry and growth of forced folds above saucer-shaped igneous sills. *Journal of Structural Geology,* 28**,** 1520-1535.

HANSEN, R. J. & KAMP, P. J. 2002. Evolution of the Giant Foresets Formation, northern Taranaki Basin, New Zealand.

HANSEN, R. J. & KAMP, P. J. 2004. Late Miocene to early Pliocene stratigraphic record in northern Taranaki Basin: condensed sedimentation ahead of Northern Graben extension and progradation of the modern continental margin. *New Zealand Journal of Geology and Geophysics,* 47**,** 645-662.

HANSEN, R. J. & KAMP, P. J. Sequence stratigraphy and architectural elements of the Giant Foresets Formation, northern Taranaki Basin, New Zealand. Geological Society of New Zealand 50th Annual Conference, 2006.

HARDMAN, R. & BOOTH, J. 1991. The significance of normal faults in the exploration and production of North Sea hydrocarbons. *Geological Society, London, Special Publications,* 56**,** 1-13.

HARDY, S. & MCCLAY, K. 1999. Kinematic modelling of extensional fault-propagation folding. *Journal of Structural Geology,* 21**,** 695-702.

HART, B. S. 1999. Definition of subsurface stratigraphy, structure and rock properties from 3-D seismic data. *Earth-Science Reviews,* 47**,** 189-218.

HAYWARD, B. W., BLACK, P. M., SMITH, I. E., BALLANCE, P. F., ITAYA, T., DOI, M., TAKAGI, M., BERGMAN, S., ADAMS, C. J. & HERZER, R. H. 2001. K-Ar ages of early Miocene arc-type volcanoes in northern New Zealand. *New Zealand Journal of Geology and Geophysics,* 44**,** 285-311.

HEALY, D., BLENKINSOP, T. G., TIMMS, N. E., MEREDITH, P. G., MITCHELL, T. M. & COOKE, M. L. 2015. Polymodal faulting: Time for a new angle on shear failure. *Journal of Structural Geology,* 80**,** 57-71.

HEIDBACH, O., TINGAY, M., BARTH, A., REINECKER, J., KURFEß, D. & MÜLLER, B. 2008. The World Stress Map database release 2008 (2008) http://dx. doi. org/10.1594/GFZ. WSM. *Rel2008*.

HEIM, S., LUTZ, R., NELSKAMP, S., VERWEIJ, H., KAUFMANN, D. & REINHARDT, L. 2013. Geological Evolution of the North Sea: Cross-border Basin Modeling Study on the Schillground High. *Energy Procedia,* 40**,** 222-231.

HEINIÖ, P. & DAVIES, R. J. 2007. Knickpoint migration in submarine channels in response to fold growth, western Niger Delta. *Marine and Petroleum Geology,* 24**,** 434-449.

HELLAND-HANSEN, W. & HAMPSON, G. 2009. Trajectory analysis: concepts and applications. *Basin Research,* 21**,** 454-483.

HERBER, R. & DE JAGER, J. 2010. Geoperspective Oil and Gas in the Netherlands–Is there a future? *Netherlands Journal of Geosciences,* 89**,** 91-107.

HERITIER, F., LOSSEL, P. & WATHNE, E. 1980. Frigg Field--Large Submarine-Fan Trap in Lower Eocene Rocks of the Viking Graben, North Sea.

HILLIS, R. & NELSON, E. In situ stresses in the North Sea and their applications: Petroleum geomechanics from exploration to development. Geological Society, London, Petroleum Geology Conference series, 2005. Geological Society of London, 551-564.

HILLIS, R. R. 1995. Quantification of Tertiary exhumation in the United Kingdom southern North Sea using sonic velocity data. *AAPG bulletin,* 79**,** 130-152.

HOLOHAN, E. P., WALTER, T. R., SCHOEPFER, M. P., WALSH, J. J., WYK DE VRIES, B. & TROLL, V. R. 2013. Origins of oblique-slip faulting during caldera subsidence. *Journal of Geophysical Research: Solid Earth,* 118**,** 1778-1794.

HOLT, W. & STERN, T. 1994. Subduction, platform subsidence, and foreland thrust loading: The late Tertiary development of Taranaki Basin, New Zealand. *Tectonics,* 13**,** 1068-1092.

HOOPER, R. J., GOH, L. S. & DEWEY, F. 1995. The inversion history of the northeastern margin of the Broad Fourteens Basin. *Geological Society, London, Special Publications,* 88**,** 307-317.

HOWARD, A. D., DIETRICH, W. E. & SEIDL, M. A. 1994. Modeling fluvial erosion on regional to continental scales. *Journal of Geophysical Research: Solid Earth,* 99**,** 13971-13986.

HUNT, D., ALLSOP, T. & SWARBRICK, R. E. 1996. Compaction as a primary control on the architecture and development of depositional sequences: conceptual framework, applications and implications. *Geological Society, London, Special Publications,* 104**,** 321-345.

HUSTOFT, S., BÜNZ, S. & MIENERT, J. 2010. Three-dimensional seismic analysis of the morphology and spatial distribution of chimneys beneath the Nyegga pockmark field, offshore mid-Norway. *Basin Research,* 22**,** 465-480.

HUSTOFT, S., MIENERT, J., BÜNZ, S. & NOUZÉ, H. 2007. High-resolution 3D-seismic data indicate focussed fluid migration pathways above polygonal fault systems of the mid-Norwegian margin. *Marine Geology,* 245**,** 89-106.

ILG, B. R., HEMMINGS-SYKES, S., NICOL, A., BAUR, J., FOHRMANN, M., FUNNELL, R. & MILNER, M. 2012. Normal faults and gas migration in an active plate boundary, southern Taranaki Basin, offshore New Zealand. *AAPG bulletin,* 96**,** 1733-1756.

IRELAND, M. T., GOULTY, N. R. & DAVIES, R. J. 2011. Influence of stratigraphic setting and simple shear on layer-bound compaction faults offshore Mauritania. *Journal of Structural Geology,* 33**,** 487-499.

ISAKSEN, G. H. 2004. Central North Sea hydrocarbon systems: Generation, migration, entrapment, and thermal degradation of oil and gas. *AAPG bulletin,* 88**,** 1545-1572.

JACKSON, C. A.-L. & ROTEVATN, A. 2013. 3D seismic analysis of the structure and evolution of a salt-influenced normal fault zone: A test of competing fault growth models. *Journal of Structural Geology,* 54**,** 215-234.

JAEGER, J. C. 1969. *Elasticity, fracture and flow: with engineering and geological applications*, Methuen.

JAEGER, J. C., COOK, N. G. & ZIMMERMAN, R. 2009. *Fundamentals of rock mechanics*, John Wiley & Sons.

JAPSEN, P. 1998. Regional velocity-depth anomalies, North Sea Chalk: a record of overpressure and Neogene uplift and erosion. *AAPG bulletin,* 82**,** 2031-2074.

KATTENHORN, S. A. & POLLARD, D. D. 2001. Integrating 3-D seismic data, field analogs, and mechanical models in the analysis of segmented normal faults in the Wytch Farm oil field, southern England, United Kingdom. *AAPG bulletin,* 85**,** 1183-1210.

KEAREY, P., BROOKS, M. & HILL, I. 2013. *An introduction to geophysical exploration*, John Wiley & Sons.

KING, P. R. & THRASHER, G. P. 1996. *Cretaceous Cenozoic geology and petroleum systems of the Taranaki Basin, New Zealand*, Institute of Geological & Nuclear Sciences.

KNELLER, B., DYKSTRA, M., FAIRWEATHER, L. & MILANA, J. P. 2016. Mass-transport and slope accommodation: implications for turbidite sandstone reservoirs. *AAPG Bulletin,* 100**,** 213-235.

KNIPE, R. 1997. Juxtaposition and seal diagrams to help analyze fault seals in hydrocarbon reservoirs. *AAPG bulletin,* 81**,** 187-195.

KNIPE, R. J., JONES, G. & FISHER, Q. 1998. Faulting, fault sealing and fluid flow in hydrocarbon reservoirs: an introduction. *Geological Society, London, Special Publications,* 147**,** vii-xxi.

KNOX, G. 1982. Taranaki Basin, structural style and tectonic setting. *New Zealand journal of geology and geophysics,* 25**,** 125-140.

KOPF, A. J. 2002. Significance of mud volcanism. *Reviews of Geophysics,* 40**,** 2-1-2-52.

KUMAR, N., GAMBOA, L., SCHREIBER, B. & MASCLE, J. 1977. Geologic history and origin of Sao Paulo Plateau (Southeastern Brazilian Margin), comparison with the Angolan margin and the early evolution of the Northern South Atlantic. *DC, Government Printing Office,* 39**,** 927-945.

LAHANN, R. & SWARBRICK, R. 2011. Overpressure generation by load transfer following shale framework weakening due to smectite diagenesis. *Geofluids,* 11**,** 362-375.

LANSON, B., BEAUFORT, D., BERGER, G., BARADAT, J. & LACHARPAGNE, J.-C. 1996. Illitization of diagenetic kaolinite-to-dickite conversion series:

Late-stage diagenesis of the Lower Permian Rotliegend sandstone reservoir, offshore of the Netherlands. *Journal of Sedimentary Research,* 66.

LASH, G. G. & BLOOD, D. 2004. Geochemical and textural evidence for early (shallow) diagenetic growth of stratigraphically confined carbonate concretions, Upper Devonian Rhinestreet black shale, western New York. *Chemical Geology,* 206**,** 407-424.

LAUBACH, S. E., SCHULTZ-ELA, D. D. & TYLER, R. 1999. Differential compaction of interbedded sandstone and coal. *Geological Society, London, Special Publications,* 169**,** 51-60.

LEE, S. E., TALLING, P. J., ERNST, G. G. & HOGG, A. J. 2002. Occurrence and origin of submarine plunge pools at the base of the US continental slope. *Marine Geology,* 185**,** 363-377.

LEVEILLE, G. P., KNIPE, R., MORE, C., ELLIS, D., DUDLEY, G., JONES, G., FISHER, Q. J. & ALLINSON, G. 1997. Compartmentalization of Rotliegendes gas reservoirs by sealing faults, Jupiter Fields area, southern North Sea. *Geological Society, London, Special Publications,* 123**,** 87-104.

LEVORSEN, A. 1966. The obscure and subtle trap. *AAPG Bulletin,* 50**,** 2058-2067.

LI, M., TAISHENG, G., XUEPING, Z., TAIJUN, Z., RONG, G. & ZHENRONG, D. 1982. Oil basins and subtle traps in the eastern part of China.

LISLE, R. J. & SRIVASTAVA, D. C. 2004. Test of the frictional reactivation theory for faults and validity of fault-slip analysis. *Geology,* 32**,** 569-572.

LISLE, R. J., SRIVASTAVA, D.C. 2004. Test of the frictional reactivation theory for faults and validity of fault-slip analysis. *Geology,* 32**,** 569-572.

LOKHORST, A. & WILDENBORG, T. 2005. Introduction on CO_2 Geological storage-classification of storage options. *Oil & gas science and technology,* 60**,** 513-515.

LONERGAN, L. & CARTWRIGHT, J. A. 1999. Polygonal faults and their influence on deep-water sandstone reservoir geometries, Alba Field, United Kingdom central North Sea. *AAPG bulletin,* 83**,** 410-432.

LØSETH, H., GADING, M. & WENSAAS, L. 2009. Hydrocarbon leakage interpreted on seismic data. *Marine and Petroleum Geology,* 26**,** 1304-1319.

LYNN, G. J., BACCIOTTI, M., VAN BERGEN, P. F. & GRAY, K. R. 2015. Depositional controls on fluid flow in the Gannet A Field. *Geological Society, London, Special Publications,* 403**,** 381-398.

MAGARA, K. 1968. Compaction and migration of fluids in Miocene mudstone, Nagaoka Plain, Japan. *AAPG Bulletin,* 52**,** 2466-2501.

MAGARA, K. 1976. Water expulsion from clastic sediments during compaction--directions and volumes. *AAPG Bulletin,* 60**,** 543-553.

MAGEE, C., BRIGGS, F. & JACKSON, C. A. 2013. Lithological controls on igneous intrusion-induced ground deformation. *Journal of the Geological Society,* 170**,** 853-856.

MAILLARD, A., GAULLIER, V., VENDEVILLE, B. C. & ODONNE, F. 2003. Influence of differential compaction above basement steps on salt tectonics in the Ligurian-Provençal Basin, northwest Mediterranean. *Marine and Petroleum Geology,* 20**,** 13-27.

MAIONE, S. J. & PICKFORD, S. 2001. Discovery of ring faults associated with salt withdrawal basins, Early Cretaceous age, in the East Texas Basin. *The Leading Edge***,** 818-829.

MALLON, A. & SWARBRICK, R. 2002. A compaction trend for non-reservoir North Sea Chalk. *Marine and Petroleum Geology,* 19**,** 527-539.

MALVIĆ, T. & RUSAN, I. 2009. Investment risk assessment of potential hydrocarbon discoveries in a mature basin. Case study from the Bjelovar Sub-Basin, Croatia. *Oil, gas-European Magazine (Hamburg),* 35**,** 67.

MANSFIELD, C. & CARTWRIGHT, J. 1996. High resolution fault displacement mapping from three-dimensional seismic data: evidence for dip linkage during fault growth. *Journal of Structural Geology,* 18**,** 249-263.

MARTIN, R. 1966. Paleogeomorphology and its application to exploration for oil and gas (with examples from western Canada). *AAPG Bulletin,* 50**,** 2277-2311.

MASSON, D., HARBITZ, C., WYNN, R., PEDERSEN, G. & LØVHOLT, F. 2006. Submarine landslides: processes, triggers and hazard prediction. *Philosophical Transactions of the Royal Society of London A: Mathematical, Physical and Engineering Sciences,* 364**,** 2009-2039.

MAYALL, M., JONES, E. & CASEY, M. 2006. Turbidite channel reservoirs—key elements in facies prediction and effective development. *Marine and Petroleum Geology,* 23**,** 821-841.

MCADOO, B. G., CAPONE, M. K. & MINDER, J. 2004. Seafloor geomorphology of convergent margins: Implications for Cascadia seismic hazard. *Tectonics,* 23.

MCFARLAND, J. M., MORRIS, A. P. & FERRILL, D. A. 2012. Stress inversion using slip tendency. *Computers & Geosciences,* 41**,** 40-46.

MCHARGUE, T., PYRCZ, M. J., SULLIVAN, M. D., CLARK, J., FILDANI, A., ROMANS, B., COVAULT, J., LEVY, M., POSAMENTIER, H. & DRINKWATER, N. 2011. Architecture of turbidite channel systems on the continental slope: patterns and predictions. *Marine and Petroleum Geology,* 28**,** 728-743.

MCHARGUE, T. R. & WEBB, J. E. 1986. Internal geometry, seismic facies, and petroleum potential of canyons and inner fan channels of the Indus submarine fan. *AAPG Bulletin,* 70**,** 161-180.

MECKEL, T., TEN BRINK, U. S. & WILLIAMS, S. J. 2007. Sediment compaction rates and subsidence in deltaic plains: numerical constraints and stratigraphic influences. *Basin Research,* 19**,** 19-31.

MEISLING, K. E., COBBOLD, P. R. & MOUNT, V. S. 2001. Segmentation of an obliquely rifted margin, Campos and Santos basins, southeastern Brazil. *AAPG bulletin,* 85**,** 1903-1924.

MELEZHIK, V. A., FALLICK, A. E., RYCHANCHIK, D. V. & KUZNETSOV, A. B. 2005. Palaeoproterozoic evaporites in Fennoscandia: implications for seawater sulphate, the rise of atmospheric oxygen and local amplification of the δ13C excursion. *Terra Nova,* 17**,** 141-148.

MELLO, M. & MAXWELL, J. 1990. Organic Geochemical and Biological Marker Characterization of Source Rocks and Oils Derived from Lacustrine Environments in the Brazilian Continental Margin: Chapter 5.

MERRIAM, D. F. 2005. Origin and development of plains-type folds in the mid-continent (United States) during the late Paleozoic. *AAPG bulletin,* 89**,** 101-118.

MILTON, N. & BERTRAM, G. 1992. Trap Styles: A New Classification Based on Sealing Surfaces (1). *AAPG Bulletin,* 76**,** 983-999.

MINISINI, D., TRINCARDI, F., ASIOLI, A., CANU, M. & FOGLINI, F. 2007. Morphologic variability of exposed mass-transport deposits on the eastern slope of Gela Basin (Sicily channel). *Basin Research,* 19**,** 217-240.

MITRA, S. 1990. Fault-propagation folds: geometry, kinematic evolution, and hydrocarbon Traps (1). *AAPG Bulletin,* 74**,** 921-945.

MIURA, D. 2005. Effects of changing stress states on the development of caldera-bounding faults: Geological evidence from Kumano caldera, Japan. *Journal of volcanology and geothermal research,* 144**,** 89-103.

MOECK, I., G., K. & ZIMMERMANN, G. 2009. Slip tendency analysis, fault reactivation potential and induced seismicity in a deep geothermal reservoir. *Journal of Structural Geology,* 31**,** 1174-1182.

MOECK, I., KWIATEK G., ZIMMERMANN, G. 2009. Slip tendency analysis, fault reactivation potential and induced seismicity in a deep geothermal reservoir. *Journal of Structural Geology,* 31**,** 1174-1182.

MOHRIAK, W., NEMČOK, M. & ENCISO, G. 2008. South Atlantic divergent margin evolution: rift-border uplift and salt tectonics in the basins of SE Brazil. *Geological Society, London, Special Publications,* 294**,** 365-398.

MOHRIAK, W. U., RABELO, J. L., DE MATOS, R. D. & DE BARROS, M. C. 1995. Deep seismic reflection profiling of sedimentary basins offshore Brazil: Geological objectives and preliminary results in the Sergipe Basin. *Journal of Geodynamics,* 20**,** 515-539.

MORRIS, A., FERRILL, D. A. & HENDERSON, D. B. 1996. Slip-tendency analysis and fault reactivation. *Geology,* 24**,** 275-278.

MOSCARDELLI, L. & WOOD, L. 2008. New classification system for mass transport complexes in offshore Trinidad. *Basin research,* 20**,** 73-98.

MOSTAFA, A., SEHIM, A. & YOUSEF, M. Unlocking subtle hydrocarbon plays through 3D seismic and well control: A case study from West Gebel El Zeit district, southwest Gulf of Suez, Egypt. Offshore Mediterranean Conference and Exhibition, 2015. Offshore Mediterranean Conference.

MUELLER, J. C. & WANLESS, H. R. 1957. Differential compaction of Pennsylvanian sediments in relation to sand-shale ratios, Jefferson County, Illinois. *Journal of Sedimentary Research,* 27**,** 80-88.

NALPAS, T., LE DOUARAN, S., BRUN, J.-P., UNTERNEHR, P. & RICHERT, J.-P. 1995. Inversion of the Broad Fourteens Basin (offshore Netherlands), a small-scale model investigation. *Sedimentary Geology,* 95**,** 237-250.

NEELE, F., TEN VEEN, J., WILSCHUT, F. & HOFSTEE, C. 2012. Independent assessment of high-capacity offshore CO_2 storage options. *TNO-report, RCI-ISA Phase,* 3.

NEWNES, S. 2014. *Tectonic reactivation as a control on gas and CO_2 leakage in the Rotliegend reservoir, Dutch North Sea.* MSc Thesis, Cardiff University.

NEWTON, C., SHIPP, R., MOSHER, D. & WACH, G. Importance of mass transport complexes in the Quaternary development of the Nile Fan, Egypt. Offshore Technology Conference, 2004. Offshore Technology Conference.

NEWTON, S. & FLANAGAN, K. The Alba Field: evolution of the depositional model. Geological Society, London, Petroleum Geology Conference series, 1993. Geological Society of London, 161-171.

NUNN, J. A. 1985. State of stress in the northern Gulf Coast. *Geology,* 13**,** 429-432.

NUR, A., MAVKO, G., DVORKIN, J. & GALMUDI, D. 1998. Critical porosity: A key to relating physical properties to porosity in rocks. *The Leading Edge,* 17**,** 357-362.

OGILVIE, S. R. & GLOVER, P. W. 2001. The petrophysical properties of deformation bands in relation to their microstructure. *Earth and Planetary Science Letters,* 193**,** 129-142.

OJEDA, H. 1982. Structural framework, stratigraphy, and evolution of Brazilian marginal basins. *AAPG Bulletin,* 66**,** 732-749.

OMOSANYA, K. D. O. & ALVES, T. M. 2014. Mass-transport deposits controlling fault propagation, reactivation and structural decoupling on continental margins (Espírito Santo Basin, SE Brazil). *Tectonophysics,* 628**,** 158-171.

OMOSANYA, K. O. & ALVES, T. M. 2013. A 3-dimensional seismic method to assess the provenance of Mass-Transport Deposits (MTDs) on salt-rich

continental slopes (Espírito Santo Basin, SE Brazil). *Marine and Petroleum Geology,* 44**,** 223-239.

OSBORNE, M. J. & SWARBRICK, R. E. 1997. Mechanisms for generating overpressure in sedimentary basins: a reevaluation. *AAPG bulletin,* 81**,** 1023-1041.

OUDMAYER, B. C. & DE JAGER, J. Fault reactivation and oblique-slip in the Southern North Sea. *In:* PARKER, J. R., ed. Petroleum Geology of Northwest Europe: Proceedings of the 4th Conference, 1993 London. The Geological Society, 1281-1290.

PASSEY, Q., CREANEY, S., KULLA, J., MORETTI, F. & STROUD, J. 1990. A practical model for organic richness from porosity and resistivity logs. *AAPG bulletin,* 74**,** 1777-1794.

PENGE, J., TAYLOR, B., HUCKERBY, J. & MUNNS, J. Extension and salt tectonics in the East Central Graben. Geological Society, London, Petroleum Geology Conference series, 1993. Geological Society of London, 1197-1209.

PEREZ-GARCIA, C., SAFRONOVA, P., MIENERT, J., BERNDT, C. & ANDREASSEN, K. 2013. Extensional rise and fall of a salt diapir in the Sørvestsnaget Basin, SW Barents Sea. *Marine and Petroleum Geology,* 46**,** 129-143.

PERRIER, R. & QUIBLIER, J. 1974. Thickness changes in sedimentary layers during compaction history; methods for quantitative evaluation. *AAPG Bulletin,* 58**,** 507-520.

PICKERING, K. & HISCOTT, R. 2015. *Deep Marine Systems: Processes, Deposits, Environments, Tectonic and Sedimentation*, John Wiley & Sons.

PICKERING, K. T. & CORREGIDOR, J. 2005. Mass transport complexes and tectonic control on confined basin-floor submarine fans, Middle Eocene, south Spanish Pyrenees. *Geological Society, London, Special Publications,* 244**,** 51-74.

PILAAR, W. & WAKEFIELD, L. 1984. Hydrocarbon generation in the Taranaki basin, New Zealand.

POSAMENTIER, H. W. 2003. Depositional elements associated with a basin floor channel-levee system: case study from the Gulf of Mexico. *Marine and Petroleum Geology,* 20**,** 677-690.

POSAMENTIER, H. W. & KOLLA, V. 2003. Seismic geomorphology and stratigraphy of depositional elements in deep-water settings. *Journal of Sedimentary Research,* 73**,** 367-388.

POUYA, A., DJÉRAN-MAIGRE, I., LAMOUREUX-VAR, V. & GRUNBERGER, D. 1998. Mechanical behaviour of fine grained sediments: experimental compaction and three-dimensional constitutive model. *Marine and Petroleum Geology,* 15**,** 129-143.

POWERS, M. C. 1967. Fluid-release mechanisms in compacting marine mudrocks and their importance in oil exploration. *AAPG bulletin,* 51**,** 1240-1254.

PRATHER, B. E. 2003. Controls on reservoir distribution, architecture and stratigraphic trapping in slope settings. *Marine and Petroleum Geology,* 20**,** 529-545.

PRICE, N. J. & COSGROVE, J. W. 1990. *Analysis of geological structures,* Cambridge, Cambridge University Press.

PURVIS, K. 1992. Lower Permian Rotliegend sandstones, southern North Sea: a case study of sandstone diagenesis in evaporite-associated sequences. *Sedimentary Geology,* 77**,** 155-171.

QIN, Y., ALVES, T., CONSTANTINE, J. A. & GAMBOA, D. 2017. The role of mass wasting in the progressive development of submarine channels (Espirito Santo Basin, SE Brazil). *Journal of Sedimentary Research*.

QUIRK, D. Interpreting the Upper Carboniferous of the Dutch Cleaver Bank High. Geological Society, London, Petroleum Geology Conference series, 1993. Geological Society of London, 697-706.

RACKLEY, S. A. 2017. *Carbon capture and storage*, Butterworth-Heinemann.

RANALLI, G. 2000. Rheology of the crust and its role in tectonic reactivation. *Journal of Geodynamics,* 30**,** 3-15.

REYNOLDS, D. J., STECKLER, M. S. & COAKLEY, B. J. 1991. The role of the sediment load in sequence stratigraphy: The influence of flexural isostasy and compaction. *Journal of Geophysical Research: Solid Earth,* 96**,** 6931-6949.

RISE, L., OLESEN, O., ROKOENGEN, K., OTTESEN, D. & RIIS, F. 2004. Mid-Pleistocene ice drainage pattern in the Norwegian Channel imaged by 3D seismic. *Quaternary Science Reviews,* 23**,** 2323-2335.

RITCHIE, B. D., HARDY, S. & GAWTHORPE, R. L. 1999. Three-dimensional numerical modeling of coarse-grained clastic deposition in sedimentary basins. *Journal of Geophysical Research: Solid Earth,* 104**,** 17759-17780.

ROWAN, M. G. & VENDEVILLE, B. C. 2006. Foldbelts with early salt withdrawal and diapirism: physical model and examples from the northern Gulf of Mexico and the Flinders Ranges, Australia. *Marine and Petroleum Geology,* 23**,** 871-891.

RUSCIADELLI, G. & DI SIMONE, S. 2007. Differential compaction as a control on depositional architectures across the Maiella carbonate platform margin (central Apennines, Italy). *Sedimentary Geology,* 196**,** 133-155.

SALAZAR, M., MOSCARDELLI, L. & WOOD, L. 2016. Utilising clinoform architecture to understand the drivers of basin margin evolution: a case study in the Taranaki Basin, New Zealand. *Basin Research,* 28**,** 840-865.

SALLER, A. H. 1996. Differential compaction and basinward tilting of the prograding Capitan reef complex, Permian, west Texas and southeast New Mexico, USA. *Sedimentary Geology,* 101**,** 21-30.

SAVRDA, C. E. & BOTTJER, D. J. 1988. Limestone concretion growth documented by trace-fossil relations. *Geology,* 16**,** 908-911.

SCHLISCHE, R. W. 1995. Geometry and origin of fault-related folds in extensional settings. *AAPG bulletin,* 79**,** 1661-1678.

SCHOLLE, P. A. 1977. Chalk diagenesis and its relation to petroleum exploration: oil from chalks, a modern miracle? *AAPG bulletin,* 61**,** 982-1009.

SCHOLZ, C. 2007. Fault mechanics. *Treatise on Geophysics (edited by Schubert, G.) Volume,* 6**,** 441-483.

SCHOLZ, C. H. 2002. *The mechanics of earthquakes and faulting*, Cambridge university press.

SCHOWALTER, T. T. 1979. Mechanics of secondary hydrocarbon migration and entrapment. *AAPG bulletin,* 63**,** 723-760.

SCHULTZ, R. A., OKUBO, C. H. & FOSSEN, H. 2010. Porosity and grain size controls on compaction band formation in Jurassic Navajo Sandstone. *Geophysical Research Letters,* 37.

SCOTT, E., GELIN, F., JOLLEY, S., LEENAARTS, E., SADLER, S. & ELSINGER, R. 2010. Sedimentological control of fluid flow in deep marine turbidite reservoirs: Pierce Field, UK Central North Sea. *Geological Society, London, Special Publications,* 347**,** 113-132.

SELLEY, R. C. & SONNENBERG, S. A. 2014. *Elements of petroleum geology*, Academic Press.

SHARP, I. R., GAWTHORPE, R. L., UNDERHILL, J. R. & GUPTA, S. 2000. Fault-propagation folding in extensional settings: Examples of structural style and synrift sedimentary response from the Suez rift, Sinai, Egypt. *GSA Bulletin,* 112**,** 1877-1899.

SHERIFF, R. E. & GELDART, L. P. 1995. *Exploration seismology*, Cambridge university press.

SHULTZ, M., FILDANI, A., COPE, T. & GRAHAM, S. 2005. Deposition and stratigraphic architecture of an outcropping ancient slope system: Tres Pasos Formation, Magallanes Basin, southern Chile. *Geological Society, London, Special Publications,* 244**,** 27-50.

SIBSON, R. H. 1985. A note on fault reactivation. *Journal of Structural Geology,* 7**,** 751-754.

SIBSON, R. H. 1995. Selective fault reactivation during basin inversion: potential for fluid redistribution through fault-valve action. *Geological Society, London, Special Publications,* 88**,** 3-19.

SMITH, D. A. 1966. Theoretical considerations of sealing and non-sealing faults. *AAPG Bulletin,* 50**,** 363-374.

SMITH, J. 1971. The dynamics of shale compaction and evolution of pore-fluid pressures. *Mathematical geology,* 3**,** 239-263.

SNARSKIY, A. 1961. Relationship between primary migration and compaction of rocks.

STAGPOOLE, V. 1999. The Awhitu volcanic complex, an offshore Pliocene volcano in the northern Taranaki Basin, New Zealand. *New Zealand Journal of Geology and Geophysics,* 42**,** 327-334.

STAGPOOLE, V. & FUNNELL, R. 2001. Arc magmatism and hydrocarbon generation in the northern Taranaki Basin, New Zealand. *Petroleum Geoscience,* 7**,** 255-267.

STAGPOOLE, V. & NICOL, A. 2008. Regional structure and kinematic history of a large subduction back thrust: Taranaki Fault, New Zealand. *Journal of Geophysical Research: Solid Earth,* 113.

STEWART, S. A. 1999. Seismic interpretation of circular geological structures. *Petroleum Geoscience,* 5**,** 273-285.

STEWART, S. A. 2006. Implications of passive salt diapir kinematics for reservoir segmentation by radial and concentric faults. *Marine and Petroleum Geology,* 23**,** 843-853.

STEWART, S. A. & COWARD, M. P. 1995. Synthesis of salt tectonics in the southern North Sea, UK. *Marine and Petroleum Geology,* 12**,** 457-475.

STIGALL, J. & DUGAN, B. 2010. Overpressure and earthquake initiated slope failure in the Ursa region, northern Gulf of Mexico. *Journal of Geophysical Research: Solid Earth,* 115.

STIRLING, E. J., FUGELLI, E. M. & THOMPSON, M. The edges of the wedges: a systematic approach to trap definition and risking for stratigraphic, combination and sub-unconformity traps. Geological Society, London, Petroleum Geology Conference series, 2018. Geological Society of London, 273-286.

SUPPE, J. 1983. Geometry and kinematics of fault-bend folding. *American Journal of science,* 283**,** 684-721.

SUPPE, J. & MEDWEDEFF, D. A. 1990. Geometry and kinematics of fault-propagation folding. *Eclogae Geologicae Helvetiae,* 83**,** 409-454.

THRASHER, G., LEITNER, B. & HART, A. Petroleum system of the northern Taranaki graben. 2002 New Zealand Petroleum Conference Proceedings, Auckland, New Zealand, February, 2002. 24-27.

TISSOT, B. W. & WELTE, D. 1984. *Petroleum Formation and Occurrence,* New York, Springler, Dpto.

TRASK, P. D. 1931. Compaction of sediments. *AAPG Bulletin,* 15**,** 271-276.

TRUDE, J., CARTWRIGHT, J., DAVIES, R. J. & SMALLWOOD, J. 2003. New technique for dating igneous sills. *Geology,* 31**,** 813-816.

UNDERHILL, J. R. 2004. Earth science: An alternative origin for the 'Silverpit crater'. *Nature,* 428.

UNDERHILL, J. R. 2009. Role of intrusion-induced salt mobility in controlling the formation of the enigmatic 'Silverpit Crater', UK Southern North Sea. *Petroleum Geoscience,* 15**,** 197-216.

VAN ADRICHEM BOOGAERT, H. & KOUWE, W. 1993. Stratigraphic nomenclature of the Netherlands, revision and update by RGD and NOGEPA. *Mededelingen Rijks Geologische Dienst,* 50**,** 1-40.

VAN ADRICHEM BOOGAERT, H. A. & KOUWE, W. F. P. 1994-1997. Stratigraphic Nomenclature of the Netherlands, revision and update by RGD and NOGEPA. *Mededelingen Rijks Geologische Dienst***,** Section A-J.

VAN BALEN, R., VAN BERGEN, F., DE LEEUW, C., PAGNIER, H., SIMMELINK, H., VAN WEES, J. & VERWEIJ, J. 2000. Modelling the hydrocarbon generation and migration in the West Netherlands Basin, the Netherlands. *Geologie en Mijnbouw,* 79**,** 29-44.

VAN DER MOLEN, A. S. 2004. *Sedimentary development, seismic stratigraphy and burial compaction of the Chalk Group in the Netherlands North Sea area*, UU Dept. of Earth Sciences.

VAN GENT, H., BACK, S., URAI, J. L. & KUKLA, P. 2010. Small-scale faulting in the Upper Cretaceous of the Groningen block (The Netherlands): 3D seismic interpretation, fault plane analysis and regional paleostress. *Journal of Structural Geology,* 32**,** 537-553.

VAN GENT, H. W., BACK, S., URAI, J. L., KUKLA, P. A. & REICHERTER, K. 2009. Paleostresses of the Groningen area, the Netherlands—Results of a seismic based structural reconstruction. *Tectonophysics,* 470**,** 147-161.

VAN HULTEN, F. F. N. Can stratigraphic plays change the petroleum exploration outlook of the Netherlands? Geological Society, London, Petroleum Geology Conference series, 2010a. Geological Society of London, 261-275.

VAN HULTEN, F. F. N. 2010b. Geological factors effecting compartmentalization of Rotliegend gas fields in the Netherlands. *Geological Society, London, Special Publications,* 347**,** 301-315.

VAN RENSBERGEN, P., RABAUTE, A., COLPAERT, A., GHISLAIN, T. S., MATHIJS, M. & BRUGGEMAN, A. 2007. Fluid migration and fluid seepage in the Connemara Field, Porcupine Basin interpreted from industrial 3D seismic and well data combined with high-resolution site survey data. *International Journal of Earth Sciences,* 96**,** 185-197.

VAN WEES, J.-D., STEPHENSON, R., ZIEGLER, P., BAYER, U., MCCANN, T., DADLEZ, R., GAUPP, R., NARKIEWICZ, M., BITZER, F. & SCHECK, M. 2000. On the origin of the southern Permian Basin, central Europe. *Marine and Petroleum Geology,* 17**,** 43-59.

VAN WIJHE, D. V. 1987. Structural evolution of inverted basins in the Dutch offshore. *Tectonophysics,* 137**,** 171-219.

VEEKEN, P. C. 2006. *Seismic stratigraphy, basin analysis and reservoir characterisation*, Elsevier.

VERWEIJ, J., SIMMELINK, H., UNDERSCHULTZ, J. & WITMANS, N. 2012. Pressure and fluid dynamic characterisation of the Dutch subsurface. *Netherlands Journal of Geosciences,* 91**,** 465-490.

VERWEIJ, J. M. & SIMMELINK, H. J. 2002. Geodynamic and hydrodynamic evolution of the Broad Fourteens Basin (The Netherlands) in relation to its petroleum systems. *Marine and Petroleum Geology,* 19**,** 339-359.

VERWEIJ, J. M., SIMMELINK, H. J., VAN BALEN, R. T. & DAVID, P. 2003. History of petroleum systems in the southern part of the Broad Fourteens Basin. *Netherlands Journal of Geosciences,* 82**,** 71-90.

VERWER, K., MERINO-TOMÉ, O., KENTER, J. A. & DELLA PORTA, G. 2009. Evolution of a high-relief carbonate platform slope using 3D digital outcrop models: Lower Jurassic Djebel Bou Dahar, High Atlas, Morocco. *Journal of Sedimentary Research,* 79**,** 416-439.

VIANA, A., FIGUEIREDO, A., FAUGRES, J.-C., LIMA, A., GONTHIER, E., BREHME, I. & ZARAGOSI, S. 2003. The Sao Tom deep-sea turbidite system (southern Brazil Basin): Cenozoic seismic stratigraphy and sedimentary processes. *AAPG bulletin,* 87**,** 873-894.

VIANA, A. R. 2001. Seismic expression of shallow-to deep-water contourites along the south-eastern Brazilian margin. *Marine Geophysical Researches,* 22**,** 509-521.

WAITE, G. P. & SMITH, R. B. 2002. Seismic evidence for fluid migration accompanying subsidence of the Yellowstone caldera. *Journal of Geophysical Research: Solid Earth (1978–2012),* 107**,** ESE 1-1-ESE 1-15.

WALSH, J., BAILEY, W., CHILDS, C., NICOL, A. & BONSON, C. 2003. Formation of segmented normal faults: a 3-D perspective. *Journal of Structural Geology,* 25**,** 1251-1262.

WALSH, J. J., NICOL, A. & CHILDS, C. 2002. An alternative model for the growth of faults. *Journal of Structural Geology,* 24**,** 1669-1675.

WARD, N. I., ALVES, T. M. & BLENKINSOP, T. G. 2018. Differential compaction over Late Miocene submarine channels in SE Brazil: Implications for trap formation. *GSA Bulletin,* 130**,** 208-221.

WEBSTER, M., O'CONNOR, S., PINDAR, B. & SWARBRICK, R. 2011. Overpressures in the Taranaki Basin: Distribution, causes, and implications for exploration. *AAPG bulletin,* 95**,** 339-370.

WEIJERMARS, R. 2013. Economic appraisal of shale gas plays in Continental Europe. *Applied energy,* 106**,** 100-115.

WELLER, J. M. 1959. Compaction of sediments. *AAPG Bulletin,* 43**,** 273-310.

WILLIAMS, S. 1987. Faulting in abyssal-plain sediments, Great Meteor East, Madeira Abyssal Plain. *Geological Society, London, Special Publications,* 31**,** 87-104.

WIPRUT, D. & ZOBACK, M. D. 2000. Fault reactivation and fluid flow along a previously dormant normal fault in the northern North Sea. *Geology,* 28**,** 595-598.

WIPRUT, D. & ZOBACK, M. D. 2002. Fault reactivation, leakage potential, and hydrocarbon column heights in the northern North Sea. *Norwegian Petroleum Society Special Publications,* 11**,** 203-219.

WONG, T. E., PARKER, N. & HORST, P. 2001. Tertiary sedimentary development of the Broad Fourteens area, the Netherlands. *Geologie en Mijnbouw,* 80**,** 85-94.

WOOD, J. M. & HOPKINS, J. C. 1989. Reservoir sandstone bodies in estuarine valley fill: Lower Cretaceous Glauconitic Member, Little Bow Field, Alberta, Canada. *AAPG Bulletin,* 73**,** 1361-1382.

WOOD, J. M. & HOPKINS, J. C. 1992. Traps Associated with Paleovalleys and Interfluves in an Unconformity Bounded Sequence: Lower Cretaceous Glauconitic Member, Southern Alberta, Canada (1). *AAPG Bulletin,* 76**,** 904-926.

WOODCOCK, N. H. 1976. Structural style in slump sheets: Ludlow series, Powys, Wales. *Journal of the Geological Society,* 132**,** 399-415.

WORUM, G. & VAN WEES, J.-D. 2017. High-resolution quantitative reconstruction of Late Cretaceous-Tertiary erosion in the West Netherlands Basin using multi-formation compaction trends and seismic data: implications for geothermal exploration. *Acta Geodaetica et Geophysica,* 52**,** 243-268.

XU, S., HAO, F., XU, C., WANG, Y., ZOU, H. & GONG, C. 2015. Differential compaction faults and their implications for fluid expulsion in the northern Bozhong Subbasin, Bohai Bay Basin, China. *Marine and Petroleum Geology,* 63**,** 1-16.

YANG, Y. & APLIN, A. C. 1998. Influence of lithology and compaction on the pore size distribution and modelled permeability of some mudstones from the Norwegian margin. *Marine and Petroleum Geology,* 15**,** 163-175.

YILMAZ, Ö. 2001. *Seismic data analysis*, Society of Exploration Geophysicists Tulsa.

ZE, T. & ALVES, T. M. 2017. The role of gravitational collapse in controlling the evolution of crestal fault systems (Espírito Santo Basin, SE Brazil)-Reply. *Journal of Structural Geology,* 98**,** 12-14.

ZHANG, Z., WANG, W., REN, Z., ZHANG, P., FANG, L. & WU, J. 2013. Lushan M S7. 0 earthquake: A special earthquake occurs on curved fault. *Chinese Science Bulletin,* 58**,** 3483-3490.

ZIEGLER, P. 1992. North Sea rift system. *Tectonophysics,* 208**,** 55-75.

ZIEGLER, P. A. 1990. *Geological atlas of western and central Europe*, Shell Internationale Petroleum, Maatschappij B.V., The Hague.

ZIEGLER, P. A., CLOETINGH, S. & VAN WEES, J.-D. 1995. Dynamics of intra-plate compressional deformation: the Alpine foreland and other examples. *Tectonophysics,* 252**,** 7-59.

ZIOLKOWSKI, A., UNDERHILL, J. R. & JOHNSTON, R. G. 1998. Wavelets, well ties, and the search for subtle stratigraphic traps. *Geophysics,* 63**,** 297-313.

ZOBACK, M. D. 2010. *Reservoir geomechanics*, Cambridge University Press.